DISSERTATION

submitted to the

Combined Faculty of Mathematics, Engineering and Natural Sciences

of Heidelberg University, Germany

for the degree of

Doctor in Natural Sciences

put forward by

Irène Elisabeth Brumer

born in Munich, Germany

Oral examination: November 30^{th} 2022

Arterial Spin Labelling MRI for non-invasive perfusion quantification in the brain and in the kidneys

Referees: Prof. Dr. rer. nat. Lothar R. Schad
Priv.-Doz. Dr. rer. nat. Tristan A. Kuder

Pour les petit·e·s et les grand·e·s.
Pour tous celleux qui font de leur mieux.

Arterielle Spin Markierung MRT für die nicht-invasive Quantifizierung der Perfusion im Gehirn und in den Nieren

Arterielle Spin Markierung (ASL) Magnetresonanztomographie ermöglicht eine völlig nicht-invasive Quantifizierung der Durchblutung, welche zur Bewertung der Gewebefunktion, -aktivität und -lebensfähigkeit wertvoll ist. Jedoch hat sich diese Technik weltweit noch nicht in der klinischen Routine etabliert, teilweise aufgrund fehlender Standardisierung. Ziel dieser Arbeit ist es einen Beitrag zum Übergang der ASL in die klinische Routine zu leisten, indem Variabilitätsquellen in der AS-basierten Pefusionsquantifizierung im Gehirn und in den Nieren untersucht werden. Erstens, wurden Quantifizierungsergebnisse, die mit unterschiedlichen Verarbeitungsoptionen und Korrekturen oder mit unterschiedlichen Aufnahmeparametern erhalten wurden, verglichen. Dafür wurden synthetische Daten, Daten von gesunden Probanden und Patientendaten analysiert. Es ergaben sich signifikante Unterschiede in der Perfusionsquantifizierung bei unterschidédlichen Verarbeitungsoptionen und Korrekturen und mit unterschiedlichen Aufnahmeparametern. Zweitens, wurden synthetische ASL-Datensätze von den Nieren, die In-vivo Aufnahmen imitieren, generiert. Eine Datenanalyse-Pipeline wurde entwickelt und anhand der synthetischen Datensätze getestet. Die Registrierung verlief für beide Nieren gut, wobei die mittleren strukturellen Ähnlichkeitsindexmaße um durchschnittlich 25% zunahmen. Die Quantifizierung der kortikalen und medullären Perfusionswerte stimmte mit einem mittleren prozentualen Unterschied von 21% und 16% zu den für die Erzeugung der synthetischen Datensätze angenommenen kortikalen und medullären Perfusionswerten überein. Die Segmentierungsergebnisse aus der Verarbeitungspipeline stimmten gut mit den ursprünglichen Segmentierungen überein, mit Dice-Indizes im Bereich von 0,80–0,93, 0,78–0,89, und 0,64–0,84 für gesamte Niere, Kortex, und Medulla. Drittens, wurden ASL-Datensätze der Nieren in gesunden Probanden erhoben und mit der entwickelten Datenanalyse-Pipeline analysiert. Für jede Person, wurden vier ASL-Messungen durchgeführt, die zwischen freier Atmung oder synchronisierter Atmung und mit oder ohne Herz-Trigger variiert haben. Die Registrierung war am erfolgreichsten, wenn das gesamte Bild betrachtet wurde, mit einer Erfolgsquote von 87% und einer durchschnittlichen Dauer von 30 Minuten. Prozentuale Unterschiede zwischen Literaturwerten und mittleren Perfusionswerten waren gleich oder kleiner als 32%, 61%, und 53% für die gesamte Niere, den Kortex, und die Medulla. Gemittelt über alle Probanden waren die Perfusionswerte, die für die vier verschiedenen Messungen erhalten wurden, nur signifikant unterschiedlich zwischen freier Atmung und synchronisierter Atmung bei Betrachtung der gesamten linken Niere. Das zeitliche Signal-zu-Rausch Verhältnis wies keinen signifikanten Unterschied zwischen den vier Messungen auf. Weiterhin war die gemessene Nierendurchblutung abhängig von der gewählten Triggerverzögerung für den Herz-Trigger. Die Studienergebnisse legen nahe, dass eine Messung mit freier Atmung und ohne Herz-Trigger die beste Wahl für klinische Anwendungen ist.

Arterial Spin Labelling MRI for non-invasive perfusion quantification in the brain and in the kidneys

Arterial spin labelling (ASL) magnetic resonance imaging allows completely non-invasive quantification of perfusion and is valuable for the evaluation of tissue function, activity, and viability. However, it has not yet been established in the clinical routine world-wide partly due to a lack of standardisation. This thesis aims to contribute to the transition of ASL into the clinical routine by investigating sources of variability in ASL-based perfusion quantification in the brain and in the kidneys. Firstly, quantification results obtained with different processing options and corrections or with different acquisition parameters were compared using synthetic data, data from healthy volunteers, and patient data. Differences in acquisition parameters and processing options used for analysis of brain ASL data resulted in significant differences in perfusion quantification. Secondly, synthetic ASL data sets of the kidneys mimicking in vivo acquisitions were generated. A data analysis pipeline was developed and evaluated using the synthetic data sets. The registration performed well for both kidneys, with mean structural similarity index measures increasing by 25% on average. The quantification yielded cortical and medullary perfusion values that agreed with a mean percentage difference of 21% and 16% for cortex and medulla, respectively, to the perfusion assumed for the generation of the synthetic data sets. Segmentation results from the processing pipeline agreed well with original segmentation masks, with Dice indices ranging 0.80-0.93, 0.78-0.89, and 0.64-0.84 for whole kidney, cortex, and medulla, respectively. Thirdly, kidney ASL data were acquired in healthy volunteers and analysed with the developed processing pipeline. Four ASL measurements were performed for each subject varying between free breathing or synchronised breathing and with or without cardiac triggering. Registration performed best when considering the entire image, with a 87% success rate and a mean duration of 30 minutes. Percentage differences between literature values and mean perfusion values were equal to or below 32%, 61%, and 53% for whole kidney, cortex, and medulla, respectively. Across subjects, perfusion values obtained for the four different measurements were only significantly different between the free breathing and synchronised breathing measurement when considering the whole left kidney. Temporal signal-to-noise ratio was not found to differ significantly between the four measurements. Renal perfusion was found to depend on the trigger delay chosen for cardiac triggering. This study's results suggest that an acquisition in free breathing without cardiac triggering is the best choice for clinical applications.

Chi la dura la vince ...

Acknowledgements

First, I would like to thank Prof. Dr. L. R. Schad for the opportunity to undertake my PhD research at his chair, especially for the support for collaborations with other research groups and for conference attendances.

My thanks also go to Priv.-Doz. Dr. T. A. Kuder for being the second referee for this thesis, and to Dr. J. Chacón Caldera and Dr. S. Hubertus for their support at the beginning of the project.

I warmly thank the ASL research group of Dr. M. A. Fernández Seara at the Clínica Universidad de Navarra for allowing and fostering a fruitful research collaboration. Thank you María and Rebeca for always being available for discussions and for answering my questions.

I also want to thank the students I had the opportunity to supervise on various projects. Thank you for your enthusiasm and dedication to your projects. Working with you has allowed me to improve my project planning, supervision and mentoring skills and I am very thankful for this.

Humble thanks to Safa, Valerie, Maša, Sophia, Anna, and Luis for proof reading parts of this thesis and thank you to all volunteers who agreed to be scanned for this thesis. Special thanks go to Safa, Sophia, Marco, Ruomin, Jorge, Tanja, and Nadia who provided me with valuable guidance and helpful support on and off topic during challenging phases of my PhD time.

Thank you to Safa, Valerie, Efe, Jorge, Ingo, Anne, Yannik, Ann-Sophie for making my time in Mannheim and Heidelberg so enjoyable. And thank you to all PhD students of CKM for the engaging after lunch discussions, the entertaining Feierabendbier times, the memorable conference experiences, the welcome Kicker breaks, and many bouldering sessions.

Last but not least, I thank Luis and both our families for always being there for me and for their loving support throughout my PhD journey.

Table of Contents

List of Figures

List of Tables

Abbreviations

AIF	arterial input function
AOC	adaptive outlier cleaning
AS	average and subtract
ATT	arterial transit time
ASL	arterial spin labelling
BBB	blood-brain-barrier
BS	background suppression
CBF	cerebral blood flow
CNR	contrast-to-noise ratio
CSF	cerebrospinal fluid
CT	computed tomograph
DCE	dynamic contrast enhanced
DI	Dice index
DRO	digital reference object
DSC	dynamic susceptibility weighted
ECG	electrocardiogram
EES	extravascular extracellular space
EPI	echo-planar imaging
FAIR	flow-sensitive alternating inversion recovery
FB	free breathing
FOCI	frequency offset corrected inversion
FOV	field of view
GKM	general kinetic model
GRE	gradient echo
GRAPPA	generalised autocalibrating partial parallel acquisition
GRASE	gradeint and spin echo
GW	grey matter
HASTE	half-fourier acquisition single-shot turbo spin echo
IR	inversion recovery
LD	labelling duration
MI	mutual infomration
MPRAGE	magnetisation prepared rapid gradient echo
MRI	magnetic resonance imaging
MSSIM	mean structural similarity index measure
MT	magnetisation transfer
NMR	nuclear magnetic resonance
OSIPI	open source initiative for perfusion imaging

pAOCSL	priors-guided slice-wise adaptive outlier cleaning
PCC	Pearson correlation coefficient
PD	proton density
PET	positron emission tomography
PLD	post labelling delay
QUIPSS	quantitative imaging of perfusion using a single substraction
QUIPSS II	quantitative imaging of perfusion using a single substraction version 2
RBF	renal blood flow
RF	radiofrequency
rpm	rounds per minute
SA	subtract and average
SAR	specific absorption rate
SB	synchronised breathing
SCORE	structural correlation-based outlier rejection
SE	spin echo
SENSE	sensitivity encoding
SNR	signal-to-noise ratio
SPECT	single photon emission computed tomography
SR	saturation recovery
TE	echo time
TI	inversion time
TR	repetition time
TSE	turbo spin echo
US	ultrasound
VIBE	volumetric interpolated breath-hold examination
WM	white matter
1D	one-dimensional
2D	two-dimensional
3D	three-dimensional

CHAPTER 1

Introduction

Perfusion (blood flow) is an important indicator of tissue function, activity, and viability as cells require continuous supply of nutrients and oxygen. This supply is delivered by the blood via the arteries and capillary beds of tissue. A decreased perfusion (hypoperfusion) or absence of perfusion limits organ function and can result in cell death. An increased perfusion (hyperperfusion) indicates an increased vascularisation and requirement of nutrients and oxygen, which is often linked to angiogenesis and abnormal cell growth occurring during tumour development. Perfusion evaluation and accurate quantification have important clinical relevance for various organs and diseases. This work focuses on perfusion in the brain and in the kidneys.

A perfusion of about 50 mL/100g/min for the entire adult brain and a perfusion ratio of 2-7 between grey and white matter is considered normal [*Wintermark et al.*, 2004; *Zaharchuk*, 2007; *van Gelderen et al.*, 2008]. Cerebral blood flow (CBF) has been shown to vary depending on age with differences from brain region to brain region [*Wintermark et al.*, 2004]. The study of CBF variations during brain development and growth are useful for understanding brain function development as well as supporting diagnosis and therapy of neurological disorders [*Biagi et al.*, 2007]. The evolution of regional and local CBF can also yield insights in mechanisms of cognitive ageing [*Haller et al.*, 2016; *Staffaroni et al.*, 2019]. For example, the assessment of perfusion allows distinction between mild cognitive impairment and early-onset Alzheimer's disease [*Zhang et al.*, 2017] and can predict the transition from mild cognitive impairment to dementia [*Chao et al.*, 2010]. CBF assessment can also provide information about potential occlusion of feeding arteries. This is highly valuable as complete occlusion of the internal carotid artery, for example, is known to heighten the risk of ischemic stroke occurrence and can result in death [*Thanvi and Robinson*, 2007]. Perfusion imaging is also relevant for the diagnosis of ischemic stroke and supports treatment decisions [*Kim et al.*, 2014]. Another widespread application in the medical field of perfusion assessment is oncology. Perfusion assessment

supports differentiation between tumour types, determination of tumour margins, and tumour grading [*Cho et al.*, 2002; *Provenzale et al.*, 2006].

Kidneys are highly perfused organs, with a normal whole kidney perfusion averaging about 220-230 mL/100g/min in adults [*Gillis et al.*, 2014, 2016]. Good kidney function is directly dependent on normal blood flow, making it an important renal biomarker [*Ebrahimi et al.*, 2014]. Acute kidney injury and impaired perfusion are in fact closely associated [*Dong et al.*, 2013; *Johnson et al.*, 2014]. Furthermore, cortical perfusion has been found to be decreased in patients suffering from chronic kidney disease [*Rossi et al.*, 2012; *Gillis et al.*, 2016; *Cai et al.*, 2017; *Li et al.*, 2017; *Zhang and Lee*, 2020] and to vary depending on the disease stage [*Mora-Gutiérrez et al.*, 2017]. Perfusion is also critical for renal allografts [*Lanzman et al.*, 2010; *Hueper et al.*, 2015; *Ren et al.*, 2016] and allows differentiation between allograft rejection and tubular necrosis [*Notohamiprodjo et al.*, 2010]. Other clinical applications of renal perfusion assessment are artery stenosis and tumours [*Grenier et al.*, 2013].

The first quantitative assessment of perfusion in humans was performed by tracking the inflow of inhaled gas in the subject's blood stream by sampling arterial and venous blood over time [*Kety and Schmidt*, 1945]. This approach is invasive, time and resource intensive, and has since then been replaced by imaging methods such as positron emission tomography (PET), single photon emission computed tomography (SPECT), computed tomography (CT), ultrasound (US), and magnetic resonance imaging (MRI). PET and SPECT are based on the use of radioactive tracer molecules, which entails complex logistics and is invasive. CT is also an invasive imaging modality as it is based on ionising radiation (x-rays) and requires the injection of contrast agent for perfusion assessment. US imaging uses sound waves and is non-invasive. However, it is limited in imaging depth and thus not suitable for every tissue in the human body. MRI makes use of the nuclear magnetic resonance properties of nuclei in an external magnetic field. It is well known for the variety of image contrasts achievable and can yield both anatomical and functional (e.g. perfusion) information. PET with ^{15}O labelled water tracer is considered as the gold standard imaging modality for correct in vivo perfusion quantification [*Herscovitch et al.*, 1983; *Raichle et al.*, 1983] but CT, US, and MRI are more commonly used in the clinical routine due to higher availability and simpler logistics. This work focuses on MRI-based perfusion quantification.

MRI-based perfusion techniques either use exogenous or endogenous contrast agents. Protons in arterial blood are the relevant endogenous contrast agents and exogenous MRI contrast agents are usually gadolinium-based. While older linear gadolinium-based MRI contrast agents found to cause nephrogenic systemic fibrosis have been banned from use in medicine [*Thomsen et al.*, 2007], the use of gadolinium-based contrast agents in MRI

still is an important topic in the medical community due to safety concerns [*McDonald et al.*, 2018]. In the past decade, multiple studies have shown that gadolinium present in contrast agents commonly used for MRI perfusion imaging is retained in the skin, in abdominal organs, in bones, and in important areas of the brain, such as the hypothalamus and cerebellum [*Kanda et al.*, 2015; *Radbruch et al.*, 2015; *Quattrocchi and Van der Molen*, 2021; *Al-Muhanna*, 2022]. Even though no negative effects of this retention have been demonstrated to date, it is preferred to avoid any contrast agent injection, especially for the paediatric population, patients with poor kidney function, and patients requiring multiple follow-ups for disease monitoring. The importance of a robust and accurate perfusion imaging technique without exposure to ionising radiation and exogenous contrast agent is evident and motivated the focus of this work on the completely non-invasive perfusion MRI technique called arterial spin labelling (ASL).

ASL makes use of blood water protons as an endogenous tracer to image perfusion. For this, blood water protons present in the arteries delivering blood to the organ of interest are magnetically labelled by spin inversion. After an inflow time, the labelled blood flows into the imaging region and images are acquired. An ASL experiment consists of acquiring a calibration image, referred to as M0, and one or multiple pairs of control and labelled images. The difference between labelled and control images lies in the presence or absence of labelling of the feeding arteries. After acquisition, labelled images are subtracted from control images and averaged to obtain a perfusion-weighted image. A quantitative perfusion map is then calculated based on a kinetic model with the perfusion-weighted image, the M0 image, acquisition-dependent parameters, and other constants as input [*Alsop et al.*, 2015; *Nery et al.*, 2020]. Despite its advantages, ASL faces multiple challenges (e.g. low signal-to-noise ratio, motion sensitivity, lengthy acquisitions) and has not yet made a breakthrough in the clinical routine worldwide. The lack of standardisation due to the multitude of existing acquisition and processing schemes and the lack of experience of clinicians with ASL are additional reasons for the absence of ASL in the clinical routine [*Essig et al.*, 2013a]. Nevertheless, the technique has shown promising results in both children and adult patients for various clinical applications (e.g. vascular abnormalities [*Jezzard et al.*, 2018; *Ho*, 2018; *Keil et al.*, 2019], ischemic stroke [*MacIntosh et al.*, 2010; *Bokkers et al.*, 2012; *Wintermark and Warfield*, 2012; *Ho*, 2018; *Keil et al.*, 2019], cognitive impairment [*Sun et al.*, 2016; *Chandra et al.*, 2019], epilepsy [*Pendse et al.*, 2010; *Pasca et al.*, 2021; *Ho*, 2018; *Keil et al.*, 2019], tumours [*Razek et al.*, 2019; *Luna et al.*, 2022; *De Bazelaire et al.*, 2005; *Lanzman et al.*, 2012], neurological disorders [*Haller et al.*, 2016], traumatic brain injury and infection [*Ho*, 2018], acute kidney injury [*Dong et al.*, 2013; *Johnson et al.*, 2014], chronic kidney disease [*Rossi et al.*, 2012; *Gillis et al.*, 2016; *Cai et al.*, 2017], renal transplantation [*Lanzman et al.*, 2010; *Hueper et al.*, 2015; *Ren et al.*, 2016]). Improved standardisation of ASL across centres will allow large scale clinical trials

to improve the understanding, diagnosis, treatment, and monitoring of blood flow altering diseases.

Variability in evaluation of organ perfusion can be caused by various effects. The measurement itself involves a large number of degrees of freedom, including the choice of labelling, readout, scanner, as well as subject compliance and individual anatomy. In addition to these data acquisition related sources of variability, differences in processing pipelines across centres further hinder useful comparison of organ perfusion quantification. This thesis aims to contribute to the standardisation of ASL for perfusion quantification in the brain and in the kidneys. For this, three projects were pursued:

(i) The comparison of different processing options and corrections for perfusion quantification in the brain.

(ii) The creation of synthetic ASL data sets of the kidneys for evaluation and comparison of processing pipelines.

(iii) The evaluation of the choice of registration strategy, the effect of respiration strategy, and the effect of electrocardiogram (ECG) triggering on ASL-based quantification of renal perfusion.

For the first project, a processing pipeline for brain ASL data was developed. Data from the ASL challenge [*Anazodo and Croal*, 2021; *Anazodo et al.*, 2021] as well as healthy volunteer data and patient data acquired at the University Hospital Mannheim were analysed. The processing pipeline comprises the realignement of all ASL images, the segmentation of the brain volume into gray matter, white matter, and CSF compartments, the registration of the anatomical data to the ASL data, the quantification according to the general kinetic model [*Buxton et al.*, 1998], and the generation of brain compartment specific perfusion maps. It includes different options for the calculation of the perfusion-weighted image, for the removal of outliers from the ASL data, and for corrections performed on the M0 image. All different options were compared using the challenge and healthy volunteer data. In addition, an evaluation of the effect of smoothing on the M0 image and a comparison between segmentation performed on the anatomical data or on the M0 image were performed. The patient data was analysed with the developed processing pipeline to evaluate whether disease indications visible on anatomical images could be recognised in the quantified perfusion maps.

For the second project, synthetic ASL data sets of the kidneys simulating in vivo acquisitions were produced and a data processing pipeline for renal ASL data was developed. The synthetic data sets were made publicly available[1] for wide-spread use in the research

[1] `https://doi.org/10.11588/data/QAHWSF`, *last accessed 26.08.2022*

community. Starting from models of the XCAT phantom [*Segars et al.*, 2010], MRI data of the abdomen was generated and perfusion signal was added based on the general kinetic model [*Buxton et al.*, 1998]. Respiratory motion was included in the generated data sets to mimic free breathing in vivo acquisitions. The processing pipeline consists of registration, quantification, and segmentation steps. The processing pipeline was evaluated step-by-step using the synthetic data sets. Registration performance was evaluated qualitatively with line profiles and quantitatively with mean structural similarity index measures [*Wang et al.*, 2004]. Perfusion values obtained from the pipeline were compared to the values assumed when generating the synthetic data. Segmentation masks obtained by semi-automated procedure of the processing pipeline were compared to the original XCAT organ masks using the Dice index [*Dice*, 1945]. Parts of this project were published in [*Brumer et al.*, 2022a].

For the third project, renal ASL data of healthy volunteers was acquired. Four ASL measurements were performed on each subject varying between free breathing or synchronised breathing and with or without ECG triggering. The available data was then analysed using the previously developed processing pipeline. A focus was set on the registration step and registration was performed with different area of the images to be considered: whole image, half image for separate left and right kidney registration, small manually drawn rectangle for separate left and right kidney registration. The quality of registration was assessed qualitatively in terms of success rate and quantitatively with mean structural similarity index measures [*Wang et al.*, 2004] and entropy correlation coefficients [*Maes et al.*, 1997]. Finally, using the best registration option, the effect of respiration strategy and ECG triggering on the final perfusion values was evaluated. Parts of this project were presented at international conferences [*Brumer et al.*, 2022b,c].

CHAPTER 2

Theoretical Background

This chapter covers the theoretical principles necessary to understand the subsequent work. In the first part, the fundamental processes of nuclear magnetic resonance (NMR) will be described. In the second part, the components necessary for moving from the detection of an NMR signal to the creation of a magnetic resonance (MR) image will be illustrated.[1] In the third part, the term perfusion will be defined and the technique arterial spin labelling (ASL), which is central to this work, will be explained. In the final part, basic anatomy information will be given for the organs considered in this work.

2.1 Nuclear Magnetic Resonance

Nuclear magnetic resonance (NMR) can occur when a nucleus subject to a constant external magnetic field is perturbed by a time-varying magnetic field. This perturbation triggers a response of the nucleus in form of an electromagnetic signal with a characteristic frequency depending on the nucleus and the external magnetic field. The physical phenomenon of NMR happens when the perturbation frequency is close to the intrinsic frequency of the nucleus, i.e., on-resonance. It is important to note, that this intrinsic frequency depends on the chemical and magnetic environment of the nucleus.

The origin of nuclear magnetic resonance (NMR) can be set to the discovery of a fundamental quantum mechanical property of nuclei, the intrinsic angular momentum or spin, by Otto Stern and Walther Gerlach in 1922 [*Gerlach and Stern*, 1922]. In the 1930's, Isidor Isaac Rabi extended this experiment and was able to observe NMR in molecular beams for the very first time [*Rabi et al.*, 1938]. For this discovery, he obtained the Nobel

[1] For a more detailed description of NMR and MR imaging, the reader is referred to [*Brown et al.*, 2014] and [*Nishimura*, 1996].

Prize in Physics in 1944. A decade after Rabi's observations, Edward Mills Purcell and Felix Bloch observed NMR in condensed matter [*Purcell et al.*, 1946; *Bloch*, 1946], for which they obtained the Nobel Prize in Physics in 1952. In the 1960's and 1970's, first applications of NMR in chemistry (Richard R. Ernst and Kurt Wüthrich) and medicine (Raymond V. Damadian) took place. To this date, NMR is still central to a multitude of research projects in physics, chemistry, biology, and medicine.

In the following sections, the properties of nuclear spin and magnetic moment, the Zeeman effect, the macroscopic magnetisation, and its dynamics governed by the Bloch equations, as well as the typical NMR signal acquisition are detailed.

2.1.1 Nuclear spin and magnetic moment

Protons and neutrons make up atomic nuclei. These two nucleons are fermions and possess an intrinsic angular momentum with spin quantum number $s = 1/2$. The total angular momentum j of a nucleon is given by the sum of its orbital angular momentum l and its spin angular momentum s: $j = |l \pm s| = |l \pm 1/2|$. Summing the total angular momentum j of all nucleons contained in a nucleus yields the total angular momentum of the nucleus itself, known as nuclear spin $\hat{\vec{I}}$. For an odd number of protons and/or neutrons, the spins of the nucleons do not cancel each other out, resulting in a non-zero nuclear spin. The nuclear spin being an angular momentum, its quantum mechanical operator $\hat{\vec{I}}$ fulfils the following commutator relations

$$[\hat{I}_i, \hat{I}_j] = i\hbar\epsilon_{ijk}\hat{I}_k \qquad\qquad [\hat{\vec{I}}_i, \hat{I}^2] = 0 \tag{2.1}$$

with the Levi-Civita or permutation symbol ϵ_{ijk} and the reduced Planck's constant $\hbar = \frac{h}{2\cdot\pi} = \frac{6.626\cdot10^{-34}\text{Js}}{2\cdot\pi}$. As $\hat{I}_i$ and $\hat{I}^2$ commute, a complete basis can be constructed with their mutual eigenstates $|I,\ m\rangle$. The eigenequations for the magnitude of the nuclear spin and its z-component (assuming a quantisation axis along the z-axis, without loss of generality) are

$$\hat{I}^2\,|I, m_I\rangle = I(I+1)\hbar^2\,|I, m_I\rangle \qquad\qquad \hat{I}_z\,|I, m_I\rangle = m_I\hbar\,|I, m_I\rangle \tag{2.2}$$

with the nuclear spin quantum number I, and the magnetic quantum number m_I. I expresses the allowed spin states of the nucleus ($I = 0, 1/2, 1, 3/2, ...$) and m_I describes the spatial orientation of the spin with respect to the z-axis with values $m_I = -I, -I+1, ..., I-1, I$. In the absence of an external magnetic field, there are $(2I+1)$ degenerate quantum states for a nucleus with nuclear spin I (m_I degeneracy). The nucleus of a hydrogen atom consists of a single proton ($I = j = s = 1/2$) and therefore $\hat{I}_z$ has two

eigenvalues: $m = \pm 1/2$. These eigenvalues correspond to the spin up and spin down states: $|1/2, +1/2\rangle$ and $|1/2, -1/2\rangle$, respectively.

Analogue to classical angular momenta, this nuclear spin is associated to a magnetic moment

$$\vec{\mu} = \gamma \vec{I} \tag{2.3}$$

where γ is a nucleus-specific constant called the gyromagnetic ratio. It can be expressed as multiples of the nuclear magneton μ_N

$$\gamma = \frac{g\ \mu_N}{\hbar} = \frac{g\ e}{2m_p} \tag{2.4}$$

with the experimentally determined Landé factor g, the proton charge $e = 1.602 \cdot 10^{-19}$ C, and the proton mass $m_p = 1.67 \cdot 10^{-27}$ kg. For protons the Landé factor is $g = 5.586$. Several nuclei present in the human body and their magnetic porperties are listed in Table 2.1.

Table 2.1: **Different nuclei present in the human body and their magnetic properties** - nuclear spin I, magnetic moment μ in units of nuclear magneton μ_N, and gyromagnetic ration γ divided by 2π. Adapted from [*Brown et al.*, 2014].

Nucleus	I	μ/μ_N	$\gamma/(2\pi)$ [MHz/T]
^{1}H	1/2	2.793	42.58
^{23}Na	3/2	2.216	11.27
^{31}P	1/2	1.131	17.25
^{17}O	5/2	-1.893	-5.77
^{19}F	1/2	2.627	40.08

2.1.2 Zeeman effect

As is common in NMR nomenclature, the magnetic flux density $\vec{B}$ will be referred to as magnetic field in this work. In the presence of an external magnetic field, the energy levels for nuclear spin states with same nuclear spin quantum number I but different magnetic quantum numbers m_I split up: the m_I degeneracy can be resolved. Without loss of generality, let us assume the external magnetic field with magnitude B_0 is oriented along the positive z-axis. The following Hamiltonian can then be used to describe the interaction of the nuclear spin I with the external magnetic field $\vec{B_0} = (0, 0, B_0)^T$:

$$\hat{\mathcal{H}} = -\hat{\vec{\mu}} \cdot \vec{B_0} = -\gamma \hat{\vec{I}} \cdot \vec{B_0} = -\gamma \hat{I}_z B_0 \tag{2.5}$$

Using this time-independent Hamiltonian, the stationary Schrödinger equation

$$\hat{\mathcal{H}} |I, m_I\rangle = E_m |I, m_I\rangle \tag{2.6}$$

can be used to calculate the eigenenergies E_m of the system

$$E_m |I, m_I\rangle = -m\hbar\gamma B_0 |I, m_I\rangle \tag{2.7}$$

For the case of $I = 1/2$, the eigenenergies are

$$E_{+1/2} = -\frac{\hbar}{2}\gamma B_0 \qquad\qquad E_{-1/2} = +\frac{\hbar}{2}\gamma B_0 \tag{2.8}$$

resulting in an energy difference between the two states of

$$\Delta E = \gamma\hbar B_0 \tag{2.9}$$

The splitting of these two energy levels in the presence of an external magnetic field is known as the Zeeman effect and is depicted in Figure 2.1.

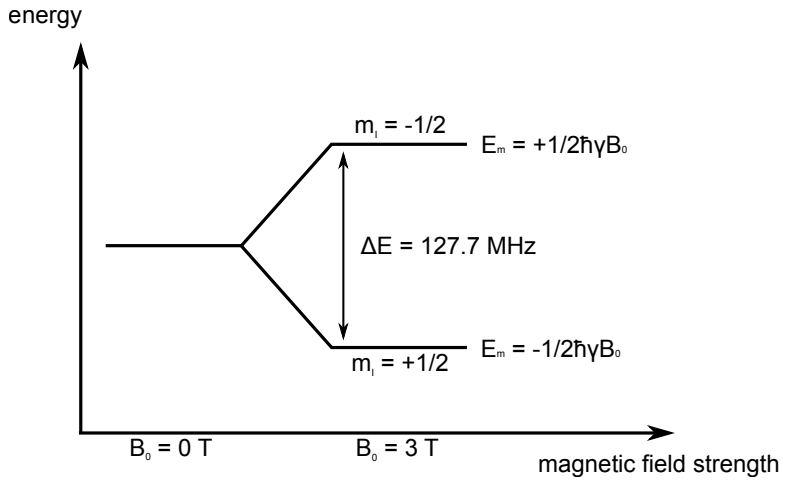

Figure 2.1: **Zeeman splitting of the nuclear energy levels for a system with nuclear spin $I = 1/2$ and $\gamma > 0$, such as a hydrogen nucleus.** When an external magnetic field B_0 is applied, the previously indistinguishable energy levels split up into two states: spin down state with energy $E_{-1/2}$ and spin up state with energy $E_{+1/2}$. At a field strength of 3 T, the energy difference between these two states is $\Delta E = 127.7$ MHz for the hydrogen nucleus.

According to the Planck Einstein relation between energy and frequency, a transition between the two energy states is possible by absorption or emission of a photon with frequency

$$\omega_0 = \gamma B_0 \tag{2.10}$$

The equation for the Larmor frequency (Equation 2.10) is the fundamental principle of NMR and with it of magnetic resonance imaging (MRI). At a magnetic field strength of 3 T, common in the clinical routine, the Larmor frequency is 127.7 MHz for the hydrogen nucleus.

2.1.3 Macroscopic magnetisation

A measured NMR signal usually comes from a large volume of nuclei and not from a single one as considered up to now. To describe systems composed of multiple nuclei, a macroscopic magnetisation $\vec{M}$ is used. It is defined as the sum of the expectation values of the magnetic moments $\hat{\vec{\mu}}_i$ of the N individual nuclei present in a unit volume V

$$\vec{M} = \frac{1}{V} \sum_{i=1}^{N} \left\langle \hat{\vec{\mu}}_i \middle| \hat{\vec{\mu}}_i \right\rangle \tag{2.11}$$

In thermal equilibrium at a temperature T and in the presence of an external magnetic field $\vec{B}_0 = (0, 0, B_0)^T$ as described previously, the macroscopic magnetisation can further be described using the population probabilities of the Zeeman levels with energy E_m

$$\vec{M} = \frac{N}{V} \, \gamma\hbar \sum_{m=-I}^{I} p_m m \; \vec{z} \tag{2.12}$$

The population probabilities of the Zeeman levels follow the Boltzmann statistics

$$p_m = \frac{1}{Z} e^{-\frac{E_m}{k_B T}} \qquad\qquad Z = \sum_{m=-I}^{I} e^{-\frac{E_m}{k_B T}} \tag{2.13}$$

where $k_B = 1.38 \cdot 10^{-23}$ J/K is the Boltzmann constant. For hydrogen nuclei with $I = 1/2$, the ratio of the number of spins in the two available states (parallel $N_{+1/2}$ and antiparallel $N_{-1/2}$ to the external magnetic field) can be calculated to be

$$\frac{N_{-1/2}}{N_{+1/2}} = \frac{p_{-1/2}}{p_{+1/2}} = \frac{e^{-\frac{1}{2}\frac{\hbar\gamma B_0}{k_B T}}}{e^{\frac{1}{2}\frac{\hbar\gamma B_0}{k_B T}}} = e^{-\frac{\hbar\gamma B_0}{k_B T}} = e^{-\frac{\Delta E}{k_B T}} \tag{2.14}$$

For $k_B T \gg \hbar\gamma B_0$, the exponential function can be approximated by $1 - (\gamma\hbar B_0)/(k_B T)$ following a Taylor expansion. At a body temperature of $T = 310$ K and a field strength of 3 T, the number of spins parallel to the external magnetic field exceeds the number of spins antiparallel to the external magnetic field by only 3 nuclei per million.

In the case mentioned above, the high temperature approximation $k_B T \gg \hbar\gamma B_0$ can be used and therefore, using the Taylor expansion of the exponential function to the first order, the macroscopic magnetisation at thermal equilibrium of hydrogen nuclei in a sample can be approximated by

$$M_0 \approx \frac{\hbar^2\gamma^2}{4k_B}\frac{N}{V}\frac{B_0}{T} \tag{2.15}$$

This equation, known as Curie's law, shows that, in thermal equilibrium, the net macroscopic magnetisation is approximately proportional to the spin density $\rho = N/V$ and the external magnetic field B_0, and inversely proportional to the temperature T.

2.1.4 Magnetisation dynamics - Bloch Equations

The time evolution of the expectation value of a magnetic moment $\hat{\vec{\mu}}$ describes its motion in an external magnetic field $\vec{B}$. Using Ehrenfest's theorem, the temporal evolution of the expectation value of the magnetic moment operator is given by:

$$\frac{d\left\langle \hat{\vec{\mu}} \middle| \hat{\vec{\mu}} \right\rangle}{dt} = \gamma \left\langle \hat{\vec{\mu}} \middle| \hat{\vec{\mu}} \right\rangle \times \vec{B} \tag{2.16}$$

This equation reflects the classical description of the torque experienced by a magnetic moment in an external magnetic field, aiming to align the magnetic moment with the magnetic field. Considering that the magnetic momenta of all nuclei in a sample are aligned, Bloch extended this description to the macroscopic magnetisation of all nuclei in a sample [*Bloch*, 1946]:

$$\frac{d\vec{M}}{dt} = \gamma\vec{M} \times \vec{B} \tag{2.17}$$

According to Equation 2.17, the macroscopic magnetisation $\vec{M}$ will thus precess around the external magnetic field $\vec{B}$ if it possesses a component which is not parallel to $\vec{B}$.

2.1.4.1 Excitation

In thermal equilibrium, however, all spins of a spin ensemble in a static external magnetic field $\vec{B_0} = (0, 0, B_0)^T$ are oriented randomly and only show a small net magnetisation along the z-direction. All components in the x-y-plane of the macroscopic magnetisation statistically add up to zero as the individual spins don't have any phase coherence. To be able to measure an NMR signal, the component of the macroscopic magnetisation in the x-y-plane, known as transverse magnetisation, has to be non-zero. This can be

achieved by perturbing the thermal equilibrium using a time-dependent magnetic field $\vec{B_1}(t)$ induced by a radio-frequency (RF) electromagnetic field, which is perpendicular to the static magnetic field $\vec{B_0}$.

Given a static magnetic field along the z-direction $\vec{B_0} = (0, 0, B_0)^T$ and a left circularly polarised RF field $\vec{B_1}(t)$ with frequency ω_1 in the x-y-plane

$$\vec{B_1}(t) = \begin{pmatrix} B_1 cos(\omega_1 t) \\ -B_1 sin(\omega_1 t) \\ 0 \end{pmatrix} \tag{2.18}$$

the spin ensemble is subject to a total external magnetic field $\vec{B} = \vec{B_0} + \vec{B_1}(t)$. The time derivative of the macroscopic magnetisation in the resting frame of reference (Equation 2.17) then becomes

$$\begin{aligned} \left(\frac{d\vec{M}}{dt}\right)_{(x,y,z)} &= \vec{M} \times \gamma\vec{B} \\ &= \vec{M} \times \gamma \begin{pmatrix} B_1 cos(\omega_1 t) \\ -B_1 sin(\omega_1 t) \\ B_0 \end{pmatrix}_{(x,y,z)} \end{aligned} \tag{2.19}$$

The transverse component of the macroscopic magnetisation precesses around the z-axis with angular velocity ω_1. The motion of the macroscopic magnetisation is a superposition of a precession around the B_0-axis and the B_1-axis.

To better understand the effect of an RF pulse on the magnetisation, a rotating frame of reference (x', y', z') with angular velocity $\vec{\Omega}$ is introduced. When switching from a resting frame of reference (x, y, z) to a rotating one, the time derivative of a function is transformed. For the macroscopic magnetisation, Equation 2.17 becomes

$$\left(\frac{d\vec{M}}{dt}\right)_{(x,y,z)} = \left(\frac{d\vec{M}}{dt}\right)_{(x',y',z')} + \vec{\Omega} \times \vec{M} \tag{2.20}$$

Using Equations 2.19 and 2.20, yields the following time derivative for the magnetisation in the rotating frame

$$\begin{aligned} \left(\frac{d\vec{M}}{dt}\right)_{(x',y',z')} &= \vec{M} \times \gamma\vec{B} + \vec{M} \times \vec{\Omega} \\ &= \vec{M} \times \gamma\Big(\vec{B} + \frac{\vec{\Omega}}{\gamma}\Big) \end{aligned} \tag{2.21}$$

In the rotating frame, the macroscopic magnetisation thus precesses about an effective magnetic field $\vec{B}_{eff} = \vec{B} + \vec{\Omega}/\gamma$. This effective magnetic field is the superposition of the static external field and a mathematically fabricated magnetic field with magnitude $|\vec{\Omega}|/\gamma$ directed along $\vec{\Omega}$.

Using Equation 2.21, Equation 2.19 can be transformed into a rotating frame with angular velocity $\vec{\Omega} = (0, 0, -\omega_1)^T$

$$\left(\frac{d\vec{M}}{dt}\right)_{(x',y',z')} = \vec{M} \times \gamma \begin{pmatrix} B_1 \\ 0 \\ B_0 - \omega_1/\gamma \end{pmatrix}_{(x',y',z')} \tag{2.22}$$

If we choose an RF field $\vec{B_1}(t)$ with Larmor frequency $\omega_1 = \omega_0$, the effective magnetic field will be aligned with the x'-axis of the rotating frame of reference. The macroscopic magnetisation will then precess about the $\vec{B_1}$ field only, yielding a measurable transverse magnetisation.

The angle by which the macroscopic magnetisation is tipped in respect to the static magnetic field $\vec{B_0}$ depends on the properties of the applied RF pulse $\vec{B_1}(t)$, namely its duration τ and magnitude B_1. This angle, called the flip angle α, can in general be calculated as

$$\alpha = \gamma \int_t^{t+\tau} B_1(t')dt' \tag{2.23}$$

For rectangular RF pulses and small flip angles, a simplified formula can be used

$$\alpha = \gamma B_1 \tau \tag{2.24}$$

2.1.4.2 Relaxation

The macroscopic magnetisation $\vec{M}$ can be separated into a component parallel to the external static field $\vec{B_0} = (0, 0, B_0)^T$ and a component perpendicular to it. The former is known as the longitudinal magnetisation M_z and the latter as the transverse magnetisation M_{xy}. After applying an RF pulse, the magnetisation will return to the state of lowest energy, its original thermal equilibrium. During this relaxation process, the spins interact with their environment via dipole-dipole interactions and with surrounding spins. These two effects are referred to as spin-lattice or longitudinal or T_1 relaxation and as spin-spin or transverse or T_2 relaxation, respectively. In homogeneous media, the relaxation process of the macroscopic magnetisation $\vec{M}$ following an excitation can mathematically

be described by the Bloch equations [*Bloch*, 1946] with relaxation times T_1 and T_2

$$\frac{d}{dt}\begin{pmatrix} M_x \\ M_y \\ M_z \end{pmatrix} = \begin{pmatrix} \gamma(\vec{M}\times\vec{B})_x - M_x/T_2 \\ \gamma(\vec{M}\times\vec{B})_y - M_y/T_2 \\ \gamma(\vec{M}\times\vec{B})_z - (M_0 - M_z)/T_1 \end{pmatrix} \tag{2.25}$$

Longitudinal relaxation - Spin-lattice coupling

To return to the original state of thermal equilibrium, a transfer of energy between the spin system and the surrounding medium through vibrations and rotations takes place. This process allows the longitudinal magnetisation M_z to grow back to its thermal equilibrium value of M_0 and is governed by the longitudinal relaxation time T_1 (see Equation 2.25). The differential equation describing the longitudinal relaxation

$$\frac{dM_z}{dt} = \gamma(\vec{M}\times\vec{B})_z - \frac{M_0 - M_z}{T_1} \tag{2.26}$$

can be solved using an exponential function

$$M_z(t) = M_z(0)e^{-t/T_1} + M_0(1 - e^{-t/T_1}) \tag{2.27}$$

For an RF field with flip angle $\alpha = 90°$, the longitudinal magnetisation right after the excitation vanishes ($M_z(0) = 0$) and the equation of motion of the longitudinal magnetisation (Equation 2.27) simplifies to

$$M_z(t) = M_0(1 - e^{-t/T_1}) \tag{2.28}$$

The longitudinal relaxation time T_1 depends on the efficiency of energy transfer between the spin system and its environment and it therefore varies between different types of materials and tissues. It is also influenced by the static magnetic field strength B_0 as it is directly related to the Larmor frequency of the spin ensemble. In case of an efficient energy transfer, the longitudinal relaxation will reach its thermal equilibrium value fast and longitudinal relaxation time will thus be short. In case of an inefficient energy transfer, the longitudinal relaxation time will be long. Literature values for T_1 times of different human tissues are listed in Table 2.2.

Transverse relaxation - Spin-spin coupling

Directly after an excitation, the spins of the system are in phase coherence and add up to a non-zero transverse magnetisation M_{xy}. As a result of Brownian motion, each spin experiences a slightly different locally fluctuating magnetic field made of the superposition of the external magnetic field B_0 and the magnetic moments of surrounding particles $B_{loc}(t)$. The Larmor frequency of each spin is thus slightly different depending on the

neighbouring spins $\omega(t) = \gamma(B_0 + B_{loc}(t))$. These differences in Larmor frequencies in the spin ensemble lead to an increasing phase difference between spins and to an irreversible loss of phase coherence over time. The transverse magnetisation thus gradually decreases due to dipole-dipole interactions between adjacent spins. Its equation of motion is described by the following set of Bloch equations:

$$\begin{aligned} \frac{dM_x}{dt} &= \gamma(\vec{M} \times \vec{B})_x - \frac{M_x}{T_2} \\ \frac{dM_y}{dt} &= \gamma(\vec{M} \times \vec{B})_y - \frac{M_y}{T_2} \end{aligned} \tag{2.29}$$

To solve this equation of motion more easily, the x and y components are combined into a complex variable

$$M_{xy}(t) = M_x(t) + iM_y(t) = |M_{xy}(t)| \cdot e^{i\phi(t)} \tag{2.30}$$

with the magnitude $|M_{xy}(t)|$ and the phase $\phi(t)$. Assuming a static magnetic field $B = (0, 0, B_0)^T = (0, 0, \omega_0/\gamma)^T$, Equation 2.29 becomes

$$\frac{dM_{xy}}{dt} = -i\gamma B_0 M_{xy} - \frac{1}{T_2} M_{xy} \tag{2.31}$$

The solution of this differential equation is

$$M_{xy}(t) = |M_{xy}(t)| \cdot e^{-i\phi(t)} = M_{xy}(0) \cdot e^{-t/T_2} \cdot e^{-i\phi(t)} \tag{2.32}$$

The magnitude of the measured signal is thus $|M_{xy}(t)| = M_{xy}(0) \cdot e^{-t/T_2}$ and its phase is $\phi(t) = \omega_0 \cdot t + \phi(0)$.

Transverse relaxation mainly depends on the local environment of the spins and is mostly independent of the static magnetic field strength. The dephasing of the transverse magnetisation is faster than the relaxation of the longitudinal magnetisation as visible in Table 2.2.

Table 2.2: **Relaxation times T_1 and T_2 of the hydrogen nucleus for different tissues at a static magnetic field strength of $B_0 = 3$ T** experimentally determined and reported by [a] *De Bazelaire et al.* [2004], [b] *Zhang et al.* [2013], and [c] the IT'IS Foundation database for MR relaxation times (`https://itis.swiss/virtual-population/tissue-properties/database/relaxation-times/`, *last accessed 08.08.2022*).

Tissue	T_1 in ms	T_2 in ms
brain - gray matter	1433[c]	92[c]
brain -white matter	866[c]	60[c]
kidney - cortex	1168[c]	76[a]
kidney - medulla	1545[c]	81[a]
blood	1650[b]; 1984[c]	275[c]

T_2^* relaxation

In addition to tissue-specific local magnetic field fluctuations $B_{loc}(t)$ causing the irreversible spin dephasing in the transverse plane, local field inhomogeneities of the static field B_0 accelerate this dephasing process. These local inhomogeneities result from an imperfect static field or susceptibility-induced local field distortions caused by objects in the field. The effect of local field inhomogeneities on the relaxation of the transverse magnetisation is governed by the time T_2' and can be reversed by applying a 180° RF pulse. Taking into consideration both dephasing effects, the total or apparent transverse relaxation time T_2^* is given by

$$\frac{1}{T_2^*} = \frac{1}{T_2} + \frac{1}{T_2'} = R_2 + R_2' \tag{2.33}$$

The signal for the transverse magnetisation with relaxation rate $1/T_2^*$ is known as the free induction decay (FID).

The longitudinal and transverse relaxation processes are independent as they result from different physical processes. Nevertheless, T_1 relaxation inevitably leads to T_2 relaxation. The trajectory of the macroscopic magnetisation in the resting frame of reference is a superposition of the motion of $M_z(t)$ and $M_{xy}(t)$ and looks like a three-dimensional helical spiral, moving from the x-y plane towards the z-axis as can be seen in Figure 2.2.

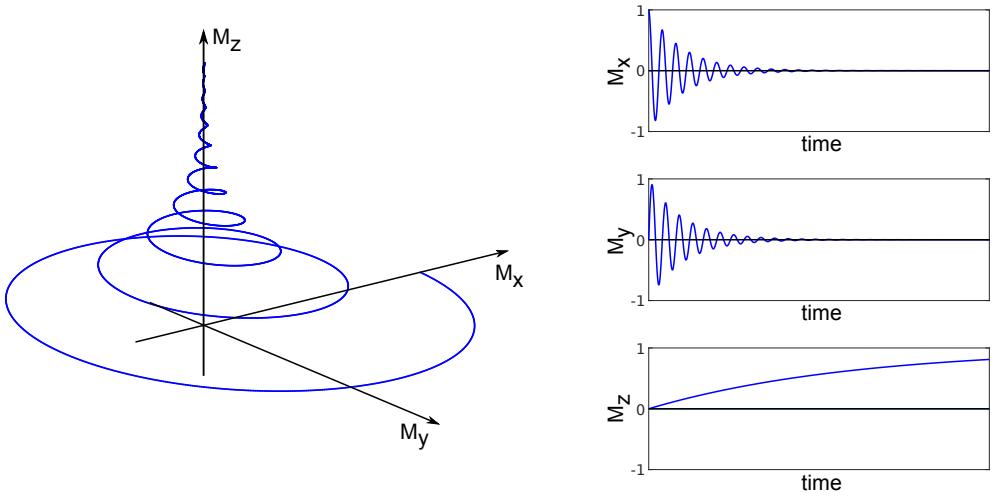

Figure 2.2: **Trajectory of the macroscopic magnetisation following an excitation.** $\vec{M}$ describes a three-dimensional helical spiral, moving from the x-y plane towards the z-axis.

2.1.5 Signal acquisition

To measure an NMR signal, the macroscopic magnetisation needs to have a component perpendicular to the external magnetic field. The magnetisation is therefore excited and tipped towards the transverse plane. The transverse component M_{xy} will then precess around the external magnetic field, as described by Equation 2.32, and will create a time-dependent magnetic flux $\Phi(t)$. Placing a receive coil with its symmetry axis perpendicular to the external magnetic field, the transverse magnetisation can be measured using Faraday's law of induction. Derived from Maxwell's equations, the induction law states that changes of magnetic flux $d\Phi/dt$ in the environment of a coil with area $\vec{S}$ induce a voltage U_{ind} in the coil

$$U_{ind}(t) = -\frac{d\Phi}{dt} = -\frac{d}{dt}\int_{S_{coil}} \vec{B}(S,t)\cdot d\vec{S} \tag{2.34}$$

The external magnetic field $\vec{B}$ can be expressed as the rotation of a vector potential $\vec{A}$

$$\vec{B} = \vec{\nabla}\times\vec{A}$$

Making use of Stoke's theorem, Faraday's induction law can be rewritten as a line integral

$$U_{ind}(t) = -\frac{d}{dt}\int_{S_{coil}} (\vec{\nabla}\times\vec{A})\cdot d\vec{S} = -\frac{d}{dt}\oint \vec{A}\cdot d\vec{l} \tag{2.35}$$

A formula easy to apply for NMR signals can then be derived by using the explicit expression of the vector potential $\vec{A}$ and the principle of reciprocity. This principle states

that the flux induced through a coil by the magnetisation can be determined by calculating the flux that would generate a magnetisation equal to the one inducing the flux in the coil. The voltage induced in the coil by the precessing magnetisation in the sample is thus given by

$$U_{ind}(t) = -\frac{d}{dt}\int_V \vec{B_1^-}(\vec{r}) \cdot \vec{M}(\vec{r},t)\ d\vec{r} \tag{2.36}$$

where $\vec{B_1^-}$ is the receive field of the coil at position $\vec{r}$ and corresponds to the magnetic field per unit current I generated by the coil at this position. The signal $\mathcal{S}$ detected by the receive coil and associated electronics is proportional to the induced voltage: $\mathcal{S} \propto U_{ind}(t)$.

To measure the transverse magnetisation, reception coils are placed with their symmetry axes perpendicular to the external magnetic field $\vec{B} = (0, 0, B_0)^T$ resulting in a coil receive field approximately equal to its transverse component. To receive the complex magnetic resonance signal, two coupled orthogonal coils with a fixed phase shift of 90° are used. The obtained signal $\mathcal{S}$ is demodulated with reference sine and cosine signals oscillating at the Larmor frequency. At time $t = 0$, the transverse magnetisation is equal to the spin density ρ of the sample and the initial phase of the signal is usually considered to be zero. The measured signal can then mathematically be expressed as

$$U_{ind}(t) \propto \mathcal{S}(t) = \mathcal{S}_0 \int_V \rho(\vec{r}) e^{-i\gamma B_0 t} e^{-t/T_2} d\vec{r} \tag{2.37}$$

2.2 Magnetic Resonance Imaging

In 1971, the physician Raymond V. Damadian reported that the relaxation times of healthy and cancerous tissues differ [*Damadian*, 1971]. He understood early-on the potential of nuclear magnetic resonance (NMR) in medicine, especially for in vivo tumour detection, and was the first to investigate the possibility of using NMR for a new imaging modality. He came up with a full-body magnetic resonance (MR) scanner as a single-point imaging technique based on a saddle-shaped magnetic field, which was resonant in one voxel only. To image an entire sample, the sample was manually moved in the scanner in order to measure the signal from different areas in subsequent acquisitions. Using this method, Damadian acquired the first full-body human MR image for cancer diagnosis [*Damadian et al.*, 1977]. However, the time intensive nature of his technique made it impossible to use in the clinical routine.

Following Damadian's demonstration of the potential of NMR in medicine, Paul C. Lauterbur (a chemist) and Sir Peter Mansfield (a physicist) invented schemes using magnetic field gradients for a faster signal acquisition resulting in an imaging technique we

now know as magnetic resonance imaging (MRI). By applying a magnetic field gradient, Lauterbur was able to measure several one-dimensional NMR signals and created a two-dimensional tomographic image by back-projecting these [*Lauterbur*, 1973]. Mansfield used a linear magnetic gradient field applied during excitation to achieve a slice-by-slice excitation [*Mansfield and Grannell*, 1973] and developed this idea further into a line-by-line imaging technique [*Mansfield and Maudsley*, 1976]. The acquisition time was thus reduced from multiple hours to a couple of seconds for comparable image quality. For these achievements, both scientists were awarded with the Nobel Prize in Physiology or Medicine in 2003, while Damadian's contribution to the development of MRI remains unhonoured.

In the following sections, the basics of MRI, in terms of spatial encoding, signal sampling, standard image acquisition schemes, and image contrast, are described.

2.2.1 Spatial encoding

Creating a magnetic resonance (MR) image entails spatially localising NMR signals. This spatial encoding can be achieved with magnetic field gradients $\vec{G}$, which are superimposed on the static magnetic field $\vec{B}_0 = (0, 0, B_0)^T$ (assumed to be directed along the z-axis without loss of generality)

$$\vec{G} = (G_x, G_y, G_z) = \left(\frac{\partial B_0}{\partial x}, \frac{\partial B_0}{\partial y}, \frac{\partial B_0}{\partial z} \right) \tag{2.38}$$

The Larmor frequency, introduced in Equation 2.10, thus becomes dependent of the spatial location

$$\omega(\vec{r}) = \gamma B(\vec{r}) = \gamma(B_0 + \vec{r} \cdot \vec{G}(\vec{r})) \tag{2.39}$$

After acquisition, Fourier analysis is applied to the spatially localised NMR signals and the spatial information is reconstructed to create a MR image. For a two-dimensional (2D) MR image, spatial encoding requires three steps each applied in one spatial direction and known as slice selection, frequency encoding and phase encoding. For a three-dimensional (3D) MR image, a slab or very large slice is excited instead of repeating the slice selection step at different spatial locations to achieve the same sample coverage and the phase encoding step is performed in two spatial directions to allow perform spatial encoding.

2.2.1.1 Slice selection

To select a slice to be imaged, a magnetic gradient along the direction of the static magnetic field $\vec{B}_0$ is applied simultaneously to the RF excitation pulse. The precession frequency thus becomes dependent on the position along the z-direction:

$$\omega(z) = \gamma(B_0 + G_z \cdot z) \tag{2.40}$$

and only the magnetisation at a given z position remains at the resonant frequency and is excited by the RF pulse. An infinitesimally small slice could be excited only in the case of an RF pulse containing a single frequency, i.e., an RF pulse with an infinite length. In reality, however, the RF excitation pulse is finite and thus possesses a bandwidth $\Delta\omega$. The thickness of the excited slice Δz depends on the RF pulse bandwidth and gradient strength G_z as follows

$$\Delta z = \frac{\Delta\omega}{\gamma G_z} \tag{2.41}$$

This relationship is schematically explained in Figure 2.3.

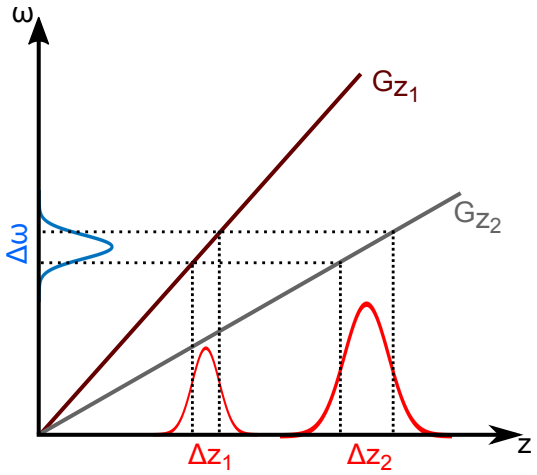

Figure 2.3: **Dependence of slice thickness Δz on RF pulse bandwidth $\Delta\omega$ and gradient strength G_z.** For a given bandwidth, the thickness of the slice where excitation takes place is smallest for the stronger gradient: $\Delta z_1 < \Delta z_2$ for $G_{z_1} > G_{z_2}$.

A sinc pulse is a typical RF pulse shape for slice excitation as it is paired with a rectangular spatial shape $rect(x)$ through the Fourier transform $\mathcal{F}$:

$$\mathcal{F}(rect(x)) = sinc(k) = \frac{sin(k)}{k} \tag{2.42}$$

where k refers to points in the frequency domain also known as k-space, and x refers to points in the spatial domain. As the duration of the RF excitation pulse is limited, the excitation pulse is cut off after several side lobes of the sinc pulse, thus creating imperfect slice profiles.

As the slice selection gradient G_z is played out simultaneously to the RF excitation pulse, we can consider G_z to be centred on the RF pulse. Assuming the magnetisation is

flipped instantaneously at the peak of the RF pulse, the resulting transverse magnetisation will experience dephasing during the second half of G_z. The dephasing will depend on the exact position z within the slice. To counteract this spatially dependent dephasing and ensure the entire excited slice is in phase, a rephasing gradient lobe is played out after G_z. In theory, complete rephasing is achieved when the area under the rephasing gradient is equal to that of the gradient that caused the dephasing and both gradients have opposite polarity.

2.2.1.2 Frequency encoding

Similarly to slice selection, a linear magnetic field gradient is also applied for the frequency encoding step. The frequency encoding gradient is played out during the measurement or readout and is sometimes also called readout gradient. Without loss of generality, we can assume the frequency encoding gradient is along the x-direction. The magnetisation precession frequencies measured thus depend on the spatial position along the x-direction as follows

$$\omega(x) = \gamma(B_0 + G_x \cdot x) \tag{2.43}$$

A combination of single signals with different frequencies constitute the measured signal. To recover the amplitudes of all single signal frequencies, a one-dimensional (1D) Fourier transform can be applied. The frequency amplitudes are then associated to their position of origin along the x-direction using Equation 2.43. The transverse magnetisation accumulates a phase during the time the frequency encoding gradient G_x is applied and the received signal $\mathcal{S}$ is calculated according to

$$\mathcal{S}(t, G_x) = \mathcal{S}(t) \int e^{-i\gamma \int_0^t G_x(T) x dT} dx \tag{2.44}$$

where $\mathcal{S}(t)$ is given by Equation 2.37.

2.2.1.3 Phase encoding

With slice selection in z-direction and frequency encoding in x-direction applied, the measured signal is a projection along the y-direction. Applying the frequency encoding method simultaneously both in x- and y-direction will however not yield a completely spatially encoded signal as it will only result in a projection perpendicular to the sum of magnetic field gradients applied in x- and y-direction. The magnetisation along the y-direction is therefore encoded before the frequency encoding and readout of the signal.

The principle of phase encoding relies on the accumulation of phase a spin experiences when a magnetic field gradient is applied for a given duration. Encoding in the third spatial dimension is thus achieved by applying a gradient G_y along the y-direction between signal excitation and signal readout. At readout, spins will have distinct phases depending on their y position. The measured signal is a combination of signals with identical frequency in y-direction but distinct phases. Note that the accumulated phase solely depends on the strength and duration of the applied magnetic gradient field. To cover the entire area to be imaged, the phase encoding step is repeated N_y times with a gradient strength G_y incremented from $-G_{y,max}$ to $+G_{y,max}$ and a fixed gradient duration τ_y. Each of these N_y measurements consists of a combination of single signals with varying phase along the y-direction, forming a set of linear equations from which the y position of the N_y signal amplitudes can be calculated. The received signal is calculated according to

$$\mathcal{S}(t, \tau_y, G_y) = \mathcal{S}(t) \int e^{-i\gamma \int_0^{\tau_y} G_y(T) y dT} dy \tag{2.45}$$

The process of frequency and phase encoding is illustrated in Figure 2.4.

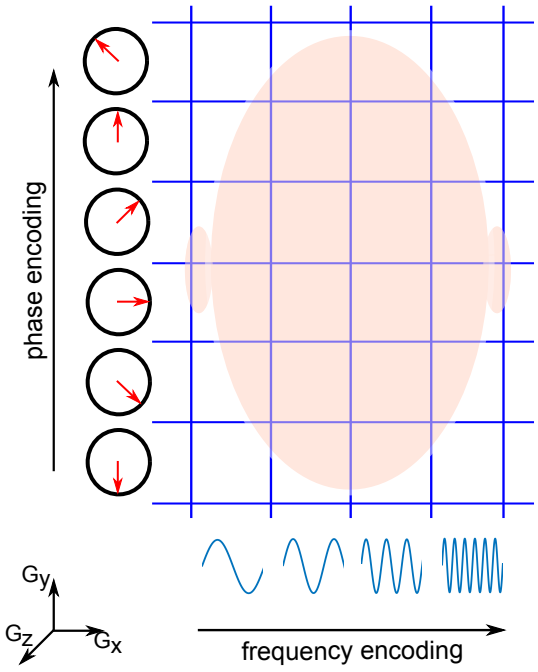

Figure 2.4: **Spatial encoding for a 2D slice of a sample.** After selection of a slice of the sample using a gradient G_z along the z-direction, steps of phase encoding in the y-direction and frequency encoding in the x-direction are performed using gradients G_y and G_x, respectively. These steps allow an association between frequency-phase patterns and spatial location of the received signal.

2.2.2 k-space sampling and image parameters

The total received signal from an excited and rephased slice of thickness Δz is given by

$$\mathcal{S}(t,\vec{G}) = \mathcal{S}_0 \int\int \rho(x,y) e^{-i\gamma\left(\int_0^t G_x(T)xdT + \int_0^t G_y(T)ydT\right)} dxdy \tag{2.46}$$

(neglecting all relaxation effects in Equations 2.44 and 2.45).

Wave numbers k_x and k_y corresponding to the integrals in the exponent can be defined as

$$k_x = \frac{\gamma}{2\pi}\int_0^t G_x(T)dT \tag{2.47}$$

$$k_y = \frac{\gamma}{2\pi}\int_0^t G_y(T)dT \tag{2.48}$$

With these definitions, Equation 2.46 can be simplified to

$$\mathcal{S}(\vec{k}(t)) = \mathcal{S}_0 \int\int \rho(x,y) e^{-i(2\pi k_x x + 2\pi k_y y)} dxdy = \mathcal{S}_0 \int \rho(\vec{r}) e^{-2\pi i \vec{k}\cdot\vec{r}} d^2\vec{r} = \mathcal{S}_0(\mathcal{F}\rho)(\vec{r}) \tag{2.49}$$

The complex MR signal $M_{xy}(\vec{r})$ can then be retrieved from the measured signal $S(\vec{k})$ by applying an inverse Fourier transform

$$M_{xy}(\vec{r}) = \mathcal{S}_0 \cdot \rho(\vec{r}) = \mathcal{F}^{-1}(\mathcal{S}(\vec{k})) = \int \mathcal{S}(\vec{k}) e^{2\pi i \vec{k}\cdot\vec{r}} d^2\vec{k} \tag{2.50}$$

The continuum of possible frequency-phase combinations to be measured is thus linked to the Fourier space, known as k-space in MRI. The entire k-space can be sampled by adapting the properties of the magnetic field gradients and the RF pulses in order to follow a chosen k-space trajectory.

The frequency domain where data is sampled can be represented in a 2D plot with the wave numbers in x- and y-direction as axes. In this representation, the centre of k-space contains the low frequencies while high frequencies are located in the periphery. It is interesting to notice that considering only a central portion of k-space for image reconstruction yields a blurry but contrast-rich and bright image. On the other hand, considering everything but the central portion of k-space yields an image with poor contrast but with well-defined edges and sharp transitions. The contribution of k-space centre and periphery is illustrated in Figure 2.5 for an axial brain slice.

In practice, k-space is not sampled continuously but in a discrete manner. Data points in k-space are sampled using an analogue-to-digital converter (ADC). The most common discrete sampling strategy is Cartesian sampling, where k-space is sampled in increments

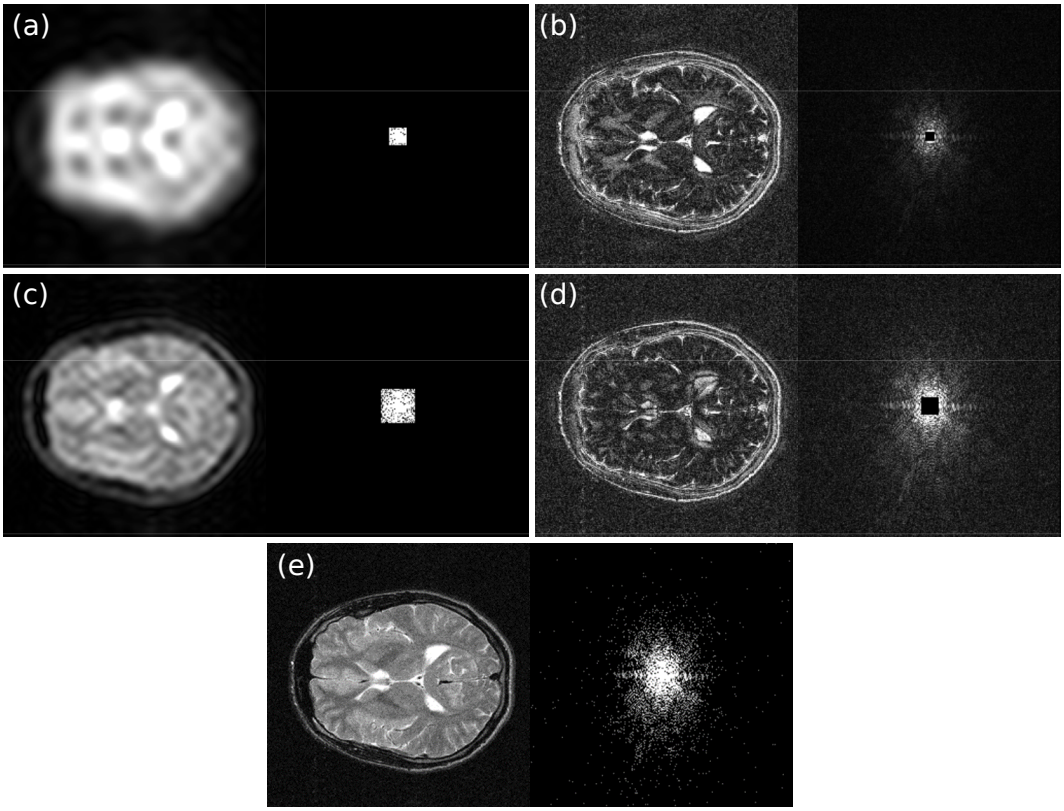

Figure 2.5: **Contribution of k-space centre and periphery to reconstructed image.** (a) Image reconstructed using only the central 1/64 portion of k-space. (b) Image reconstructed with the central 1/64 portion of k-space nulled. (c) Image reconstructed using only the central 1/32 portion of k-space. (d) Image reconstructed with the central 1/32 portion of k-space nulled. (e) Image reconstructed using the fully sampled k-space. In each image group, the data in frequency domain is on the right, and the magnitude of the signal reconstructed in spatial domain is on the left. *Images courtesy of René Botnar, KCH lectures.*

of Δk_x in frequency encoding direction and Δk_y in phase encoding direction. For sampling in the frequency encoding direction, a gradient of fixed strength G_x is applied for a duration t_x allowing N_x points to be sampled in time increments $\Delta t_x = t_x/N_x$. For sampling in the phase encoding direction, a gradient is applied during a fixed duration t_y with a varying gradient amplitude G_y from $-G_{y,max}$ to $+G_{y,max}$, allowing N_y increments of $\Delta G_y = 2G_{y,max}/N_y$. Cartesian sampling steps are thus given by

$$\Delta k_x = \frac{\gamma}{2\pi} G_x \Delta t_x \tag{2.51}$$

$$\Delta k_y = \frac{\gamma}{2\pi} \Delta G_y t_y \tag{2.52}$$

The widths of the sampling steps in k-space determine the size of the imaged area of the

sample, known as field-of-view (FOV):

$$FOV_x = \frac{1}{\Delta k_x} \tag{2.53}$$

$$FOV_y = \frac{1}{\Delta k_y} \tag{2.54}$$

In image space, the signal consists of $N_x \times N_y$ pixels, forming a 2D image. The in-plane resolution of this image depends on the number of sampling increments N_x and N_y the FOV is divided in:

$$\Delta x = \frac{FOV_x}{N_x} = \frac{2\pi}{\gamma G_x \Delta t_x N_x} \tag{2.55}$$

$$\Delta y = \frac{FOV_y}{N_y} = \frac{2\pi}{\gamma \Delta G_y t_y N_y} \tag{2.56}$$

The in-plane resolution can be increased by increasing the FOV, which is either achieved by decreasing the gradient strength G_x or duration increment Δt_x while keeping the number of sampling increments constant in the frequency encoding direction or by decreasing the gradient strength increment ΔG_y or duration t_y while keeping the number of sampling increments constant in the phase encoding direction.

Acquisition acceleration

Further options can be applied to reduce the duration of acquisition while keeping similar image quality and spatial resolution. One of these options is parallel imaging. In this widespread technique, information about the position and sensitivity of the individual coils used to receive signal is included to determine the spatial localisation of the signal. The amplitude of the signal received will be highest in the coil closest to the position of origin r of the signal as coils are more sensitive in the near field. The number of phase encoding steps can be reduced, thus reducing the time of acquisition, when coil sensitivity profiles are included to reconstruct the image. The coil sensitivity information can either be incorporated in the spatial domain or already in the frequency domain (i.e., before performing the inverse Fourier transform). The first method is known as SENSitivity Encoding (SENSE) [*Pruessmann et al.*, 1999] and the second is known as GeneRalized Autocalibrating Partial Parallel Acquisition (GRAPPA) [*Griswold et al.*, 2002]. To ensure a good image contrast, the lines passing through the centre of k-space are usually sampled completely and lines further away from the centre are sparsely sampled. Another option to accelerate image acquisition is partial Fourier. This reconstruction technique makes use of the conjugate symmetry property of the Fourier space where the frequency data is sampled. Acquiring only part (at least half) of the entire frequency space is sufficient to fully reconstruct an image as long as no phase errors occur during sampling. To reduce the time of acquisition, a partial Fourier factor of 5/8, 6/8 or 7/8 is commonly used in clinical MRI acquisitions. The higher the occurrence of phase errors, the higher this factor

should be to ensure good image quality after reconstruction.

Noise

As in every imaging modality, an important parameter in MRI is the signal-to-noise ration (SNR). It is defined as the ratio of mean signal within a region of interest (ROI) containing the imaged sample (μ_{sample}) and the standard deviation of the signal within a background ROI, i.e., a ROI containing no part of the imaged sample but only noise ($\sigma_{background}$).

$$SNR = \frac{\mu_{sample}}{\sigma_{background}} \tag{2.57}$$

Background (random) noise in MRI is primarily thermal noise and comes from the imaged sample itself or from the hardware used for imaging (coils, preamplifiers, etc.). In k-space, the noise is assumed to be Gaussian distributed and the complex signal in imaging space, which is linked via Fourier transform to k-space, is hence also Gaussian distributed. However, the noise in magnitude MR images, which do not consider real and imaginary part of the signal but solely its magnitude, is Rician distributed [*Gudbjartsson and Patz*, 1995; *Rice*, 1944]. Nevertheless, in regions where the SNR is intrinsically high (≥ 5), this noise can be approximated by a Gaussian distribution [*Reeder*, 2007].

The SNR of an image can be increased by acquiring N_A single images and averaging these. It can also be increased by increasing the voxel dimensions (Δx, Δy, Δz). In addition, the SNR depends on the readout duration T_{RO} and on the chosen pulse sequence.

$$SNR \propto \Delta x \cdot \Delta y \cdot \Delta z \cdot \sqrt{N_A} \cdot \sqrt{T_{RO}} \cdot \zeta \tag{2.58}$$

where ζ contains all sequence dependencies, which are determined by tissue properties (ρ, T_1, T_2), k-space coverage, and sequence timing [*Nishimura*, 1996].

2.2.3 Standard imaging sequences

To acquire a MR image with the desired image resolution, field of view, and contrast, the necessary RF pulses and magnetic field gradients have to be arranged in a certain order. Such an arrangement is called a pulse or imaging sequence and can be visualised in sequence diagrams. In this section, the basic MRI sequences are described.

2.2.3.1 Gradient echo

In a gradient echo (GRE) sequence, a signal echo is created using magnetic gradient fields. The sequence diagram and corresponding k-space trajectory of a 2D GRE sequence

is shown in Figure 2.6. The imaging slice is first excited using an RF pulse with flip angle α smaller than or equal to 90° and a slice-selective gradient in z direction (slice encoding direction). The slice-selective gradient causes a dephasing of the magnetisation, which is then corrected for with a gradient in the same direction but with opposite polarity and half the duration. Simultaneously, the magnetisation is dephased along the x direction (frequency encoding direction) and a phase encoding gradient is applied along the y direction (phase encoding direction). Finally, a rephasing gradient (used as a readout gradient) is applied in the x direction and an echo is generated. This frequency encoding rephasing gradient has opposite polarity to the frequency encoding dephasing gradient and is twice its size in order to create an echo at the centre of data acquisition, which occurs when the readout gradient has reached a constant amplitude. With such an arrangement of pulses, a single line in k-space can be read out. In order to acquire a full 2D image, the pulse sequence is repeated after a repetition time (TR) with a different amplitude and polarity of the phase encoding gradient for each k-space line to be acquired. The duration of the image acquisition thus depends on the chosen number of phase encoding steps and TR.

When using short TR times, some transverse magnetisation might remain instead of completely relaxing back into thermal equilibrium. Two options exist to handle this remaining transverse magnetisation: rewinding or spoiling. To rewind the remaining magnetisation, all gradients are reversed so as to bring the magnetisation back to its starting point at the centre of k-space. For spoiling, strong gradients are applied in the transverse plane to dephase the remaining magnetisation as much as possible.

In a GRE sequence, the maximal measurable signal depends on the flip angle amongst other parameters. To maximise the signal of a tissue with longitudinal relaxation time T_1, the flip angle α should follow the Ernst formula:

$$\alpha_E = arccos(e^{-\mathrm{TR}/T_1}) \tag{2.59}$$

With short TR times and appropriate Ernst flip angles, the entire k-space can be covered with high efficiency. GRE sequences are sensitive to magnetic field inhomogeneities and susceptibility related inhomogeneities as these are not compensated for in the sequence. In GRE sequences the signal is governed by transversal magnetisation and the signal is T_2^*-weighted at the echo time TE.

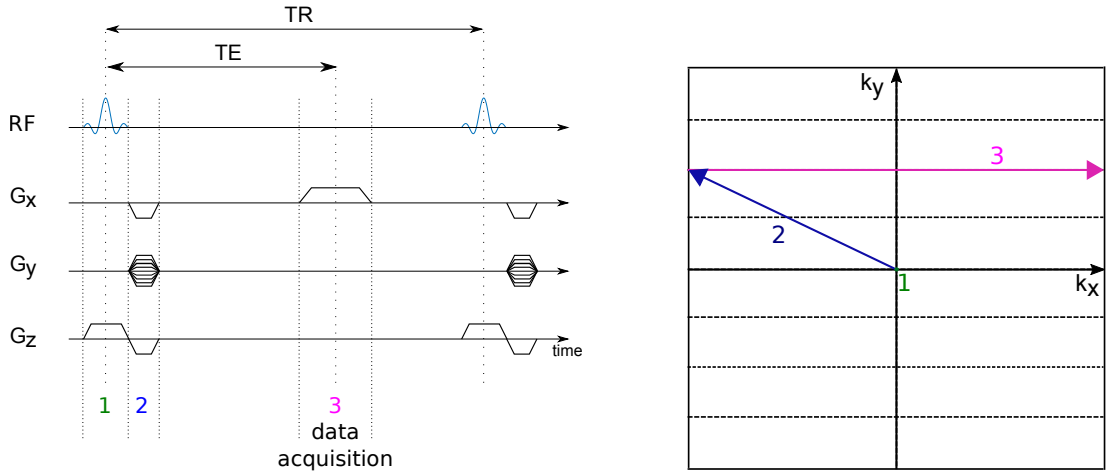

(a) Sequence diagram

(b) k-space trajectory

Figure 2.6: **2D gradient echo sequence diagram (a) and corresponding k-space trajectory (b).** The imaging slice is first excited using an RF pulse with flip angle $\alpha \leq 90°$ and a slice-selection gradient (1). Without loss of generality, the slice-selection gradient was chosen along the z-direction. The dephasing caused by the slice-selective gradient is then rephased. Simultaneously, the magnetisation is dephased in the frequency encoding direction (x-direcrtion here) and a phase-encoding gradient is applied in the y-direction (2). k-space is thus traversed from its origin to the k-space line to be read out. Finally, a frequency-encoding gradient rephases the magnetisation along the x-direction, producing an echo at time t = TE. The k-space line is sampled while the amplitude of the gradient is constant (3). This frequency-encoding gradient is also referred to as readout gradient. In order to sample the entire 2D k-space, this sequence of RF pulses and gradients is repeated at a regular time interval TR with varying amplitude of the phase-encoding gradient.

2.2.3.2 Spin echo

In a spin echo (SE) sequence, RF pulses are used to create an echo. The production of a spin echo was first discovered and explained by Edward Hahn [*Hahn*, 1950]. A SE sequence contains a 90° excitation pulse followed by a 180° refocusing pulse, which create a spin echo. The principle of formation of such a spin echo is illustrated in Figure 2.7. The 90° excitation pulse first flips the magnetisation from the longitudinal plane into the transversal plane. The magnetisation then starts to dephase in the transversal plane due to field inhomogeneities. The 180° pulse is applied at half the echo time (TE/2), so that the precession direction is inverted and the spins rotating with lowest frequency find themselves in front of those with highest frequency. All spins are then rephased and an echo is produced at the echo time TE. The 180° refocusing pulse compensates for the relaxation due to field inhomogeneities and tissue susceptibility differences, but does not compensate for the temporally varying magnetic field. The signal of a SE sequence is

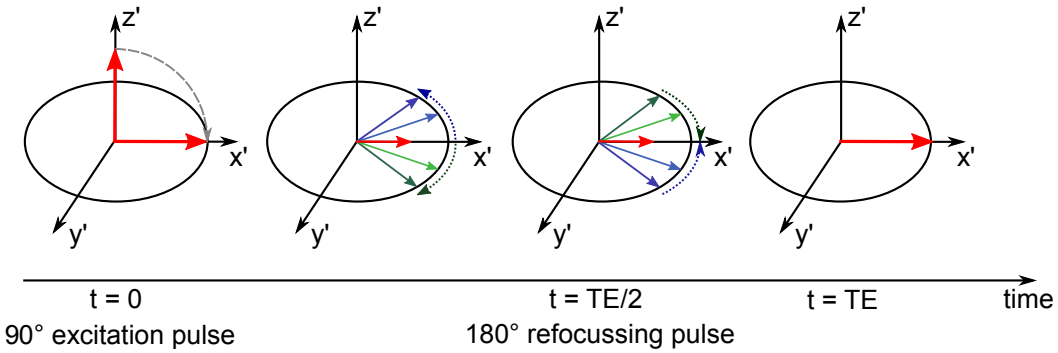

Figure 2.7: **Principle of formation of a spin echo.** At time $t = 0$, the macroscopic magnetisation (red arrow) is tipped to the transversal plane by a 90° RF excitation pulse. Without loss of generality, the magnetisation is then aligned with the x'-axis of the rotating frame of reference (no spin-lattice interaction considered). The magnetisation then starts to dephase in the transversal plane due to T_2^* relaxation. At time $t = \mathrm{TE}/2$, the precession direction of the spins is inverted by applying a 180° refocusing pulse around the x'-axis. The magnetisation now starts to rephase in the transversal plane due to T_2^* relaxation. At the echo time $t = \mathrm{TE}$, all spins are coherent again and an echo is produced.

therefore T_2-weighted at the echo time TE. In order to acquire a full 2D image, the pulse sequence is repeated after a repetition time (TR) with a different amplitude and polarity of the phase encoding gradient for each k-space line to be acquired. The sequence diagram and corresponding k-space trajectory of a 2D SE sequence is shown in Figure 2.8. Using the Bloch equations, the signal equation of a SE sequence can be written as

$$S = M_0 \cdot \left[1 - 2 \cdot exp\left(-\frac{\mathrm{TR} - \mathrm{TE}/2}{T1}\right) \cdot exp\left(-\frac{\mathrm{TR}}{T_1}\right)\right] \cdot exp\left(-\frac{\mathrm{TE}}{T_2}\right) \tag{2.60}$$

with M_0 being the longitudinal magnetisation at thermal equilibrium. When $T_1 << \mathrm{TR} - \mathrm{TE}/2$, this equation simplifies to

$$S = M_0 \cdot \left[1 - exp\left(-\frac{\mathrm{TR}}{T_1}\right)\right] \cdot exp\left(-\frac{\mathrm{TE}}{T_2}\right) \tag{2.61}$$

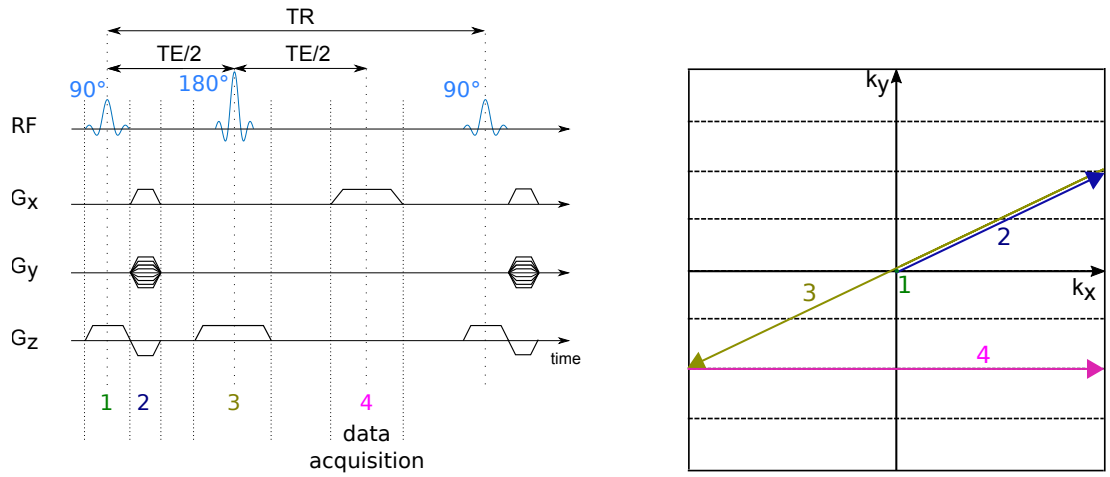

(a) Sequence diagram

(b) k-space trajectory

Figure 2.8: **2D spin echo sequence diagram (a) and corresponding k-space trajectory (b).** The imaging slice is first excited using a 90° RF pulse and a slice-selection gradient (1). Without loss of generality, the slice-selection gradient was chosen along the z-direction. The dephasing caused by the slice-selective gradient is then rephased. Simultaneously, the magnetisation is dephased in the frequency encoding direction (x-direcrtion here) and a phase-encoding gradient is applied in the y-direction (2). A 180° RF pulse is then applied at the same time as a slice-selection gradient to rephase the magnetisation (3). In k-space, the 180° refocussing pulse leads to a point reflection with respect to the center of k-space. Finally, a frequency-encoding gradient rephases the magnetisation along the x-direction, producing an echo at time t = TE. The k-space line is sampled while the amplitude of this readout gradient is constant (4). In order to sample the entire 2D k-space, this sequence of RF pulses and gradients is repeated at a regular time interval TR with varying amplitude of the phase-encoding gradient.

2.2.3.3 Inversion recovery

An inversion recovery (IR) experiment starts with a 180° RF pulse, which inverts the magnetisation. Without loss of generality, let's assume the magnetisation was along the positive z-direction. After the 180° RF pulse, it will point along the negative z-direction. The magnetisation will then relax back to its original position according to its longitudinal relaxation time T_1. The inversion pulse followed by a waiting time TI, known as inversion time, thus prepares the magnetisation before an imaging sequence takes place. After this preparation, any type of sequence that flips the existing longitudinal magnetisation into the transversal plane (e.g. a gradient echo or a spin echo) can be used to readout the signal. The measured signal depends on the T_1 relaxation of the tissue studied and the TI chosen as can clearly be seen from the signal equation of an IR experiment

$$M_z(TI) = M_0 \cdot (1 - 2 \cdot exp(-TI/T_1)) \tag{2.62}$$

IR is therefore important for measuring T_1 relaxation times or obtaining T_1-weighted images. To measure T_1 relaxation times, a sequence with IR magnetisation preparation is repeated for different values of TI. This allows to sample the recovery of the longitudinal magnetisation M_z and estimate T_1 by fitting the signal equation to the obtained data. IR magnetisation preparation can also be used to null the signal from a specific tissue or to maximise the contrast between two tissue types. As each tissue has a specific T_1 relaxation time, the magnetisation from different tissue types will have different time courses after an inversion pulse. To illustrate this, the time courses of the longitudinal magnetisation of two tissues are shown in Figure 2.9. The TI can be chosen to coincide with an non-existing longitudinal magnetisation for one of the tissues before the imaging sequence so that no NMR signal originating from this tissue can be detected.

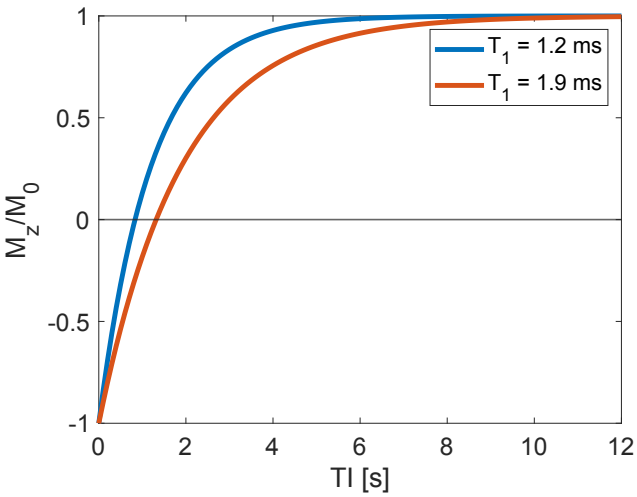

Figure 2.9: **Time course of the longitudinal magnetisation of two tissues with distinct longitudinal relaxation times T_1 after a 180° RF pulse (inversion recovery experiment).** The inversion time TI between inversion pulse and readout can be chosen to null the signal of one type of tissue.

2.2.3.4 Saturation recovery

Saturation recovery (SR) is another useful type of magnetisation preparation, which can be applied before any type of imaging sequence. A SR experiment starts with a 90° RF pulse, which flips the magnetisation into the transversal plane. With time, the longitudinal magnetisation will build itself back up. Multiple 90° saturation pulses can be applied at small time intervals in order to saturate the NMR signal. After each pulse, the longitudinal magnetisation will have little time to build up before being flipped back into the transversal plane. This can be repeated until the magnetisation available for relaxing back to the longitudinal plane is reduced to zero. No longitudinal magnetisation will thus be left to tip into the transversal plane before the imaging sequence, so that no NMR signal will be produced.

2.2.4 Image contrast

The contrast in a MR image is a result of the different properties of tissue in terms of proton density (PD) and relaxation times T_1 and T_2. Depending on the chosen imaging parameters, the contribution of individual tissues can be more or less pronounced. The time between consecutive identical points in a sequence with repeating RF pulses is called repetition time (TR), and the time between the excitation pulse and the echo is called echo time (TE). When a short TR is chosen, the net magnetisation has little time to recover between one excitation and the subsequent one, which enhances the influence of the longitudinal relaxation T_1. On the other hand, if a short TE is chosen, the transverse magnetisation has little time to dephase and the influence of the transversal relaxation time T_2 is limited. Images acquired with short TR and short TE generally enhance T_1 contrast and are therefore referred to as T_1-weighted images. Images acquired with long TR and long TE generally enhance T_2 contrast and are referred to as T_2-weighted images. When a long TR and a short TE are chosen for imaging, the effects of both longitudinal and transversal relaxation times is limited and only contrast due to the PD of the different tissue types is left. Such images are referred to as PD-weighted images. An optimal image contrast is achieved when TR and TE are approximately equal to T_1 and T_2 of the tissue of interest, respectively.

Images of a representative brain slice acquired with a spin echo sequence with different TR and TE values are shown in Figure 2.10. In T_1-weighted images, tissues with a short T_1 relaxation time relax faster to equilibrium and thus yield more signal, while tissues with a long T_1, such as cerebrospinal fluid, will yield less signal. In T_2-weighted images, tissues with a short T_2 relaxation time dephase faster and thus yield less signal, while tissues with a long T_2, such as cerebrospinal fluid, will yield more signal. T_1-weighting is thus preferred for morphological imaging, where soft tissue contrast is paramount, and T_2-weighting is used for comparing water content in different tissues and thus preferred for imaging pathology. Further modifications in sequence and parameter choice allow the creation of diffusion-weighted and perfusion-weighted image contrasts.

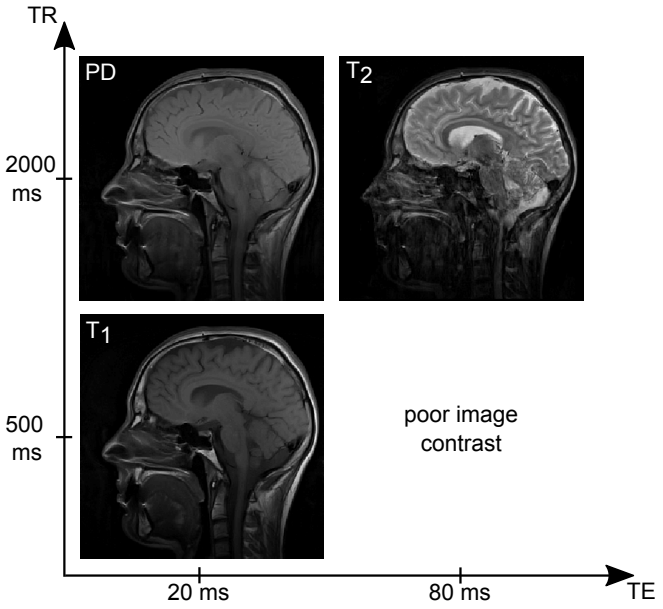

Figure 2.10: **Dependence of image contrast on chosen repetition time TR and echo time TE exemplified on a sagittal brain slice acquired with a spin echo sequence.**

2.3 Perfusion

This section first introduces the term perfusion, then describes the different perfusion MRI techniques with a focus on arterial spin labelling (ASL), and finally describes the existing models for perfusion quantification of ASL data.

2.3.1 Definition

Perfusion or micro-vascular blood flow refers to the regional delivery of oxygen and nutrients to the capillary bed of a tissue via arterial blood and includes the exchange of water, hormones, electrolytes, and heat between the capillary bed and surrounding cells. Quantitatively, perfusion is defined as the volume of arterial blood ΔV passing through a tissue of weight m during a time interval Δt

$$perfusion = \frac{\Delta V}{m \cdot \Delta t} \tag{2.63}$$

Its unit is most often $\frac{ml}{100g \cdot min}$.

Quantitative measurements of perfusion have a high clinical value as abnormal or reduced perfusion can indicate reduced organ function or vascular diseases. Positron emission tomography (PET) with ^{15}O labelled water as radioactive tracer is considered as the gold standard for in vivo perfusion measurements [*Herscovitch et al.*, 1983; *Raichle et al.*, 1983]. However, due to the need of radioactive tracer molecules with the invasiveness and complex logistics it entails, perfusion is more commonly assessed with other techniques

such as MRI in the clinical routine. Normal ranges of perfusion values for the human brain and kidneys are shown in Table 2.3.

Table 2.3: Normal range of perfusion values measured with ASL MRI for human brain and kidney from [a] *Deibler et al.* [2008], [b] *van Gelderen et al.* [2008], [c] *Roberts et al.* [1995], [d] *Odudu et al.* [2018].

Organ	perfusion [mL/100g/min]
brain - gray matter	40-70 [a], 60-110 [b]
brain - white matter	10-80 [b]
kidney cortex	278 ± 55 [c], 139-427 [d]
kidney medulla	55 ± 25 [c]

2.3.2 MRI-based perfusion

The MRI acquisition is less complex and less invasive than the gold standard method, PET, as it does not require the production and intake of radioactively labelled molecules. Multiple studies have been carried out to demonstrate the good agreement of quantitative perfusion measurements resulting from PET and MRI acquisitions [*Heijtel et al.*, 2014; *Fan et al.*, 2016]. Perfusion measurements based on MRI offer the possibility to quantitatively assess multiple blood flow related variables.

2.3.2.1 Perfusion MRI techniques

Two types of MRI-based perfusion techniques exist, which can be differentiated by the type of tracer used [*Calamante et al.*, 1999]. The first one relies on the injection of an exogenous contrast agent (usually an extracellular Gadolinium (Gd) based tracer), whose uptake in tissue is then imaged. This type comprises two techniques known as dynamic susceptibility contrast (DSC)-MRI, which makes use of the susceptibility effects of the tracer, and dynamic contrast enhanced (DCE)-MRI, which makes use of the relaxivity effects of the tracer [*Essig et al.*, 2013a]. Tthe second type of MRI-based perfusion techniques, known as arterial spin labelling (ASL), uses water molecules present in arterial blood as a freely diffusible endogenous tracer [*Williams et al.*, 1992; *Detre et al.*, 1992]. In the next paragraphs, DSC-MRI and DCE-MRI are briefly introduced before focusing on ASL.

DSC-MRI and DCE-MRI

In the mid 1980s, MR images acquired before and after injection of an exogenous contrast agent were used to measure tissue perfusion for the first time [*Runge et al.*, 1984; *Pettigrew et al.*, 1986]. Gadolinium-based exogenous contrast agents pass through tissues via the bloodstrream and create local magnetic field distortions, which reduce both the longitudinal and transversal relaxation times (T_1 and T_2, respectively) [*McRobbie et al.*, 2017]. The analysis of the temporal evolution of the signal can then be used to determine blood flow and volume.

DSC-MRI makes use of the spin dephasing due to susceptibility changes during the passing of the contrast agent, resulting in a decrease in apparent T_2 values [*Calamante et al.*, 1999]. For DSC-MRI, the injection of a contrast agent bolus is immediately followed by rapid acquisition of multiple images in order to monitor the first pass of the bolus [*Essig et al.*, 2013a]. During such an acquisition, the contrast agent remains mainly in the intravascular space. Parameters, such as time-to-peak of the bolus in the organ of interest (linked to blood flow) or the total amount of contrast agent passing through a tissue region (linked to blood volume), can then be easily determined in a semi-quantitative fashion. A fully quantitative calculation of blood flow and blood volume from DSC images is however challenging and may result in different values depending on the processing software used [*Essig et al.*, 2013b]. Furthermore, DSC-MRI is sensitive to susceptibility artefacts and partial volume effects [*Essig et al.*, 2013a].

Using time-resolved T_1-weighted images, DCE-MRI allows imaging of the tracer diffusion into extravascular extracellular space (EES) by tracking the concentration of the contrast agent bolus [*Essig et al.*, 2013b]. Due to shortened T_1, areas with higher Gadolinium concentration will appear brighter on the acquired MR images. Signal curves showing the tracer concentration over time are then extracted in a voxel-wise fashion from the MR images. For most tissues, the endothelium between intravascular space and EES is such that the molecules of Gadolinium-based contrast agent can diffuse passively. For the brain and spinal cord, however, the endothelium normally creates a tight blood-brain-barrier (BBB) preventing the passage of contrast agnet molecules into the EES. If the BBB is disrupted by a tumour or other pathology, a contrast enhancement can be observed on DCE-MRI images, demonstrating that the tracer has passively diffused into the EES. DCE can be used to quantitatively determine the exchange rate of tracer between the intravascular space and EES (indication of vascular permeability) as well as blood flow using pharmacokinetic models [*Essig et al.*, 2013b]. Disadvantages of DCE-MRI are the complex acquisitions and pharmacokinetic model processing needed [*Essig et al.*, 2013a]. DCE-MRI has long been considered as the standard method for perfusion quantification outside of the brain [*Brix et al.*, 2004; *Dujardin et al.*, 2005], yielding valuable functional

parameters especially for kidneys [*Sourbron et al.*, 2008].

However, especially for longitudinal follow-up of diseases, paediatric applications, and in case of reduced kidney function or other contrast agent contraindications, exogenous contrast-based MRI methods such as DCE and DSC are preferably avoided due to their invasive nature. Furthermore, recent studies have shown that Gadolinium present in contrast agents commonly used for MRI perfusion imaging is retained in important areas of the brain such as the hypothalamus and cerebellum [*Kanda et al.*, 2015; *Radbruch et al.*, 2015]. Even though no negative effects of this retention have been demonstrated to this day, it is nevertheless preferred to avoid contrast agent injections as much as possible.

ASL

ASL makes use of blood water protons as an endogenous tracer to image perfusion. For this, blood water protons present in the arteries delivering blood to the organ of interest are labelled and after an inflow time TI, the labelled blood flows into the imaging region. In the first introduction of ASL in 1992, the labelling of blood water protons was achieved through repeated saturation [*Detre et al.*, 1992]. Shortly after this first publication, the group improved the technique by labelling the water molecules via adiabatic inversion [*Williams et al.*, 1992]. An ASL experiment consists of acquiring two (or multiples of two) T_1-weighted images, the control and the labelled image, and one proton density weighted image, referred to as M0. The difference between labelled and control images lies in the presence or absence of labelling pulses applied to the feeding arteries. After acquisition, the labelled image is subtracted from the control image to obtain a perfusion-weighted image. If the labelling pulse is perfect and relaxation effects are negligible, the static tissue present in both the control and the labelled images will cancel out and only signal from in-flowing blood will remain in the perfusion-weighted image. This is illustrated schematically in Figure 2.11. For quantification of perfusion, the perfusion-weighted image scaled by the M0 image and other factors is used to produce a quantitative perfusion map. The process of acquisition and quantification of perfusion using ASL is shown in Figure 2.12.

The ASL technique presents a clear advantage of being completely non-invasive as it does not require the injection of exogenous contrast agent. In addition, it is not influenced by blood-brain barrier leakages as is the case with exogenous contrast-based perfusion MRI [*Keil et al.*, 2019]. Furthermore, the quantification procedure is more straight forward than for DSC- and DCE-MRI. Studies have also shown a good correlation between the gold standard ^{15}O PET and ASL measurements in brain for different conditions and in different populations [*Detre et al.*, 2009; *Xu et al.*, 2010; *Zhang et al.*, 2014; *Heijtel et al.*, 2014; *Fan et al.*, 2016]. However, the perfusion difference signal is only 0.5-1.5% of the measured signal for the brain [*Petersen et al.*, 2006a] and of the order of 5% for the

kidneys [*Nery et al.*, 2020], which results in perfusion maps with low SNR. ASL is thus very sensitive to motion, which makes it especially challenging for abdomen imaging (e.g. for the kidneys). Furthermore, individual differences in the duration of transition of the labelled blood to the imaging region, known as arterial transit time (ATT), can lead to inaccurate perfusion quantification based on ASL data.

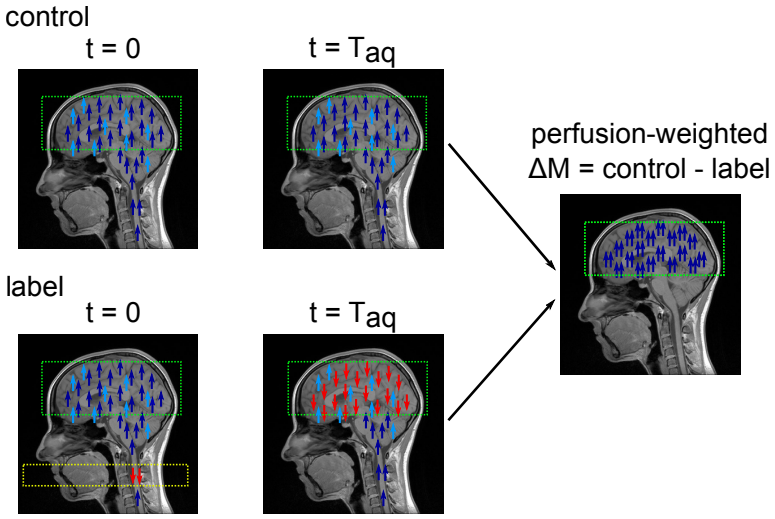

Figure 2.11: **Principle of ASL.** ASL uses blood water protons as endogenous tracer of perfusion. In order to do this, blood water protons flowing into the organ of interest (the brain in this example) have to be labelled. The labelling is achieved by inverting the spins of blood water protons in a slab proximal to the imaging slab (green box). Labelled and control images of an ASL experiment differ in the presence or absence of such an inversion slab (yellow box). In this schematic representation of the principle of ASL, the spins of blood water protons are shown as arrows: blue and pointing upwards for non-inverted spins or red and pointing downwards for inverted spins. The spins of static tissue are indicated as light blue. At time $t = 0$, the spins located in the inversion slab are inverted in case of the labelled image or remain pointing upwards in case of the control image. At the time of image acquisition $t = T_{aq}$, the blood water protons originally located in the inversion slab will have flown into the imaging slab. If the inversion used for labelling is perfect and relaxation effects are negligible, the static tissue in the control and the labelled images will cancel out and only signal from in-flowing blood will remain in the subtraction image of control and label, known as perfusion-weighted image. The increased number of arrows representing the magnetisation of blood water proton spins in the perfusion-weighted image illustrates the increased magnetisation magnitude resulting from the subtraction of labelled and control images.

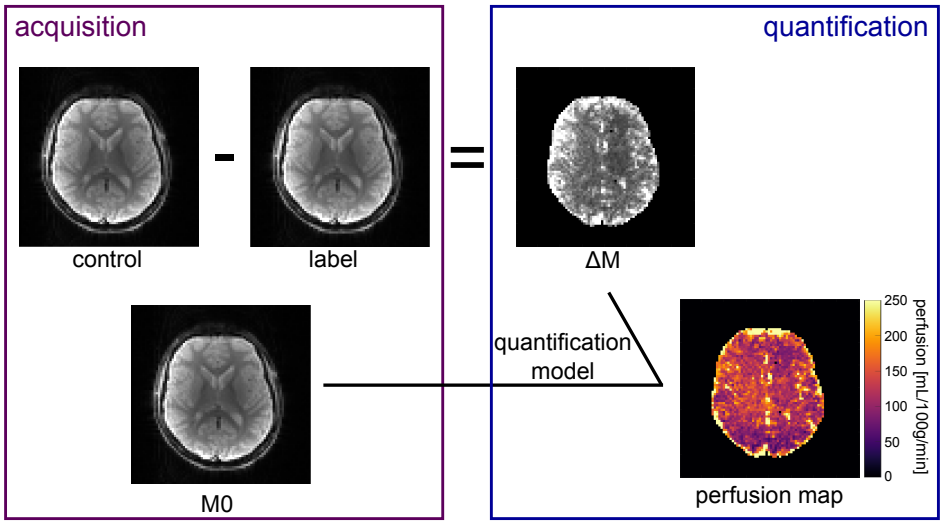

Figure 2.12: **Acquisition and basis of quantification of perfusion ASL MRI data exemplified for brain imaging.** An ASL experiment consists of acquiring two T_1-weighted images, the control and the label, and one proton density weighted image, referred to as M0. After acquisition, the labelled image is subtracted from the control image to obtain a perfusion-weighted image ΔM. Finally, the perfusion-weighted and M0 images are used to produce a quantitative perfusion map. (For better visualisation, the background around the head has been removed in all images.)

2.3.2.2 Adiabatic inversion

Adiabatic inversion pulses allow the uniform inversion of magnetisation with high robustness against B_1 field inhomogeneities. This is advantageous for ASL as the achieved perfusion signal directly depends on the inversion efficiency. The flip angle α by which the magnetisation vector is flipped after an RF pulse usually depends on the magnetic field which is induced by this RF pulse as described in Equation 2.23. This relation holds for all RF pulses which have a constant frequency, as is the case for most RF pulses used in MRI. For such pulses, an inhomogeneous B_1 field will cause the magnetisation of protons to be flipped by different angles depending on their spatial location. Adiabatic inversion pulses overcome this problem by using a B_1 field with modulated amplitude and frequency, so that equation 2.23 does not hold anymore. For this reason, adiabatic pulses are also called frequency modulated or chirped pulses [*Bernstein et al.*, 2004]. Following the adiabatic passage principle, the macroscopic magnetisation follows the direction of the effective magnetic field during an adiabatic pulse, provided the magnetic field does not change its direction during the duration of one precession of the magnetisation around it. Mathematically, this adiabatic condition can be stated as

$$\left| \frac{d}{dt} arctan\left(\frac{B_{xy}}{B_z}\right) \right| << \gamma |\vec{B_{eff}}| \tag{2.64}$$

where B_{xy} and B_z are the transverse and longitudinal components of the effective magnetic field $\vec{B_{eff}}$ in the rotating frame of reference, respectively. In case the adiabatic condition is fulfilled, an initial magnetisation perpendicular to the effective magnetic field will precess in a plane normal to the field and an initial magnetisation parallel to the field will remain parallel to it. Common adiabatic pulses are the adiabatic half-passage (AHP) and the adiabatic full-passage (AFP), which cause a rotation of the effective magnetic field of 90° or 180°, respectively, the B1-insensitive rotation (BIR), which allow rotations of arbitrary flip angles of all spins in a plane normal to the effective magnetic field. A hyperbolic secant (HS) pulse is often used for selective adiabatic inversion and the special case of frequency offset corrected inversion (FOCI) pulse [*Ordidge et al.*, 1996], which is very robust to off-resonance effects, is commonly used for labelling in PCASL sequences.

2.3.2.3 Magnetisation transfer

Magnetisation transfer (MT) processes occurring in biological tissue have to be taken into consideration in ASL as they can lead to erroneous perfusion quantification. Protons contributing to the MR signal from a biological tissue can be assumed to exist in two pools: the free pool and the bound pool. Protons in free water and in some adipose tissue make up the free pool, and macromolecules and water protons bound to these make up the bound pool [*Boer*, 1995]. Magnetisation transfer refers to the exchange of magnetisation (i.e., transfer of energy) between these two pools via chemical and physical processes such as diffusion, chemical exchange, and cross relaxation [*Boer*, 1995]. Magnetisation transfer effects were first observed in MR spectroscopy [*Forsén and Hoffman*, 1963] and later in MR imaging [*Wolff and Balaban*, 1989]. The absorption spectrum of the free pool differs from that of the bound pool. Free water protons have a sharp absorption peak (i.e., narrow resonant frequency range) due to their long transversal relaxation time T_2, while protons bound to macromolecules have a broad absorption spectrum due to their short T_2. Nevertheless, both pools are centred on the same resonant frequency ω (Figure 2.13). The bound pool can be selectively saturated by an off-resonant RF pulse in respect to the Larmor frequency ω_0, which will lead to a difference in magnetisation between the two pools. Water protons bound to macromolecules allow magnetisation to be transferred from the bound pool to the free pool via chemical exchange and dipole-dipole coupling [*Henkelman et al.*, 2001]. This exchange eventually leads to a saturation of the free pool, thus reducing its net magnetisation. In ASL, it is important that spins in both control and labelled images experienced the same MT effects to ensure no signal arising from differences in MT is present after subtraction.

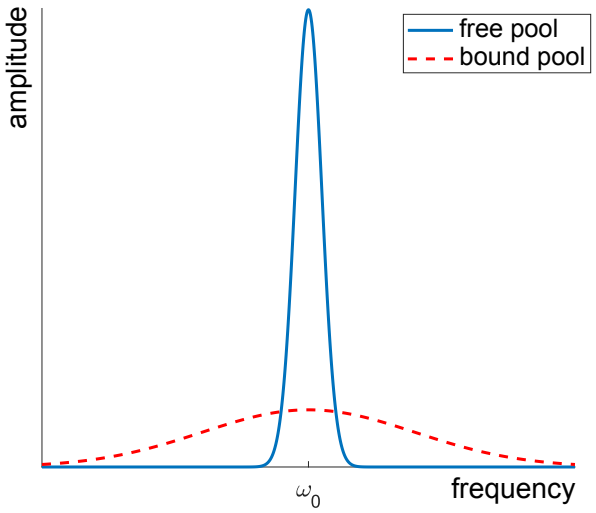

Figure 2.13: **Simplified absorption spectrum of the free pool** (continuous blue line) **and bound pool** (dashed red line) **of protons.** Both spectrum are centred around the same resonance frequency ω_0.

2.3.2.4 ASL labelling schemes

Different categories of ASL labelling schemes and implementation of these, presenting distinct advantages and disadvantages, exist. These schemes will be described in the next paragraphs following the historical development of ASL.

Continuous ASL

The first ASL technique, known as continuous ASL (CASL), was introduced in the late 20^{th} century [*Detre et al.*, 1992; *Alsop and Detre*, 1996, 1998]. In this technique, a continuous RF wave (2-4 seconds) is used to label blood water protons. During this time, the resonance frequency of the protons passing through the labelling region gradually changes and is eventually inverted. This technique is also known as flow-driven adiabatic inversion and was first introduced in MR angiography before being used for ASL measurements [*Dixon et al.*, 1986]. Theoretically, this technique has a high sensitivity, however in reality full sensitivity is difficult to achieve due to labelling inefficiency [*Alsop and Detre*, 1998]. The labelling efficiency is highly dependent on flow velocity and CASL is thus sensitive to vascular geometry [*Chen et al.*, 2011], which complicates good labelling positioning. An important drawback of CASL is the high power deposition in the body resulting from the continuous RF wave employed, leading to high specific absorption rate (SAR) and potential tissue temperature increase [*Chen et al.*, 2011]. In addition, the required continuous RF wave is technically challenging to achieve and might require dedicated hardware [*Detre and Alsop*, 1999]. Nowadays, CASL is rarely used for in vivo human MR measurements.

Pulsed ASL

In pulsed ASL (PASL), a frequency-modulated adiabatic inversion pulse is used to instantaneously invert a large blood volume [*Kwong et al.*, 1992; *Edelman et al.*, 1994; *Kim*, 1995]. The inversion pulse used is about 10 milliseconds long [*Chen et al.*, 2011] and all PASL schemes use a thick labelling slab placed upstream of the organ of interest and separated from the imaging slab by a gap. The main difference between the various PASL labelling schemes lies in the strategy used to control for MT effects, which follow two main ideas. The first idea is to saturate the bound pool before labelling to ensure no magnetisation transfer is possible between the bound and free pool. The second idea is to achieve the same level of MT in both control and labelled images by delivering the same RF power to the tissue in both images but causing no inversion in the case of the control image. The reader is referred to the resources of the Open Source Initiative for Perfusion Imaging (OSPI)[2] for an overview of existing PASL versions. A known drawback of the PASL scheme is the inherently lower SNR achievable compared to CASL [*Wong et al.*, 1998a; *Zaharchuk*, 2007] but, at the same time, the labelling efficiency is higher than in CASL and less dependent on the distribution of flow velocities [*Wong et al.*, 1998a]. The PASL scheme has the clear advantage of lower SAR [*Chen et al.*, 2011] but is more sensitive to arterial transit time uncertainties than CASL [*Alsop and Detre*, 1996]. To reduce this systematic error as well as reduce the inclusion of intravascular signal from vessels in the imaging slice which are not perfusing the organ of interest, a technique called Quantitative Imaging of Perfusion using a Single Substraction (QUIPSS) was developed [*Wong et al.*, 1996] and further improved (QUIPSS II) [*Wong et al.*, 1997]. This technique uses an RF saturation pulse (often referred to as QUIPSS or QUIPSS II saturation pulse), which is applied to the imaging region (QUIPSS) or to the labelling region (QUIPSS II) and played out at a delay time TI_1 after the labelling pulse for both the labelled and the control images. The saturation pulse ensures that the tail of the labelling bolus flowing into the imaging region is cut off at a specific time. It limits the actual length of the labelling bolus to a fixed temporal width of TI_1, thus reducing uncertainties in blood flow quantification. The labelled or control image is then acquired after a delay time δt, with $TI_2 = TI_1 + \delta t$. For all PASL schemes, it is recommended to use a QUIPSS II saturation pulse [*Alsop et al.*, 2015].

Pseudo-continuous ASL

Pseudo-continuous ASL (PCASL) is a variant of CASL, which achieves flow-driven adiabatic inversion with a time averaged gradient and a train of short selective RF pulses (about one per millisecond) instead of a continuous RF pulse and thus reduces safety risks and hardware demands [*Dai et al.*, 2008]. The labelling is achieved through phase shifts

[2] `https://osipi.org/resources/` and `https://docs.google.com/document/d/1vj0Tp4yur4dpJntF90yy2bOBUx33FG-w/edit`, *last accessed 31.08.2022*

resulting from the application of gradients between RF pulses [*Chen et al.*, 2011]. For PCASL, equation 2.64 can be rewritten in terms of velocity [*Maccotta et al.*, 1997; *Zhao et al.*, 2017]:

$$\frac{\gamma B_1^2}{G_{ave}} < v < \frac{B_1}{G_{ave} T_2} \tag{2.65}$$

The range of flow velocities for which the adiabatic condition holds is thus limited by the strength of the transmit field B_1 and the transversal relaxation time T_2. The average gradient amplitude G_{ave} of the labelling pulses set the velocity for which maximum labelling efficiency is achieved. The waveform of the selective gradient applied between successive RF pulses can be either balanced or unbalanced [*Wu et al.*, 2007]. In the balanced case, the gradient is not completely rephased and results in an average gradient applied during labelling for both control and labelled images. In the unbalanced case, the gradient is entirely rephased between subsequent RF pulses for the control image and not completely rephased for the labelled image. The phase of the RF pulses are successively incremented for the labelled image, while for the control image, subsequent RF pulses always have a phase difference of 180°. PCASL uses a thin labelling slab placed perpendicular to the feeding artery and upstream of the organ of interest. For PCASL measurements in the brain, the labelling plane should be placed 84 mm below the line connecting the anterior commissure and posterior commissure (AC-PC line) [*Aslan et al.*, 2010], refer to Figure 2.18. For PCASL measurements in the kidneys, the labelling plane should be placed 8-10 cm above the centre of the highest kidney [*Nery et al.*, 2020]. PCASL depends less on flow velocity and shows less MT effects than CASL [*Chen et al.*, 2011; **?**; *Alsop et al.*, 2015; *Nery et al.*, 2020]. PCASL presents higher SNR and less T_1 relaxation effects than PASL but has lower labelling efficiency and robustness [*Nery et al.*, 2018].

(Vessel) Selective ASL

Vessel selective (or territorial) ASL uses spatially-dependent labelling such as PASL or (P)CASL to separately label different vessels involved in blood and nutrient supply to the organ of interest [*Davies and Jezzard*, 2003]. This is especially interesting to check if and from which artery a potential blood supply deficit arises. In certain pathologies involving vessel malformations or occlusions and especially for brain imaging, this approach has been shown to be of great diagnostic value [*van Laar et al.*, 2008].

Velocity and acceleration selective ASL

Velocity selective and acceleration selective ASL (VSASL and AccASL) are the newest additions to ASL labelling schemes [*Wong et al.*, 2006; *Schmid et al.*, 2014]. Instead of a spatially selective labelling, VSASL and AccASL use the spin velocity and acceleration, respectively, as labelling condition. These methods are thus transit time independent in principle, which is their main advantage for clinical applications. The labelling condition is ensured by employing motion sensitising gradients set to the cutoff velocity/acceleration.

For the labelled image, spins that satisfy the labelling condition, i.e., spins with velocity/acceleration above or below the cutoff velocity/acceleration, acquire a phase shift with each RF pulse and are completely inverted at the end of the labelling module. For the control image, spins do not acquire a phase shift but are simply tipped back and forth with each RF pulse pair, ensuring the same MT effect is present in control and labelled images [*Zaharchuk*, 2007]. Two main types of VSASL labelling pulses, presenting various advantages and disadvantages, exist: velocity-selective saturation pulses (dual refocused hyperbolic secant [*Wong et al.*, 2006], symmetric BIR-8 [*Guo et al.*, 2014], multi-module VSASL [*Guo and Wong*, 2015]) and Fourier transform velocity-selective inversion or saturation pulses (rectangular envelope [*Qin and van Zijl*, 2016], sinc envelope [*Landes et al.*, 2020] or [*Qin et al.*, 2016; *Shin et al.*, 2013]). For a review of VSASL, the reader is referred to *Qin et al.* [2022]. VSASL and AccASL do not require a delay time to ensure the labelled blood spins arrive in the organ of interest as they are spatially-independent techniques, resulting in smaller TR. However, they have been shown to yield low SNR and tSNR due to sensitivity to motion, diffusion effects, and eddy currents. Furthermore, VSASL and AccASL labelling modules are more sensitive to B_0 and B_1 inhomogeneities than PASL and PCASL [*Hernandez-Garcia et al.*, 2019].

2.3.2.5 ASL readout schemes

In general, an ASL sequence is composed of three building blocks: the labelling, some tissue preparation (e.g. saturation pulses) and the readout. The choice of readout is independent of the labelling scheme and should ideally provide a high signal-to-noise ratio (SNR), good image quality, limited susceptibility artefacts, good coverage of the studied organ, and short acquisition time (hence short echo time) [*Cercignani et al.*, 2018; *Nery et al.*, 2020]. Whether a 2D or a 3D readout is chosen depends on the priorities and limitations of individual studies and centres. 3D readouts mainly differ from 2D readouts by the use of a phase encoding gradient in a second spatial direction instead of a slice-selective gradient. In comparison to 2D readouts, 3D readouts have the advantage of yielding a higher SNR per volume with isotropic voxels and have a higher sensitivity as the number of signals sampled per voxel is larger [*Günther et al.*, 2005; *Nery et al.*, 2018]. Furthermore, no inter-slice correction has to be performed for 3D readouts as the delay time between labelling and acquisition is independent of the slice position since the entire image volume is excited. Optimal background suppression can be achieved in 3D readouts but not in multi-slice 2D readouts due to the slice-dependent excitation. However, 3D readouts are slower and more susceptible to physiological changes than 2D readouts [*Poser et al.*, 2010]. While various readouts have been reported for ASL MRI in the literature, only the two readouts most commonly used and currently recommended

for in vivo imaging of the kidneys [*Nery et al.*, 2020] and the brain [*Alsop et al.*, 2015] are presented in the following paragraphs.

Echo-planar imaging

Echo-planar imaging (EPI) can achieve whole k-space sampling in a single excitation, thus allowing fast image acquisition. The sequence diagram and k-space sampling of a 2D EPI sequence is shown in Figure 2.14. After excitation of the imaging slice, phase and frequency encoding gradients are applied simultaneously to move from the centre of k-space to one of its corners. A frequency encoding gradient is applied to sample the first k-space line, followed by a short phase encoding gradient called blip. The blip allows to jump from the already acquired k-space line to the k-space line to be acquired next. The process of sampling and jumping to the next line is repeated by using a series of blips and frequency encoding gradients of alternating polarities and results in a zig-zag-like coverage of k-space. EPI thus requires high frequency of gradient switching, which makes the sequence hardware demanding and susceptible to off-resonance effects and other artefacts. Despite these challenges, the potential of EPI for human imaging was successfully demonstrated early on by Mansfield's group [*Mansfield*, 1977] and 2D EPI is currently the recommended readout for ASL imaging in the kidneys [*Nery et al.*, 2020].

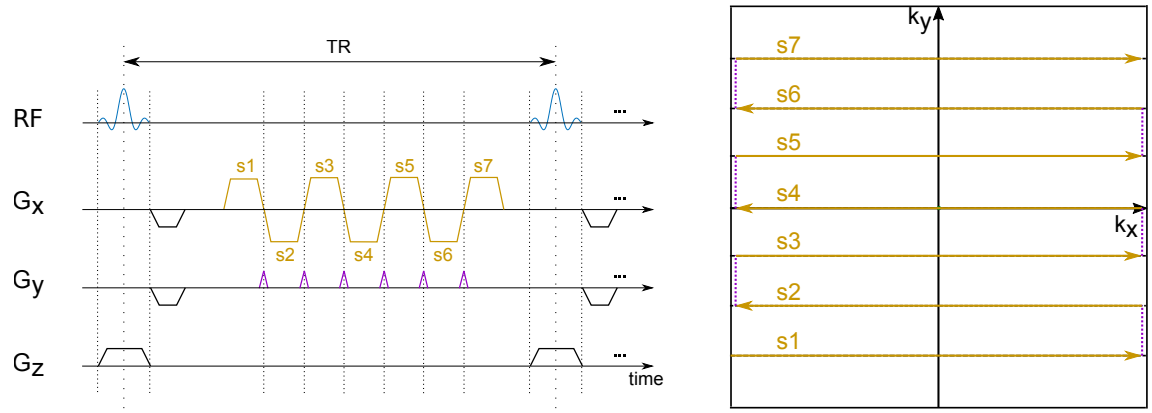

(a) Sequence diagram

(b) k-space trajectory

Figure 2.14: **2D echo-planar imaging sequence diagram (a) and corresponding k-space trajectory (b).** After the excitation pulse, negative gradients in x- and y-direction are applied followed by a positive readout gradient in x-direction for acquiring the first k-space line. A short positive phase encoding gradient in y-direction, called blip, is then applied to jump to the subsequent k-space line and another readout gradient in x-direction with negative polarity is used to sample this k-space line. The process of jumping and sampling is repeated for multiple lines with alternating polarity of the readout gradient in x-direction. After a repetition time TR, the series of RF pulses and gradients will be repeated to acquire a different part of k-space.

Gradient and spin echo

The gradient and spin echo (GRASE) sequence [*Oshio and Feinberg*, 1991] combines multiple gradient and spin echoes within a single TR and thus allows fast sampling of k-space. The sequence diagram and k-space sampling of a 2D GRASE sequence is shown in Figure 2.15. After excitation of the imaging slice using a 90° RF pulse, rephasing gradients are applied on the frequency and slice axes. After a time TE/2, the slice is refocused using a 180° RF pulse resulting in a spin echo being produced at time TE after the excitation just as in the standard SE sequence (see section 2.8). In GRASE, additional gradient echoes are produced before and after the spin echo to sample multiple k-space lines after the refocusing pulse. The polarity of frequency gradients is alternated to switch directions along the frequency encoding axis and gradient blips are employed to jump to the next k-space line along the phase encoding direction. Still within the same TR, additional 180° refocusing RF pulses producing additional spin echoes surrounded by multiple gradient echoes can be used to acquire additional k-space lines. The frequency gradients will be identical for all spin echo trains within a TR. Whereas the phase gradients will be

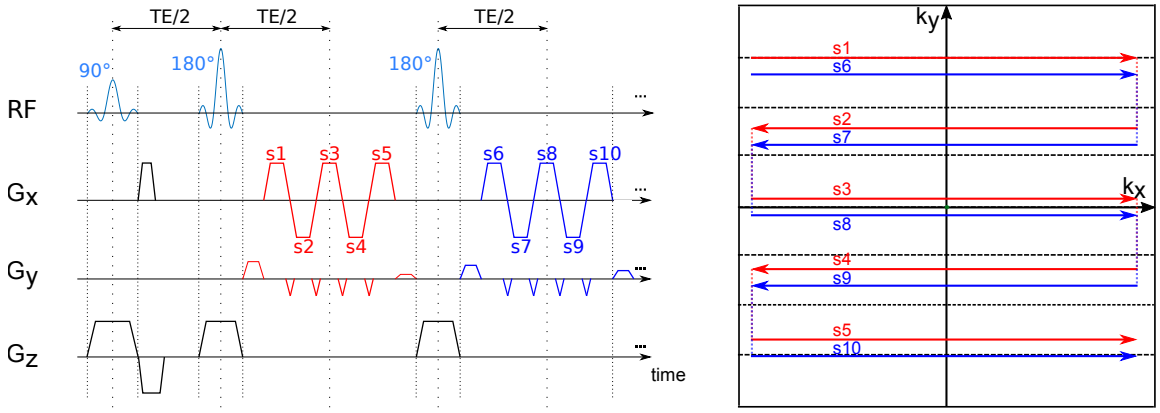

(a) Sequence diagram

(b) k-space trajectory

Figure 2.15: **2D gradient and spin echo sequence diagram (a) and corresponding k-space trajectory (b).** After the excitation pulse, rephasing gradients in x- and z-direction are applied and followed by a first 180° refocusing pulse at time TE/2. A positive phase encoding gradient in y-direction followed by a positive frequency encoding gradient in x-direction produce the first gradient echo (s1) of the first spin echo train (in red). A negative gradient blip in y-direction and a change of polarity of the frequency encoding gradient produce the second gradient echo (s2). Repeating negative gradient blips and frequency encoding gradients of alternating polarity produce the spin echo (s3) and additional gradient echoes (s4 and s5) of the first echo train. The second echo train (in blue) uses the same scheme of frequency gradients and gradient blips as the first one but the amplitude of the phase encoding gradients in y-direction are changed: the first has a reduced amplitude while the last has an increased amplitude. This ensures all spins have the same phase at the end and beginning of each spin echo train. In this example, four gradient echoes and one spin echo are acquired in each spin echo train.

modified for each spin echo train in order to cover different k-space lines while keeping the phase at the end of each spin echo train identical. The number of signals acquired within each TR depends on the number of spin echo trains N_{SE} and the number of gradient echoes N_{GRE}. The GRASE sequence yields similar contrast as a spin echo sequence but all necessary k-space lines can be acquired in much less time as a total of $N_{SE} \cdot N_{GRE}$ signals are acquired within each TR. The GRASE readout is less sensitive to phase errors resulting from field inhomogeneity than EPI but requires more complex signal reordering. A 3D GRASE readout is the current recommendation for ASL measurements of the brain.

2.3.3 Perfusion quantification

The first quantification of perfusion in humans was performed by *Kety and Schmidt* in 1945. They used an inhaled gas, nitrous oxide (N_2O), as freely diffusible tracer and measured the rate of gas inhalation, the arterial and venous tracer concentration until an equilibrium was reached in order to estimate cerebral perfusion in healthy subjects. Arterial and venous tracer concentrations were determined by direct measurements in blood samples acquired at different time points after gas inhalation. Using Fick's principle [*Fick*, 1870], they calculated the cerebral perfusion f as

$$\frac{dC_T}{dt} = f \cdot (C_A(t) - C_V(t)) \tag{2.66}$$

where C_T is the quantity of tracer concentration of N_2O taken up by the brain tissue, C_A is the quantity of N_2O brought to the brain by arterial blood, and C_V is the quantity of N_2O removed by venous blood. This model was then adapted to MR perfusion imaging by *Detre et al.* (1992), who modified the Bloch equation to take into account flow in order to quantitatively calculate perfusion values from ASL data.

2.3.3.1 Modified Bloch equation

To include flow, the Bloch equation used to describe the longitudinal relaxation of tissue magnetisation $M_T(t)$ can be modified to [*Detre et al.*, 1992; *Calamante et al.*, 1999]

$$\begin{aligned} \frac{dM_T(t)}{dt} &= \frac{M_{0,T} - M_T(t)}{T_{1,T}} + f \cdot \Big(M_b(t) - M_T(t)\Big) \\ &= \frac{M_{0,T} - M_T(t)}{T_{1,T}} + f \cdot M_b(t) - \frac{f}{\lambda} \cdot M_T(t) \end{aligned} \tag{2.67}$$

where $M_{0,T}$ is the fully relaxed longitudinal magnetisation of tissue, f is the blood flow, M_b is the inflowing longitudinal magnetisation of arterial blood, and λ is the blood-tissue

partition coefficient. This equation assumes a well-mixed compartment model with water as a freely diffusible tracer, so that the magnetisation of venous spins leaving the tissue is given by $M_V = M_T/\lambda$ [*Detre et al.*, 1992]. In steady state, $M_T(t)$ becomes $M_{SS,T}$ and the blood flow (perfusion) can then be quantified using following equation [*Detre et al.*, 1992]

$$f = \frac{\lambda}{T_{1,T}^{app}} \left(1 - \frac{M_{SS,T}}{M_{0,T}}\right) \tag{2.68}$$

The apparent relaxation time of tissue, which is influenced by the blood flow, is defined as

$$\frac{1}{T_{1,T}^{app}} = \frac{1}{T_{1,T}} + \frac{f}{\lambda} \tag{2.69}$$

2.3.3.2 General kinetic model

In 1998, *Buxton et al.* [1998] introduced a general kinetic model (GKM) to quantify perfusion by considering the difference in longitudinal magnetisation, which is proportional to the ASL signal, as the magnetisation delivered in a voxel by arterial blood. In this model, the amount of magnetisation in a tissue depends on the delivery of magnetisation through the arteries, the clearance of magnetisation through the veins (and urine in case of the kidneys), and the longitudinal relaxation of the magnetisation. Mathematically, the amount of magnetisation in a voxel at time t can thus be described using three functions:

1. the delivery function $c(t)$: describes the normalised arterial concentration of magnetisation that arrives in the imaged voxel at time t
2. the residue function $r(t, t')$: describes the fraction of labelled water molecules arrived in the voxel at the time of arrival t' and remains in the voxel at time t
3. the magnetisation relaxation function $m(t, t')$: describes the fraction of longitudinal magnetisation of the labelled water molecules in the voxel at the time of arrival t' that remains at time t

The difference (control-label) in longitudinal magnetisation measured in a voxel at time t can then be written as

$$\Delta M(t) = 2 \cdot M_{0,b} \cdot f \cdot \int_0^t c(t') \cdot r(t - t') \cdot m(t - t')\ dt' \tag{2.70}$$

Hereby, $2 \cdot M_{0,b} \cdot f \cdot c(t')$ describes the history of magnetisation delivery to the voxel with $M_{0,b}$ being the equilibrium longitudinal magnetisation of arterial blood and f the local perfusion. $r(t - t') \cdot m(t - t')$ represents the longitudinal magnetisation arrived at

time t' that remains in the voxel at time t. With this general model, processes such as transit delay between labelling and imaging region, longitudinal magnetisation decay, water exchange between blood and tissue, magnetisation clearance, and different labelling schemes can be taken into account in the perfusion quantification by choosing appropriate delivery, residue, and magnetisation relaxation functions.

For the standard ASL kinetic model, the delivery, residue, and magnetisation relaxation functions are defined as [*Buxton et al.*, 1998]

$$c(t) = \begin{cases} 0 & 0 < t < \Delta t \\ \alpha\ e^{-t/T_{1,b}}\ \text{(PASL)} & \Delta t \leq t < \Delta t + \tau \\ \alpha\ e^{-\Delta t/T_{1,b}}\ \text{((P)CASL)} & \Delta t \leq t < \Delta t + \tau \\ 0 & \Delta t + \tau \leq t \end{cases} \tag{2.71}$$

$$r(t) = e^{-ft/\lambda}$$

$$m(t) = e^{-t/T_{1,t}}$$

In this model, the labelling efficiency is taken into account by the factor α defined as the fraction of actual change in longitudinal magnetisation achieved through labelling to the maximum change available. For perfect inversion, α is equal to 1, and for perfect saturation, α is equal to 0.5 [*Alsop and Detre*, 1996].

Assumptions of the GKM

This model is based on three main assumptions. Firstly, a uniform plug flow is assumed for the delivery of labelled blood in a voxel. This means that no labelled blood arrives before a certain arterial transit time Δt; during the time from Δt to $\Delta t + \tau$, the labelled blood arrives in the voxel; and after $\Delta t + \tau$, the blood arriving in the voxel is unlabelled. τ is thus the temporal duration of the labelled blood bolus and is known as labelling duration or bolus duration or bolus length. During the ATT, the longitudinal magnetisation will relax with the longitudinal time constant of arterial blood T_{1A}. The delivery functions resulting from these assumptions differ for PASL, and (P)CASL schemes as shown schematically in Figure 2.16.

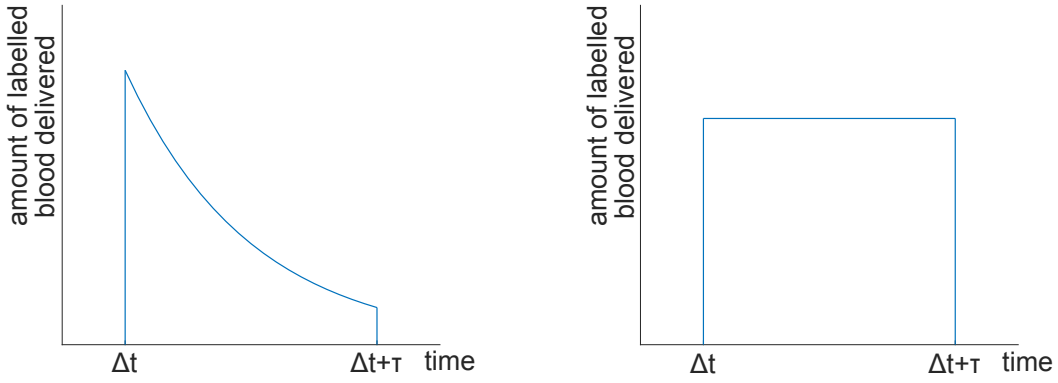

(a) PASL (b) (P)CASL

Figure 2.16: **Delivery function for the general kinetic model.** The amount of labelled blood arriving at a voxel, described by the delivery function, depends on the amount of labelled spins and the amount of relaxation that has occurred after the labelling. (a) In PASL, the distance between labelling and imaging is not identical for all spins since a whole slab is used as labelling region. Labelled spins thus need different amounts of time before reaching the imaging region, resulting in different amounts of relaxation after labelling and with it an exponentially decreasing delivery of labelled spins to the imaging region. (b) In (P)CASL, a single labelling plane is used so that the distance between labelling and imaging is constant, resulting in a fixed amount of relaxation for all spins after the labelling. The amount of relaxation is determined by the arterial transit time Δt.

Secondly, a single compartment model is assumed for the exchange of water between blood and tissue. This model considers tissue and blood to be homogeneous so that all exchange of water between the vasculature and the tissue is instantaneous, i.e., the exchange is rapid enough for concentration fractions of sub-units of blood or tissue to remain unchanged. Therefore, it is assumed that the ratio of total tissue concentration and venous concentration is constant and equal to the tissue-blood partition coefficient of water λ. The residue function is thus a mono-exponential with perfusion dependent decay rate f/λ.

Thirdly, this model assumes that water is immediately extracted from the vascular space when arriving in the voxel. Thus, the longitudinal magnetisation of the labelled water initially decays with the relaxation time of arterial blood $T_{1,b}$ but, at arrival in the voxel, it decays with the relaxation time of tissue $T_{1,t}$.

The three assumptions used for the general kinetic model allow a simplified description of the measured ASL signal. To estimate the effect of these assumptions on the signal description, *Buxton et al.* (1998) modified the delivery, residue, and magnetisation relaxation functions to better reflect the reality and compared the results to the standard model. A smoother delivery function was chosen to take into account varying transit times

from the labelling region to the imaging region. While this change resulted in no difference for the (P)CASL signal, the PASL signal was found to be stronger for short transit times. In case of longer transit times, the perfusion signal will be underestimated by the general kinetic model unless the delay time is adapted to be also longer. The residue function was modified to take into account the time necessary for a water molecule to leave the voxel as well as the incomplete extraction of water from blood into tissue. This modification had little effect on the PASL signal compared to results obtained with the general kinetic model. For (P)CASL, this modification resulted in a slight decrease in perfusion signal. The magnetisation relaxation function was modified to account for the time between the entering of water molecules in the voxel and the beginning of exchange of the water molecules between blood and tissue in the voxel. This modification resulted in a strong difference in (P)CASL and PASL signals, indicating an overestimation of perfusion when using the standard ASL kinetic model (i.e., assuming an instantaneous exchange of water molecules).

Solutions of the GKM

Solving Equation (2.70) for the case of PASL, we obtain:

$$\Delta M(t) = \begin{cases} 0 & 0 < t < \Delta t \\ 2 \cdot M_{0,b} \cdot f \cdot (t - \Delta t) \cdot \alpha \cdot e^{-t/T_{1,b}} \cdot q_p(t) & \Delta t \leq t < \Delta t + \tau \\ 2 \cdot M_{0,b} \cdot f \cdot \tau \cdot \alpha \cdot e^{-t/T_{1,b}} \cdot q_p(t) & \Delta t + \tau \leq t \end{cases} \tag{2.72}$$

with

$$q_p(t) = \begin{cases} \frac{e^{kt} \cdot (e^{-k\Delta t} - e^{-kt})}{k \cdot (t - \Delta t)} & \Delta t \leq t < \Delta t + \tau \\ \frac{e^{kt} \cdot (e^{-k\Delta t} - e^{-k(\tau + \Delta t)})}{k \cdot \tau} & \Delta t + \tau \leq t \end{cases}$$

and

$$k = \frac{1}{T_{1,b}} - \frac{1}{T_{1,T}} - \frac{f}{\lambda} = \frac{1}{T_{1,b}} - \frac{1}{T_{1,T}^{app}}$$

The factor $q_p(t)$ can be understood as a correction factor, which accounts for (1) the change in T_1 relaxation due to the exchange of labelled blood magnetisation with unlabelled tissue magnetisation leading to an apparent longitudinal relaxation time of tissue $T_{1,T}^{app}$, and (2) the clearance of the labelled magnetisation by venous blood flow [*Buxton et al.*, 1998; *Wong et al.*, 1998b]. Typically, these two effects are small, with $q_p(t)$ values ranging from 0.85 to 1.00 in practice [*Wong et al.*, 1998b].

Solving Equation (2.70) for the case of (P)CASL, we obtain:

$$\Delta M(t) = \begin{cases} 0 & 0 < t < \Delta t \\ 2 \cdot M_{0,b} \cdot f \cdot T_{1,T}^{app} \cdot \alpha \cdot e^{-\Delta t / T_{1,b}} \cdot q_{ss}(t) & \Delta t \leq t < \Delta t + \tau \\ 2 \cdot M_{0,b} \cdot f \ T_{1,T}^{app} \cdot \alpha \cdot e^{-\Delta t / T_{1,b}} \cdot e^{-(t-\tau-\Delta t)/T_{1,T}^{app}} \cdot q_{ss}(t) & \Delta t + \tau \leq t \end{cases} \tag{2.73}$$

with

$$q_{ss}(t) = \begin{cases} 1 - e^{-(t-\Delta t)/T_{1,T}^{app}} & \Delta t \leq t < \Delta t + \tau \\ 1 - e^{-\tau / T_{1,T}^{app}} & \Delta t + \tau \leq t \end{cases}$$

Equations (2.72) and (2.73) show that the measured signal difference between control and labelled image is directly proportional to the perfusion f. The proportionality factor depends on properties of arterial blood (equilibrium longitudinal magnetisation $M_{0,b}$), properties of the tissue of interest (longitudinal relaxation time $T_{1,T}^{app}$, arterial transit time Δt), as well as acquisition parameters (labelling/bolus duration τ and time of acquisition t). For blood flow quantification, Equations (2.72) and (2.73) have to be solved for blood flow f. For simplification, we can assume that the blood entering the voxel relaxes with the longitudinal relaxation time of arterial blood ($T_{1,b}$) and not the apparent the longitudinal relaxation time of tissue ($T_{1,T}^{app}$) used in the Buxton model [*Hernandez-Garcia et al.*, 2019], which reduces the model to a single-compartment model. With this assumption, the quantification formula for PASL (Equation 2.72) simplifies nicely as k can be set to 0 and $q_p(t)$ to 1 [*Buxton et al.*, 1998]. Furthermore, we can assume that acquisition takes place at a time $t \geq \Delta t + \tau$. These two assumptions together are most commonly used for ASL-based perfusion quantification and will be referred to as simplified GKM throughout this document. The perfusion rate f is given in units of 1/s. In order to convert it into the commonly used unit in medical perfusion quantification of ml/100g/min (f'), we can use the blood-tissue partition coefficient λ and make use of the relation $M_{0,b} = M_{0,T}/\lambda$, which assumes instantaneous equilibrium between tissue and veins. The blood-tissue partition coefficient indicates the relative composition of the organ of interest in terms of tissue weight and blood volume. It is generally defined as the water weight per tissue weight divided by the weight of water in grams per volume of blood in millilitres. It follows that $f' = 6000 \cdot f \cdot \lambda$. For 3D or single-slice 2D ASL acquisitions, blood flow or perfusion is then quantified in mL/100g/min using the following equation [*Alsop et al.*, 2015; *Nery*

et al., 2020]

$$f' = \begin{cases} \dfrac{6000 \cdot \lambda \cdot \Delta M \cdot e^{TI/T_{1,b}}}{2 \cdot \alpha \cdot M_{0,T} \cdot TI_1} & \text{PASL with QUIPSS II} \\ \dfrac{6000 \cdot \lambda \cdot \Delta M \cdot e^{\mathrm{PLD}/T_{1,b}}}{2 \cdot \alpha \cdot M_{0,T} \cdot T_{1,b} \cdot (1 - e^{-\tau/T_{1,b}})} & \text{(P)CASL} \end{cases} \tag{2.74}$$

In case of 2D sequential multi-slice acquisitions, the inflow duration of the labelled spins is slice dependent. Hence, the real PLD and TI are different for each slice and the equations can be rewritten as:

$$f' = \begin{cases} \dfrac{6000 \cdot \lambda \cdot \Delta M \cdot e^{(TI + t_s \cdot (n-1))/T_{1,b}}}{2 \cdot \alpha \cdot M_{0,T} \cdot TI_1} & \text{PASL with QUIPSS II} \\ \dfrac{6000 \cdot \lambda \cdot \Delta M \cdot e^{(\mathrm{PLD} + t_s \cdot (n-1))/T_{1,b}}}{2 \cdot \alpha \cdot M_{0,T} \cdot T_{1,b} \cdot (1 - e^{-\tau/T_{1,b}})} & \text{(P)CASL} \end{cases} \tag{2.75}$$

where n is the slice number and t_s is the time between two subsequent slice acquisitions. Equations 2.74 and 2.75 use the nomenclature convention adopted by the ASL and OSIPI[3] communities [*Alsop et al.*, 2015; *Nery et al.*, 2020]. It can be seen that for PASL, the acquisition time t has been replaced by the delay time (or inflow time) TI and the bolus duration τ has been replaced by TI_1 corresponding to the QUIPPSS/QUIPPSS II controlled bolus duration. For (P)CASL, the acquisition time t has been replaced by $\mathrm{PLD} + \tau$, where PLD is the delay time (or post-labelling delay) and τ is the labelling duration as previously defined. The simplified equations thus apply only for $TI \geq \Delta t + TI_1$ and $\mathrm{PLD} \geq \Delta t$ for PASL and (P)CASL, respectively.

Current consensus publications recommend values to be used for the tissue-blood partition coefficient λ, the labelling efficiency α, and the longitudinal relaxation time of arterial blood $T_{1,b}$. In the brain, a constant value of $\lambda = 0.9$ mL/g is commonly used [*Herscovitch and Raichle*, 1985; *Alsop et al.*, 2015] and the same is recommended for quantification in the kidneys due to a lack of a reliable reference value specifically for the kidneys [*Nery et al.*, 2020]. A labelling efficiency of $\alpha = 0.95$ and $\alpha = 0.85$ are assumed for PASL and (P)CASL, respectively [*Alsop et al.*, 2015; *Nery et al.*, 2020]. In case background suppression (BS) pulses are used for control and labelled images, these constant values need to be corrected to account for the loss in labelling efficiency resulting from BS pulses applied after the labelling pulses [*Garcia et al.*, 2005; *Nery et al.*, 2020]. The overall labelling efficiency α' is then given by $\alpha \cdot 0.93^{nBS}$, where nBS denotes the number of BS pulses

[3] `https://osipi.org/resources/` and `https://docs.google.com/document/d/1vj0Tp4yur4dpJntF90yy2bOBUx33FG-w/edit`, *last accessed 31.08.2022*

applied after the labelling pulses. The longitudinal relaxation of arterial blood is assumed to be $T_{1,b} = 1.65$ s at a field strength of 3T and $T_{1,b} = 1.48$ s at a field strength of 1.5T [*Zhang et al.*, 2013].

2.3.3.3 Model-free approach

The assumptions of the GKM might not be accurate especially in pathological cases. To move away from any restrictive assumption and allow a quantification for all pathologies, a model-free ASL quantification was proposed [*Petersen et al.*, 2006b]. This method is based on deconvolution and requires the estimation of the arterial input function (AIF). As such, it bears resemblance to the quantification of DSC-MRI data. In the model-free ASL quantification method, the AIF is estimated by subtracting two perfusion-weighted images acquired with and without crusher gradients, which remove the signal from spins with high velocity. While the idea of reducing the number of assumptions is appealing, this model-free approach also has several drawbacks. It requires additional acquisitions, depends on the intrinsic scanner sensitivity and AIF estimation is affected by the crusher gradient design. Therefore, the simplified GKM (Equations 2.74 and 2.75) remains more widely used by the ASL community.

2.3.3.4 Limitations of quantification

The quality of quantification will depend on the accurate knowledge of labelling/bolus duration, arterial transit time, T_1 value of blood (and tissue for two-compartment models), and the quality of field shim [*Buxton et al.*, 1998]. Especially in patients with pathologies such as stroke or vessel stenosis, the arterial transit time will be longer than in healthy subjects. Therefore, the delay time has to be adjusted to avoid an underestimation of perfusion in the affected areas. Most models assume that the T_1 of tissue is equal to the T_1 of blood (single compartment models). In the case of brain perfusion, this leads to an overestimation of perfusion in white matter as the actual T_1 of white matter is lower than the T_1 of blood [*Kwong et al.*, 1995; *van Gelderen et al.*, 2008]. Furthermore, single tissue compartment models do not take into account that some of the arterial blood water passing through the voxel does not exchange with tissue water [*Hernandez-Garcia et al.*, 2019]. In addition, such models do not take into account the effect of partial volume due to tissues surrounding the tissue of interest (e.g. cererbospinal fluid when quantifying perfusion in brain). As the T_1 of cerebrospinal fluid is longer than the T_1 of both gray and white matter, perfusion will be underestimated [*Kwong et al.*, 1995]. Nevertheless, single compartment models with delay times adapted to the studied population remain the easiest to implement and are currently the most used in clinical and research applications.

2.4 Basics of Anatomy and Physiology

2.4.1 Anatomical terminology

To facilitate the description of anatomy, terminology for different planes and directions are commonly used and briefly introduced here. The sagittal plane goes from back to front and from top to bottom. The transverse plane goes from left to right and from back to front. The coronal plane goes from left to right and from top to bottom. Superior refers to the direction from foot to head, and inferior from head to foot. Lateral describes the direction from left to right or right to left. Dorsal refers to the direction from front to back, and ventral from back to front. Anterior means in front and posterior means behind. Figure 2.17 shows these planes and directions.

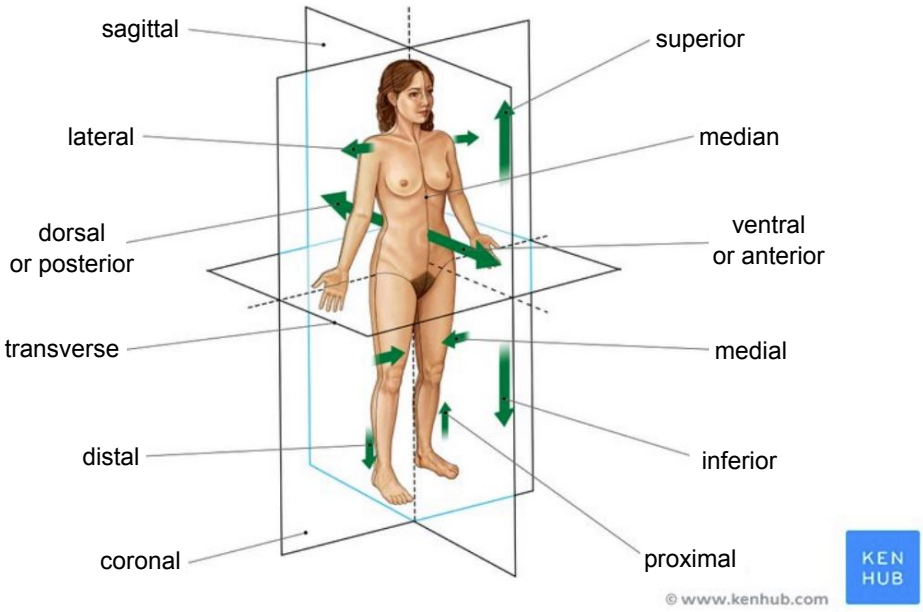

Figure 2.17: **Schematic definition of anatomical planes and directions.** Image adapted from `https://www.kenhub.com/en/library/anatomy/anatomical-terminology`, *last accessed 08.08.2022*

2.4.2 Brain

The brain is a complex and multi-functional organ, which plays a central role in the nervous system. A schematic sagittal view of the brain is depicted in Figure 2.18. The brain is composed of two hemispheres connected by a fibre bundle known as the corpus callosum. Each brain hemisphere can be separated into four lobes (frontal, parietal, occipital, temporal) and a cerebellar hemisphere. Both cerebellar hemispheres form the cerebellum, which controls motor functions and is probably also involved in many other brain functions. The brain hemispheres (except the cerebellum) are responsible for body functions in the opposite body side (i.e., the left hemisphere is responsible for the right body side and the right hemisphere for the left body side) while the cerebellar hemispheres are involved in functions in the same body side.

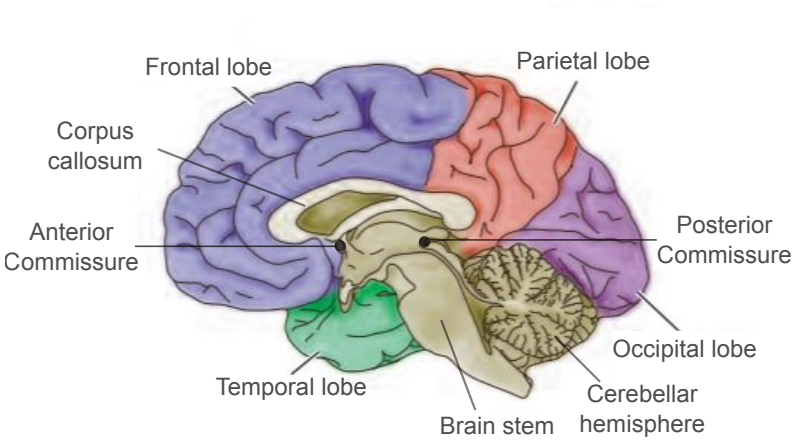

Figure 2.18: **Schematic sagittal view of the brain.** Note the positions of the anterior comissure (AC) and posterior commissure (PC), which are important anatomical landmarks for planning PCASL MRI acquisitions. Image adapted from `https://wiki.tum.de/display/btt/Anatomy+of+brain`, *last accessed 08.08.2022*

Brain tissue is separated into two groups: gray matter (GM) and white matter (WM) [*Wen and Chklovskii*, 2005]. GM contains local networks of neurons, synapses and mainly nonmyelinated axons. WM mainly contains myelinated axons, responsible for global transmission. Circulating around the brain and in the brain ventricles, is the cerebrospinal fluid (CSF). The role of the CSF is to ensure buoyancy of the brain, protect brain tissue, maintain the internal chemical and physical state of the brain, and clear waste products. GM, WM and CSF can be clearly distinguished in MR images with appropriate repetition and echo times. Figure 2.19 shows a MRI of a healthy brain with distinct signal levels in GM, WM, and CSF regions.

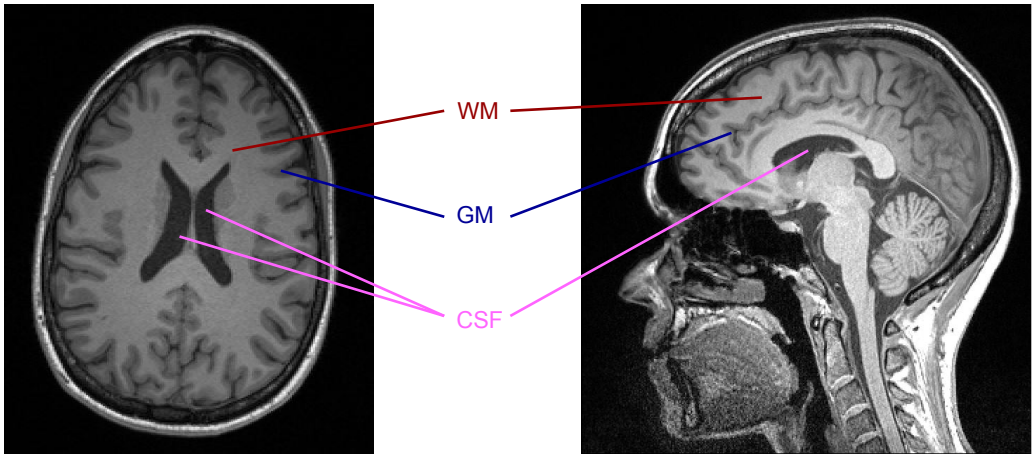

Figure 2.19: **MRI of the brain:** Axial (left) and sagittal (right) planes with clearly distinguishable gray matter (GM), white matter (WM), and cerebrospinal fluid (CSF) areas.

Pathologies, which modify tissue characteristics, can be detected in MR images as regions with abnormal signal intensities. Furthermore, pathologies also affect function and can be described using functional MR images and derived quantitative maps such as perfusion maps.

2.4.3 Kidney

The kidneys are bean shaped organs positioned on each side of the spine in the abdomen region. The liver and the spleen lie superior to the right kidney and left kidney, respectively. The renal artery is positioned slightly anterior to both kidneys. A MRI of a healthy volunteer depicting both kidneys, the liver, and the spleen is shown in Figure 2.20.

Kidneys are mainly responsible for the excretion of waste materials produced by body metabolism via urine [*Rayner et al.*, 2020]. They are also key for maintaining steady internal chemical and physical conditions in the body. Amongst other, they control blood pressure, acidity, haemoglobin levels, regulate the electrolyte balance, and are involved in hormone syntheses. For excreting metabolic waste products from the body, about 80% of the blood plasma is cleaned by active transporters on tubules close to tissue capillaries and the rest is filtrated through the glomerular filtration barrier. Autoregulation of the kidneys ensures the glomerular filtration rate (GFR) is kept steady over a range of artery pressures.

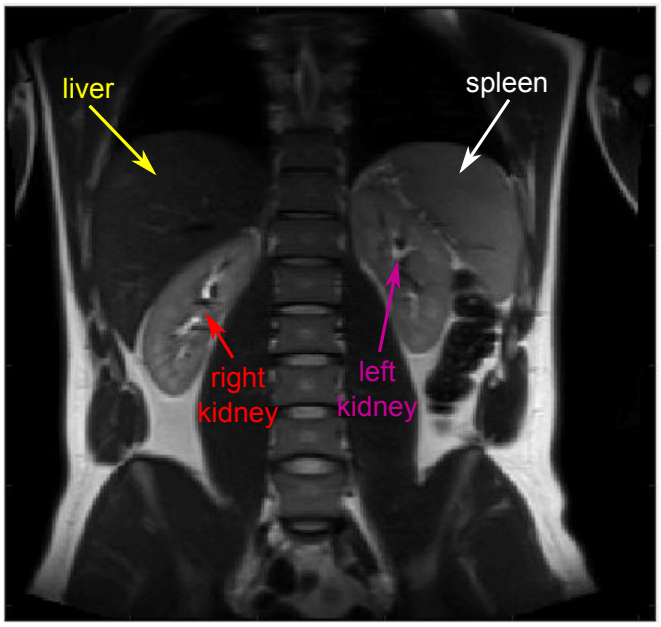

Figure 2.20: **MRI of the abdomen showing the position of both kidneys, liver, and spleen.**

The inner structure of the kidney, schematically shown in Figure 2.21, has three main compartments: the cortex, the medulla, and the renal pelvis. The cortex corresponds to the outer tissue layer, has a granular structure, and contains arterioles, venules and glomerular capillaries (blood vessels of different sizes). The medulla, makes up the inner part of the renal tissue and is composed of triangular shaped structures known as pyramids. These pyramids contain numerous nephrons, also called functional units of the kidneys. Each nephron reaches from the cortex to the renal pelvis and ensures filtration and regulation via a capillary network intricately wound around it and a glomerular capsule at the cortex end. The kidney pelvis is the entry and exit point of the renal blood vessels and nerves as well as the exit point of the ureters, which bring the urine from the kidneys to the urinary bladder.

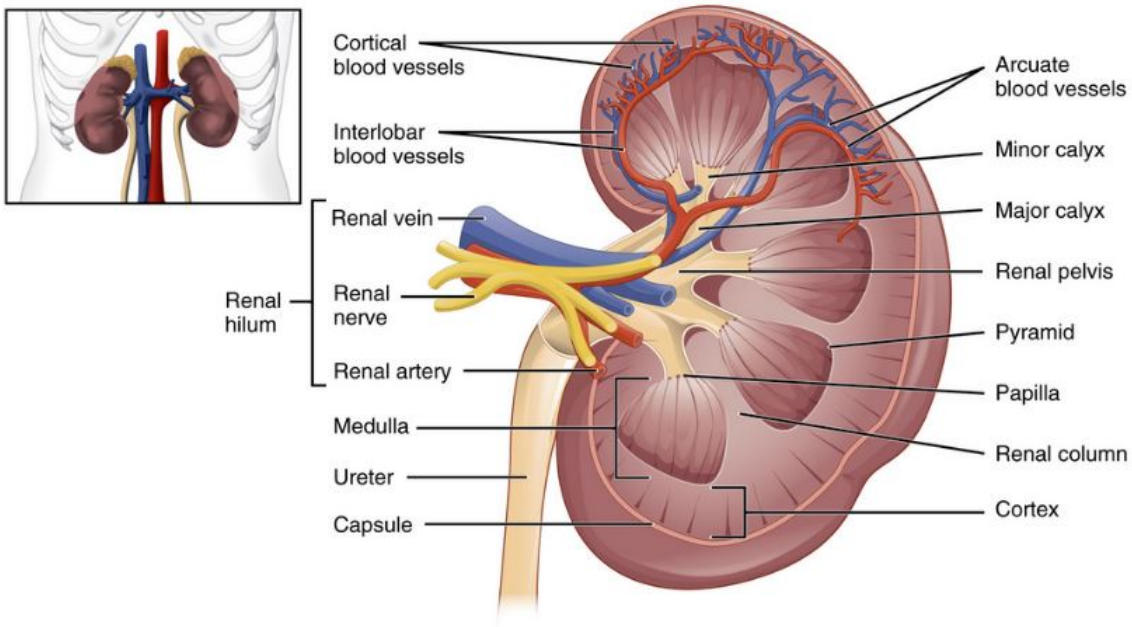

Figure 2.21: **Kidney anatomy.** Perfusion quantification in the cortex and medulla are of special interest in clinical kidney imaging. Image from `https://openstax.org/books/anatomy-and-physiology/pages/25-3-gross-anatomy-of-the-kidney`, *last accessed 08.08.2022*

CHAPTER 3

Materials and Methods

The first section of this chapter briefly describes the hardware used to acquire MRI data. The following sections are divided according to the organ of interest, starting with the brain and finishing with the kidneys. In each of these sections, the developed analysis pipeline and the data used are described. The last section of this chapter briefly introduces relevant metrics and statistical tests. Parts of this chapter have been published in [*Brumer et al.*, 2022a][1] and the description of the corresponding materials and methods is partly replicated here.

3.1 Hardware

Two whole body MRI scanners with a field strength of 3 T available at the radiology department of the University Hospital Mannheim, Germany, were used in this work: the MAGNETOM Tim Trio and MAGNETOM Tim Skyra systems (Siemens Healthcare GmbH, Erlangen, Germany) depicted in Figure 3.1. Both Trio and Skyra systems include a superconducting coil cooled with liquid helium for the main magnetic field of 3 T, a gradient system for spatial encoding, shim coils for improved homogeneity of the main magnetic field, and a whole body transmit coil for RF pulse transmission. Additional receive coils are available for different body parts. Scanner specifications can be found in Table 3.1.

[1] CC BY License

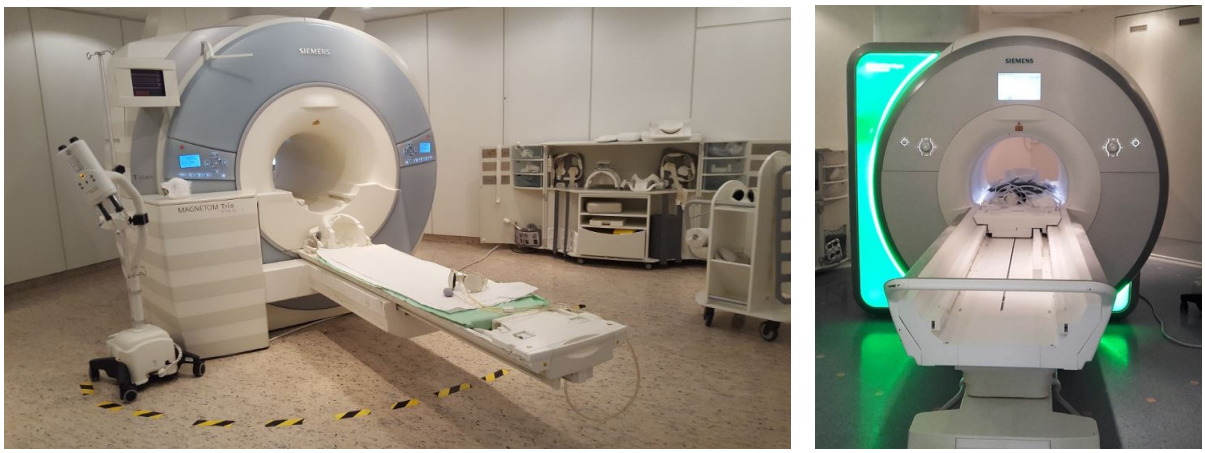

(a) Trio (b) Skyra

Figure 3.1: **MRI systems used for data acquisition:** (a) 3T MAGNETOM Tim Trio (Siemens Healthcare GmbH, Erlangen, Germany) and (b) 3T MAGNETOM Tim Skyra (Siemens Healthcare GmbH, Erlangen, Germany).

Table 3.1: **MRI scanner system specifications** for MAGNETOM Tim Trio and MAGNETOM Tim Skyra systems (Siemens Healthcare GmbH, Erlangen, Germany) available at `https://www.siemens-healthineers.com/magnetic-resonance-imaging` (*last accessed 08.08.2022*).

MRI system	Trio	Skyra
field strength [T]	3	3
system length [m]	2.13	1.73
bore diameter [m]	0.60	0.70
maximum gradient amplitude [mT/m]	40	45
maximum gradient slew rate [T/m/s]	200	200

3.2 Brain

3.2.1 Analysis Pipeline

The data analysis pipeline for brain ASL data was developed as a MATLAB® script (Version 2020a, MathWorks, Natick, Massachusets) with SPM12 (Wellcome Trust Centre for Neuroimaging, University College London, UK) batches. It is summarised in Figure 3.2 and the individual steps are detailed in the next sections.

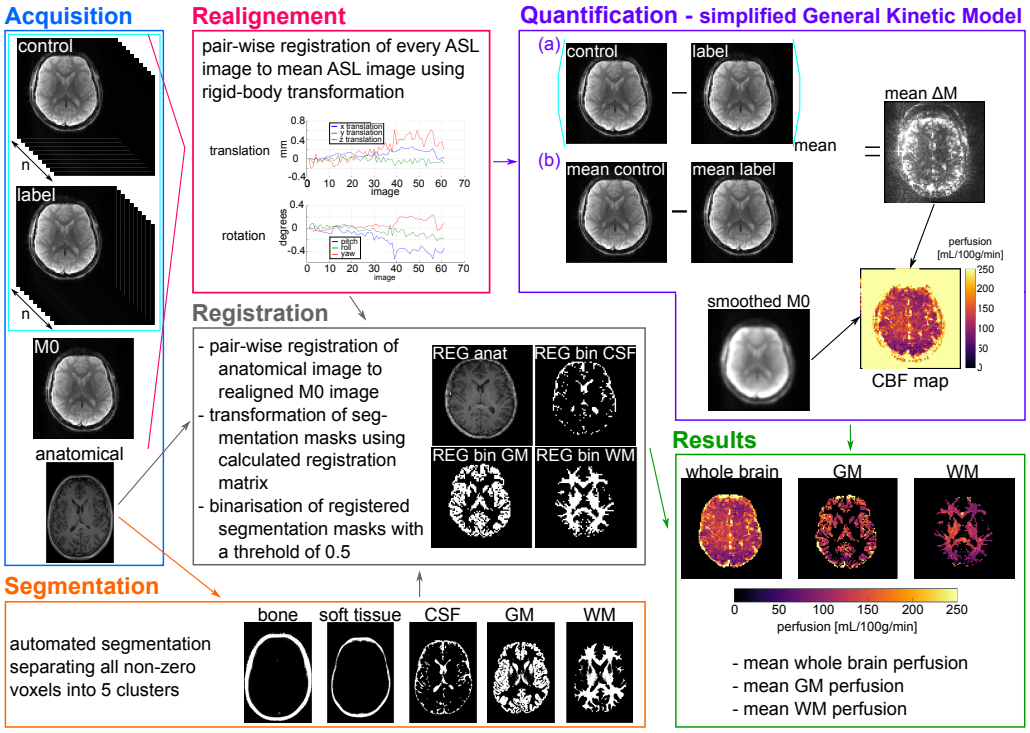

Figure 3.2: **Analysis pipeline for brain ASL data.** After acquisition of ASL (M0 and control-label pairs) and anatomical images, the ASL data is first realigned. If available, the anatomical data is segmented and then registered to the realigned M0 image. Otherwise, the M0 image is used for segmentation after realignement. The realigned control and label pairs are either (a) subtracted and averaged (SA mehtod) or (b) averaged and subtracted (AS method) to calculate a mean perfusion-weighted image ΔM. A perfusion (CBF) map is then calculated using the simplified general kinetic model *Buxton et al.* [1998]; *Alsop et al.* [2015]; *Nery et al.* [2020]. In the quantification step, outliers can be removed from the control and labelled time series or from the ΔM time series or from the CBF time series depending on the chosen option. For the final results, the binarised and registered segmentation masks are applied on the perfusion map and mean perfusion values are calculated. For easier visualisation, only a single slice of the acquired brain volume is shown here but the analysis pipeline works for any number of slices. *Abbreviations used: n - number of control-label pairs acquired; CSF: cerebrospinal fluid; GM: gray matter; WM - white matter; REG - registered; bin - binarised; CBF - cerebral blood flow.*

3.2.1.1 Realignement

After acquisition of the ASL (M0 and multiple label-control pairs) and the anatomical data, all the images are loaded as matrices in MATLAB®. All ASL images are first realigned to the mean image using a rigid body transformation provided in SPM12 (Realign - Estimate and Reslice). This realignement is necessary to correct for subject motion during the acquisition. The SPM12 graphics window allows a visualisation of the motion (three translation and three rotation degrees of freedom) present in the entire time series. A final visual check of the realignement procedure is also possible within the SPM12 graphical user interface.

3.2.1.2 Segmentation

Segmentation is performed on the anatomical data in the anatomical space or on the M0 image in ASL space in case no anatomical data is available. The segmentation is based on SPM12 (Segment). It separates all non-background voxels into 5 clusters (bone, soft tissue, cerebrospinal fluid, gray matter, white matter) and creates tissue probability maps for each cluster. In case of abnormal brain anatomy, manual segmentations of regions of interest (ROI) can be used instead of automated tissue segmentation.

3.2.1.3 Registration

When the segmentation is performed in the anatomical space, a registration of the anatomical space to the ASL space is necessary. A pairwise registration of the anatomical data to the realigned M0 image is performed using standard SPM12 rigid body transformation with a 4-th order B-spline interpolation (Coregister - Estimate and Reslice). In case of automated segmentation, the tissue probability maps for gray matter (GM), white matter (WM) and cerebrospinal fluid (CSF) are then transformed from the anatomical to the ASL space using the transformation matrix obtained from the pairwise registration. In case manual segmentation masks are available, these are also transformed from the anatomical to the ASL space using the transformation matrix obtained from the pairwise registration. As a final step, the registered segmentation masks are binarised using a threshold fixed at half the highest voxel value within the mask, thus yielding binary segmentation masks in the ASL space.

3.2.1.4 Quantification

Quantification is performed based on the general kinetic model. Different methods for the calculation of the perfusion-weighted image, options for the removal of outliers, and corrections for the M0 image used in the quantification formula exist in the literature. For comparison purposes, multiple options were implemented in the analysis pipeline.

Perfusion-weighted image calculation

The mean perfusion-weighted image can either be calculated by pairwise subtraction of realigned control and labelled images followed by averaging (SA method) or by first averaging all realigned control and all realigned labelled images before subtracting the mean labelled image from the mean control image (AS method). Additional variations consist in taking the absolute value of the subtracted images (|SA| and |AS| methods, respectively). To visualise the quality of the ASL data, the signal averaged over the entire

brain (CSF and WM and WM) or averaged over a specific brain compartment (CSF or GM or WM) is plotted for each control and each labelled image acquired. In case the SA method is used, the temporal SNR (tSNR) of the time series of perfusion-weighted images is calculated and the evolution of the signal of the individual perfusion-weighted images is plotted. In case the AS method is used, the tSNR of the time series of control and labelled images is calculated and the evolution of the signal of the individual control and labelled images is plotted.

Outlier removal

In addition to the choice of method for the calculation of the perfusion-weighted image, seven options to exclude outlier images before the final quantification are implemented:

1. SA $\mu \pm 2 \cdot \sigma$
2. AS $\mu \pm 2 \cdot \sigma$
3. SA z-scoreVol
4. SA z-scoreSli
5. SA AOC
6. SA pAOCSL
7. SA SCORE

The options are either applicable for the SA or the AS method. Options 1 and 3 use the perfusion-weighted (ΔM) images, option 2 uses the control and labelled images, and options 4-6 use the CBF images to determine outliers.

Option 1 is applicable for the SA method and consists of removing all control-label pairs for which the mean perfusion-weighted signal intensity is outside the mean ± twice the standard deviation ($\mu \pm 2 \cdot \sigma$) range of the entire perfusion-weighted image time series. The mean and standard deviations are calculated over the entire brain (CSF and GM and WM).

Option 2 is applicable to the AS mehtod and compares the mean signal intensity of all control images or all labelled images to the mean ± twice the standard deviation ($\mu \pm 2 \cdot \sigma$) range of the entire control image or labelled image time series, respectively. Here, the removal criteria is checked for each brain compartment (CSF, GM, WM) individually and an image is discarded if signal intensities are outside the comparison range for at least two of the three compartments.

Options 3 and 4 are based on the method by *Tan et al.* (2009), which considers both the mean and standard deviation distributions of the perfusion-weighted images to determine outliers. The original method first creates a brain tissue mask by averaging all control and labelled images and thresholding this mean image in order to discard background voxels. In our pipeline, the brain is automatically segmented and the produced brain mask is used

instead. Considering only the intensities of voxels within the brain, outliers are determined on an image-by-image or slice-by-slice basis (z-scoreVol and z-scoreSli, repsectively). For simplification, the following explanation is in terms of images but is also applicable to slices. Images with mean value M_i and standard deviation S_i for which either of the following criteria applies are discarded as outliers: $|M_i| > \mu_M + 2.5 \cdot \sigma_M$ and $S_i > \mu_S + 1.5 \cdot \sigma_S$. μ_M represents the mean of the distribution of means of tissue intensity across all perfusion-weighted images and μ_S represents the mean of the distribution of the standard deviations of tissue intensity across all perfusion-weighted images. σ_M and σ_S represent the standard deviation of the distribution of means of tissue intensity and the standard deviation of the distribution of the standard deviations of tissue intensity, respectively. The factors 1.5 and 2.5 were empirically chosen based on clinical PASL data as presented in the original publication of the method [*Tan et al.*, 2009]. In addition, the outlier removal procedure is only performed if $ln(max(S_i) - min(S_i)) > 1$, this condition was added by *Tan et al.* (2009) to avoid overfiltering.

Option 5, published as adaptive outlier cleaning (AOC) [*Wang et al.*, 2013], uses Pearson correlation coefficients (PCCs) to determine which CBF image has a correlation to the mean CBF image below a fixed threshold or outside the range of mean ± standard deviation of all PCCs. The removal procedure adopted here is iterative and the mean CBF image is recalculated after each removal and new PCCs for each CBF image are computed and compared to the fixed threshold. The threshold was set to 0.15, the significance level for PCC calculation was set to 10^{-6}, and the procedure was stopped after two iterations as in the original publication [*Wang et al.*, 2013].

Option 6 was introduced as an improvement of the AOC method and is called priors-guided slice-wise adaptive outlier cleaning (pAOCSL) [*Li et al.*, 2018a]. This method employs a pseudo CBF image as reference to alleviate the issue that the mean CBF image used as reference for PCC calculation in AOC already has poor SNR. As CBF contrast is similar to that of a GM density map, a low-noise pseudo CBF image reproducing this contrast is used as reference. The pseudo CBF image is created by thresholding the tissue probability maps of GM and WM obtained in the segmentation step with a threshold of 0.4 and 0.8, respectively, and combining these with a weighting of 1.8 for GM and 1 for WM [*Li et al.*, 2018a]. For each slice, PCCs are then used to determine which CBF image slice has a correlation with the corresponding pseudo CBF image slice below a fixed threshold set to 1. For options 4 and 5, the freely available outlier removal functions from the ASLtbx pipeline [2] were incorporated in the in-house developed analysis pipeline.

Option 7 corresponds to the implementation of the structural correlation-based outlier rejection (SCORE) algorithm published by *Dolui et al.* (2017). In contrary to AOC and pAOCSL, SCORE defines outlier CBF volumes as those most correlated to the mean

[2] `https://cfn.upenn.edu/zewang/ASLtbx.php`, *last accessed 08.08.2022*

CBF. Using an iterative procedure, PCCs between individual CBF volumes of each brain compartment (CSF, GM, WM) and the mean whole brain CBF volume are calculated. The stopping criteria for the removal procedure is based on the pooled variance, which reflects spatial variance in each brain compartment and should decrease after removing an outlier with artefacts. The volume with the highest PCC accross all brain compartments is removed in each iteration and the new pooled variance and mean CBF are then calculated. If the new pooled variance is decreased compared to its previous value, a new iteration takes place. Otherwise, the mean CBF from the previous iteration is taken as final CBF map. As no significance level for the calculation of the PCCs is specified in [*Dolui et al.*, 2017] publication, it was set to 10^{-6} as for the AOC option.

M0 corrections

The realigned M0 image can be corrected for different effects. Five correction types were considered:

- no correction
- T_1 correction
- T_2 or T_2^* correction
- λ correction
- all corrections

The T_1 correction (or long-TR calibration) corrects for signal loss due to choosing a TR which does not allow for full relaxation of all labelled spins. For each brain compartment $BC \in \{\text{CSF, GM, WM}\}$, the voxel-wise correction is applied according to the following equation

$$M_{0,b}^{T_1 corr} = \sum_{BC} \frac{M_{0,T} \cdot \text{BCM}}{1 - e^{-\frac{TR_{M_0}}{T_{1,BC}}}} \tag{3.1}$$

$M_{0,b}$ being the voxel signal intensity of the blood M0 image, BCM being the specific brain compartment binary mask, $M_{0,T}$ being the voxel signal intensity of the acquired tissue M0 image and TR_{M_0} the repetition time used to acquire it, and $T_{1,BC}$ the longitudinal relaxation time of the brain compartment BC ($T_{1,\text{CSF}} = 4300$ ms, $T_{1,\text{GM}} = 1300$ ms, $T_{1,\text{WM}} = 1000$ ms).

The T_2 or T_2^* correction takes into account differences between the transversal relaxation time of arterial blood ($T_{2,b} = 275$ ms, $T_{2,b}^* = 50$ ms) and tissue, thus allowing the derivation of an arterial M0 image from the acquired tissue M0 image. Whether the correction should be T_2 or T_2^* depends on the readout used to acquire ASL data. For each brain compartment $BC \in \{\text{CSF, GM, WM}\}$, the voxel-wise correction is applied according to the following

equations

$$M_{0,b}^{T_2 corr} = \sum_{BC} M_{0,T} \cdot \mathrm{BCM} \cdot e^{-TE \cdot \left(\frac{1}{T_{2,BC}} - \frac{1}{T_{2,b}} \right)}$$
$$M_{0,b}^{T_2^* corr} = \sum_{BC} M_{0,T} \cdot \mathrm{BCM} \cdot e^{-TE \cdot \left(\frac{1}{T^*_{2,BC}} - \frac{1}{T^*_{2,b}} \right)} \tag{3.2}$$

$M_{0,b}$ being the voxel signal intensity of the blood M0 image, BCM being the specific brain compartment binary mask, $M_{0,T}$ being the voxel signal intensity of the acquired tissue M0 image, TE the echo time used to acquire the ASL data, and $T_{2,BC}$ and $T^*_{2,BC}$ the real and apparent transversal relaxation time of the brain compartment BC ($T_{2,\mathrm{CSF}} = 1710$ ms, $T_{2,\mathrm{GM}} = 92.6$ ms, $T_{2,\mathrm{WM}} = 60.8$ ms; $T^*_{2,\mathrm{CSF}} = 400$ ms, $T^*_{2,\mathrm{GM}} = 60$ ms, $T^*_{2,\mathrm{WM}} = 50$ ms), respectively.

The λ correction takes into account the different blood-tissue partition coefficients of CSF ($\lambda_{\mathrm{CSF}} = 1.15$ mL/g), GM ($\lambda_{\mathrm{GM}} = 0.98$ mL/g), and WM ($\lambda_{\mathrm{WM}} = 0.82$ mL/g) instead of using a brain-averaged blood-tissue partition coefficient for the entire brain (usually $\lambda = 0.9$ mL/g [*Herscovitch and Raichle*, 1985]). For each brain compartment $BC \in \{\mathrm{CSF}, \mathrm{GM}, \mathrm{WM}\}$, the voxel-wise correction is applied according to the following equation

$$M_{0,b}^{\lambda\ corr} = \sum_{BC} \frac{M_{0,T} \cdot \mathrm{BCM}}{\lambda_{BC}} \tag{3.3}$$

$M_{0,b}$ being the voxel signal intensity of the blood M0 image, BCM being the specific brain compartment binary mask, and $M_{0,T}$ being the voxel signal intensity of the acquired tissue M0 image.

The fifth correction option consists in applying all the above mentioned corrections together. Values for longitudinal relaxation times T_1 and real transversal relaxation times T_2 of blood, GM, and WM at 3 T were taken from the IT'IS Foundation database[3]. Values for real transversal relaxation times T_2 of CSF at 3 T were taken from [*Spijkerman et al.*, 2018]. Values for the apparent transversal relaxation times of arterial blood and tissues at 3 T and blood-tissue partition coefficients were taken from *Pinto et al.* [2020]. For reduction of spatial noise, the (corrected) M0 is smoothed with a Gaussian kernel (SPM12 Smooth) before using it for the perfusion quantification.

Slice-timing correction

In case of 2D multi-slice acquisitions, the real inflow duration of the labelled spins has to be determined for each slice. The time between two subsequent slice acquisitions t_s

[3] `https://itis.swiss/virtual-population/tissue-properties/database/relaxation-times/`, *last accessed 08.08.2022*

can be determined as follows for a PCASL scheme:

$$TR_{min} = \tau + \text{PLD} + nSli \cdot t_s \tag{3.4}$$

where TR_{min} is the minimal possible repetition time of the sequence, τ is the labelling duration, PLD is the post-labelling-delay, and $nSli$ is the number of acquired slices. Hence t_s can be calculated as:

$$t_s = \frac{TR_{min} - \tau - \text{PLD}}{nSli} \tag{3.5}$$

Finally, the simplified general kinetic model is applied following equations 2.74 and 2.75.

3.2.1.5 Results

After quantification, the binarised (and registered) segmentation masks are applied on the calculated perfusion map in the ASL space. The generated tissue perfusion maps can be visualised for detection of local hypo- or hyperperfusion. In addition, mean perfusion values and standard deviations are calculated for the different brain compartments and can be used for intra- or inter-subject comparisons.

3.2.2 ASL Challenge

As part of an effort to standardise the processing of brain ASL data, the Open Science Initiative for Perfusion Imaging (OSIPI)[4] together with the International Society for Magnetic Resonance in Medicine (ISMRM) launched a challenge in 2021 [*Anazodo and Croal*, 2021; *Anazodo et al.*, 2021]. The data consisted of one population-averaged (Pop-Avg) digital reference object (DRO) and nine synthetic DROs generated using the freely available ASL DRO framework [*Oliver-Taylor et al.*, 2021a]. All necessary data information for the ASL data is listed in Table 3.2. The anatomical data was acquired with a 3D turbo field echo with TE/TR = 3.14/6.76 ms, FA = 9°, voxel size = (1 mm)^3 for the population-averaged DRO and a magnetisation prepared rapid gradient echo (MPRAGE) with TE/TR = 2.14/2400 ms, FA = 8°, voxel size = (0.7 mm)^3 for the synthetic DRO.

[4] `https://osipi.org/index.html`, *last accessed 08.08.2022*

Table 3.2: **Data information for the ASL data of the ASL challenge.**

	Pop-Avg	Synthetic
field strength [T]	3	3
labelling strategy	PCASL	PCASL
delay time [ms]	2025	1800
labelling duration [ms]	1650	1800
readout	2D EPI	3D GRASE
TR control-label [ms]	4800	4800
TR M0 [ms]	10000	10000
TE [ms]	10.4	10.4
FOV [mm^2]	220×220	208×300
number of slices	36	42
inter-slice time [ms]	43.7647	0
matrix size	64×64	52×75
voxel size [mm^3]	$3.5 \times 3.5 \times 4.5$	$4 \times 4 \times 4$
number of background suppression pulses	0	0
number of ASL control-label pairs	30	30

The data from the ASL challenge data was used to evaluate different aspects of the in-house developed analysis pipeline described in section 3.2. The effect of the choice of perfusion-weighted image calculation method, the choice of outlier removal, the choice of M0 correction option, the choice of smoothing kernel full width at half maximum (FWHM) used for the M0 image, and the choice of image used for segmentation was investigated. CBF values were calculated for the scenarios listed in Table 3.3. For scenario XIII, a T_2^* correction was used for the population-averaged data as it used a (GRE-)EPI readout and a T_2 correction was used for the synthetic data as these are based on a GRASE sequence, where the centre of k-space is acquired by spin echoes. Scenario I was considered as reference and results from all other scenarios were compared to it in terms of mean CBF values and SNR. Statistical significant differences in group mean CBF and SNR were assessed with the Wilcoxon signed-rank test [*Wilcoxon*, 1992] because the mean CBF and SNR values across data sets were not normally distributed as evaluated with the Lilliefors test [*Lilliefors*, 1967]. The segmentation masks obtained in scenario I and XIX were compared using the Dice index [*Dice*, 1945].

Table 3.3: **Scenarios for CBF calculation**. $|\cdot|$ *stands for the absolute value.*

	method	outlier removal	M0 correction	FWHM [mm^3]	segmentation
I	SA	none	none	6x6x6	anat
II	|SA|	none	none	6x6x6	anat
III	AS	none	none	6x6x6	anat
IV	|AS|	none	none	6x6x6	anat
V	SA	$\mu \pm 2 \cdot \sigma$	none	6x6x6	anat
VI	AS	$\mu \pm 2 \cdot \sigma$	none	6x6x6	anat
VII	SA	z-scoreVol	none	6x6x6	anat
VIII	SA	z-scoreSli	none	6x6x6	anat
IX	SA	AOC	none	6x6x6	anat
X	SA	pAOCSL	none	6x6x6	anat
XI	SA	SCORE	none	6x6x6	anat
XII	SA	none	T_1	6x6x6	anat
XIII	SA	none	T_2 or T_2^*	6x6x6	anat
XIV	SA	none	λ	6x6x6	anat
XV	SA	none	all	6x6x6	anat
XVI	SA	none	none	1x1x1	anat
XVII	SA	none	none	3x3x3	anat
XVIII	SA	none	none	9x9x9	anat
XIX	SA	none	none	12x12x12	anat
XX	SA	none	none	6x6x6	M0

3.2.3 In vivo studies

3.2.3.1 ASL Imaging sequences

An unbalanced pseudo-continuous ASL (PCASL) sequence with 2D or 3D GRE-EPI readout [*Poser et al.*, 2010] was used for brain ASL imaging. The sequence diagrams for the two sequences are shown in Figure 3.3. The thickness of the labelling plane was set to 3 mm, an average gradient of 8 mT/m and a maximum to average gradient ratio of 7 were used for the labelling pulses. For the 2D readout, the PLD of each slice has to be corrected for the inter-slice time t_s. Using the values recommended in the brain ASL consensus paper (τ = 1800 ms, PLD = $1800ms for healthy subjects and$PLD= 2000 ms for patients [*Alsop et al.*, 2015]) and equation 3.5, this yields t_s = 42.86 ms for measurements acquired with the PCASL 2D GRE-EPI sequence.

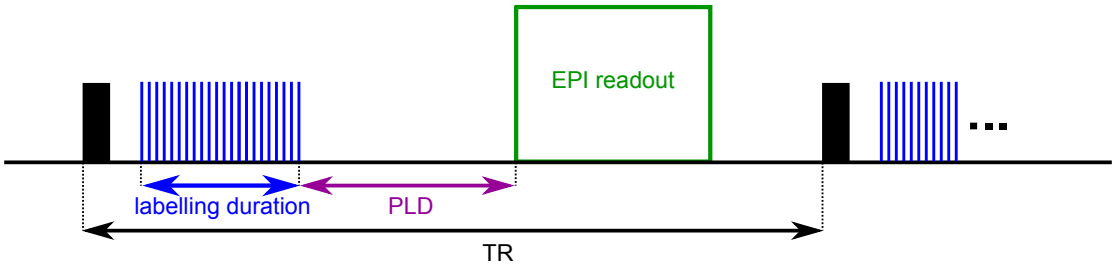

(a) PCASL with 2D GRE-EPI readout

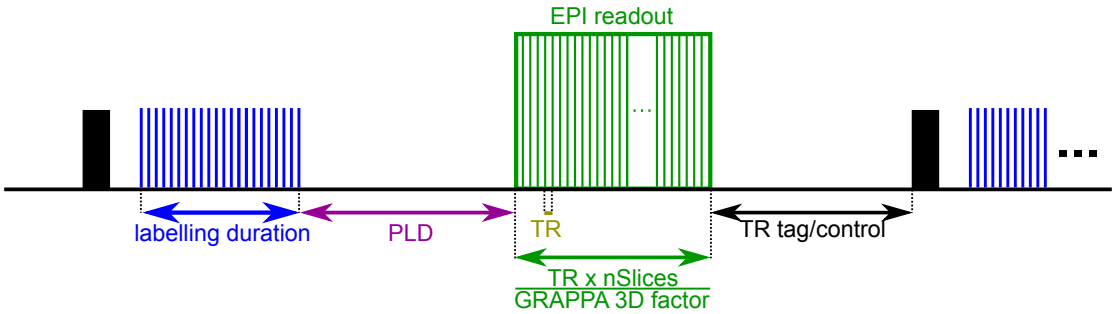

(b) PCASL with 3D GRE-EPI readout

Figure 3.3: **Sequence diagram for the PCASL (a) 2D and (b) 3D EPI sequences used for brain ASL measurements.** In both cases, an initial pre-saturation pulse (in black) is followed by the PCASL labelling pulses (in blue) and, after a post-labelling delay (PLD) time, the GRE-EPI readout (in green) is played out. To ensure complete relaxation of all spins between subsequent acquisitions, the time between end of labelling and following pre-saturation pulse should be at least $3 \cdot T_1$, which is about 4950 ms for human blood ($T_{1,blood} = 1650$ ms [*Zhang et al.*, 2013]).

3.2.3.2 Healthy subjects

Two cohorts of healthy volunteers measured with the Trio system using a 32-channel head coil are considered in this work. All acquisitions were approved by the local ethics committee. For Cohort 1, data from 11 non-smoker healthy volunteers was acquired with the PCASL 2D and 3D GRE-EPI sequences. PLD and delay time τ were set to 1800 ms following current recommendations [*Alsop and Detre*, 1996]. All necessary data information for the ASL data is listed in Table 3.4. The anatomical data was acquired with a MPRAGE (TE/TR = 2.71/1900 ms, FA = 8°, voxel size = $(0.7 \text{ mm})^3$) for subjects 6-11 only. Cohort 2 is composed of data acquired as part of a study to evaluate the effect of smoking on brain oxygenation [*Thomas et al.*, 2020]. As part of this study, data from 10 non-smoker healthy volunteers was acquired with the PCASL 2D GRE-EPI sequence using the same readout parameters as for Cohort 1. PLD and delay time τ were 1500 ms for Cohort 2 and only 49 of control-label pairs were acquired, corresponding to an acquisition time of 510 seconds. No restrictions on food or caffeine intake before the ASL acquisition were applied for either cohort.

Table 3.4: **Data information for the in vivo studies in healthy volunteers.**

readout	2D GRE-EPI	3D GRE-EPI
TR control-label [ms]	5000	5000
TR M0 [ms]	5000	5000
TE [ms]	16	16
bandwidth [Hz/pixel]	2016	2016
FOV [mm^2]	240×240	240×240
number of slices	28	32
inter-slice time [ms]	42.86	0
matrix size	80×80	80×80
voxel size [mm^3]	$3 \times 3 \times 3$	$3 \times 3 \times 3$
phase oversampling	0%	0%
parallel imaging GRAPPA	2	2
partial Fourier	off	7/8
number of background suppression pulses	0	0
number of ASL control-label pairs	50	50
acquisition time [s]	525	1048

For the analyses of the data from Cohort 1 and Cohort 2, the focus was set on the effect of outlier removal options and M0 corrections. For this, analyses were run for scenarios I and V-XV listed in Table 3.3. For scenario XIII, a T_2^* correction was used as the data was acquired with a GRE-EPI sequence. In addition, data from Cohort 1 was used to evaluate the effect of number of control-label pairs on CBF quantification by down-sampling the full ASL dataset with 50 pairs to data sets with 5 to 45 pairs in steps of 5, thus allowing a comparison of 10 CBF maps for each subject. Data from Cohort 1 was also used for a comparison between 2D and 3D readout. Scenario I was considered as reference and results from all other scenarios were compared to it in terms of mean CBF values and SNR. Differences in group mean CBF and SNR distributions were tested for significance using paired t-test or Wilcoxon signed-rank test depending on the results of the Lilliefors test for normality.

3.2.3.3 Patients

As part of a study on oxygen extraction fraction quantified using MRI, ASL data from 17 patients was acquired with the Trio system [*Baazaoui et al.*, 2021]. The PCASL 3D GRE-EPI sequence with a 32-channel head coil was used for the first two patients. For all

other patients, the 12-channel head coil, which is routinely used for clinical acquisitions, was used to reduce disturbance to the clinical workflow. The PCASL 2D GRE-EPI sequence was used for all acquisitions with the 12-channel coil as the SNR achieved with the 3D sequence was shown to be very low in a test measurement of a healthy volunteer. For all measurements, 45 control-label pairs with a PLD of 2000 ms and a bolus duration of 1800 ms were acquired. A longer PLD was chosen for the patient measurements than for the healthy volunteer measurements to account for prolonged arterial transit times which are common in patients [*Alsop et al.*, 2015].

For each patient, the ASL data was analysed using the in-house developed processing pipeline described in section 3.2 using scenario I (Table 3.3) to assess whether pathology indications could also be recognised in the quantified perfusion maps.

3.3 Kidney

3.3.1 Analysis Pipeline

The analysis pipeline for kidney ASL data was developed as a MATLAB® script (Version 2020a, MathWorks, Natick, Massachusets). It consists of registration, quantification, and segmentation steps as summarised in Figure 3.4. The individual steps are detailed in the next sections.

3.3.1.1 Registration

The first pre-processing step is the registration of all images, which is performed using the open-source elastix toolbox[5] [*Klein et al.*, 2009a; *Shamonin et al.*, 2014]. All acquired images are registered to a mean group image (groupwise registration). Different areas of the image are considered for the registration. The five options are:

- W - whole image, both kidneys together
- H - half of the image with same image size as original (i.e. half of the image is filled with zeros), left and right kidney separately
- H-c - half of the image cropped to half the size of the original image, left and right kidney separately
- R - manually drawn rectangles to crop area around kidney with same image size as original image (i.e. everything except the drawn rectangle is filled with zeros), left and right kidney separately

[5] `https://elastix.lumc.nl/`, *last accessed 08.08.2022*

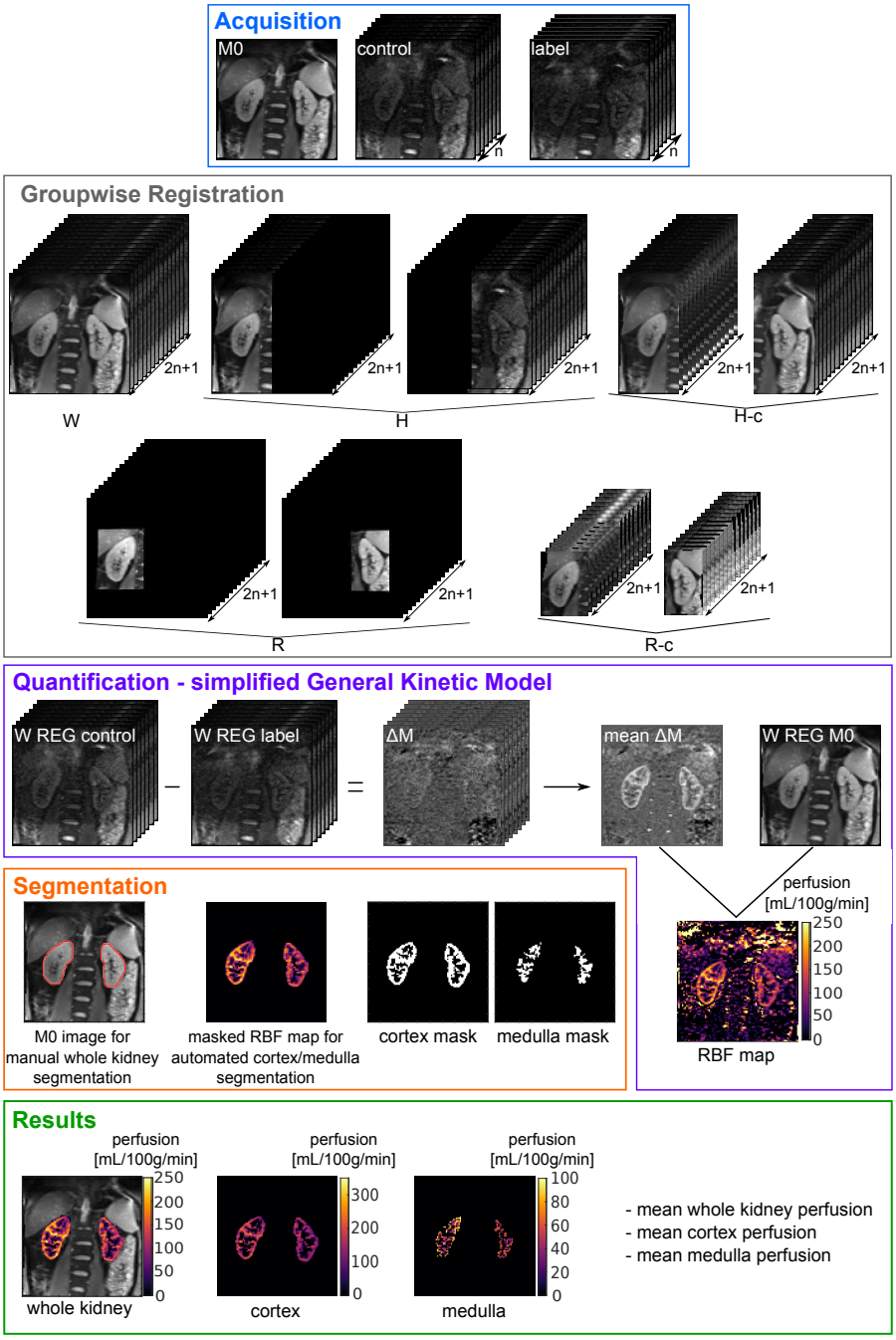

Figure 3.4: **Analysis pipeline for kidney ASL data.** After acquisition of ASL images (one M0 and multiple control-label pairs), the data is registered using a groupwise strategy. Five different areas of the image (W, H, H-c, R, R-c) can be considered for registration. The registered control and labelled images are subtracted and averaged to obtain a mean perfusion-weighted image ΔM. RBF is quantified with the simplified general kinetic model. For the segmentation, the kidney contour is first manually drawn for each kidney. The obtained whole kidney masks are applied on the RBF map and a k-means clustering algorithm is employed for cortex/medulla segmentation. The final results are RBF maps of the whole kidneys, cortex, and medulla, as well as mean RBF values for each. *Abbreviations used: n - number of control-label pairs acquired; REG - registered; RBF - renal blood flow.*

- R-c - images cropped to manually drawn rectangles around kidney of interest, left and right kidney separately

All registrations are performed on a slice-by-slice basis and use a multi-resolution strategy with a non-rigid transformation, a 3^d-order B-spline interpolator, an adaptive stochastic gradient descent optimiser [*Klein et al.*, 2009b], and principal-component-analysis-based metric (PCAMetric2) [*Huizinga et al.*, 2016].

To evaluate the quality of registration, visual checks (scrolling through all images and looking at line profiles) as well as metrics are used. Relevant metrics are the mean structural similarity index measure (MSSIM) and a normalised version of the mutual information metric (MI) known as entropy correlation coefficient (ECC). These metrics are described in section 3.4.

3.3.1.2 Perfusion quantification

Once all images are registered, the ASL data is used to calculate a quantitative perfusion map using the single-compartment quantification formulas (equation 2.74). Following the consensus [*Nery et al.*, 2020], a T_1 of blood of 1650 ms at 3 T, a blood-tissue partition coefficient 0.9 mL/g, and a labelling efficiency of 0.95 and 0.85 for PASL and PCASL, respectively, with correction factor of $0.93^{n_{BS}}$ to account for n_{BS} background suppression pulses between labelling and readout, are assumed.

$$\mathrm{RBF} = \frac{6000 \cdot 0.9 \cdot \Delta M \cdot e^{1600/1650}}{2 \cdot (0.85 \cdot 0.93^{nBS}) \cdot M_0 \cdot 1.65 \cdot (1 - e^{1200/1650})} \tag{3.6}$$

No slice-dependent time correction for the inflow duration of the labelled spins is included here as single-slice acquisitions are recommended for renal ASL [*Nery et al.*, 2020].

3.3.1.3 Segmentation

Whole kidney segmentation is first performed manually on the M0 image. A k-means clustering algorithm is then used to automatically segment cortex and medulla. The clustering is applied on the quantified perfusion map masked by the manually drawn whole kidney masks for left and right kidney separately. To further improve the accuracy of the medulla segmentation mask, an additional erosion step is performed. For this, the manually drawn whole kidney masks are eroded using [0 0 0 1 1; 0 0 1 0 0; 0 1 1 0 0; 1 1 0 0 0] and [1 1 0 0 0; 0 0 1 0 0; 0 0 1 1 0; 0 0 0 1 1] as structuring elements for left and right kidney, respectively. The medulla mask produced by the clustering algorithm is then multiplied with the eroded whole kidney mask to remove any voxels on the outer edge of the kidney.

3.3.1.4 Results

The final output of the analysis pipeline are the perfusion map and mean perfusion values for the whole kidney, cortex, and medulla for left and right kidney, separately.

3.3.2 Synthetic data

3.3.2.1 Synthetic data generation

Synthetic MRI data was generated based on the anatomical structures provided by the XCAT phantom [*Segars et al.*, 2010], which offers multiple body models. These models differ in overall size, organ shapes and dimensions, and fat content. XCAT voxel values were first converted into MRI magnitude values using the spin echo sequence equation (equation 2.61). Coronal-oblique slice position (rotation angle of 12°), voxel dimension of 3x3x5 mm^3, repetition time TR = 5000 ms, and echo time TE = 23 ms were chosen to match recommendations for in vivo acquisitions [*Nery et al.*, 2020]. Relative proton density ρ, T_1 and T_2 relaxation times at field strengths of 3 T were taken from the literature [*Wissmann et al.*, 2014; *De Bazelaire et al.*, 2004; *Stanisz et al.*, 2005] and are listed in Table B.1. For the relative proton density, air is used as reference so any tissue or organ filled with air (e.g. lung, intestine) will have a relative proton density ρ equal to one. Noise was modeled as an additive white Gaussian noise to produce signal-to-noise ratio similar to in vivo acquisitions. Respiratory motion during free breathing acquisition was simulated by generating 100 synthetic MR images at equally spaced time points around the exhalation part of the respiratory cycle.

The generated proton-density weighted MR images with respiratory motion were used as basis for the M0 and multiple control-labelled image pairs. ASL data sets with fixed number $nMeas$ of images (one M0 and multiple control-label pairs) were then generated by randomly selecting $nMeas$ images from the available 100 time points. BS used for control and labelled images was modelled by reducing the signal intensity of all control and labelled images to 20% of the signal of the M0 image. Assuming the apparent longitudinal relaxation time of tissue equals the longitudinal relaxation time of arterial blood, the general kinetic model [*Buxton et al.*, 1998] was used to create both pseudo-continuous ASL (PCASL) and pulsed ASL (PASL) data sets using the following equations:

PCASL:

$$\Delta M(\mathrm{PLD}) = \begin{cases} 0 & 0 < \mathrm{PLD} < \Delta t \\ 2 \cdot \alpha' \cdot M_{0,T} \cdot \frac{f'}{6000 \cdot \lambda} \cdot T_{1,b} \cdot \left(e^{-\frac{\Delta t}{T_{1,b}}} - e^{-\frac{(\mathrm{PLD}+\tau)}{T_{1,b}}} \right) & \Delta t \leq \mathrm{PLD} < \Delta t + \tau \\ 2 \cdot \alpha' \cdot M_{0,T} \cdot \frac{f'}{6000 \cdot \lambda} \cdot T_{1,b} \cdot \left(e^{-\frac{\mathrm{PLD}}{T_{1,b}}} - e^{-\frac{(\mathrm{PLD}+\tau)}{T_{1,b}}} \right) & \Delta t + \tau \leq \mathrm{PLD} \end{cases} \tag{3.7}$$

PASL:

$$\Delta M(TI) = \begin{cases} 0 & 0 < TI < \Delta t \\ 2 \cdot \alpha' \cdot M_{0,T} \cdot \frac{f'}{6000 \cdot \lambda} \cdot (TI - \Delta t) \cdot e^{-\frac{TI}{T_{1,b}}} & \Delta t \leq TI < \Delta t + TI_1 \\ 2 \cdot \alpha' \cdot M_{0,T} \cdot \frac{f'}{6000 \cdot \lambda} \cdot TI_1 \cdot e^{-\frac{TI}{T_{1,b}}} & \Delta t + TI_1 \leq TI \end{cases} \tag{3.8}$$

α' accounts for the labelling efficiency of PCASL or PASL given by literature as well as the applied BS pulses. To match sequences used for in vivo imaging, two BS pulses were assumed, resulting in $\alpha' = 0.85 \cdot 0.93^2$ and $\alpha' = 0.95 \cdot 0.93^2$ for PCASL and PASL, respectively.

3.3.2.2 Synthetic ASL data sets

Synthetic ASL data without respiratory motion was first considered. For this, a single XCAT model (model 77) was used. 3 T PCASL and PASL data sets with 25 control-labelled image pairs, PLD = 1200 ms and τ = 1600 ms for PCASL and TI = 1800 ms and TI_1 = 1200 ms for PASL were generated. To reproduce healthy kidneys, a perfusion ratio of 5 was assumed between cortex and medulla [*Roberts et al.*, 1995], with cortical perfusion f'_c set to 250 mL/100g/min and medullary perfusion f'_m set to 50 mL/100g/min. Arterial transit times Δt of 1123 ms and 1141 ms were assumed for medulla and cortex, respectively [*Kim et al.*, 2017].

In a second step, healthy ASL data sets with respiratory motion composed of 25 control-labelled image pairs, resulting in 51 images randomly selected from the 100 available time points of the respiratory cycle, were generated. PCASL data was generated with PLD = 1200 ms and τ = 1600 ms and PASL data was generated with TI = 1800 ms and TI_1 = 1200 ms to match recommendations for in vivo acquisitions. Data sets for 3 T were generated for 5 different XCAT body models (models 77, 80, 92, 93, 108).

Additionally to data sets presenting healthy kidney perfusion, a synthetic data set with respiratory motion and showing decreased perfusion in the right kidney with cortical perfusion f'_c set to 100 mL/100g/min and medullary perfusion f'_m set to 20 mL/100g/min was generated (model 92). This additional data set was used to check that the abnormal

perfusion present in the data set was not affected by the processing pipeline and would still be distinguishable from the healthy data sets.

The synthetic ASL data sets with respiratory motion are publicly available at `https://doi.org/10.11588/data/QAHWSF` (*last accessed 26.08.2022*).

3.3.2.3 Synthetic data evaluation

The perfusion signal evolution of the generated synthetic ASL data from one XCAT model (model 77) was analysed by generating data sets of three images (i.e., single control-labelled image pair) without respiratory motion for various time delays. ASL data was generated for delay times (PLD or TI) ranging from 0 to 4000 ms in steps of 200 and with $\tau = 1600$ ms or $TI_1 = 1200$ ms for PCASL and PASL data, respectively. The mean perfusion-weighted signal in cortex and medulla was plotted against the delay time.

3.3.2.4 Analysis pipeline evaluation

All data sets were analysed with the analysis pipeline described in section 3.3.1. The pipeline was evaluated in terms of registration, quantification, and segmentation.

Registration

The GR registration with six resolution levels (10, 8, 2, 4, 2, 1) was used. The registration parameter file can be found in Appendix B.2.1. To assess the effect of the registration step in the absence of respiratory motion, the data set without respiratory motion was analysed both with and without the registration step of the analysis pipeline. The capacity of the registration to correct respiratory motion was assessed qualitatively using line profiles across the time dimension of the ASL data sets as well as quantitatively with mean structural similarity index measures (MSSIMs) [*Wang et al.*, 2004] calculated for all possible image pairs of a data set.

Quantification

The quantification step was evaluated by comparing the mean cortical and medullary perfusion obtained from the analysis to the values assumed to generate the data sets.

Segmentation

The segmentation results obtained from the processing pipeline were compared to the segmentation masks provided by the XCAT phantom. For this, the organ masks from the XCAT phantom were first transformed with the registration matrix used to correct for the respiratory motion and then rebinarised. Whole kidney, cortex, and medulla binary masks were finally compared using the Dice index [*Dice*, 1945].

3.3.3 In vivo study

3.3.3.1 Imaging sequence

A PCASL sequence with 2D SE-EPI readout was used for perfusion quantification in the kidneys [*Echeverria-Chasco et al.*, 2021; *Nery et al.*, 2020]. The parameters for the SE-EPI readout are given in Table 3.5. The TE was set to the lowest possible value to reduce scan duration. An oblique-coronal image orientation was adopted for all ASL imaging sequences. Three background suppression (BS) pulses (FOCI pulses with timings BS1 = 3008.7 ms, BS2= 1228.9 ms, BS3 = 289.8 ms prior to readout [*Echeverria-Chasco et al.*, 2021]) were applied to null the background tissue signal to 10% [*Taso et al.*, 2019], with the first BS pulse played out before the labelling and the two other BS pulses played out between labelling and read-out. Each ASL measurement consisted of 25 control-label pairs and an M0 image (without pre-saturation and inversion pulses) acquired at the beginning of the measurement.

Table 3.5: **Acquisition parameters of the SE-EPI readout used for the kidney study.**

readout	2D SE-EPI
TR control-label [ms]	5000
TR M0 [ms]	5000
TE [ms]	23
bandwidth [Hz/pixel]	1890
FOV [mm^2]	288×288
number of slices	1
matrix size	96×96
voxel size [mm^3]	$3 \times 3 \times 5$
phase oversampling	25%
parallel imaging GRAPPA	2
partial Fourier	6/8
fat suppression	Yes (before excitation pulses)
number of background suppression pulses	3 (2 after labelling pulses)
number of control-label pairs	25
acquisition time [s]	270

The PCASL sequence adopts an unbalanced configuration with Hann-shaped pulses (duration $\delta = 500$ μs and period $T = 1$ ms), an average gradient of 0.4 mT/m, a maximum to average gradient ratio of 7, and an average RF pulse amplitude B_1 of 1.6 μT (flip angle

24.6°) [*Echeverria-Chasco et al.*, 2021]. The PLD was set to 1200 ms and the labelling duration to 1600 ms. The sequence diagram for the PCASL 2D SE-EPI sequence is shown in Figure 3.5. For all acquisitions, the inversion plane with a thickness of 10 mm was placed 8 cm above the centre of the highest kidney and kept perpendicular to the aorta to ensure a high labelling efficiency. Details of the sequence planning are shown in Figure 3.6.

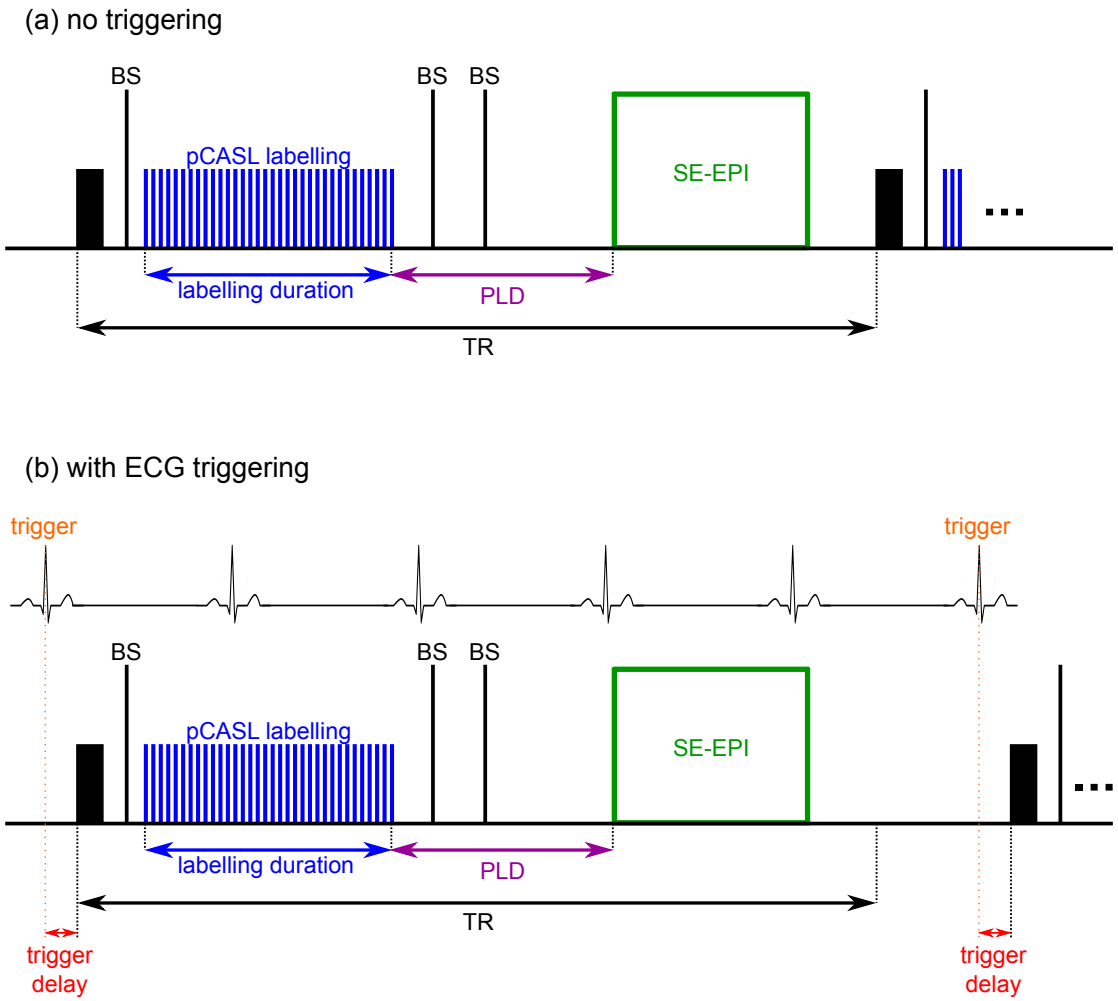

Figure 3.5: **Sequence diagram for the PCASL SE-EPI sequence used for kidney imaging:** (a) without triggering and (b) with ECG triggering.

In addition to sequences for ASL perfusion imaging, standard sequences for anatomical imaging were used. A volumetric interpolated breath-hold examination (VIBE) sequence with axial slice orientation was used to obtain T_1-weighted images and a Half Fourier Single-shot Turbo spin-Echo (HASTE) sequence with coronal slice orientation was used to obtain T_2-weighted images. Furthermore, a Modified-Look-Locker-Inversion (MOLLI) recovery sequence [*Messroghli et al.*, 2004] with the same oblique-coronal slice orientation as the ASL sequences and 8 contrasts with different inversion times TI (174, 254, 1174, 1254, 2174, 2254, 3174, 4174 ms) was used for T_1-mapping.

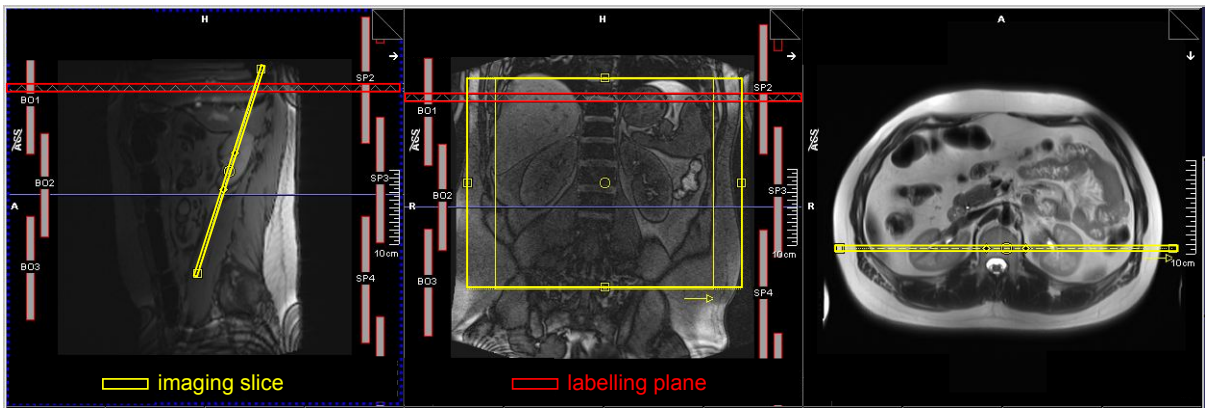

Figure 3.6: **Planning for coronal-oblique PCASL kidney image acquisition.** The imaging slice, shown in yellow, is placed along the long kidney axis, and the labelling plane, shown in red, is placed 8 cm above the centre of the highest kidney.

3.3.3.2 Measurement series

A total of eleven healthy volunteers were scanned with the Skyra system using a 18-channel body coil. Four subjects were excluded after imaging as the ASL measurements presented very low perfusion signal. The remaining subjects included 2 women and 5 men, aged 27 ± 3 years.

Each volunteer underwent a series of subsequent single-slice MR acquisitions amounting to a total of 25 minutes and according to the following protocol:

1. Localiser
2. Anatomical images
    - T2-weighted - HASTE sequence - transversal
    - T1-weighted - VIBE sequence - coronal
3. Perfusion - PCASL 2D SE-EPI sequence - coronal oblique
    - test for arm positioning
    - no ECG triggering, free breathing
    - with ECG triggering, free breathing
    - test for synchronised breathing
    - no ECG triggering, synchronised breathing
    - with ECG triggering, synchronised breathing
4. T1 mapping - MOLLI sequence - coronal oblique

The test measurements for arm positioning and synchronised breathing refer to short ASL measurements performed to assess the effect of aliasing artefacts caused by arms positioned along the body and to allow the subject to adjust themselves to the synchronised breathing pattern.

ECG triggering is set on the peak of the R-wave of the heart cycle as shown schematically in the sequence diagram in Figure 3.5. The trigger delay, i.e., the time between the set off of the trigger and the start of the sequence, was set to 0 ms for this study. Additional measurements to evaluate the effect of the trigger delay duration were performed on two subjects (Subject 1 and 6).

Synchronised breathing (SB) refers to a respiratory scheme where the readout occurs in expiration state. Consequently, the subject always inhales after the SE-EPI readout, which is acoustically well recognisable for the subject being scanned. To ensure a good understanding and synchronisation for this respiration strategy, all scanned volunteers had the opportunity to familiarise with the readout sound and try out the synchronisation before the measurements and during the dedicated test measurement. The synchronised respiration strategy is shown schematically in Figure 3.7.

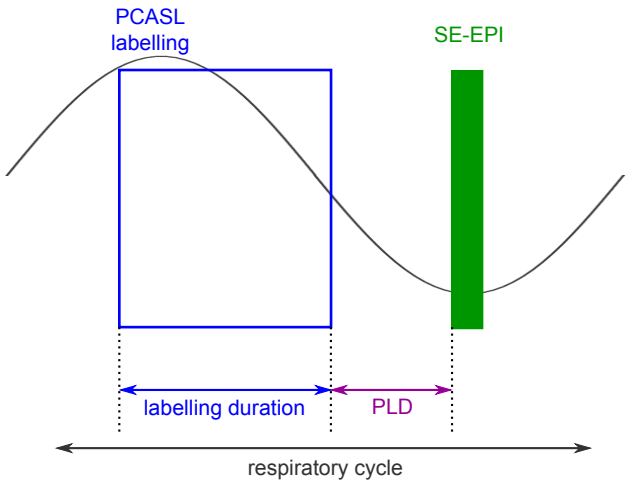

Figure 3.7: **Ideal respiratory scheme for the synchronised respiration strategy.** The data acquisition should always occur during the expiration phase of the respiratory cycle.

3.3.3.3 Data Analysis

The in vivo acquired data was analysed using the processing pipeline described in section 3.3.1. Groupwise registration of all ASL images was performed with all available image area options and using four resolution levels (2, 2, 1, 1). The registration parameter file can be found in Appendix B.2.2. The labelling efficiency was set to $0.85 \cdot 0.93^2$ to account for the two BS pulses played out after the labelling pulses.

The different registration options were compared qualitatively with visual checks and quantitatively in terms of MSSIM, ECC, and duration. Differences in MSSIM and ECC distributions before and after registration were tested for statistical significance using the t-test [*Student*, 1908] or Wilcoxon signed-rank test [*Wilcoxon*, 1992] depending on the results of the Lilliefors test for normality [*Lilliefors*, 1967]. Considering the best registration option, the influence of the cardiac cycle and respiration strategy on the ASL measurement was then evaluated in terms of mean RBF distributions obtained for the different measurements. Differences in mean RBF distributions were tested for statistical significance using the t-test [*Student*, 1908] or Wilcoxon signed-rank test [*Wilcoxon*, 1992] depending on the results of the Lilliefors test for normality [*Lilliefors*, 1967].

3.4 Metrics and statistical tests

Metrics used for image quality assessment, metrics for segmentation or registration comparisons and statistical tests employed in this work are briefly introduced in this section.

3.4.1 Signal-to-Noise Ratio

The quality of an image can be assessed by the signal-to-noise ratio (SNR) calculated according to equation 2.57. In this work, the SNR of CBF maps was calculated as the mean CBF signal across the whole brain divided by the standard deviation across every voxel outside of the whole brain. The whole brain mask was composed of the automated tissue segmentation masks obtained for CSF, GM, and WM.

Another useful metric used to assess signal variations over time is the temporal signal-to-noise ration (tSNR). It is defined as the mean signal intensity of the time series divided by its standard deviation. In this work, the tSNR of perfusion-weighted, control, or label time series was calculated over the whole organ (brain or both kidneys together).

3.4.2 Dice Index

The Dice Index DI was first introduced as a coincidence index to quantify the natural cooperation of two species [*Dice*, 1945]. Since then it has become a well-known metric in the field of (medical) imaging where it is commonly used to compare binary segmentation masks. The Dice Index compares the extent of overlap of two volumes A and B to the sum of their total extent

$$DI = \frac{2 \cdot (A \cap B)}{A + B} \tag{3.9}$$

As shown by the equation, DI ranges from 0 to 1, with 0 corresponding to no overlap and 1 corresponding to complete overlap between the two considered volumes.

3.4.3 Structural Similarity Index Measure

To evaluate registration results, similarity metrics comparing image features are necessary. The Structural Similarity Index Measure (SSIM) allows a pixel-by-pixel comparison of two images considering luminance, contrast, and structure content [*Wang et al.*, 2004]. It ranges from 0 to 1, with 1 corresponding to the comparison of two equivalent images. It is recommended to calculate the SSIM locally rather than globally over entire images. For this, the approach presented by *Wang et al.* (2004) was followed and is the basis for the mathematical description below. This approach uses a 11 x 11 circular-symmetric Gaussian weighting function with 1.5 standard deviation.

The luminance of an image composed of discrete signals is estimated as the mean signal intensity. The luminance comparison function for two signals $\mathbf{x}$ and $\mathbf{y}$ is then defined as

$$l(\mathbf{x}, \mathbf{y}) = \frac{2 \cdot \mu_x \cdot \mu_y + C_1}{\mu_x^2 + \mu_y^2 + C_1} \tag{3.10}$$

with the mean signal intensities

$$\mu_x = \sum_{i=1}^{N} x_i \cdot w_i \quad \text{and} \quad \mu_y = \sum_{i=1}^{N} y_i \cdot w_i$$

N is the total number of pixels per image and w_i are the individual Gaussian weighting factors. The constant C_1 ensures stability of the luminance function when the sum of squared signal intensities tends to zero. It is chosen to be $C_1 = (K_1 \cdot L)^2$, where L is the dynamic range of the images and $K_1 << 1$.

The contrast of an image is estimated by the standard deviation of the signal intensity. The contrast function comparing two signals $\mathbf{x}$ and $\mathbf{y}$ is thus defined as

$$c(\mathbf{x}, \mathbf{y}) = \frac{2 \cdot \sigma_x \cdot \sigma_y + C_2}{\sigma_x^2 + \sigma_y^2 + C_2} \tag{3.11}$$

with the standard deviation of signal intensities

$$\sigma_x = \sqrt{\sum_{i=1}^{N} w_i \cdot (x_i - \mu_x)^2} \quad \text{and} \quad \sigma_y = \sqrt{\sum_{i=1}^{N} w_i \cdot (y_i - \mu_y)^2}$$

The constant C_2 ensures stability of the contrast function when the sum of squared signal contrasts tends to zero. Similarly to C_1, it is chosen to be $C_2 = (K_2 \cdot L)^2$ with $K_2 << 1$.

The structure of an image is estimated by the normalised signal intensity. The structure

function comparing image signals $\mathbf{x}$ and $\mathbf{y}$ is then defined as

$$s(\mathbf{x}, \mathbf{y}) = \frac{\sigma_{xy} + C_3}{\sigma_x \cdot \sigma_y + C_3} \tag{3.12}$$

with

$$\sigma_{xy} = \sqrt{\sum_{i=1}^{N} w_i \cdot (x_i - \mu_x)(y_i - \mu_y)}$$

The constant C_3 ensures stability of the contrast function, similarly to C_1 and C_2.

The SSIM is mathematically defined as a function of the above defined components

$$\mathrm{SSIM}(\mathbf{x}, \mathbf{y}) = f\big(l(\mathbf{x}, \mathbf{y}), c(\mathbf{x}, \mathbf{y}), s(\mathbf{x}, \mathbf{y})\big) = l(\mathbf{x}, \mathbf{y})^{\alpha} \cdot c(\mathbf{x}, \mathbf{y})^{\beta} \cdot s(\mathbf{x}, \mathbf{y})^{\gamma} \tag{3.13}$$

where α, β, γ control the importance of each component. Specifically, the parameters were set as $\alpha = \beta = \gamma = 1$, $K_1 = 0.01$, $K_2 = 0.03$, and $C_3 = C_2/2$ following [*Wang et al.*, 2004]. To facilitate comparison between two images, a single value can be defined to quantify the overall similarity between two images. For this purpose, the mean SSIM (MSSIM) is considered:

$$\mathrm{MSSIM}(\mathbf{X}, \mathbf{Y}) = \frac{1}{M} \sum_{j=1}^{M} \mathrm{SSIM}(\mathbf{x}_j, \mathbf{y}_j) \tag{3.14}$$

where $\mathbf{X}$ and $\mathbf{Y}$ are the original and registered images, respectively. $\mathbf{x}_j$ and $\mathbf{y}_j$ are the local image content at the j^{th} window. In this work, MSSIMs were calculated using the pre-implemented MATLAB® function [*Wang et al.*, 2004] and were used to evaluate registration results.

3.4.4 Mutual Information

Another useful similarity metric is the mutual information (MI) which stems from information theory [*Maes et al.*, 1997; *Pluim et al.*, 2003]. It can be understood as the quantity of information an image contains about another image. In the context of image registration, a maximised MI, i.e., when the information about an image contained in another image is maximal, corresponds to the best possible registration between two images. Mathematically, the MI of images X and Y is defined as

$$MI = H_X + H_Y - H_{X,Y} \tag{3.15}$$

H_X and H_Y are the marginal entropies of images X and Y, respectively, and $H_{X,Y}$ is the joint entropy of images X and Y. Using Shanon's entropy formulation [*Shannon*,

1948a,b], the marginal entropy of an image I with discrete values is defined as

$$H_I = -K \sum_a p_I(a) \cdot log(p_I(a)) \tag{3.16}$$

where K is a positive constant and $p_I(a)$ is the probability of signal intensity a in image I. In the same formalism, the joint entropy of two images X and Y is defined as

$$H_{X,Y} = -K \sum_{a,b} p_{X,Y}(a,b) \cdot log(p_{X,Y}(a,b)) \tag{3.17}$$

where $p_{X,Y}(a,b)$ is the probability of the signal intensity pair (a,b) in the image pair (X,Y). The marginal and joint entropies are estimated using using histogram distributions of signal intensities. As demonstrated by *Hacine-Gharbi et al.* (2012), the optimal total number of bins k is given by

$$k = round\left(\frac{\zeta}{6} + \frac{2}{3 \cdot \zeta} + \frac{1}{3}\right) \tag{3.18}$$

with $\zeta = \sqrt[3]{8 + 324 \cdot N + 12 + \sqrt{36 \cdot N + 729 \cdot N^2}}$, N the total number of pixels in the image, and $round(\cdot)$ indicating rounding to the closest integer.

On one hand, the marginal entropy of an image can be understood as the average information contained in the image. On the other hand, the joint entropy of two images can be understood as the total information contained in the two images. The MI thus corresponds to the overlap of information contained in both images [*Maes et al.*, 1997]. As the marginal entropies of two images are fixed, maximising the MI is achieved by minimising the joint entropy and therefore corresponds to minimising the information contained in the information overlap of the two images. As such, the information overlap can be minimised without considering how well the information of the two images actually correspond. To alleviate this drawback of the MI, two normalised metrics were introduced: 1) the entropy correlation coefficient (ECC) [*Maes et al.*, 1997] and 2) the the normalised mutual information (NMI) [*Studholme et al.*, 1999]. These normalised metrics are defined as follows:

$$\text{ECC} = \frac{2 \cdot MI}{H_x + H_y} \tag{3.19}$$

$$\text{NMI} = \frac{H_x + H_y}{H_{x,y}} \tag{3.20}$$

ECC and NMI are related by

$$\text{NMI} = \frac{2}{2 - \text{ECC}} \tag{3.21}$$

The ECC ranges from 0 to 1, with 1 indicating a perfect agreement between the two images compared. The NMI ranges from 1 to 2, with 2 corresponding to the comparison

of two identical images. In this work, the quality of registration is assessed using the ECC as its range corresponds to the range of MSSIM, the other metric considered for assessment of registration quality.

3.4.5 Lilliefors test

The Lilliefors test is used to assess the normality of a distribution by comparing the actual distribution of data points to a normal distribution [*Lilliefors*, 1967]. In contrary to the Kolmogorov-Smirnov test [*Kolmogorov*, 1933; *Smirnov*, 1939] on which it is based, it does not assume that the normal distribution used for comparison is the standard normal distribution, i.e., with mean equal to zero and standard deviation equal to one. As such, the Lilliefors test is convenient for testing normality of distributions, which are expected to differ from the standard normal distribution. The calculation procedure is similar to the one used for the Kolmogorov-Smirnov test, except for the initial calculation of the mean and standard deviation of the distribution at hand instead of assuming the properties of the standard normal distribution. All Lilliefors tests were performed using the pre-implemented MATLAB® function. The output of the Lilliefors test is a hypothesis value h, which is 0 if the tested distribution is normal and 1 otherwise, and a probability value p, which gives the significance level of the hypothesis rejection. A value of $p < 0.05$ was considered statistically significant.

3.4.6 Paired t-test

t-tests allow the comparison of the mean of two distributions [*Student*, 1908]. While one sample t-tests use a reference distribution with mean equal to zero to which the available sample is compared, two sample t-tests directly compare the mean of two samples. The two samples can be either independent, in which case an unpaired t-test is used, or they can be dependent and require a paired t-test. In this work, t-tests are used to compare values obtained for the same data sets using different analysis options or obtained from different measurements of the same subjects. Thus the paired t-test is relevant here. For a small sample size, as is the case in this work, the results of a t-test are only meaningful if the distributions being compared follow normal distributions. All t-tests were performed using the pre-implemented MATLAB® function. The output of the paired t-test is a hypothesis value h, which is 0 if the difference of the tested distributions come from a normal distribution with 0 mean and 1 otherwise, and a probability value p, which gives the significance level of the hypothesis rejection. A value of $p < 0.05$ was considered statistically significant.

3.4.7 Wilcoxon signed-rank test

The Wilcoxon signed-rank test is used to compare the median of two distributions [*Wilcoxon*, 1992]. Unlike the t-test, it is a non-parametric test and thus does not require normal distribution of the samples even for small sample sizes. The Wilcoxon signed-rank test is applicable for dependent samples that can be ranked, which corresponds to the type of data compared in this work. All Wilcoxon signed-rank tests were performed using the pre-implemented MATLAB® function. The output of the Wilcoxon signed-rank test is a hypothesis value h, which is 0 if the difference of the tested distributions come from a normal distribution with 0 median and 1 otherwise, and a probability value p, which gives the significance level of the hypothesis rejection. A value of $p < 0.05$ was considered statistically significant.

CHAPTER 4

Results

In this chapter, the results of the three projects are presented. First the results from the brain project are shown followed by the results from the kidney projects, starting with the synthetic data and finishing with the in vivo study. Parts of this chapter have been published in [*Brumer et al.*, 2022a][1] and the description of the corresponding results is partly replicated here.

4.1 Brain

4.1.1 Output of processing pipeline

The final output of the processing pipeline developed for analysis of brain ASL data are quantified perfusion maps for the whole brain, gray matter (GM), white matter (WM), GM+WM as well as mean and standard deviation of the CBF distribution of these compartments. All slices of the perfusion maps calculated for GM and WM for the population-averaged (Pop-Avg) data set of the ASL challenge are shown in Figure 4.1.

Another useful output of the processing pipeline is the evolution of the perfusion-weighted (or control and label) signal averaged over the whole brain and all slices for the different control-label pairs and the corresponding temporal SNR (tSNR). The evolution of the perfusion-weighted signal obtained for the 2D acquisition of Subject 1 from Cohort 1 is shown in Figure 4.2.

[1] CC BY License

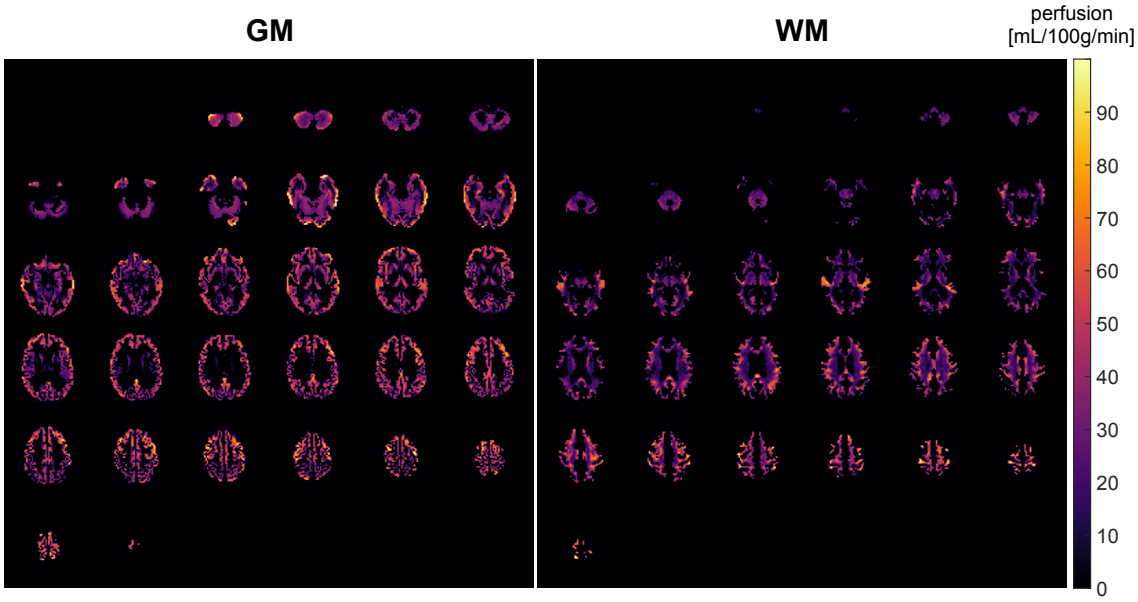

Figure 4.1: **Perfusion maps of GM and WM** of the population-averaged data set of the ASL challenge calculated with scenario I.

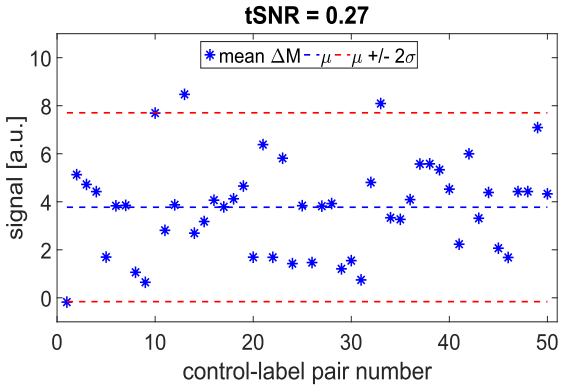

Figure 4.2: **Evolution of the perfusion-weighted ΔM signal** obtained for the 2D acquisition of Subject 1 from Cohort 1 calculated with scenario I. Each data point is the mean signal difference between a pair of subsequent control and labelled image. When using scenario V to analyse the data, control-label pairs number 1, 13, and 33 would be removed before perfusion quantification as they are outside of the range of mean $\mu \pm$ twice the standard deviation σ.

4.1.2 General remarks

Mean CBF and SNR values for all scenarios averaged over the different subject groups (ASL challenge data, 2D Cohort 1, 3D Cohort 1, Cohort 2) are listed in the Appendix A in Tables A.1, A.2, A.3, A.4, and A.5. Between subject variations are smaller for the ASL challenge data than for the in vivo acquired data (Cohort 1 and Cohort 2). For the reference scenario (scnario I), the standard deviation of mean CBF distributions range 5-6 and 4-10 for the ASL challenge data and the in vivo acquired data, respectively.

In each scenario, the SNR of the population-averaged data with order of magnitude of 10^{-17} is substantially lower than that of any synthetic DRO data (order of magnitude of 10^{-2}). The SNR of the synthetic DROs show about half the SNR of any healthy volunteer acquisition. All data sets of the ASL challenge showed very smooth signal evolutions for the perfusion-weighted or control and labelled images with signal standard deviations across control-label pair number of 0.1-1 a.u.. In vivo acquired data showed signal standard deviations of up to 8 a.u. and 2 a.u. between control-label pairs for the 2D and 3D acquisitions, respectively.

4.1.3 Effect of perfusion-weighted image calculation method - ASL challenge data

The contrast between gray and white matter perfusion is noticeably lower for the subtract average (SA) method with absolute value (scenario II) than for the SA method (scenario I) or the average subtract (AS) method with or without absolute value (scenarios III and IV, respectively) as shown in Figure 4.3. The SA and AS methods (scenarios I and III) show differences in mean CBF only for the population-averaged data set. Looking at the individual voxels of the perfusion maps of the whole brain, a maximal difference of the order of 10 is observed for the population-averaged data and 10^{-12} for the synthetic data. The population-averaged data set is an outlier of the group for both scenarios I and III and the subject ranking is identical in both scenarios (Figure 4.4). The differences in group mean CBF between scenarios I and III were found to be not significant (Wilcoxon signed-rank test, $p<0.05$). Applying the absolute value to either SA or AS method (scenarios II and IV) clearly shifts the mean CBF values to higher numbers and yields significantly different group mean CBF distributions compared to scenario I (Figure 4.4). Especially for the SA method applying the absolute value (scenario II) yields mean and standard deviation of individual data sets that are much higher than is to be expected for healthy subjects, which leads to a large group standard deviation for scenario II. The group SNR distributions are much broader for scenario II and IV than for scenarios I and III but only scenario IV was found to differ significantly from scenario I.

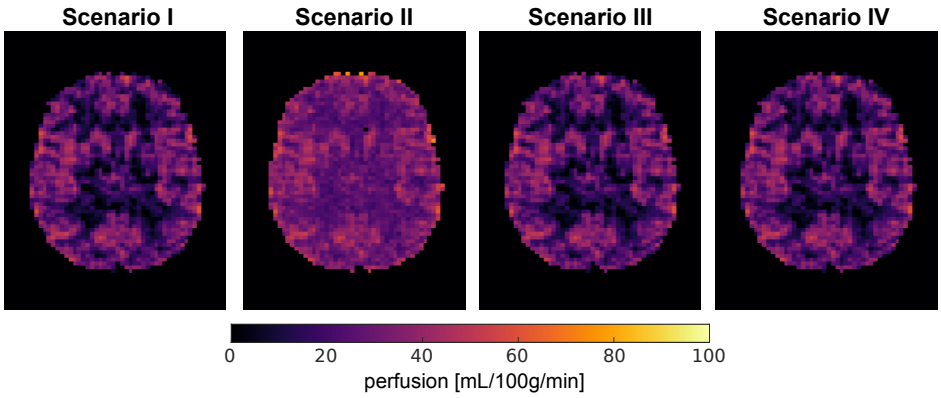

Figure 4.3: **Representative slice of CBF maps obtained for scenarios I-IV for DRO-1.**

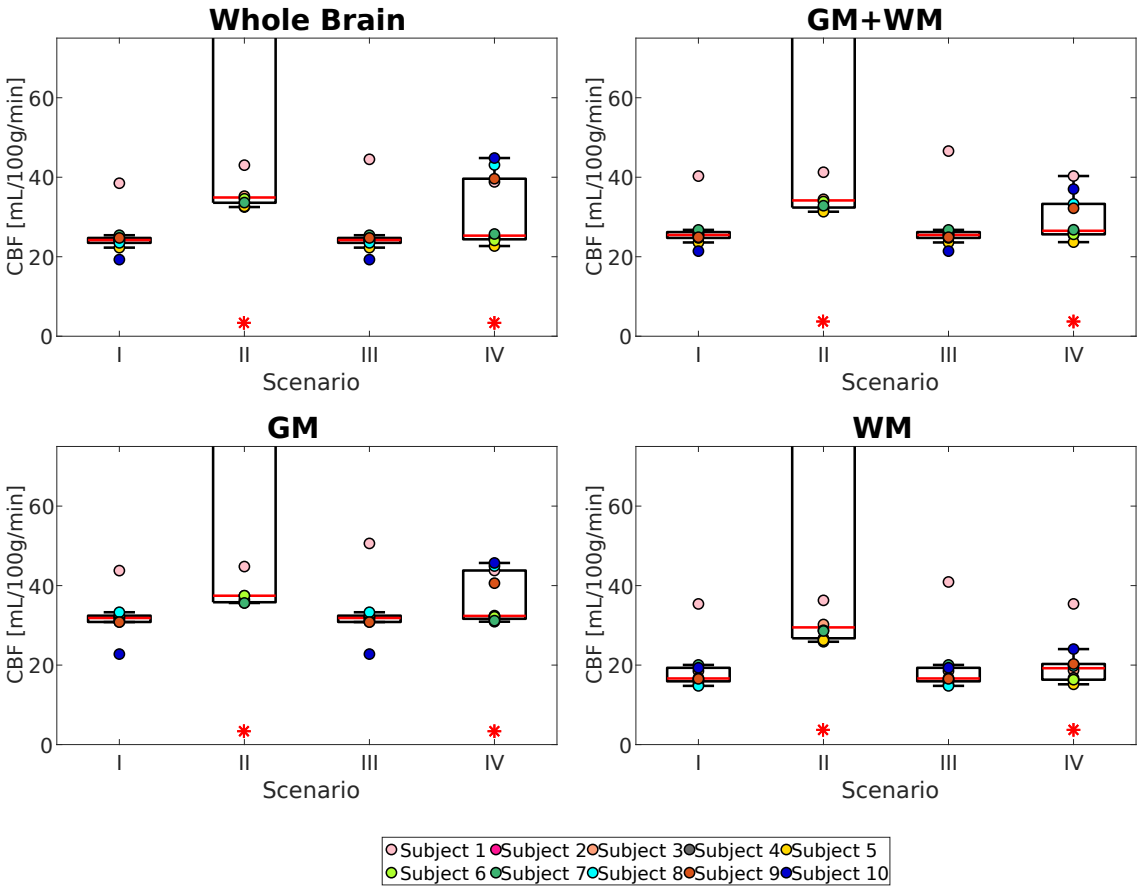

Figure 4.4: **CBF versus perfusion-weighted image calculation methods (scenarios I and II-IV) for the data sets from the ASL challenge calculated for whole brain, GM, WM, GM+WM.** The red line in each boxplot shows the median of the distribution of mean CBF across all data sets considered. The top and bottom part of each boxplot represent the 25^{th} and 75^{th} percentiles. The boxplots' whiskers extend to the highest and lowest data points not considered as outliers. Mean CBF values for each data set are colour-coded and overlaid on the boxplots representing the entire cohort. Statistically significant differences between each scenario and the reference scenario I are indicated by the red stars ($p<0.05$).

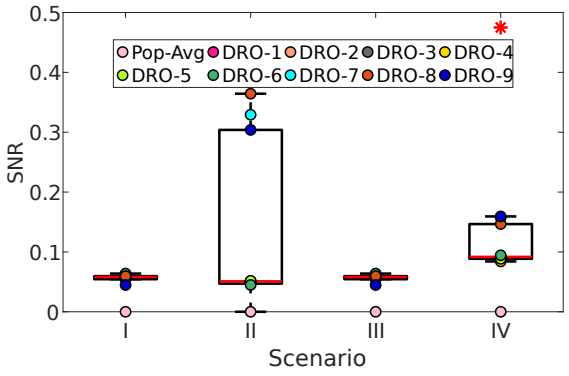

Figure 4.5: **SNR versus perfusion-weighted image calculation methods (scenarios I and II-IV) for the data sets from the ASL challenge.** The red line in each boxplot shows the median of the distribution of SNR across all data sets considered. The top and bottom part of each boxplot represent the 25^{th} and 75^{th} percentiles. The boxplots' whiskers extend to the highest and lowest data points not considered as outliers. SNR values for each data set are colour-coded and overlaid on the boxplots representing the entire cohort. Statistically significant differences between each scenario and the reference scenario I are indicated by the red stars ($p<0.05$).

4.1.4 Effect of outlier removal

4.1.4.1 ASL challenge data

Subject rankings of mean CBF and SNR slightly change depending on which outlier removal option was chosen, especially for scenario VI and IX (Figures 4.6 and 4.7). However, no statistically significant differences in mean CBF distributions between scenario I and scenarios V-XI were observed. Differences in SNR distributions were significant between scenario I and scenarios IX-X. The number of volumes or slices removed before the final perfusion map is calculated depends on the outlier removal option chosen as can be seen in Table 4.1. Scenario VII discards no volumes as outliers in any of the data sets. Scenario X removes more slices than scenario VIII for most data sets.

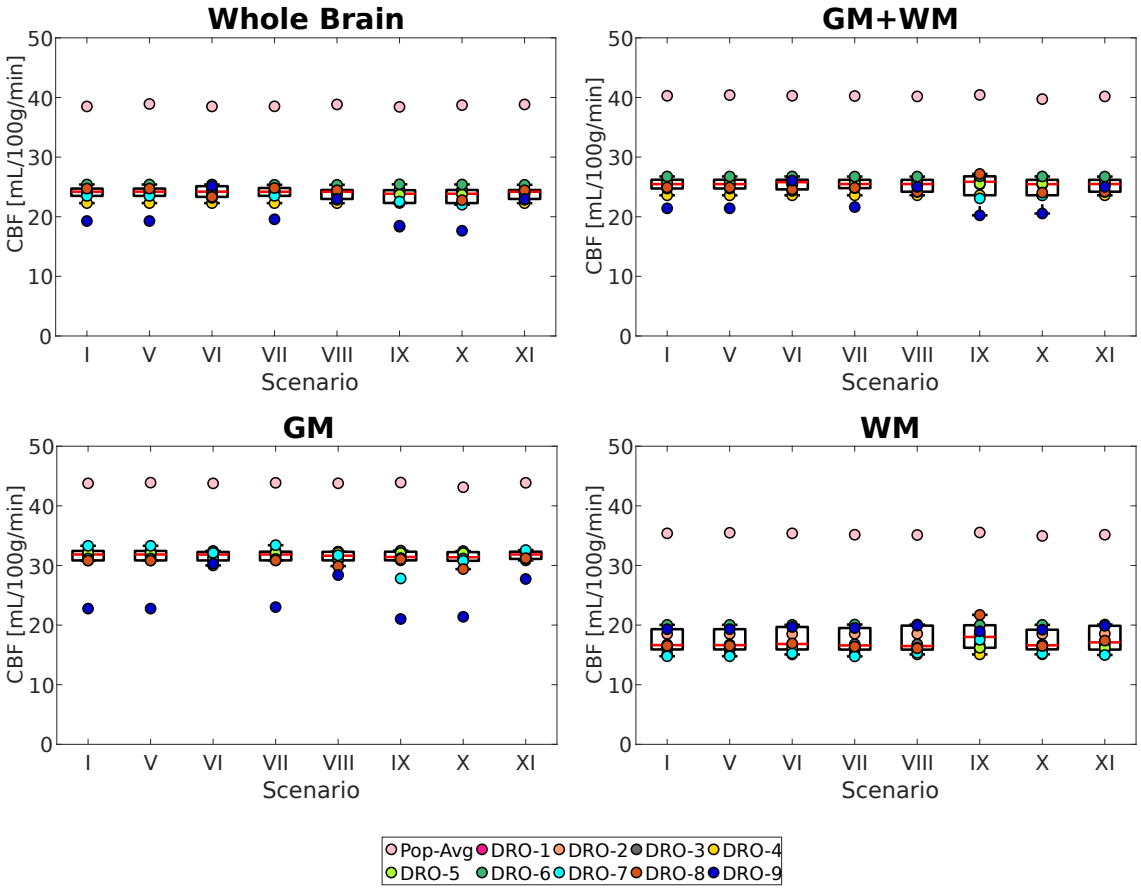

Figure 4.6: **CBF versus outlier removal options (scenarios I and V-XI) for the data sets from the ASL challenge calculated for whole brain, GM, WM, GM+WM.** The red line in each boxplot shows the median of the distribution of mean CBF across all data sets considered. The top and bottom part of each boxplot represent the 25^{th} and 75^{th} percentiles. The boxplots' whiskers extend to the highest and lowest data points not considered as outliers. Mean CBF values for each data set are colour-coded and overlaid on the boxplots representing the entire cohort. No statistically significant differences between each scenario and the reference scenario I were found ($p<0.05$).

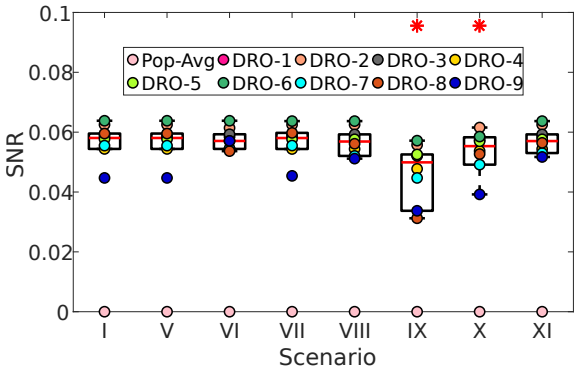

Figure 4.7: **SNR versus outlier removal options (scenarios I and V-XI) for the data sets from the ASL challenge.** The red line in each boxplot shows the median of the distribution of SNR across all data sets considered. The top and bottom part of each boxplot represent the 25^{th} and 75^{th} percentiles. The boxplots' whiskers extend to the highest and lowest data points not considered as outliers. SNR values for each data set are colour-coded and overlaid on the boxplots representing the entire cohort. Statistically significant differences between each scenario and the reference scenario I are indicated by the red stars ($p<0.05$).

Table 4.1: **Number of outlier volumes or slices removed during CBF quantification for the ASL challenge data sets.** Scenarios VIII and X discard individual slices whereas all other scenarios remove entire volumes. Scenario VI removes control and label volumes separately and the number of removed outliers are listed as control/label.

	Pop-Avg	DRO-1	DRO-2	DRO-3	DRO-4	DRO-5	DRO-6	DRO-7	DRO-8	DRO-9
V	2	0	0	0	0	0	0	0	0	0
VI	0/0	0/0	1/1	0/0	0/0	0/1	0/0	0/1	3/2	2/1
VII	0	0	0	0	0	0	0	0	0	0
VIII	79	0	0	0	0	0	1	100	103	111
IX	12	6	6	7	7	5	6	9	13	11
X	426	41	34	42	31	26	176	159	102	111
XI	0	0	0	0	0	0	0	2	1	2

4.1.4.2 In vivo studies - Healthy Volunteers

Cohort 1 2D

The subject ranking varies only little between the different outlier removal options, most visible differences are for scenario IX (Figure 4.8). Statistically significant differences of mean CBF distributions were only found between scenario I and scenarios X-XI for the whole brain and GM, between scenario I and scenarios VI, XI for WM, and between scenario I and scenario X for GM+WM. Scenario IX shows no statistically significant difference when considering the entire cohort. However, on a subject-by-subject basis, mean CBF values differ noticeably. Differences in SNR distributions were found to be significant between scenario I and scenarios VII-X, with scenario IX yielding lower SNR for most subjects (Figure 4.9). The number of volumes or slices removed by each outlier removal option are listed in in Table 4.2.

Table 4.2: **Number of outlier volumes or slices removed during CBF quantification for the 2D data sets from Cohort 1.** Scenarios VIII and X discard individual slices whereas all other scenarios remove entire volumes. Scenario VI removes control and label volumes separately and the number of removed outliers are listed as control/label.

Subject	1	2	3	4	5	6	7	8	9	10	11
V	3	4	2	2	1	3	2	2	3	3	3
VI	1/1	2/2	1/2	1/2	1/2	1/1	2/2	0/1	1/0	1/2	0/0
VII	5	4	3	3	4	5	2	4	4	2	5
VIII	118	137	87	107	146	133	70	110	104	98	99
IX	48	43	0	0	42	48	47	0	39	49	1
X	121	123	90	75	206	196	213	131	128	224	0
XI	0	0	0	0	0	1	0	0	0	0	0

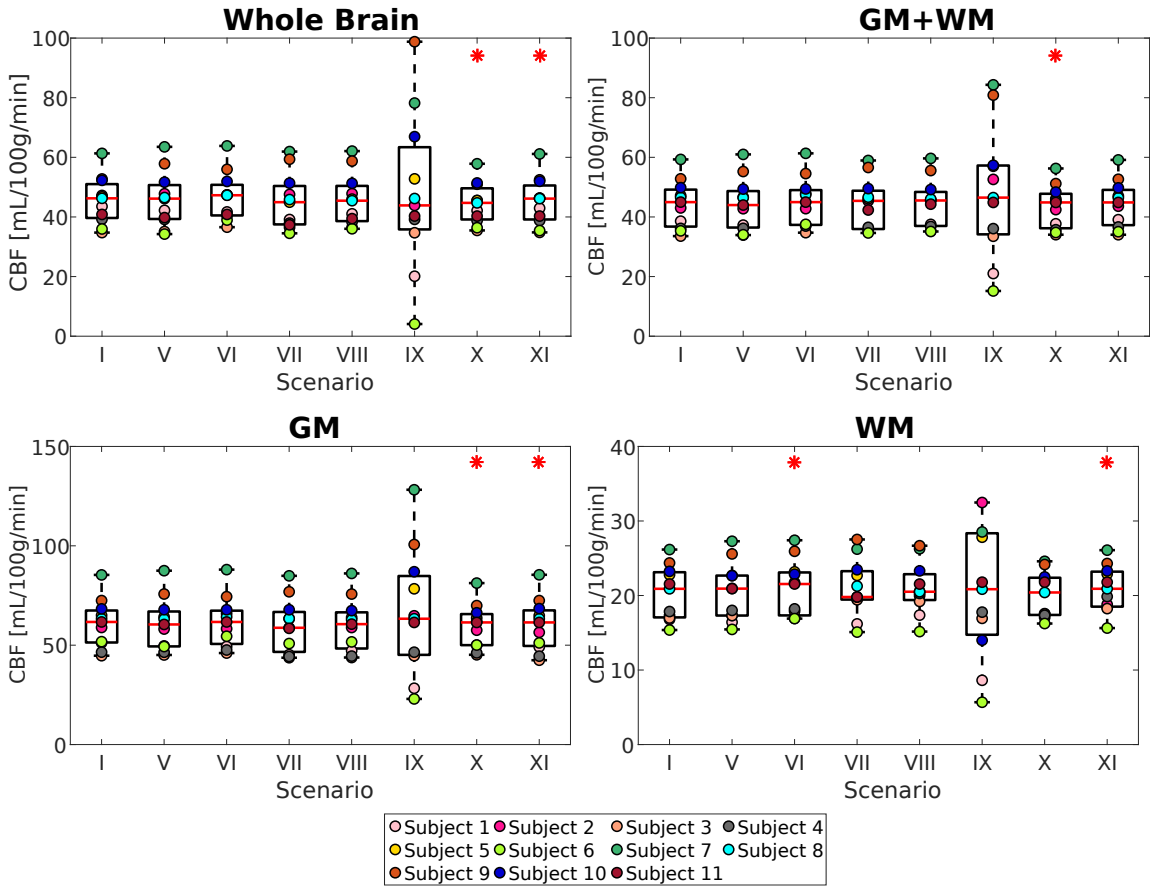

Figure 4.8: **CBF versus outlier removal options (scenarios I and V-XI) for the 2D data sets from Cohort 1 calculated for whole brain, GM, WM, GM+WM.** The red line in each boxplot shows the median of the distribution of mean CBF across all data sets considered. The top and bottom part of each boxplot represent the 25^{th} and 75^{th} percentiles. The boxplots' whiskers extend to the highest and lowest data points not considered as outliers. Mean CBF values for each data set are colour-coded and overlaid on the boxplots representing the entire cohort. Statistically significant differences between each scenario and the reference scenario I are indicated by the red stars ($p<0.05$).

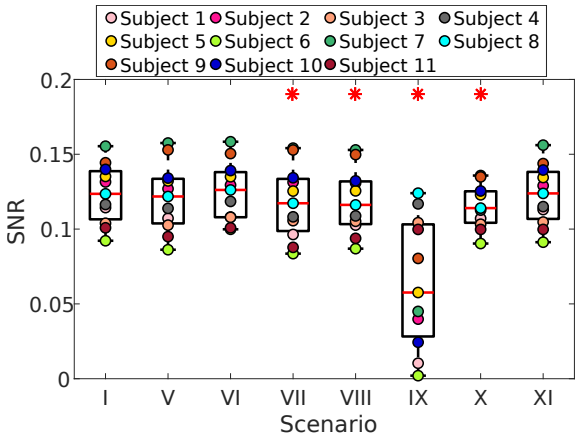

Figure 4.9: **SNR versus outlier removal options (scenarios I and V-XI) for the 2D data sets from Cohort 1.** The red line in each boxplot shows the median of the distribution of SNR across all data sets considered. The top and bottom part of each boxplot represent the 25^{th} and 75^{th} percentiles. The boxplots' whiskers extend to the highest and lowest data points not considered as outliers. SNR values for each data set are colour-coded and overlaid on the boxplots representing the entire cohort. Statistically significant differences between each scenario and the reference scenario I are indicated by the red stars ($p<0.05$).

Cohort 1 3D

The subject ranking and the inter-subject variation of mean CBF vary only little between the different outlier removal options (Figure 4.10). Only scenarios V and IX for the whole brain, scenario XI for GM and scenario VIII for WM show a clear asymmetry of the group as the median is not centred between the 25^{th} and 75^{th} percentiles. Statistically significant differences of mean CBF distributions were found between scenario I and scenarios VI, VIII-IX for the whole brain, GM, GM+WM, and between scenario I and scenarios VI for WM. SNR distributions yield similar inter-subject variations but scenario IX yields much lower values. Differences in SNR distributions were found to be significant between scenario I and scenarios V-VI, VIII-X (Figure 4.11). The number of volumes or slices removed by each outlier removal option are listed in in Table 4.3.

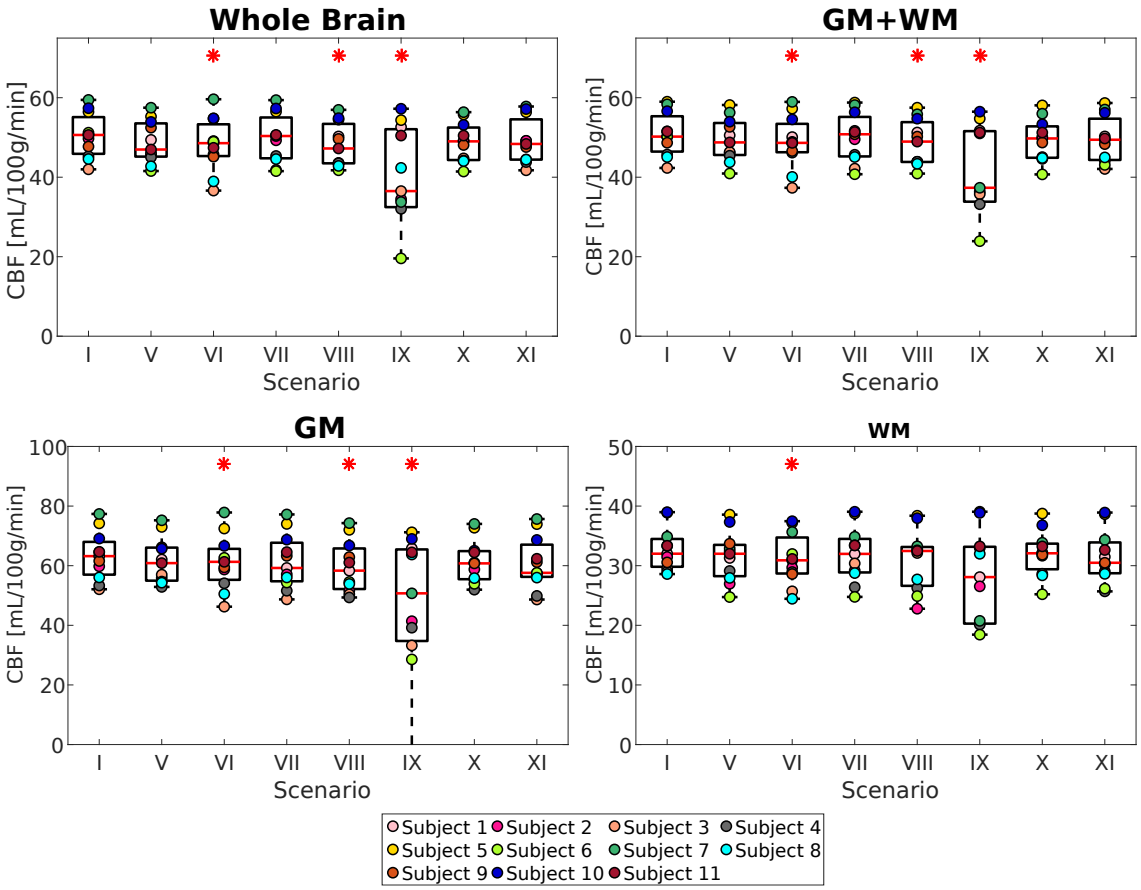

Figure 4.10: **CBF versus outlier removal options (scenarios I and V-XI) for the 3D data sets from Cohort 1 calculated for whole brain, GM, WM, GM+WM.** The red line in each boxplot shows the median of the distribution of mean CBF across all data sets considered. The top and bottom part of each boxplot represent the 25^{th} and 75^{th} percentiles. The boxplots' whiskers extend to the highest and lowest data points not considered as outliers. Mean CBF values for each data set are colour-coded and overlaid on the boxplots representing the entire cohort. Statistically significant differences between each scenario and the reference scenario I are indicated by the red stars ($p<0.05$).

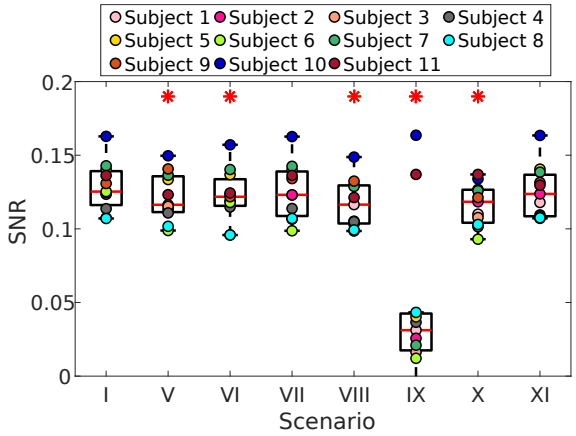

Figure 4.11: **SNR versus outlier removal options (scenarios I and V-XI) for the 3D data sets from Cohort 1.** The red line in each boxplot shows the median of the distribution of SNR across all data sets considered. The top and bottom part of each boxplot represent the 25^{th} and 75^{th} percentiles. The boxplots' whiskers extend to the highest and lowest data points not considered as outliers. SNR values for each data set are colour-coded and overlaid on the boxplots representing the entire cohort. No statistically significant differences between each scenario and the reference scenario I were found ($p<0.05$).

Table 4.3: **Number of outlier volumes or slices removed during CBF quantification for the 3D data sets from Cohort 1.** Scenarios VIII and X discard individual slices whereas all other scenarios remove entire volumes. Scenario VI removes control and label volumes separately and the number of removed outliers are listed as control/label.

Subject	1	2	3	4	5	6	7	8	9	10	11
V	1	1	2	2	3	2	1	1	2	2	2
VI	1/0	2/2	1/0	2/4	2/1	1/1	2/2	1/0	2/3	4/3	2/2
VII	0	0	0	0	0	2	0	0	3	0	0
VIII	141	147	139	116	105	80	156	113	85	122	132
IX	46	45	48	39	45	46	46	39	48	0	1
X	245	141	186	267	270	272	220	110	272	324	0
XI	2	0	0	1	0	1	1	0	0	0	1

Cohort 2

The inter-subject variation of mean CBF is smaller than for Cohort 1, with scenario IX resulting in the largest variations (Figure 4.12). Statistically significant differences of mean CBF distributions were found between scenario I and scenarios VIII, XI for the whole brain, between scenario I and scenarios VII-VIII, XI for GM and GM+WM, and between scenario I and scenarios VII-VIII, X-XI for WM. SNR distributions yield similar inter-subject variation, with scenario VIII resulting in the smallest variation (Figure 4.13). Scenario IX yields lowest SNR for all subjects except subject 8, for which no outliers were detected. Statistically significant difference in SNR distributions were found between scenario I and scenarios IX-X. The number of volumes or slices removed by each outlier removal option are listed in in Table 4.4.

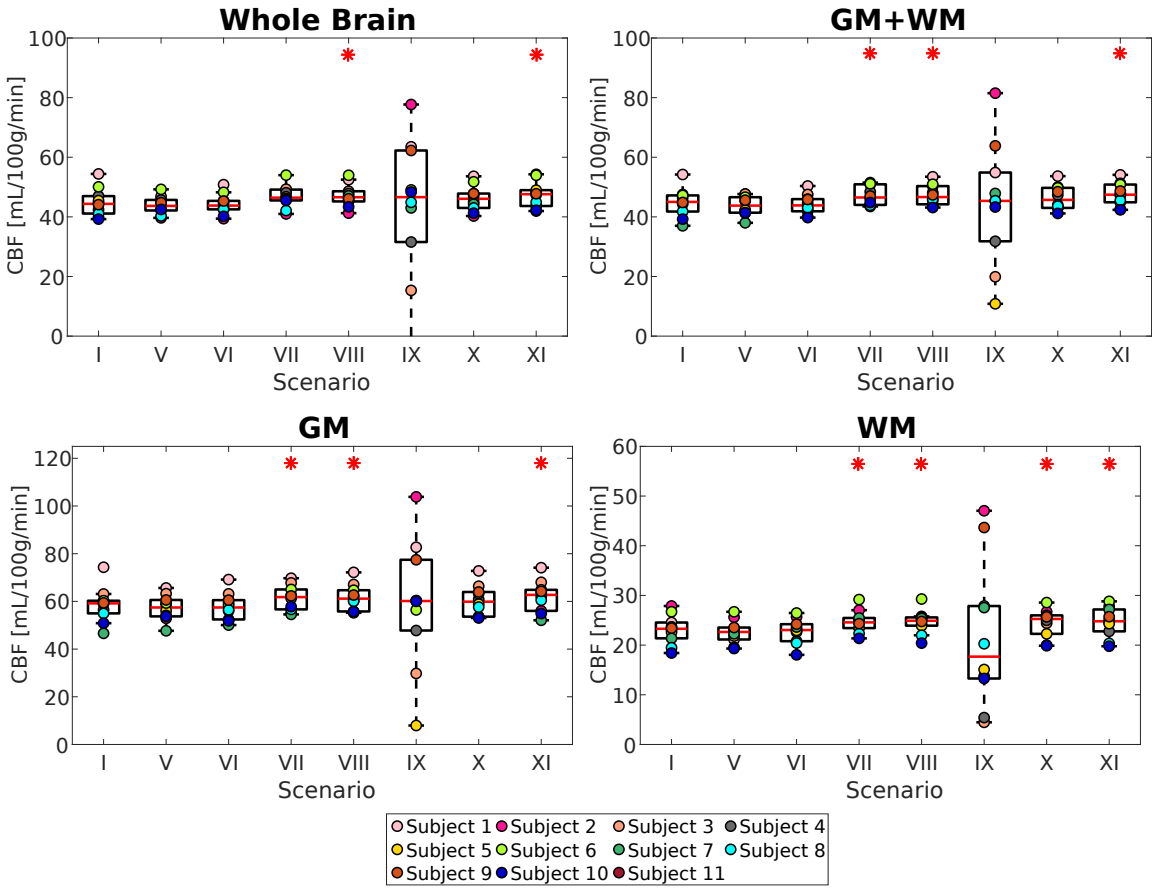

Figure 4.12: **CBF versus outlier removal options (scenarios I and V-XI) for the data sets from Cohort 2 calculated for whole brain, GM, WM, GM+WM.** The red line in each boxplot shows the median of the distribution of mean CBF across all data sets considered. The top and bottom part of each boxplot represent the 25^{th} and 75^{th} percentiles. The boxplots' whiskers extend to the highest and lowest data points not considered as outliers. Mean CBF values for each data set are colour-coded and overlaid on the boxplots representing the entire cohort. Statistically significant differences between each scenario and the reference scenario I are indicated by the red stars ($p<0.05$).

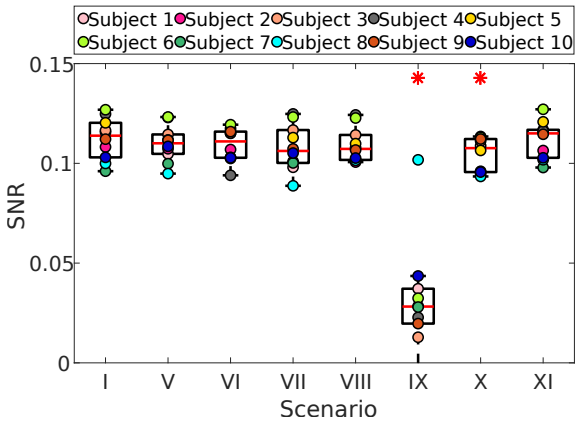

Figure 4.13: **SNR versus outlier removal options (scenarios I and V-XI) for the data sets from Cohort 2.** The red line in each boxplot shows the median of the distribution of SNR across all data sets considered. The top and bottom part of each boxplot represent the 25^{th} and 75^{th} percentiles. The boxplots' whiskers extend to the highest and lowest data points not considered as outliers. SNR values for each data set are colour-coded and overlaid on the boxplots representing the entire cohort. Statistically significant differences between each scenario and the reference scenario I are indicated by the red stars ($p<0.05$).

Table 4.4: **Number of outlier volumes or slices removed during CBF quantification for the data sets from Cohort 2.** Scenarios VIII and X discard individual slices whereas all other scenarios remove entire volumes. Scenario VI removes control and label volumes separately and the number of removed outliers are listed as control/label.

Subject	1	2	3	4	5	6	7	8	9	10	11
V	2	2	2	2	1	1	2	3	3	3	
VI	1/1	1/1	1/1	2/1	3/3	2/3	1/2	1/1	1/2	2/2	
VII	5	3	2	5	2	3	4	7	2	5	
VIII	88	103	74	137	95	80	114	102	100	90	
IX	44	47	42	31	47	44	44	0	47	40	
X	121	232	125	165	121	204	146	156	70	156	
XI	0	1	0	1	0	0	2	0	0	0	

4.1.5 Effect of M0 corrections

4.1.5.1 ASL challenge data

Brain compartment specific M0 corrections (scenarios XII-XV) all yield similar subject ranking and degree of inter-subject variation of mean CBF (Figure 4.14). Scenario XV yields the highest mean CBF values and scenario XIII yields the highest SNR (Figure 4.15). Differences in mean CBF and SNR distributions between scenario I and scenarios XII-XVI were found to be statistically significant.

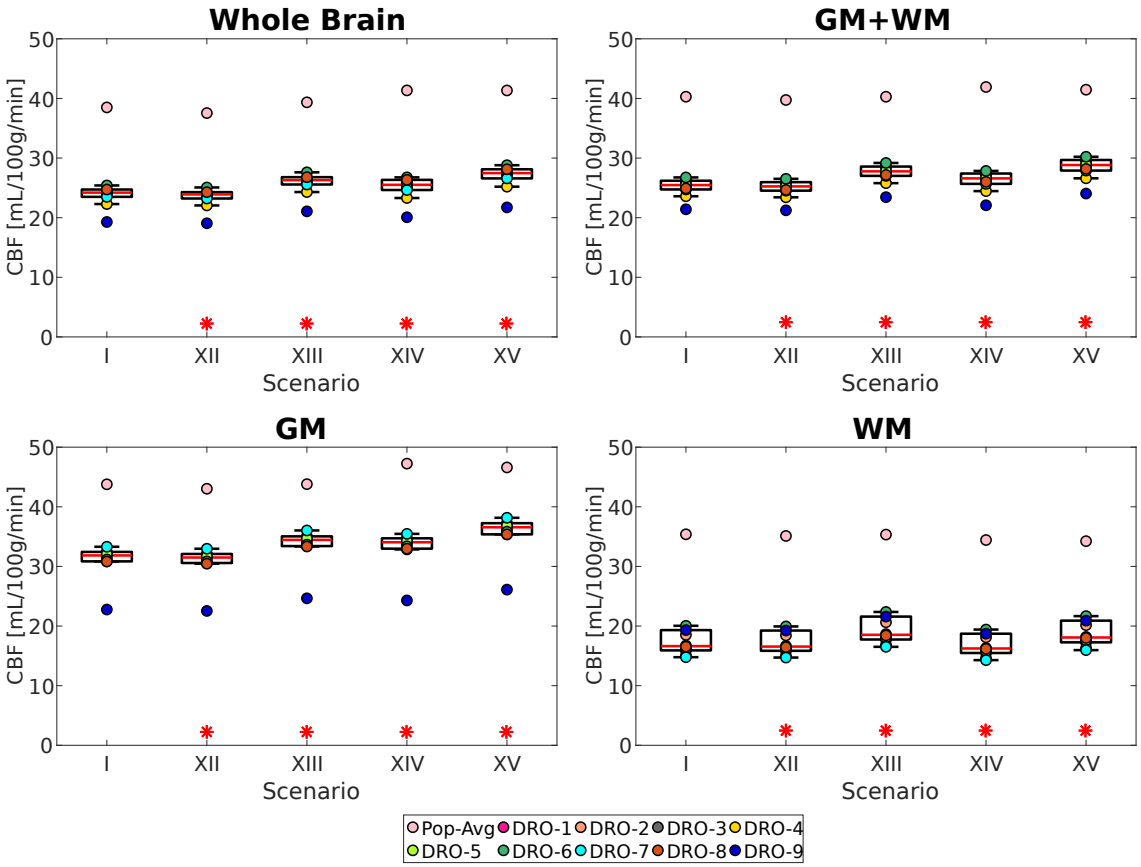

Figure 4.14: **Mean CBF versus M0 correction options (scenarios I and XII-XV) for the data sets from the ASL challenge calculated for whole brain, GM, WM, GM+WM.** The red line in each boxplot shows the median of the distribution of mean CBF across all data sets considered. The top and bottom part of each boxplot represent the 25^{th} and 75^{th} percentiles. The boxplots' whiskers extend to the highest and lowest data points not considered as outliers. Mean CBF values for each data set are colour-coded and overlaid on the boxplots representing the entire cohort. Statistically significant differences between each scenario and the reference scenario I are indicated by the red stars ($p<0.05$).

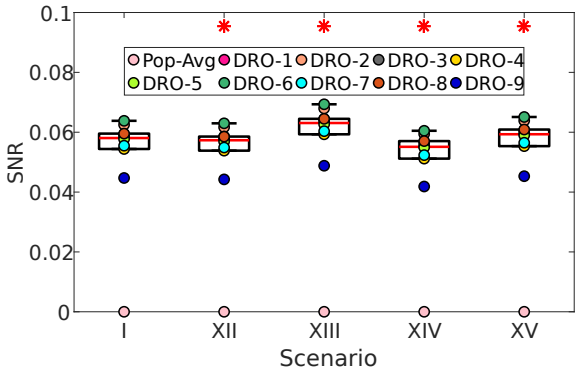

Figure 4.15: **SNR versus M0 correction options (scenarios I and XII-XV) for the data sets from the ASL challenge.**The red line in each boxplot shows the median of the distribution of SNR across all data sets considered. The top and bottom part of each boxplot represent the 25^{th} and 75^{th} percentiles. The boxplots' whiskers extend to the highest and lowest data points not considered as outliers. SNR values for each data set are colour-coded and overlaid on the boxplots representing the entire cohort. Statistically significant differences between each scenario and the reference scenario I are indicated by the red stars ($p<0.05$).

4.1.5.2 In vivo studies - Healthy Volunteers

Cohort 1 2D

Mean CBF subject rankings and inter-subject variations are also similar for scenarios I and XII-XV (Figure 4.16). Scenario XIV yields highest mean CBF values and scenario XIII yields highest SNR (Figure 4.17). Differences between mean CBF calculated over the whole brain were found to be significant between scenario I and scenarios XII-XV. Differences in mean CBF calculated over GM and GM+WM were found to be significant between scenario I and scenarios XII-XIV. No statistically significant differences in mean CBF calculated over WM were found between any of these scenarios, indicating that the considered M0 corrections affect WM the least. Differences in SNR distributions between scenario I and scenarios XII-XVI were found to be statistically significant.

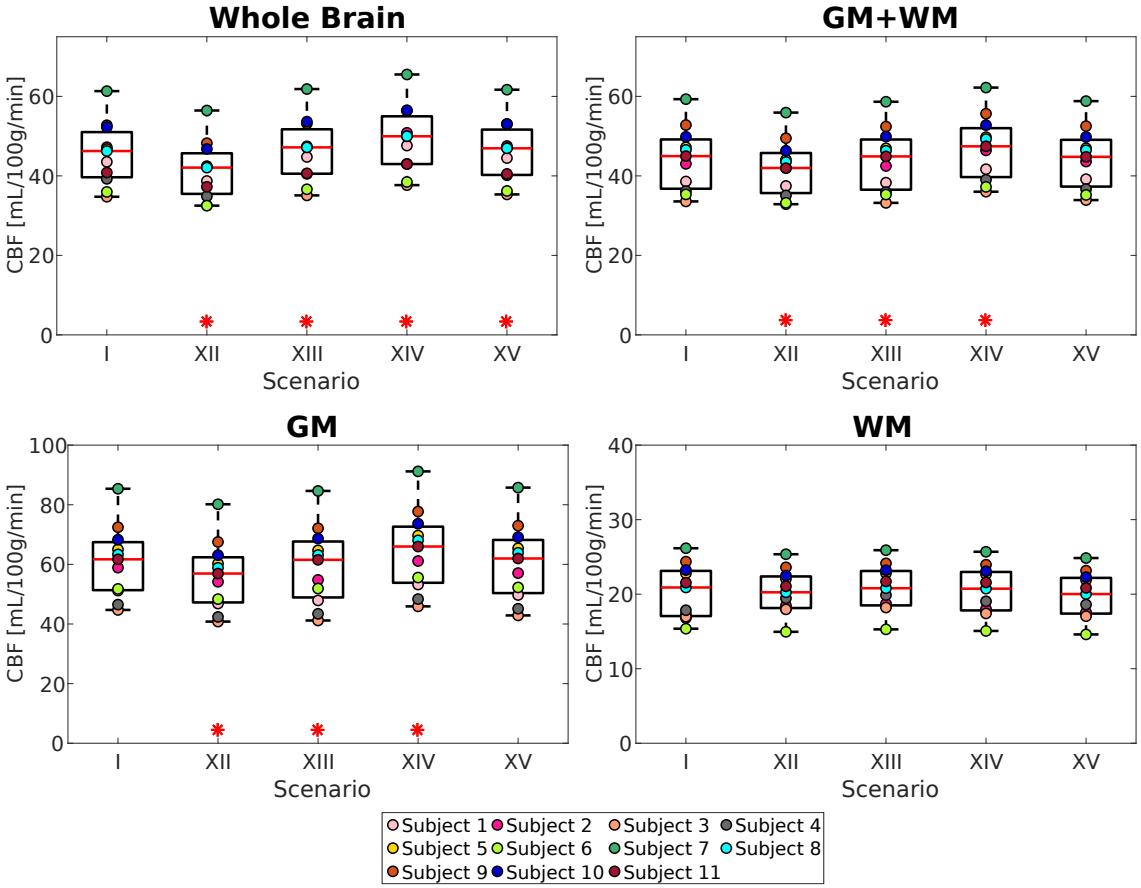

Figure 4.16: **CBF versus M0 correction options (scenarios XII-XV) for for the 2D data sets from Cohort 1 calculated for whole brain, GM, WM, GM+WM.** The red line in each boxplot shows the median of the distribution of mean CBF across all data sets considered. The top and bottom part of each boxplot represent the 25^{th} and 75^{th} percentiles. The boxplots' whiskers extend to the highest and lowest data points not considered as outliers. Mean CBF values for each data set are colour-coded and overlaid on the boxplots representing the entire cohort. Statistically significant differences between each scenario and the reference scenario I are indicated by the red stars ($p<0.05$).

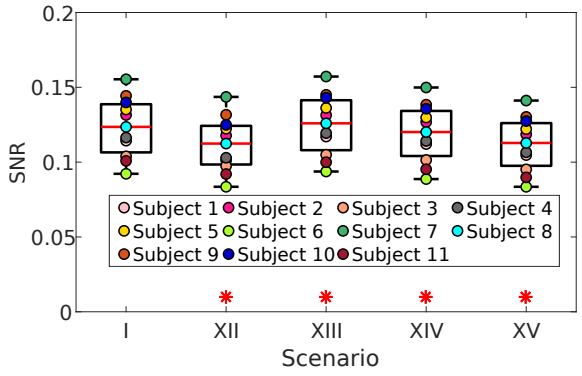

Figure 4.17: **SNR versus M0 correction options (scenarios I and XII-XV) for for the 2D data sets from Cohort 1.** The red line in each boxplot shows the median of the distribution of SNR across all data sets considered. The top and bottom part of each boxplot represent the 25^{th} and 75^{th} percentiles. The boxplots' whiskers extend to the highest and lowest data points not considered as outliers. SNR values for each data set are colour-coded and overlaid on the boxplots representing the entire cohort. Statistically significant differences between each scenario and the reference scenario I are indicated by the red stars ($p<0.05$).

Cohort 1 3D

Mean CBF subject rankings and inter-subject variations are similar for scenarios I and XII-XV (Figure 4.20). Scenario XIV yields highest mean CBF values for whole brain, GM and GM+WM, while scenarios I and XIII yield highest mean CBF values for WM. Scenario XIII yields highest SNR (Figure 4.21). Differences between mean CBF calculated over the whole brain were found to be significant between scenario I and scenarios XII, XIV. Differences in mean CBF calculated over GM were found to be significant between scenario I and scenarios XII-XIV. Differences in mean CBF calculated over WM were found to be significant between scenario I and scenarios XII, XIV, XV. Differences in mean CBF distributions calculated over GM+WM were found to be significant between scenario I and scenarios XII-XV. Differences in SNR distributions between scenario I and scenarios XII, XV, XVI were found to be statistically significant.

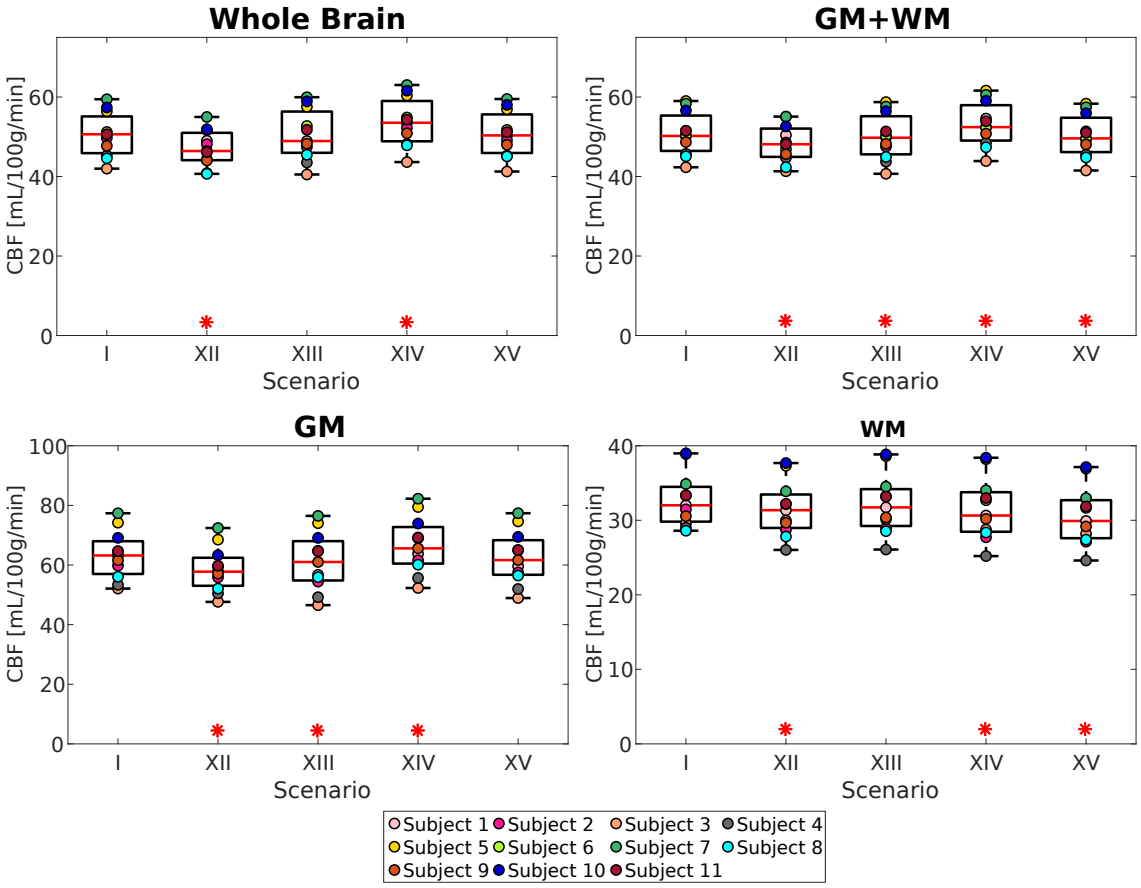

Figure 4.18: **CBF versus M0 correction options (scenarios XII-XV) for for the 3D data sets from Cohort 1 calculated for whole brain, GM, WM, GM+WM.** The red line in each boxplot shows the median of the distribution of mean CBF across all data sets considered. The top and bottom part of each boxplot represent the 25^{th} and 75^{th} percentiles. The boxplots' whiskers extend to the highest and lowest data points not considered as outliers. Mean CBF values for each data set are colour-coded and overlaid on the boxplots representing the entire cohort. Statistically significant differences between each scenario and the reference scenario I are indicated by the red stars ($p<0.05$).

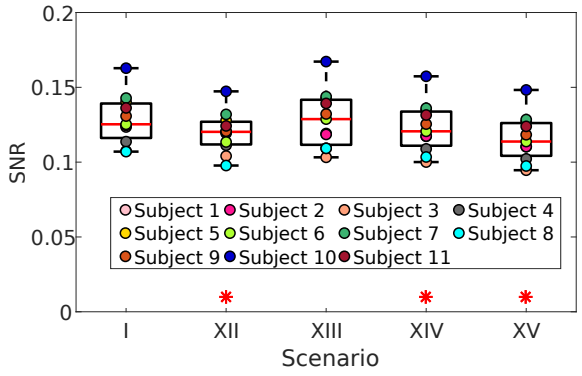

Figure 4.19: **SNR versus M0 correction options (scenarios I and XII-XV) for for the 3D data sets from Cohort 1.** The red line in each boxplot shows the median of the distribution of SNR across all data sets considered. The top and bottom part of each boxplot represent the 25^{th} and 75^{th} percentiles. The boxplots' whiskers extend to the highest and lowest data points not considered as outliers. SNR values for each data set are colour-coded and overlaid on the boxplots representing the entire cohort. Statistically significant differences between each scenario and the reference scenario I are indicated by the red stars ($p<0.05$).

Cohort 2

Mean CBF subject rankings and inter-subject variations are similar for scenarios I and XII-XV but show some differences when considering the whole brain (Figure 4.20). Scenario XIV yields highest mean CBF values and scenario XIII yields highest SNR (Figure 4.21). Differences between mean CBF calculated over the whole brain were found to be significant between scenario I and scenarios XII-XV. Differences in mean CBF calculated over GM and GM+WM were found to be significant between scenario I and scenarios XIII-XV and differences in mean CBF calculated over WM were found to be significant between scenario I and scenarios XII-XIV. Differences in SNR distributions between scenario I and scenarios XII-XVI were found to be statistically significant.

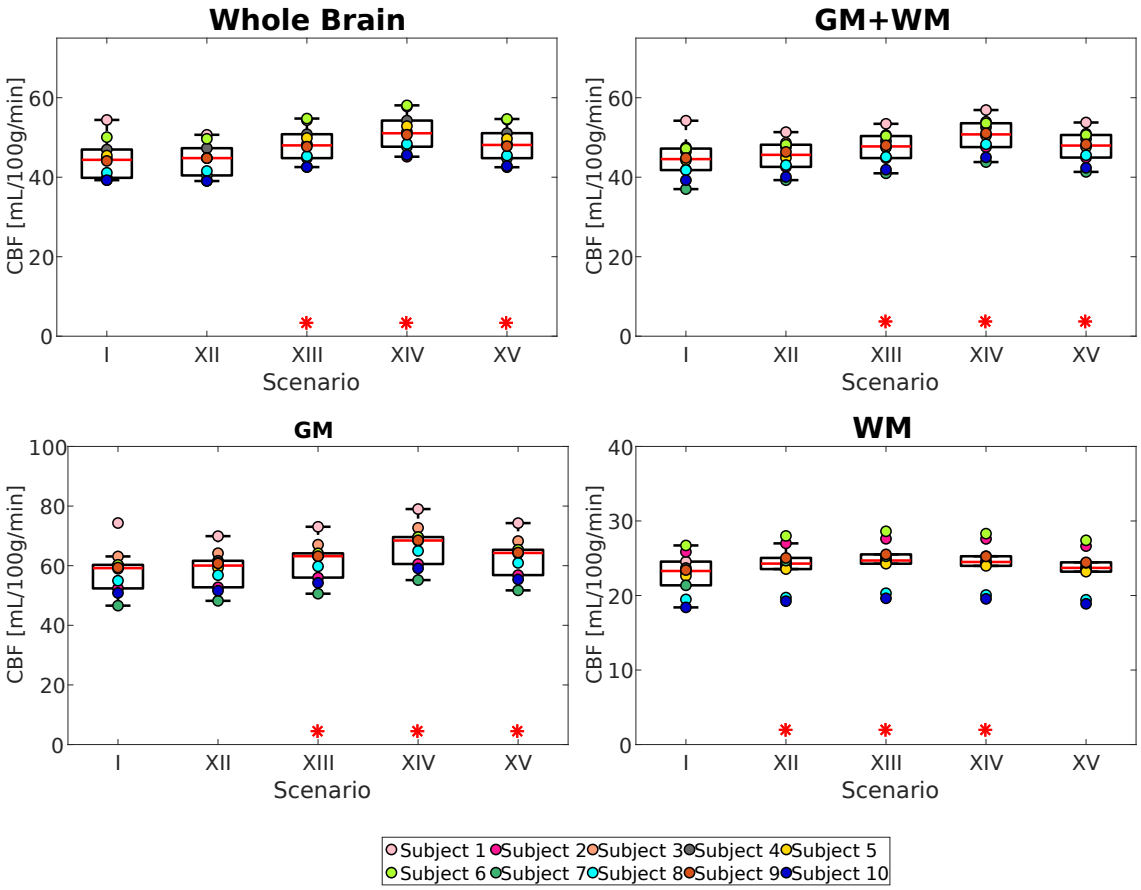

Figure 4.20: **CBF versus M0 correction options (scenarios XII-XV) for for the data sets from Cohort 2 calculated for whole brain, GM, WM, GM+WM.** The red line in each boxplot shows the median of the distribution of mean CBF across all data sets considered. The top and bottom part of each boxplot represent the 25^{th} and 75^{th} percentiles. The boxplots' whiskers extend to the highest and lowest data points not considered as outliers. Mean CBF values for each data set are colour-coded and overlaid on the boxplots representing the entire cohort. Statistically significant differences between each scenario and the reference scenario I are indicated by the red stars ($p<0.05$).

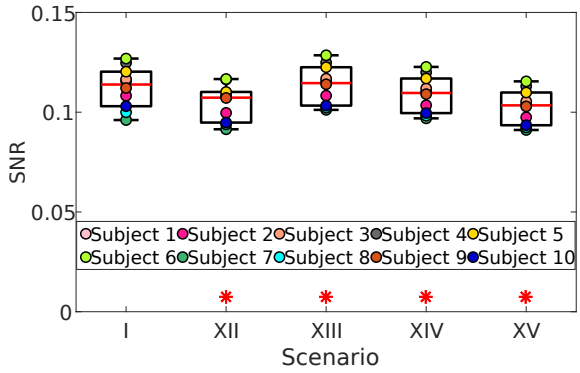

Figure 4.21: **SNR versus M0 correction options (scenarios I and XII-XV) for for the data sets from Cohort 2.** The red line in each boxplot shows the median of the distribution of SNR across all data sets considered. The top and bottom part of each boxplot represent the 25^{th} and 75^{th} percentiles. The boxplots' whiskers extend to the highest and lowest data points not considered as outliers. SNR values for each data set are colour-coded and overlaid on the boxplots representing the entire cohort. Statistically significant differences between each scenario and the reference scenario I are indicated by the red stars ($p<0.05$).

4.1.6 Effect of M0 smoothing - ASL challenge data

Increasing the size of the full width at half maximum (FWHM) of the isotropic Gaussian smoothing kernel results in an increase of mean CBF and SNR values (Figures 4.22 and 4.23). SNR values are substantially worse for no smoothing (scenario XVI). Changing the FWHM does not affect the subject ranking. Differences in mean CBF distributions between scenario I and scenarios XII-XVI were all found to be statistically significant except for WM and scenario XVII. Differences in SNR distributions between scenario I and scenarios XII-XIX were also found to be statistically significant.

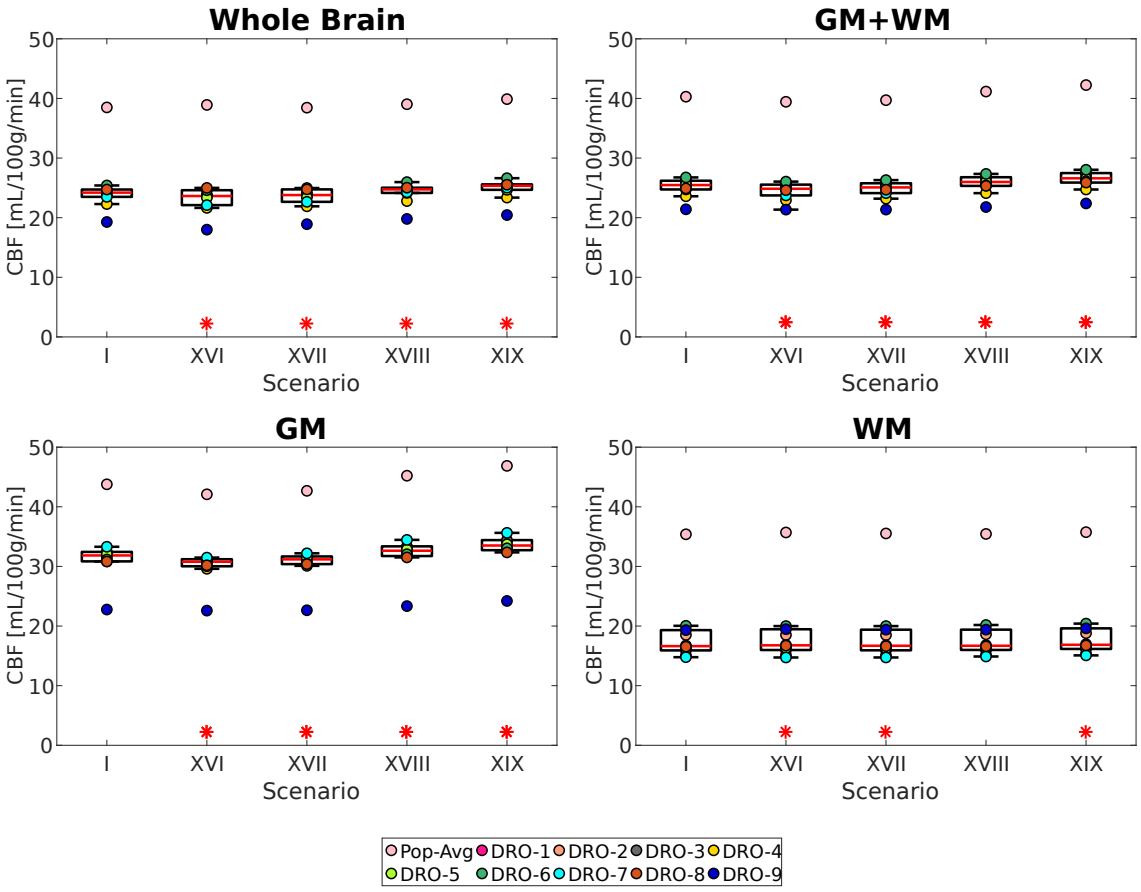

Figure 4.22: **CBF versus full width at half maximum of smoothing kernel applied on M0 image (scenarios I and XVI-XIX) for the data sets from the ASL challenge calculated for whole brain, GM, WM, GM+WM.** The red line in each boxplot shows the median of the distribution of mean CBF across all data sets considered. The top and bottom part of each boxplot represent the 25^{th} and 75^{th} percentiles. The boxplots' whiskers extend to the highest and lowest data points not considered as outliers. Mean CBF values for each data set are colour-coded and overlaid on the boxplots representing the entire cohort. Statistically significant differences between each scenario and the reference scenario I are indicated by the red stars ($p<0.05$).

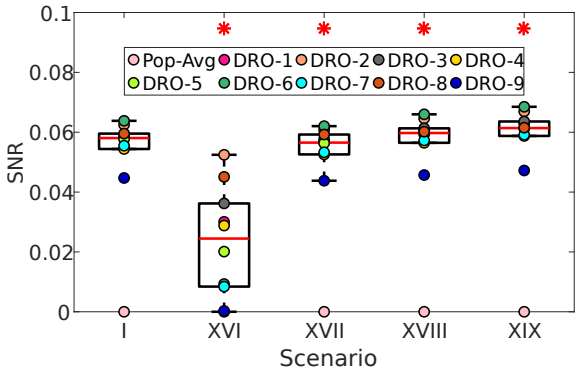

Figure 4.23: **SNR versus full width at half maximum of smoothing kernel applied on M0 image (scenarios I and XVI-XIX) for the data sets from the ASL challenge.** The red line in each boxplot shows the median of the distribution of SNR across all data sets considered. The top and bottom part of each boxplot represent the 25^{th} and 75^{th} percentiles. The boxplots' whiskers extend to the highest and lowest data points not considered as outliers. SNR values for each data set are colour-coded and overlaid on the boxplots representing the entire cohort. Statistically significant differences between each scenario and the reference scenario I are indicated by the red stars ($p<0.05$).

4.1.7 Comparison of segmentations - ASL challenge data

CBF maps were calculated for the ASL challenge data using either the realigned M0 image or the registered anatomical image for the automated segmentation (scenarios I and XX). The overlap of binary segmentation masks obtained from the two segmentation options for CSF, GM, and WM is shown in Figure 4.24 for a representative slice of four data sets. It is clearly visible that differences exist between masks, especially for CSF in DRO-1, DRO-5, DRO-9, where segmentation using the M0 image classifies the ventricles as GM instead of CSF. Similar observations can be made for the entire volume of the segmentation masks, which were compared with the Dice index (DI) [*Dice*, 1945]. DIs calculated for each brain compartment and each data set are plotted in Figure 4.25. Agreement between the two segmentation options is good for GM and WM for all data sets with DIs ranging from 0.69 to 0.78 and from 0.68 to 0.80, respectively. For CSF, the agreement is poor for all synthetic data sets with DIs ranging from 0.18 to 0.25 and yields a DI of 0.51 for the population-averaged data. As can be seen in Figure 4.26, the subject ranking based on mean CBF differs between the two scenarios, indicating that the agreement between segmentation masks is subject-dependent. Statistically significant differences between mean CBF distributions were found for GM, WM, and GM+WM. The difference between SNR distributions was also found to be significant (Figure 4.27).

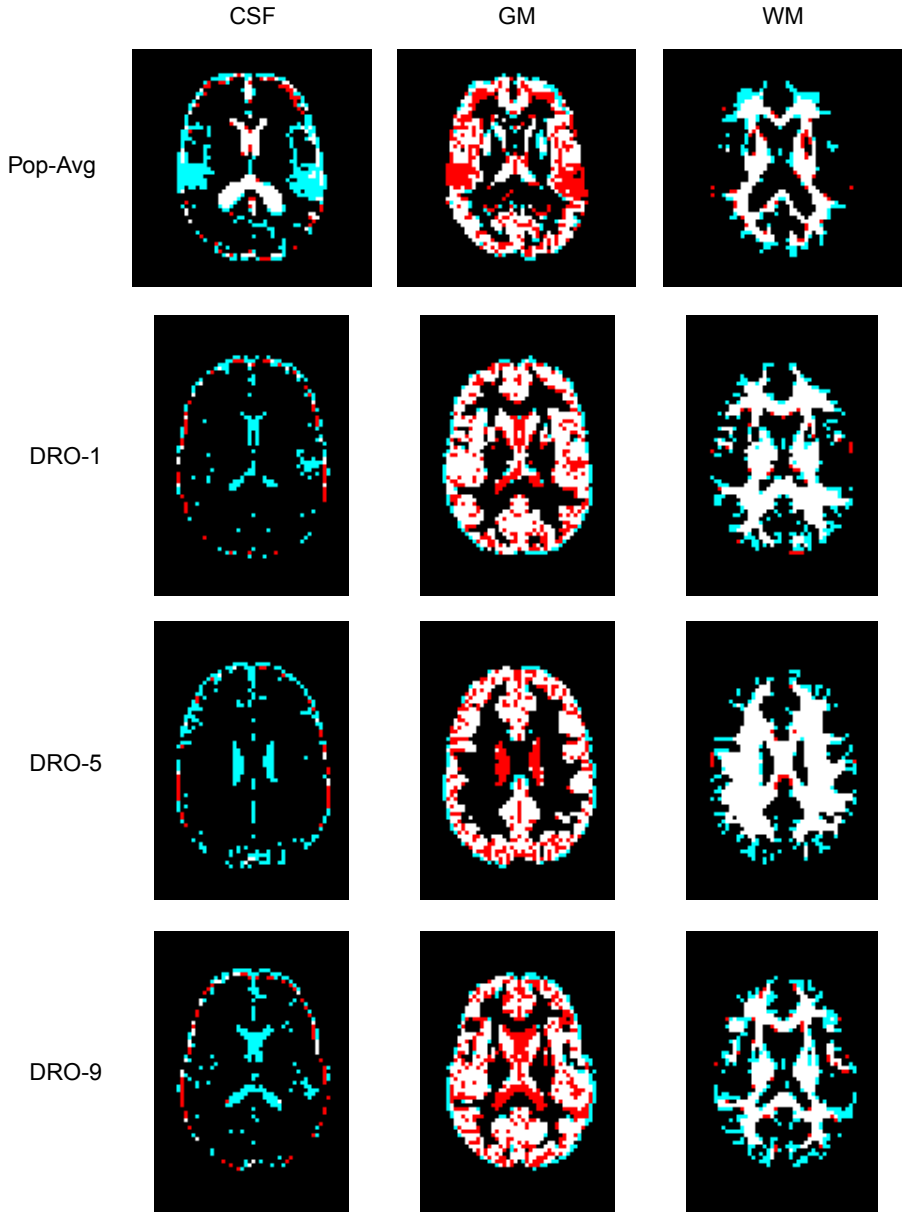

Figure 4.24: **Comparison of binary masks obtained from automated segmentation on the M0 and on the anatomical image for a representative slice of four data sets of the ASL challenge data.** For each brain compartment, the masks obtained from the M0 are shown in red, the masks obtained from the registered anatomical data are shown in cyan, and pixels which are present in both masks are shown in white.

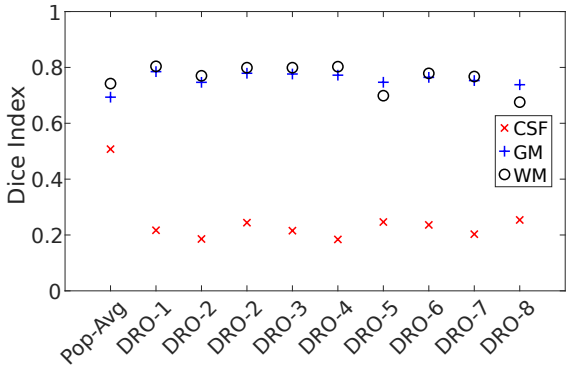

Figure 4.25: **Quantitative comparison of segmentation masks obtained from automated segmentation on the M0 and on the anatomical image using the Dice index.**

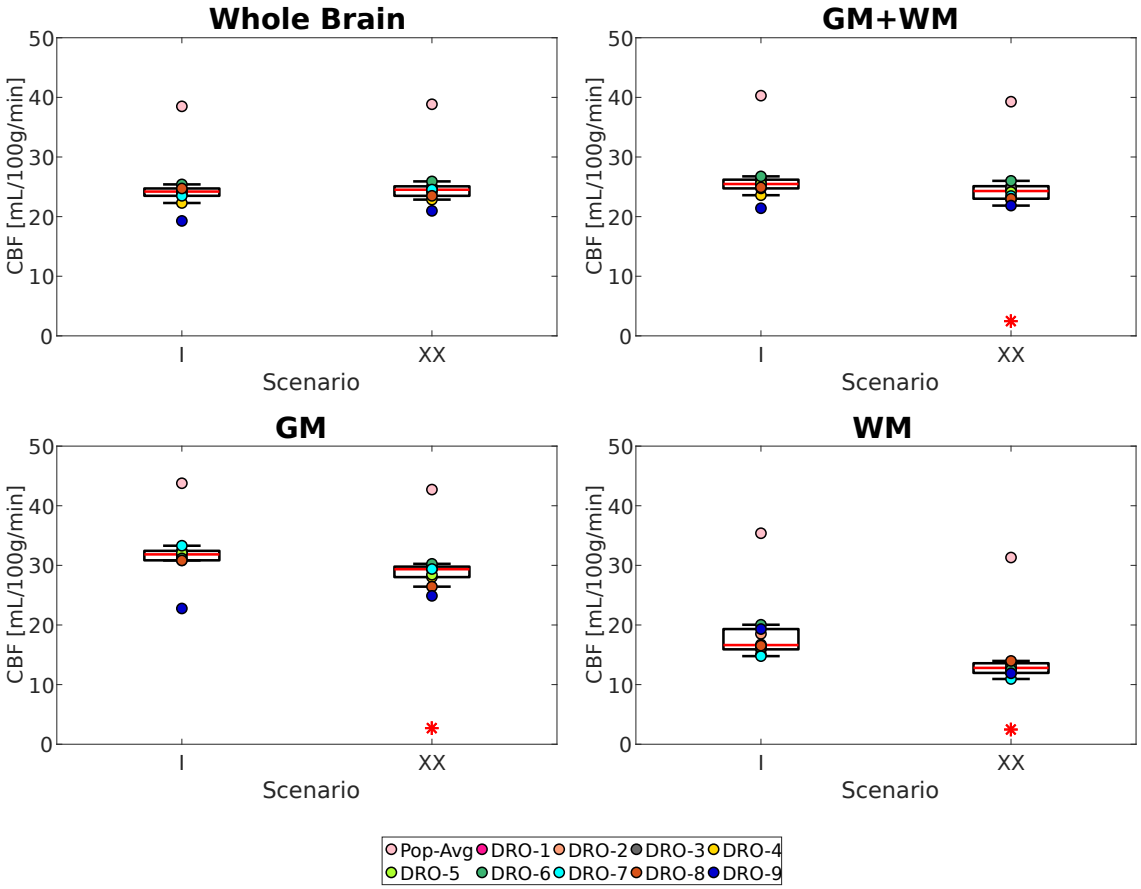

Figure 4.26: **CBF versus segmentation image Sscenarios I and XX) for the data sets from the ASL challenge calculated for whole brain, GM, WM, GM+WM.** The red line in each boxplot shows the median of the distribution of mean CBF across all data sets considered. The top and bottom part of each boxplot represent the 25^{th} and 75^{th} percentiles. The boxplots' whiskers extend to the highest and lowest data points not considered as outliers. Mean CBF values for each data set are colour-coded and overlaid on the boxplots representing the entire cohort. Statistically significant differences between each scenario and the reference scenario I are indicated by the red stars ($p<0.05$).

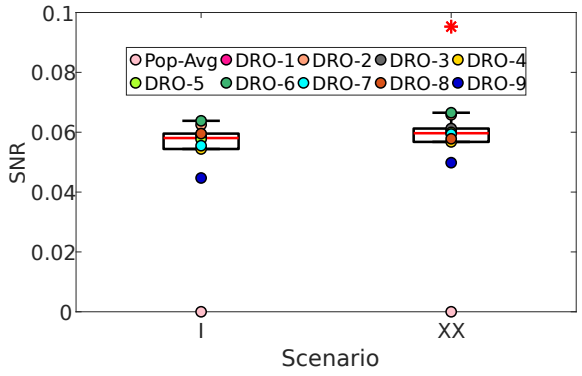

Figure 4.27: **SNR versus segmentation image (scenarios I and XX) for the data sets from the ASL challenge.** The red line in each boxplot shows the median of the distribution of SNR across all data sets considered. The top and bottom part of each boxplot represent the 25^{th} and 75^{th} percentiles. The boxplots' whiskers extend to the highest and lowest data points not considered as outliers. SNR values for each data set are colour-coded and overlaid on the boxplots representing the entire cohort. Statistically significant differences between each scenario and the reference scenario I are indicated by the red stars ($p<0.05$).

4.1.8 Effect of number of control-label pairs - Cohort 1 data

Mean and standard deviation of CBF distributions versus number of control-label pairs for 2D and 3D data sets of subjects 5-8 of Cohort 1 are shown in Figure 4.28. As expected, the standard deviation decreases with increasing number of control-label pairs considered for CBF quantification. However, in some subjects, the mean CBF also changes with increasing number of control-label pairs and it is difficult to define an optimal number of control-label pairs applicable to all subjects. Data points for the whole brain and for GM+WM differ only slightly for all subjects, indicating that the CSF contributes only little to the CBF, as is to be expected. Looking at the group mean CBF distributions shown as boxplots in Figure 4.29, it is visible that the range between 25^{th} and 75^{th} percentiles decreases with increasing number of control-label pairs, especially for up to 25 pairs. Furthermore, the median value decreases with increasing number of control-label pairs for the 3D readout. Outliers are only present for 3D acquisitions of WM and disappear for a number of control-label pairs higher than 25. For both 2D and 3D acquisitions, group mean CBF of GM and WM are in the lower part or directly below the literature range of CBF values for GM and WM of healthy subjects taken from [*Deibler et al.*, 2008; *van Gelderen et al.*, 2008].

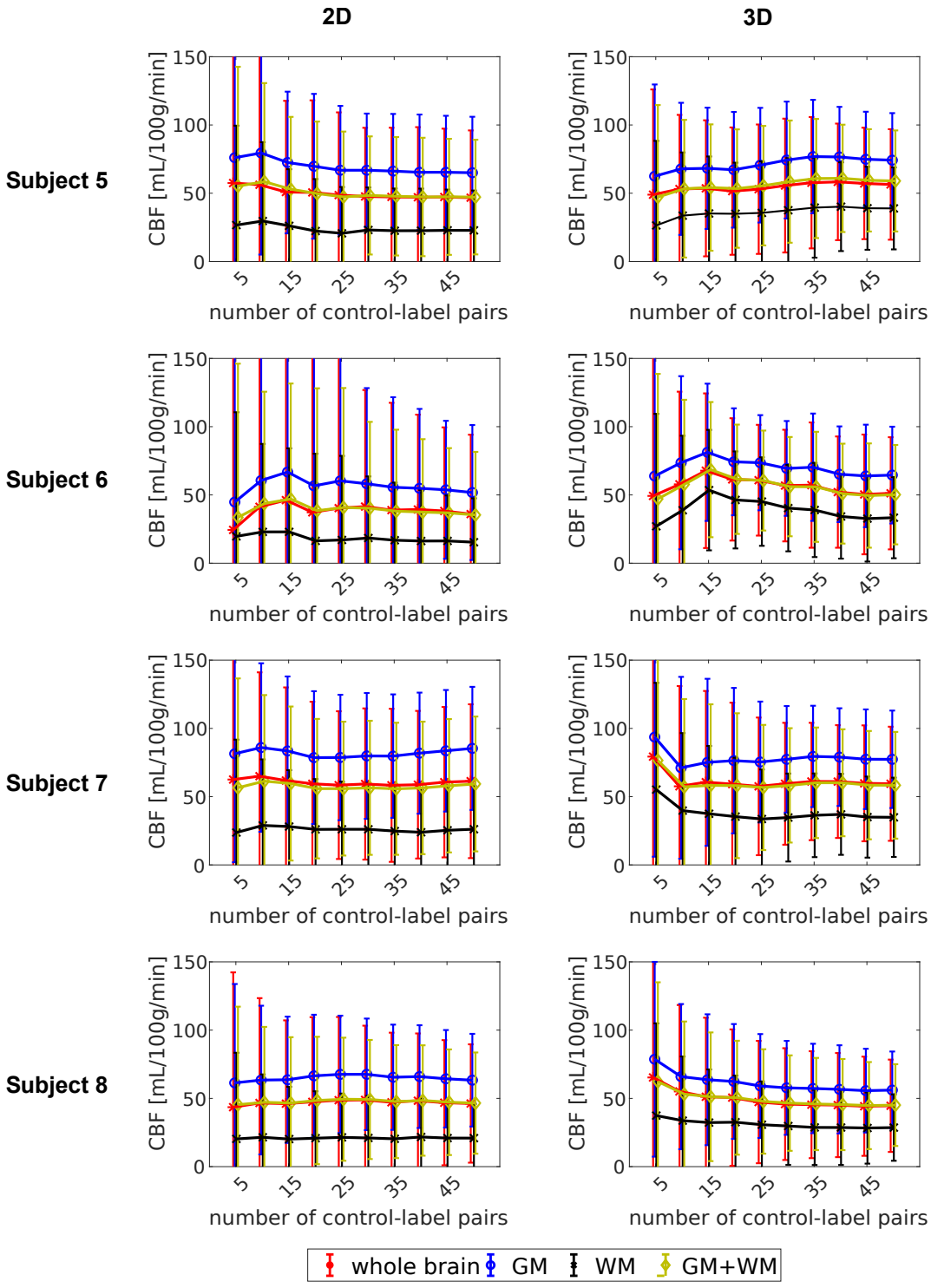

Figure 4.28: **CBF versus number of control-label pairs** for 2D and 3D data sets of subjects 5-8 of Cohort 1 (scenario I). Individual data points indicate mean CBF values averaged over the whole brain, GM, WM, and GM+WM and corresponding standard deviations are indicated by the error bars.

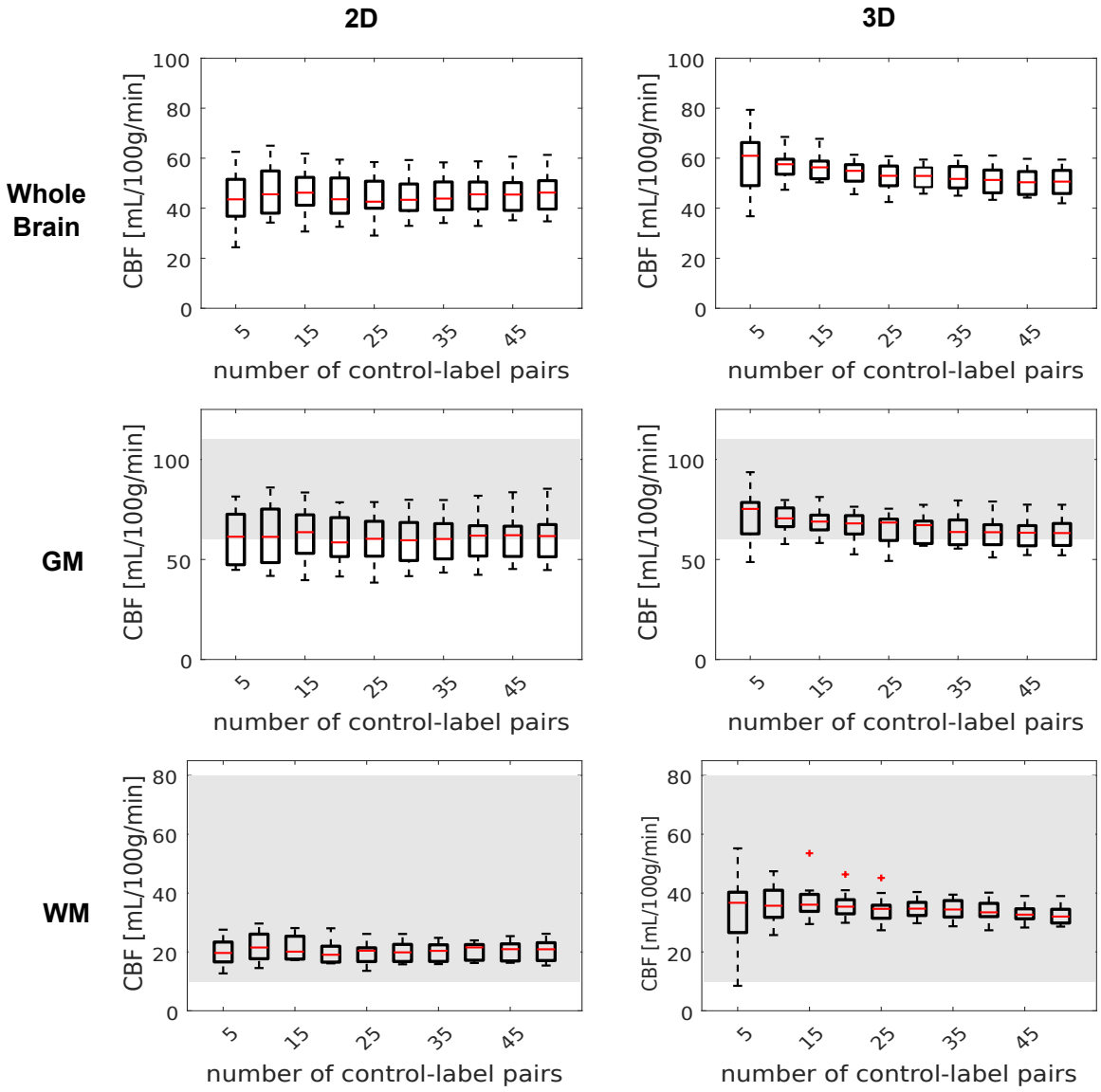

Figure 4.29: **Boxplots of group mean CBF versus number of control label-pairs for all data sets of Cohort 1 (scenario I).** The red line in each boxplot shows the median of the distribution of mean CBF across all data sets considered. The top and bottom part of each boxplot represent the 25^{th} and 75^{th} percentiles. The boxplots' whiskers extend to the highest and lowest data points not considered as outliers. Outliers are indicated as red +. The gray patches indicate the literature range of CBF values for GM and WM of healthy subjects [*Deibler et al.*, 2008; *van Gelderen et al.*, 2008].

4.1.9 Comparison of 2D and 3D readout - Cohort 1 data

A comparison between 2D and 3D EPI readout can be made by analysing the group mean CBF distributions shown in Figure 4.29. The first thing to notice, is the overall higher mean CBF values obtained with the 3D readout. Furthermore, the inter-subject variation (boxplot whiskers) is smaller with the 3D readout than with the 2D readout. Interestingly, the inter-subject variation decreases substantially between 5 and 10 control-label pairs for the 3D data sets, whereas for the 2D data sets, the inter-subject variation only decreases slightly with increasing number of control-label pairs. Subject rankings are not identical between 2D and 3D acquisitions as can be seen by comparing identical scenarios in Figures 4.8 and 4.10.

4.1.10 Comparison of patients to healthy volunteers

A single slice of the anatomical image and perfusion maps obtained for GM and WM for two patients and two healthy volunteers are shown in Figures 4.30 and 4.31, respectively. From these examples, three main observations can be made. The first observation is the lower signal intensity of the CBF maps in the patient measurements compared to healthy volunteer measurements. This difference is due to the difference in number of channels in the receive coil used for acquiring the data, only 12 for the patient data versus 32 for the healthy volunteer data. The second observation concerns the distribution of perfusion values across the brain. On the anatomical image, both patients present a pathology with abnormal signal intensity compared to surrounding tissue and to the contralateral side (same area in the other brain hemisphere). Around this area, the perfusion maps show a decrease in perfusion compared to the contralateral side. This asymmetry of the perfusion map is not observed in the healthy subjects. The third observation concerns the performance of the automated segmentation. Looking at the tissue-specific perfusion maps of the patients, a mismatch can be seen where areas corresponding to WM are classed as GM by the segmentation and vice-versa. This can be explained by the intensity-based nature of the segmentation procedure, which is confounded by the abnormal signal intensities occurring due to the present pathology.

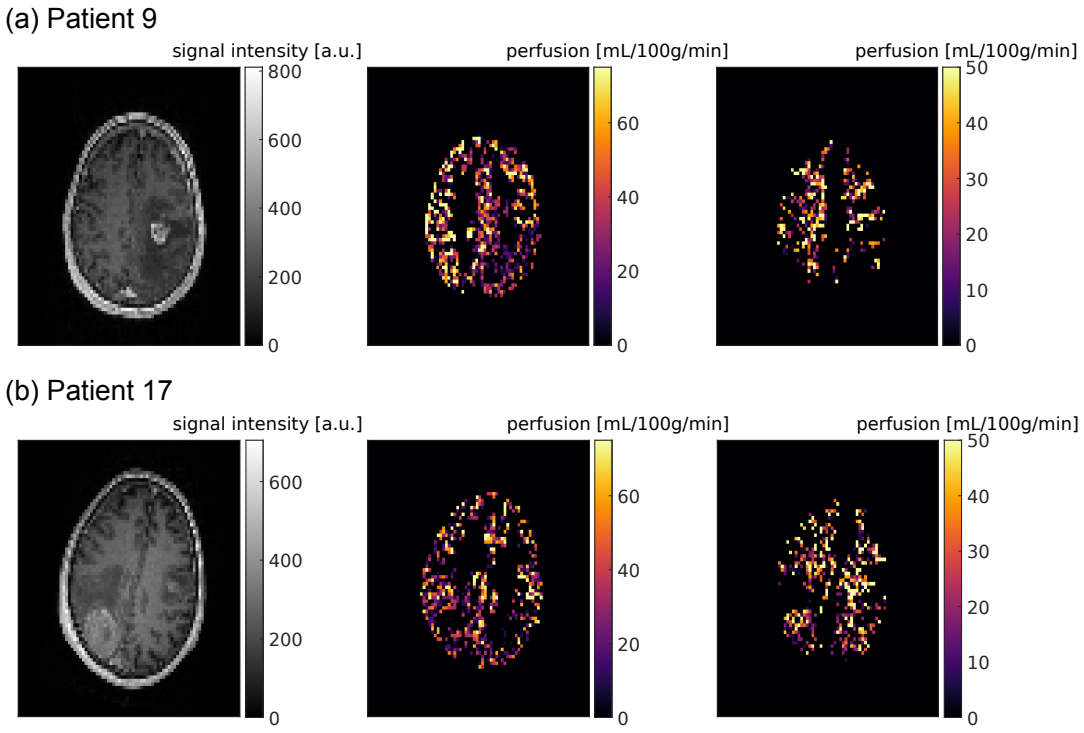

Figure 4.30: **Single slice of anatomical image** (left) **and perfusion map for GM** (middle) **and WM** (right) of patients 9 and 17. Images are shown in the ASL space.

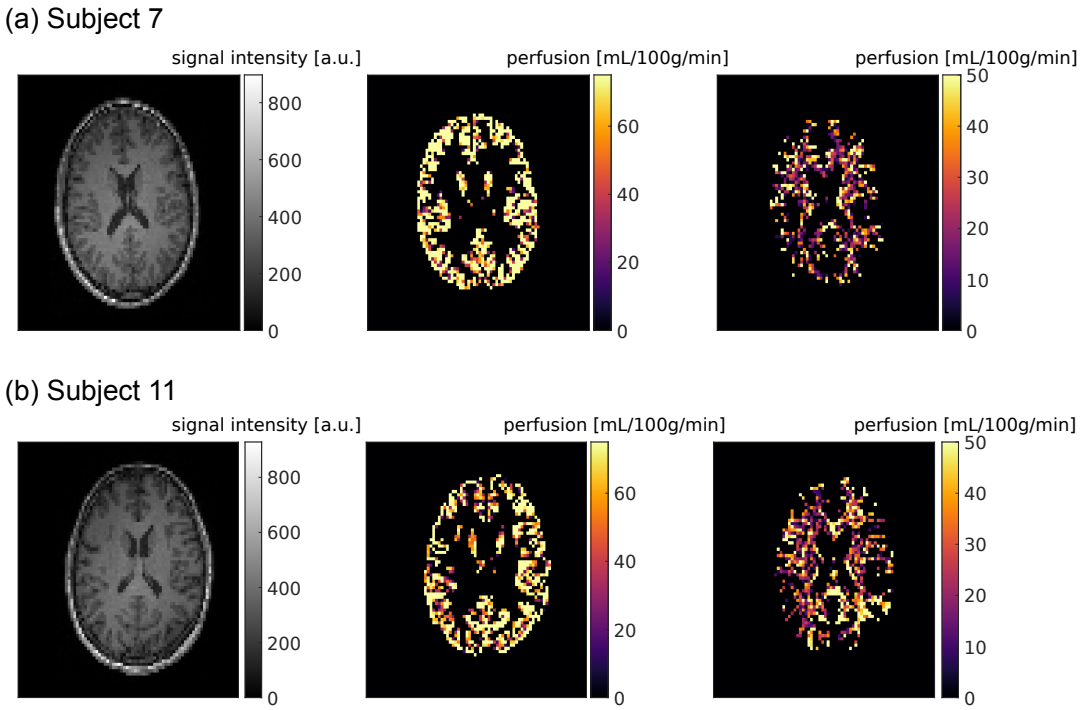

Figure 4.31: **Single slice of anatomical image** (left) **and perfusion map for GM** (middle) **and WM** (right) of subjects 7 and 11 from Cohort 1 obtained for the 2D data sets. Images are shown in the ASL space.

4.2 Kidney - Synthetic data

4.2.1 Data evaluation

The M0, first control and first labelled images of synthetic single-slice PASL and PCASL data sets are shown in Figure 4.32. The time course of the perfusion-weighted (ΔM) signal in cortex and in medulla for PASL and PCASL data sets are shown in Figure 4.33.

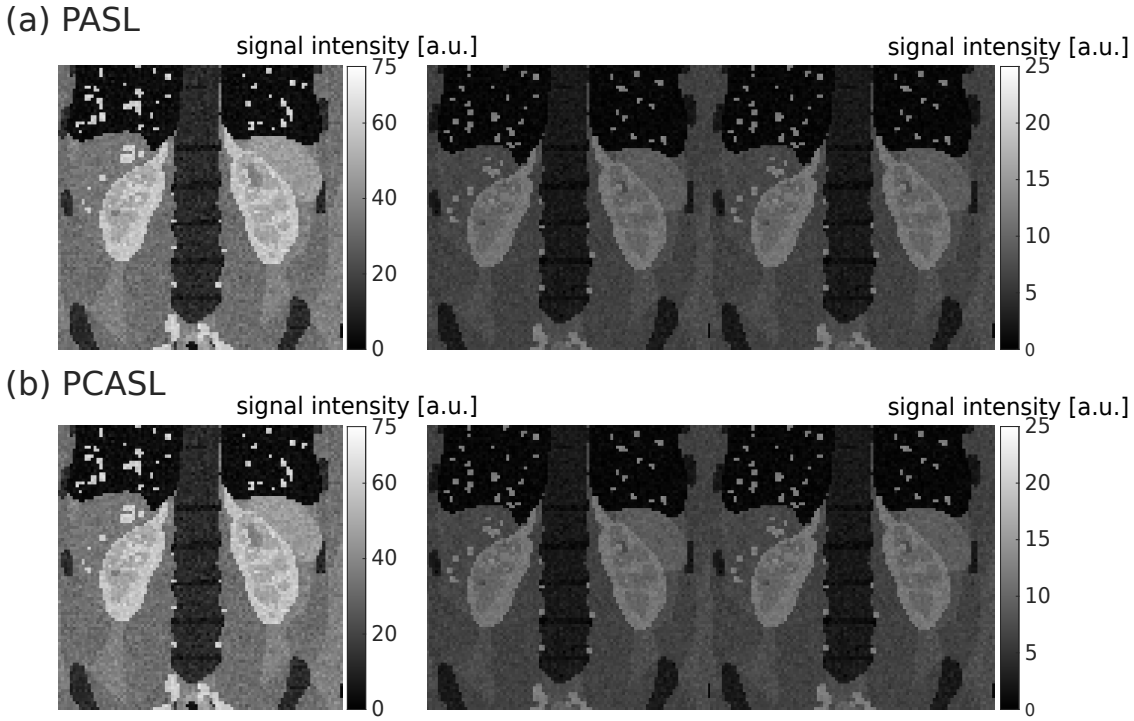

Figure 4.32: **Exemplary PASL (a) and PCASL (b) single-slice data sets** (model 77). Left column: M0 images; middle column: first control images; right column: first labelled images. The signal intensity of control and labelled images is lower than that of the M0 due to background suppression.

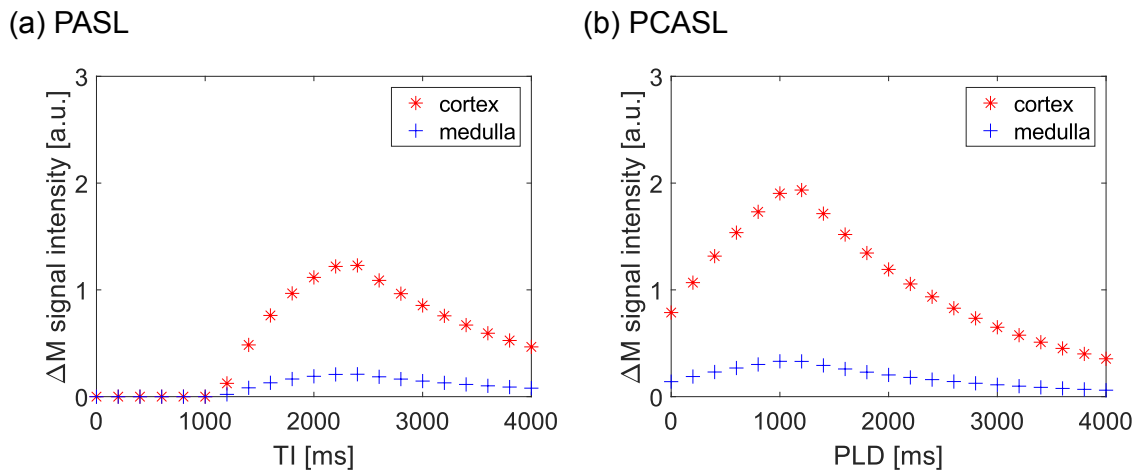

Figure 4.33: **Time course of the perfusion-weighted (ΔM) signal** in cortex and in medulla for the PASL (a) and PCASL (b) data sets of model 77.

4.2.2 Pipeline evaluation

4.2.2.1 Registration

As expected, the registration step has no effect on the images in the absence of respiratory motion. Horizontal and vertical line profiles for both right and left kidneys of a synthetic ASL data set with respiratory motion are shown in Figure 4.34(a). Some movement is visible between subsequent ASL images in both horizontal and vertical direction before registration. The movement is noticeably reduced after the registration as indicated by the smoother line profiles and the less abrupt changes in signal intensity. Quantitative evaluation of the registration for all available healthy data sets with respiratory motion is shown in Figure 4.34(b) in terms of MSSIM distributions before and after registration. For each model, the MSSIMs increase after registration, indicating that the resemblance between all images compared increases with the registration. Before registration, mean and standard deviation of MSSIMs across all healthy data sets with respiratory motion are 0.4 ± 0.2 and 0.4 ± 0.1 for PASL and PCASL, respectively. After registration, mean and standard deviation of MSSIMs across all healthy data sets with respiratory motion are 0.5 ± 0.2 and 0.5 ± 0.1 for PASL and PCASL, respectively. The comparison includes the comparison of identical images, which explains the MSSIM outliers equal to 1 in each distribution. The lowest MSSIMs are obtained for comparisons between M0 and all control or labelled images as M0 differs from all other ASL images in terms of intensity due to the assumed background suppression. As expected, the MSSIM values differ little between PASL and PCASL data sets. Across all models, no difference in MSSIM distributions can be observed between left and right kidney (0.4 ± 0.2 before registration and 0.5 ± 0.1 after registration for both).

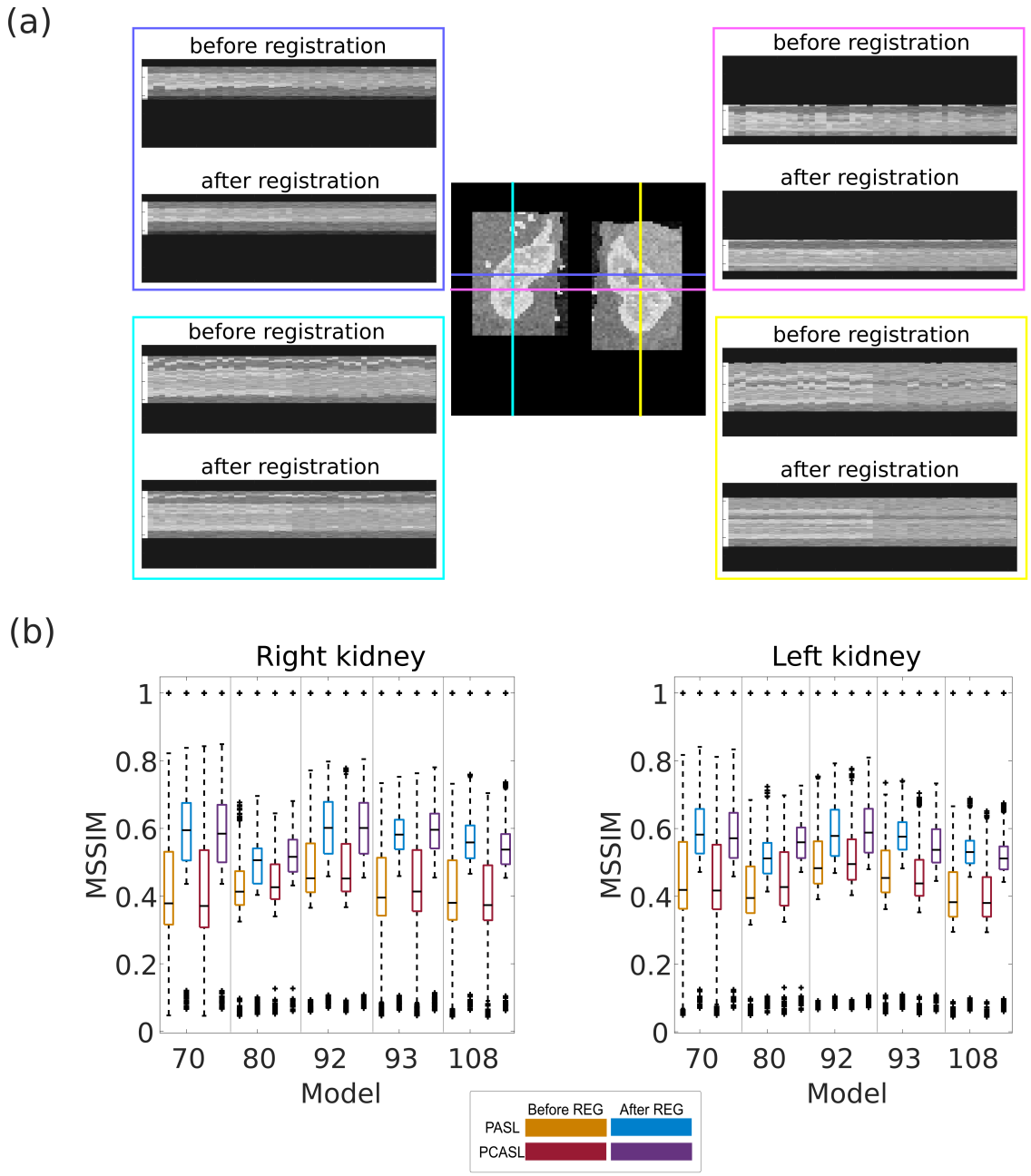

Figure 4.34: **Registration evaluation.** (a) Line profiles across all ASL images before and after registration (model 93, PASL). (b) MSSIMs calculated before and after registration for all possible image pairs within each healthy data set with respiratory motion. The black line in each boxplot shows the median of the distribution of mean perfusion across all models. The top and bottom part of each boxplot represent the 25th and 75th percentiles. The boxplots' whiskers extend to the highest and lowest data points not considered as outliers. Outliers are shown as black '+'.

4.2.2.2 Quantification

Perfusion maps obtained for the healthy and abnormal PCASL data sets from model 92 are shown in Figure 4.35(a). The decreased perfusion in the right kidney of the abnormal

data set is well distinguishable from the normal perfusion. The distributions of perfusion values in each data set for whole kidney, cortex and medulla are shown in Figure 4.35(b). A clear difference between both data sets is visible for the right kidney with mean perfusion and standard deviation of 220±40 mL/100g/min and 90±30 mL/100g/min for the cortex and 50 ± 50 mL/100g/min and 10 ± 30 mL/100g/min for the medulla for healthy and abnormal data sets, respectively. At the same time, both data sets present very similar perfusion distributions for the left kidney with mean and standard deviation of 210 +/- 50 mL/100g/min for the cortex and 30 +/- 50 mL/100g/min for the medulla. This indicates a good reproducibility of the generation of synthetic ASL data as well as the quantification step of the processing pipeline.

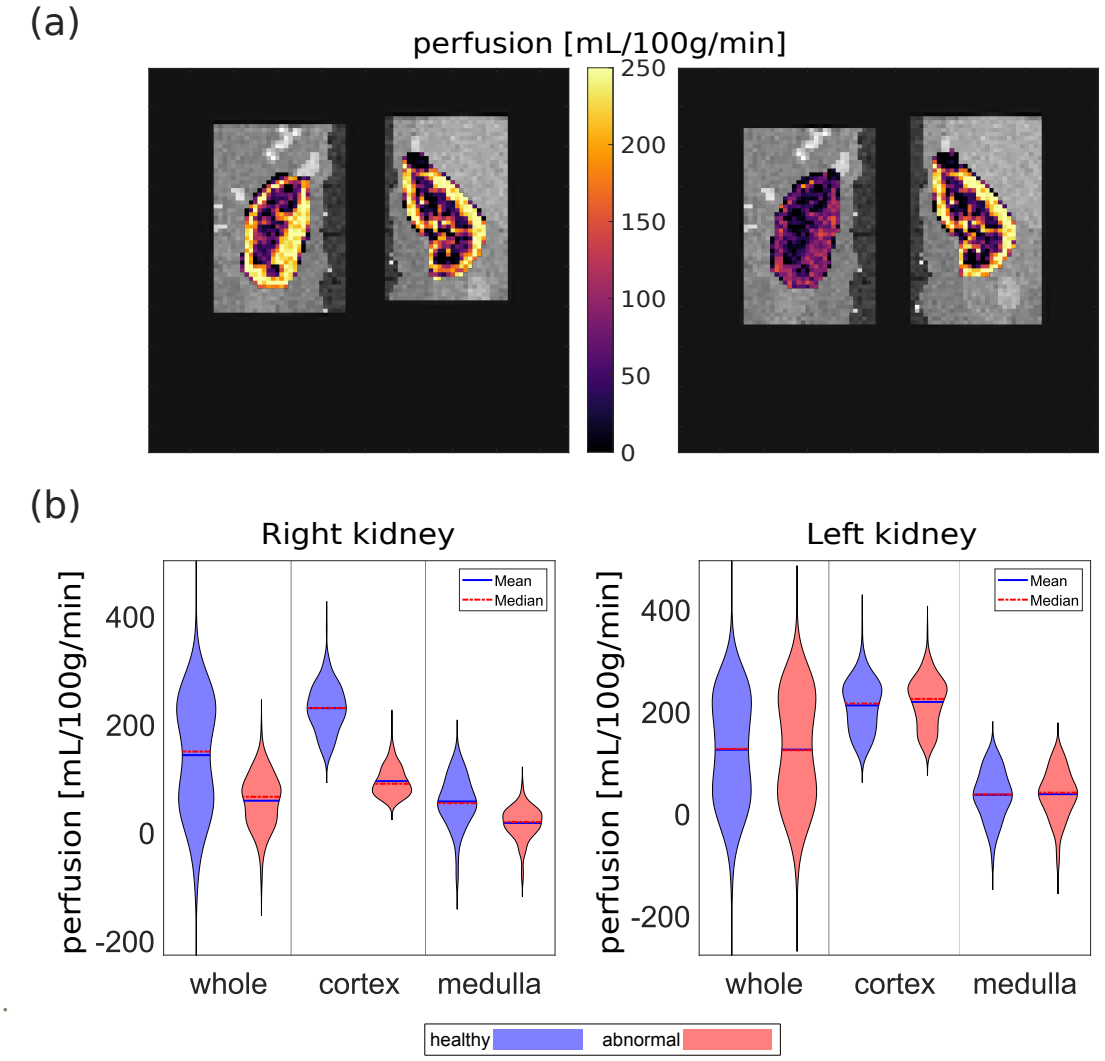

Figure 4.35: **Healthy versus abnormal perfusion** (a) M0 image cropped to rectangles used for separate left and right registration with overlaid perfusion map obtained for the healthy (left) and abnormal (right) PCASL data sets of model 92. (b) Distributions of perfusion values for both data sets.

Looking at all the data sets with healthy perfusion (Figure 4.36), a narrow interquartile range of mean perfusion can be observed for whole kidney, cortex, and medulla for both left and right kidneys and for both labelling strategies. For the whole kidney, mean and standard deviation of renal perfusion across all healthy data sets with respiratory motion are 150±40 mL/100g/min and 130±10 mL/100g/min for PASL and PCASL, respectively. For the cortex, mean and standard deviation of renal perfusion across all healthy data sets with respiratory motion are 240 ± 40 mL/100g/min and 210 ± 20 mL/100g/min for PASL and PCASL, respectively. For the medulla, mean and standard deviation of renal perfusion across all healthy data sets with respiratory motion are 50 ± 20 mL/100g/min and 49 ± 8 mL/100g/min for PASL and PCASL, respectively. This corresponds well to the perfusion values originally assumed to generate the synthetic data (250 mL/100g/min and 50 mL/100g/min for the cortex and medulla, respectively).

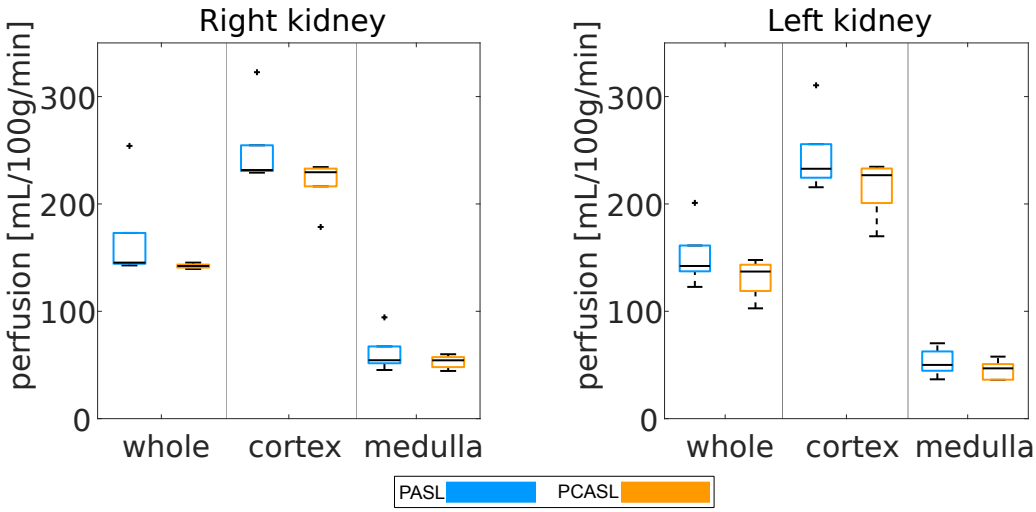

Figure 4.36: **Mean renal perfusion averaged over the whole kidney, the cortex, and the medulla** for all healthy data sets with respiratory motion. The black line in each boxplot shows the median of the distribution of mean perfusion across all models. The top and bottom part of each boxplot represent the 25^{th} and 75^{th} percentiles. The boxplots' whiskers extend to the highest and lowest data points not considered as outliers. Outliers are shown as black '+'.

4.2.2.3 Segmentation

A comparison of segmentation masks obtained for one of the data sets is shown in Figure 4.37(a). The segmentation masks for whole kidney, cortex and medulla obtained from the processing pipeline match the XCAT segmentation masks well. Dice index distributions across all models for PASL and PCASL data sets can be found in Figure 4.37(b). Very good agreement between segmentations is found for whole kidney and cortex, with Dice indices ranging from 0.80 to 0.93 and from 0.79 to 0.89, respectively. Differences between

medulla masks are larger but still reasonably good, with Dice indices ranging from 0.64 to 0.84.

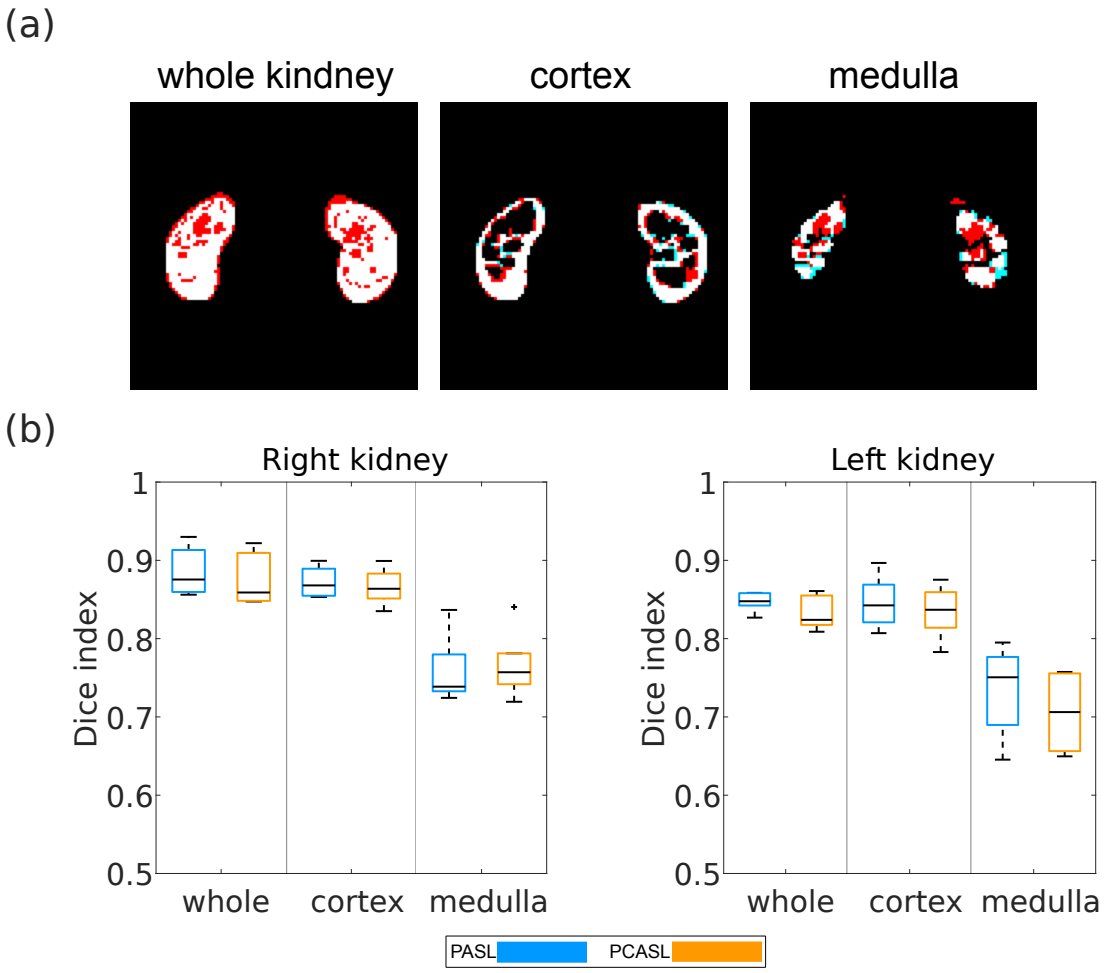

Figure 4.37: **Segmentation evaluation.** (a) Comparison of segmentation masks of the PCASL data set of model 108 obtained from the processing pipeline (red) and the XCAT phantom (cyan). White areas correspond to pixels present in both masks being compared. (b) Boxplots of Dice indices calculated for the 5 models for the PASL and PCAL data sets for whole kidney, cortex, and medulla. The black line in each boxplot shows the median of the distribution of mean Dice index across all models. The top and bottom part of each boxplot represent the 25^{th} and 75^{th} percentiles. The boxplots' whiskers extend to the highest and lowest data points not considered as outliers. Outliers are shown as black '+'.

4.3 Kidney - In vivo study

4.3.1 Effect of registration

Registration of all data sets was first visually checked for remaining displacement and distortions present after each registration option. These qualitative results for all subjects and the four measurements are shown in Figure 4.38. The bad registration result obtained

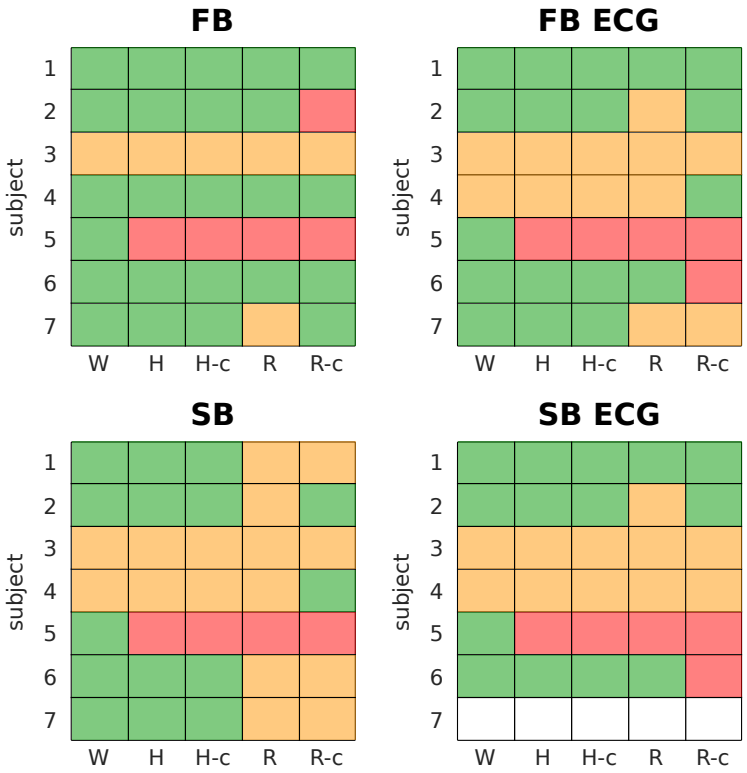

Figure 4.38: **Registration distortions.** Green indicates a good registration for both kidneys. Yellow indicates some movement or small distortion is present after registration on either left or right kidney or both. Red indicates a severe distortion on either left or right kidney or both. No SB ECG measurement was obtained for subject 7 due to poor signal from the ECG electrodes.

for subject 3 can be attributed to poor SNR present in all measurements. For subject 4, the SNR of the first measurement (FB) was visibly better than that of the three subsequent measurements (FB ECG, SB, SB ECG). This explains the poor performance of the registration on all measurements except FB for subject 4. Interestingly, the registration option R-c is successful despite poor SNR for two out of three measurements (FB ECG, SB) for subject 4. All measurements of subject 5 contained an artefact of unclear origin (bright spot) above the right kidney in all control and labelled images, which was not visible on the M0 images. Reducing the image in any manner resulted in a bad registration of the M0 image with severe distortion of the right kidney. The registration considering the whole image (W) had, however, no problem with this artefact. Overall, registration option R has the lowest percentage of successful registration (48%) and registration option W has the highest (87%). The percentage of successful registration is 79%, 79%, and 70%

for H, H-c, and R-c, respectively.

Considering only the kidneys with good registration, quantitative results in terms of MSSIMs and ECCs calculated before and after registration for the different registration options are shown in Figure 4.39 and 4.40, respectively. In each case, MSSIMs and ECCs are significantly higher after registration than before (Wilcoxon signed-rank test with $p<0.05$). MSSIMs and ECCs are lowest for the registration options R and R-c. Highest MSSIMs and ECCs were obtained with the registration option H for all measurements. Overall, the increases of mean MSSIMs and mean ECCs from before to after registration are small. The increase of mean MSSIMs from before to after registration is largest with the registration option R for FB (0.099), SB (0.092), SB ECG (0.10), and with R-c for FB ECG (0.086). This increase is smallest with the registration option H-c for FB (0.016), Sb (0.062), and SB ECG (0.048), and with the registration option R for FB ECG (0.054). The increase of mean ECCs from before to after registration is largest with the registration

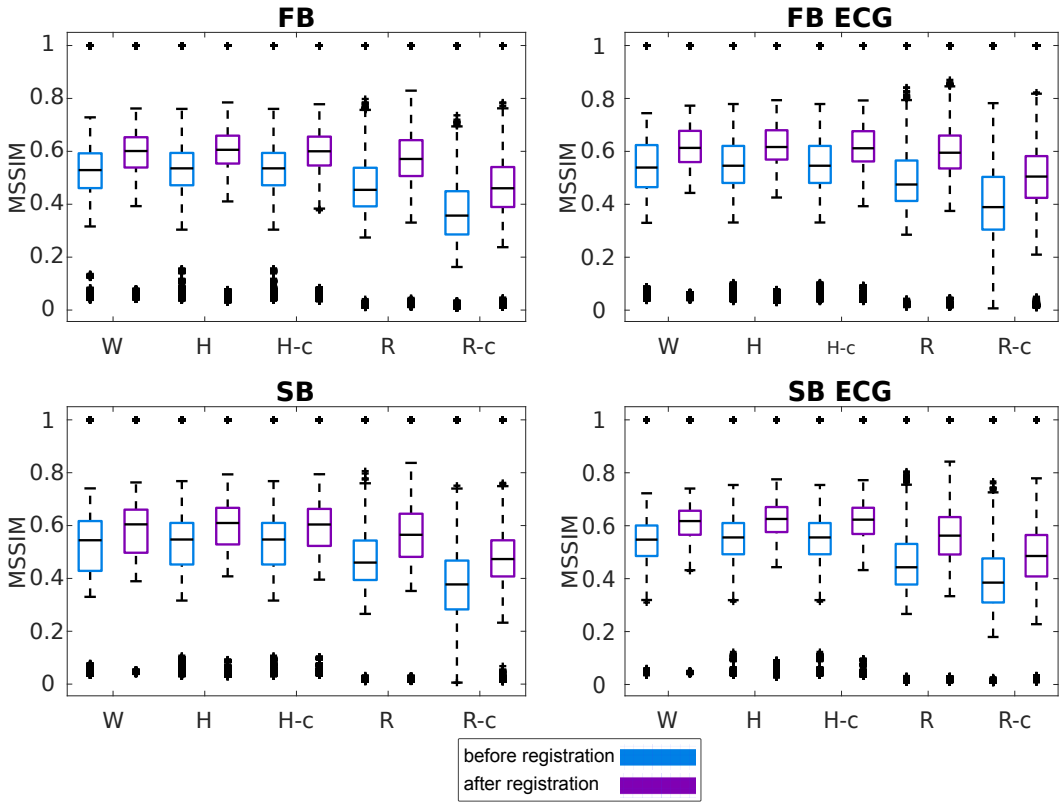

Figure 4.39: **Boxplots of MSSIM** calculated before and after registration for all registration options considering only the kidneys with successful registration. The black line in each boxplot shows the median of the distribution of MSSIMs. The top and bottom part of each boxplot represent the 25^{th} and 75^{th} percentiles. The boxplots' whiskers extend to the highest and lowest data points not considered as outliers. Outliers are shown as black '+'. All MSSIM distributions were found to be statistically different after registration compared to before for each registration option (Wilcoxon signed-rank test, $p<0.05$).

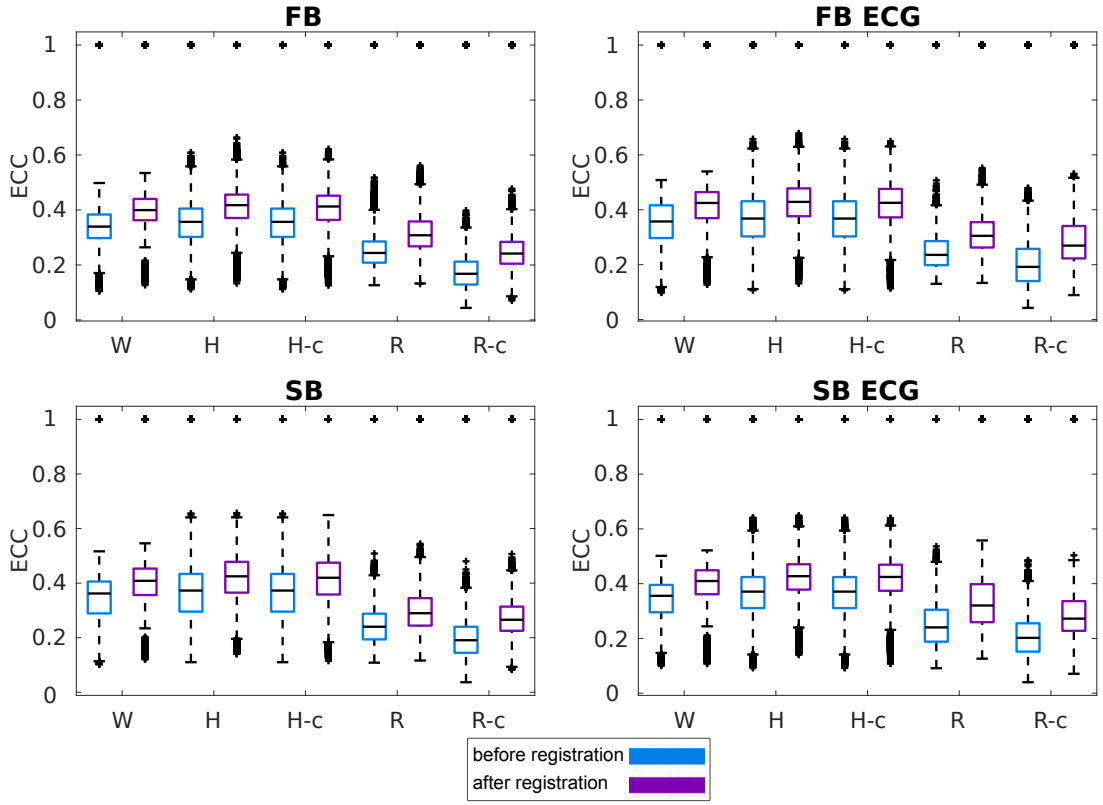

Figure 4.40: **Boxplots of ECC** calculated for before and after registration for all registration options considering only the kidneys with successful registration. The black line in each boxplot shows the median of the distribution of ECCs. The top and bottom part of each boxplot represent the 25^{th} and 75^{th} percentiles. The boxplots' whiskers extend to the highest and lowest data points not considered as outliers. Outliers are shown as black '+'. All ECC distributions were found to be statistically different after registration compared to before for each registration option (Wilcoxon signed-rank test, $p<0.05$).

option H for FB (0.093), with R-c for FB ECG (0.074) and SB (0.076), and with R for SB ECG (0.078). This increase is always smallest with the registration option H-c.

The distribution of registration duration measured across all subjects and measurements for the five registration options is shown in figure 4.41. As expected, option W requires the least amount of time (31 ± 4 minutes). The H-c option requires the most time with 73 ± 1 minutes and the other three options require about 60 minutes (H - 60 ± 3 minutes; R - 58 ± 2 minutes; R-c - 55 ± 11 minutes).

The registration option W neither achieves the highest nor the lowest increase in MSSIMs or ECCs from before to after registration. However, considering the registration success rate and the duration, the registration option W stands out as the best suited one.

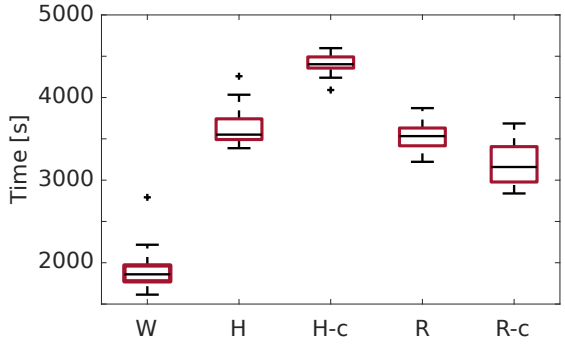

Figure 4.41: **Registration duration** measured for all registration options considering all subjects and measurements together. The black line in each boxplot shows the median of the distribution of registration duration. The top and bottom part of each boxplot represent the 25^{th} and 75^{th} percentiles. The boxplots' whiskers extend to the highest and lowest data points not considered as outliers. Outliers are shown as black '+'.

4.3.2 Influence of cardiac cycle and respiration strategy

Based on the results of section 4.3.1, the registration considering the entire image was chosen and only the data sets with good registration were considered for evaluating the influence of cardiac cycle and respiration strategy on ASL-based renal perfusion quantification.

While non ECG triggered acquisitions took 4 minutes and 27 seconds, ECG triggering resulted in acquisitions of up to 6 minutes 57 seconds and was not possible for one of the measurements (subject 7 SB ECG) as the detected electrode signal was too low.

RBF maps obtained for one representative subject for each measurement are shown in Figure 4.42. Mean perfusion values calculated for whole kidney, cortex, and medulla for all subjects and each measurement are shown in Figure 4.43. Mean and standard deviation of perfusion in whole kidney, cortex, and medulla averaged over all kidneys with good registration for each measurement type are listed in Table 4.5. Differences in perfusion are noticeable between the four measurements when considering only a single subject but when considering all subjects, the distributions of mean perfusion are similar. Only the distribution of mean perfusion for the whole left kidney obtained with the SB measurement was found to be significantly different from the FB results (t-test, $p<0.05$).

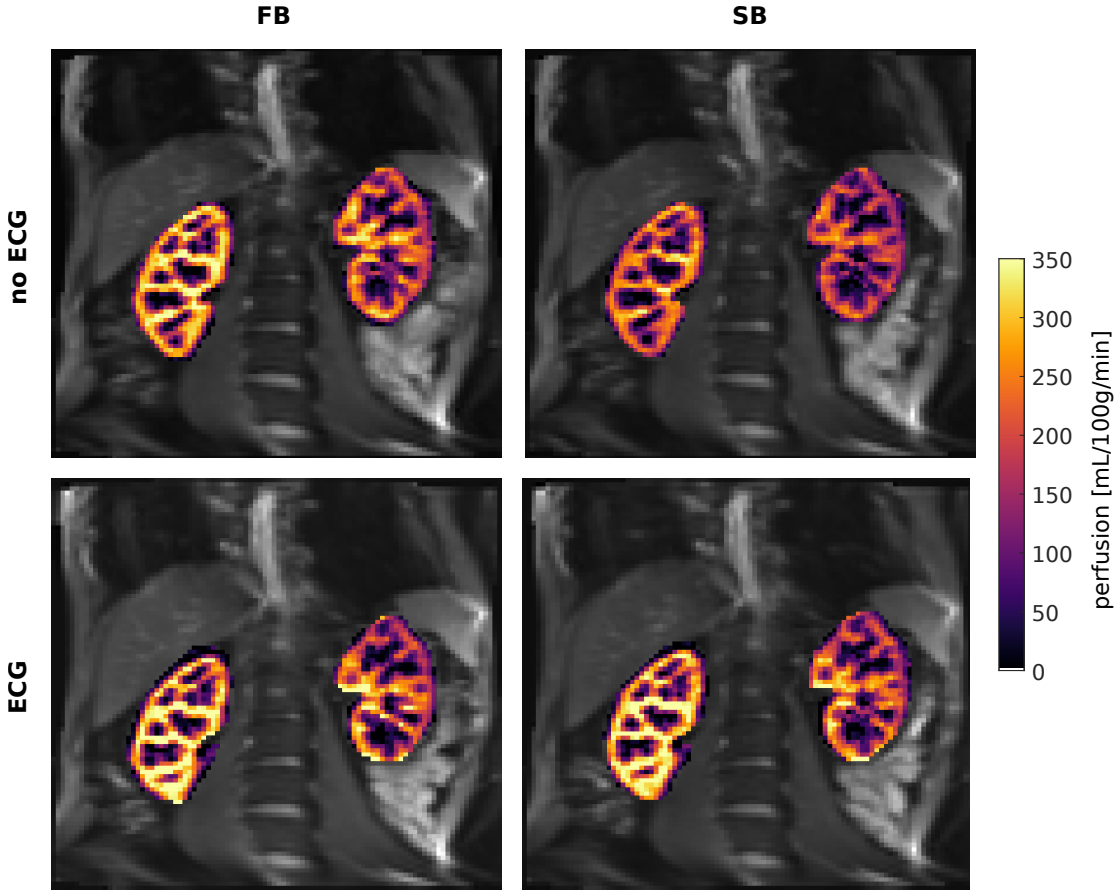

Figure 4.42: **RBF maps** for subject 2 for each measurement.

Table 4.5: **Mean and standard deviation of perfusion** in whole kidney, cortex, and medulla averaged over all kidneys with good registration for each measurement type.

	FB	FB ECG	SB	SB ECG
whole kidney [mL/100g/min]	121 ± 35	118 ± 41	109 ± 42	128 ± 39
cortex [mL/100g/min]	158 ± 62	162 ± 75	148 ± 72	173 ± 68
medulla [mL/100g/min]	31 ± 26	37 ± 33	31 ± 24	39 ± 28

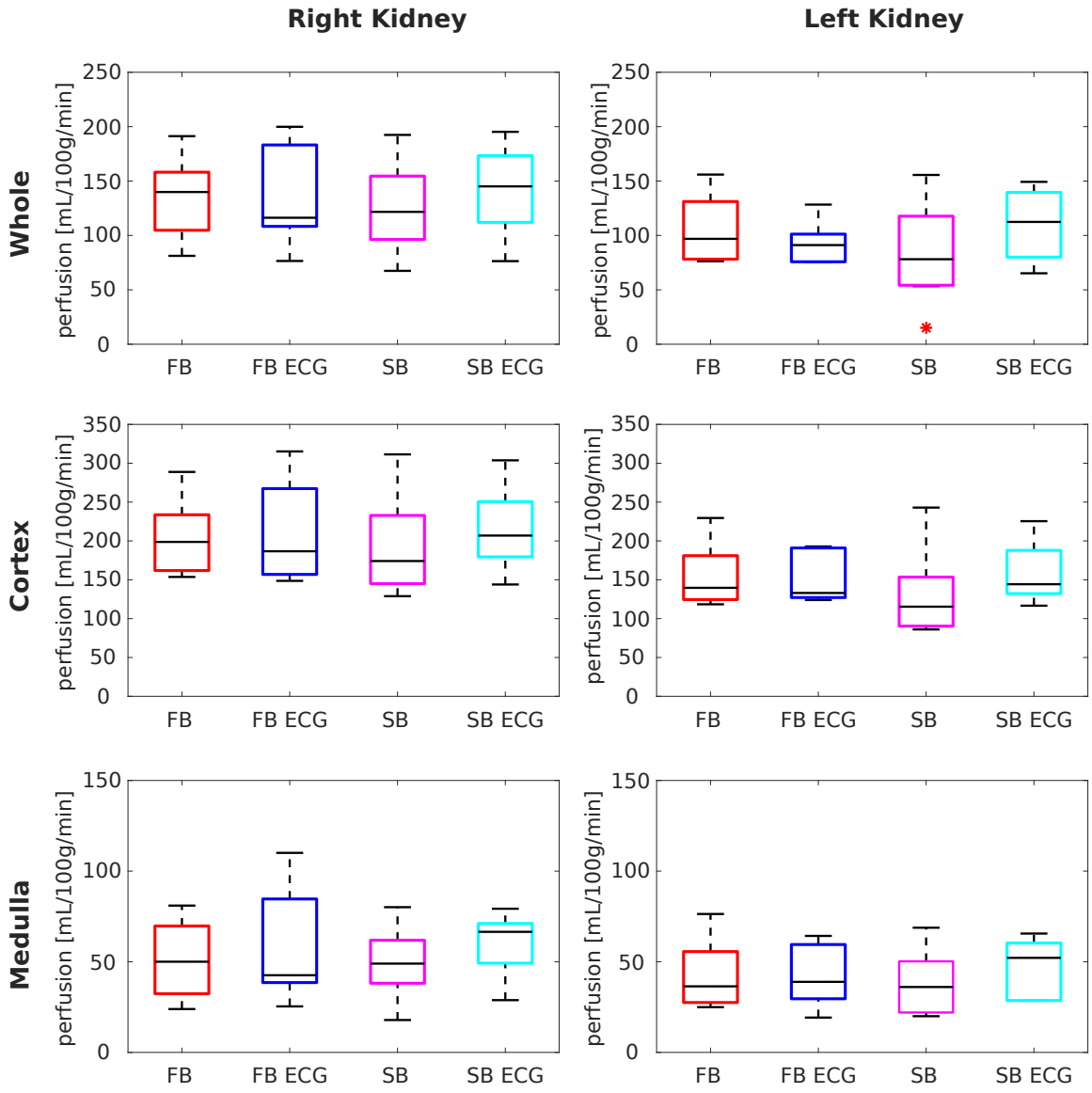

Figure 4.43: **Mean perfusion distributions** for all subjects and each measurement. The black line in each boxplot shows the median of the distributions. The top and bottom part of each boxplot represent the 25^{th} and 75^{th} percentiles. The boxplots' whiskers extend to the highest and lowest data points not considered as outliers. No outliers are present in any of the distributions. Only the distribution of mean RBF obtained with the SB measurement for the whole left kidney was found to be significantly different from the FB results (t-test, $p<0.05$).

The temporal SNR (tSNR) of the perfusion-weighted signal calculated for all subjects for each measurement is shown in Figure 4.44. Mean and standard deviation of tSNR across all subjects were 0.9 ± 0.2 for FB, 0.9 ± 0.2 for FB ECG, 0.8 ± 0.3 for SB, and 0.9 ± 0.2 for SB ECG. Results of the t-test showed no statistically significant difference between tSNR distributions of the four measurement types ($p<0.05$).

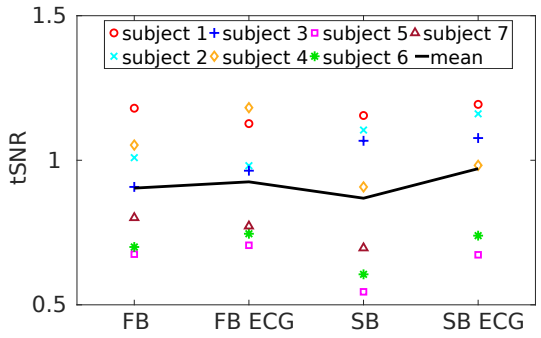

Figure 4.44: **Temporal SNR** of the perfusion-weighted signal calculated for all subjects for each measurement. No statistically significant difference in tSNR is present (t-test, $p<0.05$).

The effect of the trigger delay used for ECG triggering on the perfusion quantification is shown in Figure 4.45 for two subjects. The subject's heart rate was 72 beats per minute and 63 beats per minute, and their interval between subsequent R-wave peaks were 835 ± 5 ms and 962 ± 32 ms, for subject 1 and subject 6 respectively. Each subject demonstrates an individual evolution of the perfusion with increasing trigger delay. For both subjects, this evolution is however similar for both left and right kidneys and for whole kidney, cortex, and medulla. For subject 1, the highest perfusion is obtained for a trigger delay of 300 ms for whole kidney and cortex, and 200 for the medulla. In contrast, subject 6 has a drop in perfusion at a trigger delay of 400 ms.

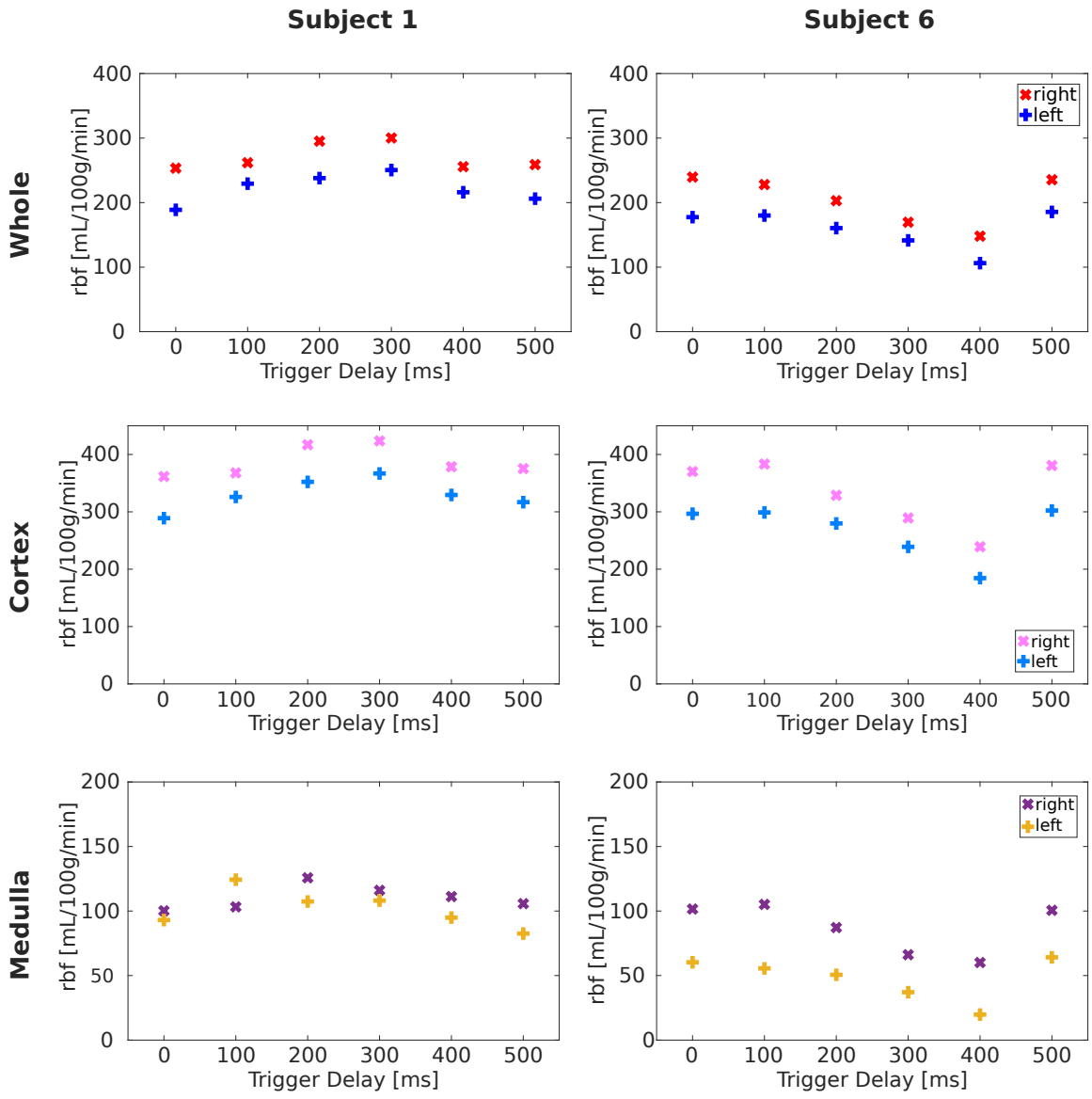

Figure 4.45: **RBF versus trigger delay** for two subjects (columns) and whole kidney, cortex, and medulla (rows).

CHAPTER 5

Discussion

The findings of the three projects of this thesis are discussed in this chapter. First, the comparison of processing options for brain ASL data is addressed. Second, the generation of synthetic ASL data of the kidneys and evaluation of the in-house developed processing pipeline are discussed. Third, the evaluation of the influence of cardiac triggering and respiration strategy on ASL-based renal perfusion quantification is considered. Parts of this chapter have been published in [*Brumer et al.*, 2022a][1] and the corresponding discussion is partly replicated here.

5.1 Brain

A total of 42 data sets from the ASL challenge and from healthy volunteers acquired with different sequences and ASL parameters were analysed. Different methods to calculate the perfusion-weighted image, to remove outliers, to correct the M0 image, to smooth the M0 image, and to obtain segmentation masks that were implemented in the in-house developed processing pipeline presented in section 3.2 were used. The aim of this project was to assess differences in CBF quantification and in perfusion map SNR arising from processing options and acquisition parameters.

[1] CC BY License

5.1.1 Effect of mean perfusion-weighted image calculation method

The calculation of the mean perfusion-weighted image is central for blood flow quantification based on ASL MRI. The analyses effectuated in this work show that the order of subtraction and averaging of the individual control and labelled images (SA or AS) does not yield any significant difference in CBF. Furthermore, no absolute value of signal difference should be taken as this results in erroneous perfusion values. Subtraction and averaging are two linear operations and therefore changing the order in which these operations are performed should not affect the final mean perfusion results. This is true for all synthetic data sets but not for the population-averaged data, for which higher mean CBF values were obtained with the AS method. This difference might indicate the limitations of synthetically generated data: it is difficult to reproduce in vivo acquired data with perfect accuracy. When looking at the available brain ASL literature, all above considered methods are used and often it is unclear how the perfusion-weighted image was calculated exactly, especially in more clinical publications.

5.1.2 Effect of outlier removal

Seven outlier removal options based on volume or slice rejection were compared in terms of CBF and SNR distributions. No statistically significant differences between CBF distributions obtained with different outlier removal options was observed for the data sets from the ASL challenge and the SNR was found to be significantly decreased when using the AOC (scenario IX) and pAOCSL (scenario X) options. For the data sets from Cohort 1 and Cohort 2, CBF and SNR distributions seem similar but are significantly different in some cases. AOC always yielded a larger inter-subject variation and resulted in the lowest SNR for most subjects. Across all considered cohorts, only the SA mean $\pm$ two standard deviation option (scenario V) yielded no statistically significant difference to no outlier removal (scenario I). The difference between results obtained with the ASL challenge data sets and the in vivo acquired data, highlights an important reality: synthetic data and digital reference objects (DROs) are of great value but the transfer of findings based on DROs to actual data is limited and further investigation is warranted to understand the origin of the observed differences. In this case, difference may originate from differences in the employed readout and ASL parameters for the population-averaged data set.

Previous ASL publications focusing on outlier removal options assess the quality of outlier removal options in terms of SNR, reproducibility, and differentiability of CBF maps. *Tan et al.* (2009) introduced the z-score based filtering approach on a volume-by-volume

and a slice-by-slice basis (scenarios VII and VIII, respectively). They demonstrated that these filters allowed the reduction or even removal of ring, CSF shine-through, and edge artefacts. In many cases where perfusion maps were found to be useless when using all acquired data, it was possible to produce diagnostically valuable perfusion maps after outlier removal. Nevertheless, some of the observers (three neuroradiologists and a physician) preferred the unfiltered images presenting a slightly higher SNR to the filtered images, highlighting the importance of image evaluation by specialised diagnosticians. *Maumet et al.* (2014) applied a Huber's M-estimator for voxel-by-voxel outlier removal using simulated and real data. They demonstrated that both their method and the z-score method yielded more robust CBF maps, with a clear superiority of their method for the simulated data. *Fazlollahi et al.* (2015) compared the z-score method [*Tan et al.*, 2009] to the Huber's M-estimator method [*Maumet et al.*, 2014] and to a generalised linear model (GLM) approach [*Wang*, 2012]. They observed an improvement in CBF reliability for all outlier removal options they considered. The generalised linear model approach yielded the largest improvement in CBF and was the only one resulting in an increased tSNR. *Wang et al.* (2013) first introduced the adaptive outlier cleaning (AOC) algorithm (scenario IX), which uses Pearson correlation coefficients between individual CBF maps and the mean CBF map and removes volumes with smallest correlation. However, their study focused on multi-site CBF evaluation in cognitively normal adults and adults with mild Alzheimer's disease and did not explicitly evaluate or discuss the effect of outlier removal. *Dolui et al.* (2017) introduced the SCORE algorithm (scnario XI), which makes an opposite assumption than the AOC algorithm and removes CBF volumes with highest correlation to the mean CBF. They compared SCORE to volume-based z-score [*Tan et al.*, 2009], Huber's M-estimator [*Maumet et al.*, 2014], GLM [*Wang*, 2012] and AOC [*Wang et al.*, 2003] methods. They found SCORE to outperform all other methods in terms of reproducibility in healthy subjects and differentiability between healthy and diseased subjects. While all methods were able to differentiate between healthy and diseased subjects, SCORE yielded the lowest standard errors leading to higher statistical power for lower sample sizes. Overall, more volumes were discarded by SCORE than by z-score and AOC. In our much smaller group of data sets, SCORE always removed less volumes than z-score and AOC. The AOC method was later refined by including prior knowledge of the expected perfusion contrast and modifying it to a slice-by-slice method called pAOCSL (scenario X) [*Li et al.*, 2018a]. The work demonstrated that pAOCSL yields significantly higher SNR than AOC and further improves repeatability of CBF quantification. This finding was reproduced in the cohorts considered here, with AOC yielding much lower SNR than pAOCSL for nearly all subjects. In some cases (e.g. Subject 8 from Cohort 2), no outlier was found with the AOC option but some slices were removed by the pAOCSL option, resulting in a decrease in SNR.

Overall, the literature is consistent in recommending the removal of outliers. However, as applying different outlier removal options partly results in significantly different CBF values, it is impossible to determine the best option as long as no CBF ground truth is available. Furthermore, a detailed evaluation of the effect of outlier removal on patient data is warranted to ensure real perfusion abnormality remain after outlier removal.

5.1.3 Effect of M0 corrections

The individual and combined effect of T_1, T_2 or T_2^*, λ corrections applied to the M0 image in comparison to no correction was assessed in terms of CBF and SNR. Overall, the T_1 correction had the smallest effect of all individual corrections on CBF. This is not surprising as all data sets were acquired or generated with a TR longer or equal to 5 seconds, which allows for sufficient relaxation of the labelled spins between each excitation. The T_2 or T_2^* correction lead to an increase of CBF values for all cohorts except the 3D data sets from Cohort 1. Proper T_2^* correction would require dedicated measurements as the apparent relaxation time is dependent on the scanner. This was not done in this work as it would have increased the acquisition time. Instead, the values reported by *Pinto et al.* (2020) were assumed. The λ correction yields an increase of CBF values for GM and a decrease for WM. Combining all corrections resulted in an increase of CBF for the ASL challenge data but a decrease for all other cohorts. This suggests the T_1 correction has most impact on the healthy volunteer data acquired at our institute whereas the other corrections are more important for the challenge data sets. This finding highlights that the effect of different corrections is cohort dependent and might have to be assessed for each imaging centre individually. Differences in SNR are overall small but statistically significant. The highest SNR was achieved with the T_2 or T_2^* correction for all cohorts.

The approach used in this work, combines the available brain compartment segmentation masks and literature values for blood-tissue partition coefficients and relaxation times to obtain the equilibrium magnetisation of blood $M_{0,b}$ from the measured magnetisation equilibrium $M_{0,BC}$ of all brain compartments (GM, WM, and CSF). Several studies have also looked into the estimation of $M_{0,b}$. Using literature values and own measurements for apparent transversal relaxation times, *Çavuşoğlu et al.* (2009) compared three methods to obtain $M_{0,b}$ from $M_{0,BC}$ from global scaling factor from WM, or CSF, or local scaling from GM. They found highest CBF values for the method based on GM and lowest CBF for the method based on CSF. They used a blood-tissue partition coefficient λ of 0.84, 1.15, 1.02 for WM, CSF, and GM, respectively. The apparent transversal relaxation time measured were 44.7 ms, 74.90 ms, and 44.2 ms for WM, CSF, and GM, respectively. While the blood-tissue partition coefficient differ only little from the values

assumed in this work, the apparent transversal relaxation times are all lower in the study by *Çavuşoğlu et al.* (2009), especially for CSF. *Fazlollahi et al.* (2015) reproduced the methods compared by *Çavuşoğlu et al.* (2009) and an additional method with global scaling from GM. They found the method using local scaling to yield best reproducibility and highlight its advantage with respect to the correction of B_1 inhomogeneities. More recently, *Pinto et al.* (2020) looked into the effect of using a brain-averaged blood-tissue partition coefficient versus a brain compartment specific or a partial volume corrected coefficient. Overall, they found considerable differences in quantified CBF depending on the choice of coefficient.

M0 corrections based on local corrections are theoretically most accurate but the accuracy directly depends on precise knowledge of the correction factors (relaxation times and blood-tissue coefficient). This can be challenging in patients presenting brain compartments with altered relaxation properties, carrying the risk of a wrong perfusion quantification when using this type of corrections. It is therefore of the utmost importance that any perfusion quantification reports include all details about corrections employed as no meaningful comparison between studies is otherwise possible.

5.1.4 Effect of M0 smoothing

The M0 image used as scaling in the perfusion quantification model is often smoothed before it is used in order to diminish spatial noise. In this work, smoothing was performed with a Gaussian filter and its full width at half maximum (FWHM) was varied in multiples of the voxel size of the ASL challenge data. The smoothing procedure always showed to have a significant effect on the final CBF quantification. The larger the FWHM, the less variation in CBF was observed between analysed data sets. This could be explained by excessive blurring (oversmoothing) occurring when using large FWHM. Nevertheless, it is recommended to use some smoothing to reduce the effect of partial volume present at voxel sizes larger than the anatomical structure detail as is the case in ASL data.

Fazlollahi et al. (2015) evaluated the effect of smoothing both the perfusion-weighted and M0 image and compared different filters (Gaussian smoothing, Wiener, anisotropic diffusion, wavelets). They found the Gaussian filter to yield best reproducibility but noticed it also caused some oversmoothing. *Pinto et al.* (2020) compared median filters with different kernel sizes applied to smooth the M0 image. They found also significant differences between the final CBF values but emphasised that these differences are small. But, contrary to the results in this study, they found the default smoothing kernel to yield no significant difference as compared to using no smoothing. No assessment in terms of SNR was performed by *Pinto et al.* (2020).

From this work and previous work, it remains unclear which filter is best and this choice probably also depends on the data to be analysed. Nonetheless, the smoothing filter used and its properties have a significant impact on the perfusion quantification (noise reduction, oversmoothing) and should therefore be reported in full detail to allow meaningful comparison between multiple studies.

5.1.5 Comparison of segmentations

To obtain CBF values specific for GM and WM, a segmentation is necessary. Two images can be considered as basis for the segmentation: an anatomical image if available or the M0 image used for perfusion quantification. A direct comparison of these two segmentation possibilities has not been performed before and most published studies use an anatomical image. The M0 image has a lower resolution than the anatomical image so a segmentation performed on the higher resolution image is expected to be more accurate, which the analysis shown here also confirms. While CBF values calculated over the entire brain are unaffected by the image chosen to perform the segmentation, differences in mean CBF values obtained for GM and WM are statistically significant. Nevertheless, when no anatomical data is available or in cases where the registration between anatomical and ASL data is challenging, using the M0 image as basis for the segmentation is feasible and still yields useful perfusion information.

5.1.6 Effect of number of control-label pairs

Increasing the number of control-label pairs acquired increases the SNR of the perfusion map at the expense of increased acquisition time. A total of 50 pairs of control and labelled images was acquired for the healthy volunteer data and perfusion quantification was performed on sub-samples of the images to assess the change in CBF with increasing number of images considered for the analysis. Overall, the change in CBF mean and standard deviation calculated across the whole brain, GM, WM is subject-dependent and it was not possible to determine an optimal number of control-label pairs that would fit all measured subjects. Choosing the number of control and labelled images acquired for ASL-based perfusion quantification depends on numerous factors and the number of pairs used varies from study to study. It always has to be a compromise between achieved SNR and acquisition time, especially for clinical applications.

5.1.7 Comparison of 2D and 3D readout

Two PCASL sequences using 2D or 3D GRE-EPI readout were used for the healthy volunteer data acquisition. CBF values obtained with the two different readouts are not necessarily comparable as final CBF values across the healthy volunteers considered here showed overall higher values obtained with the 3D readout. This is because a 3D readout yields higher SNR per volume thus ensuring a better signal level for the perfusion-weighted image and quantified perfusion map. The sequences used here do not include any background suppression. Therefore the effect of a varying background suppression efficiency across slices in the 2D acquisitions does not have to be considered. When choosing which sequence to use, it is important to take all aspects into consideration. 3D acquisitions have an SNR advantage but 2D multi-slice acquisitions contain additional valuable information. As each acquired slice has a different effective delay time, a single delay time 2D multi-slice acquisition is intrinsically a multi-delay time acquisition. This additional information can be used to determine the arterial transit time [*Camargo and Wang*, 2022].

5.1.8 Comparison of patients to healthy volunteers

The in-house developed pipeline was able to reproduce perfusion asymmetries resulting from brain tumour or metastases in patients. Unfortunately, no segmentation of the tumour and surrounding oedema was available for the patient data. As such it was not possible to do the standard comparison of perfusion in pathology and normal appearing contralateral side. Instead, automated segmentation into CSF, GM, WM was performed and yielded erroneous brain compartment masks close to the pathology. An interesting approach to avoid this issue are deformable brain atlases, which account for changes in tissue appearance and position due to pathology. Future work should look into expanding the developed analysis pipeline to yield more valuable perfusion information for patient data sets.

5.1.9 Limitation

The main limitation of the comparison of processing options presented here is the lack of ground truth. For in vivo acquired data, literature values of healthy organ perfusion can be used for comparison but the range of perfusion values currently found for brain is large. Furthermore, the influence of the measurement chosen to assess perfusion is not straightforward and differences between literature values and measured values may well

arise from differences in measurement method (e.g. sequence type and parameters). For the data provided by the ASL challenge, the ground truth information will be available once the results have been published but the exact publication date has been postponed and is still unknown. Once the ground truth is available, the scenarios evaluated here should be compared to it in order to assess which of the scenarios yield CBF distributions closest to the ground truth.

5.2 Kidney - Synthetic data

Synthetic data mimicking in vivo acquisitions is of great value as it does not include any variability stemming from acquisition and allows focusing solely on data processing. For this purpose, synthetic renal ASL data sets of the kidneys simulating in vivo acquisitions were generated using body models from the XCAT phantom, the general kinetic model and literature values for tissue properties. Sequence and ASL parameters were set in accordance with the current consensus [*Nery et al.*, 2020]. The synthetic data was then used to evaluate the in-house developed renal ASL processing pipeline (section 3.3.1) in terms of registration, quantification, and segmentation.

5.2.1 Data evaluation

The generation of synthetic renal ASL data presented in this work allows flexible choice of parameters and benefits from the multitude of available XCAT body models presenting different organ sizes and shapes. An additional style transfer to further increase the resemblance between synthetic and real ASL data would be beneficial. This could be done using CycleGAN networks as previously demonstrated [*Bauer et al.*, 2021]. The five models included in this work were selected at random from the available adult models. Future work should also involve the expansion of the synthetic data sets to additional models as well as include additional pathological data sets (e.g. representing different stages of chronic kidney disease).

In 2019, *Antolak and Jackson* (2019) introduced a simple ASL digital reference object to compare software packages. It consists of a square block of voxels with a range of perfusion values (10-210 mL/100g/min), considering only PCASL labelling and including noise [*Antolak and Jackson*, 2019]. This simple approach does not resemble real-life cases and thus allows only limited evaluation or comparison of processing software. More recently a brain ASL digital reference object was introduced [*Oliver-Taylor et al.*, 2021a] and used to set up a challenge for comparison of ASL processing options employed in

research and clinical settings [*Anazodo and Croal*, 2021; *Anazodo et al.*, 2021]. The authors also looked into generating synthetic ASL data of the kidneys using the same framework [*Oliver-Taylor et al.*, 2021b]. Their approach used cortex and medulla segmented from an in vivo MR scan of a single healthy volunteer and a perfusion of 215 mL/100g/min and 81 mL/100g/min were assigned to cortex and medulla, respectively. This approach requires actual MRI acquisitions, which can be challenging to obtain due to scanner availability and potential artefacts.

5.2.2 Pipeline evaluation

5.2.2.1 Registration

Good registration to correct for respiratory motion is crucial for accurate perfusion quantification based on ASL MRI data as it requires the subtraction of labelled images from control images. A mismatch of anatomical structures between any of the images used for calculation of the perfusion map would result in erroneous perfusion values.

The registration strategy employed in the in-house developed processing pipeline performs well on the synthetic data. A separate registration of left and right kidney was chosen as each organ may experience a different motion during the respiratory cycle. As a coronal oblique slice positioning was used, the respiratory motion, which is mainly along the craniocaudal direction, will result in a displacement of the kidneys not only within the plane of imaging but also out of it. This can result in varying organ shapes across the ASL time series and motivated the choice of a non-rigid registration strategy.

Finding the best suited registration strategy and parameters is difficult and some adaption might be necessary when analysing data from different cohorts. The performance of groupwise registration applied to ASL might be hindered by the difference of signal intensity between M0, and control and labelled images. Another registration strategy which has been shown to yield good results for motion correction in ASL of the myocardium consists of a combination of groupwise registration of control and of labelled images followed by pairwise registration of mean control image and mean labelled image to the M0 image [*Vidaurreta*, 2020]. Variational frameworks for non-rigid registration have been shown to yield good results for dynamic contrast enhanced (DCE) MR images of the kidneys [*Merrem et al.*, 2013] and could be evaluated for renal ASL. Deep learning based registration is also an interesting alternative as it has already demonstrated great potential [*Zöllner et al.*, 2020]. However, the success and transferability of this approach is limited by the amount of data available for training. The framework for generation of synthetic ASL data presented here can be used to complement in vivo acquired data for

network training purposes, as previously suggested for other imaging applications [*Bauer et al.*, 2021].

5.2.2.2 Quantification

The quantification model employed here is a single compartment model and assumes the same longitudinal relaxation time for tissue and blood. While this corresponds to the current recommendations [*Nery et al.*, 2020], it contains a number of assumptions simplifying the complexity of blood and nutrient delivery to an organ. The framework for generation of synthetic ASL data presented here can easily be modified to include perfusion-weighting in the images based on a different and more complex model. In addition, it offers a large flexibility to modify other assumed tissue properties to simulate diseases involving impaired renal perfusion as well as altered tissue relaxation times and arterial transit times.

5.2.2.3 Segmentation

The segmentation procedure employed in the in-house developed processing pipeline is a compromise between time-intensive manual segmentation and accuracy of automated segmentation. Automated whole kidney segmentation is complicated, especially for the left kidney due to the closeness of the spleen, which presents similar intensities as the kidneys in the M0 image used for segmentation. Automated segmentation of cortex and medulla works well on the quantified perfusion map as perfusion differs greatly between cortex and medulla in healthy kidneys. However, this approach will not yield good results in cases where cortical and medullary perfusion are similar and further improvement is warranted for application in clinical cohorts.

Kidney segmentation based on k-means clustering has previously been used on entire MR images with three clusters (cortex, medulla, background) [*Zöllner et al.*, 2009] instead of running it on each kidney separately and thus using only two clusters (cortex and medulla) as done in this work. In the ASL processing pipeline used here, the image is already separated in two for separate registration of left and right kidney. A segmentation performed separately on each kidney is thus more straightforward. Another automated segmentation for DCE MR images yielding good results uses wavelet-based clustering [*Li et al.*, 2012]. However, it is not directly applicable to ASL images as it makes use of the DCE-specific changes in signal intensity during contrast agent uptake, which reflect kidney functionality. An automated segmentation of the kidneys in twelve concentric objects (TLCO) has been introduced for evaluation of renal oxygenation [*Milani et al.*, 2017].

However, this method does not allow separation of cortical and medullary compartments of the kidneys and is thus less appealing for assessment of renal perfusion. Deep learning has also successfully been applied for kidney segmentation for both healthy and diseased kidneys [*Schnurr et al.*, 2019; *Zöllner et al.*, 2021; *Bones et al.*, 2022]. In most cases, cortex/medulla segmentation is performed on anatomical T_1-weighted or T_2-weighted data or even on quantified relaxometry maps [*Zöllner et al.*, 2021, 2012; *Bones et al.*, 2022]. However, this requires an additional step of registration of the anatomical and ASL data, which is not always easily achievable.

5.3 Kidney - in vivo study

While a consensus on ASL acquisition and processing has been published in 2015 for brain imaging [*Alsop et al.*, 2015], kidney ASL imaging had been lacking such a consensus until recently. In 2020, a consensus for kidney ASL imaging based on experts' answers to questionnaires was published [*Nery et al.*, 2020]. To assess in more detail certain aspects of kidney ASL imaging and support this first consensus with data, a study in healthy volunteers was performed in collaboration with the radiology department of the Clínica Universidad de Navarra, Pamplona, Spain. The project aimed to determine whether the cardiac cycle and respiration strategy have a significant effect on renal perfusion quantification based on ASL MRI data. For each volunteer, ASL data was acquired both in free breathing and synchronised breathing and with or without ECG triggering.

5.3.1 Effect of registration strategy

The registration is an essential part of the processing of ASL data as the perfusion quantification requires the subtraction of labelled images from control images and any mismatch of structures would result in erroneous perfusion values. A total of 27 data sets of healthy volunteers was analysed using the in-house developed processing pipeline with each of the five registration options. Good registration was only obtained in 73% of the cases. This was partly due to poor SNR, especially of labelled images (subject 3 and 4), or due to prominent artefacts close to a kidney (subject 5). From the five image areas considered for registration, best results were obtained when considering the whole image (good registration for 47 out of 54 kidneys). The MSSIMs and ECCs calculated for each image pair of a data set increased significantly after registration compared to before for all registration options, indicating that all registration options improve the similarity between all ASL images. Overall, MSSIMs were always larger than ECCs but both metrics showed equivalent results for the comparison of registration options. Another important aspect

is the duration of registration. Only the whole image option performs the registration for left and right kidney simultaneously and was therefore the fastest (31 ± 4 minutes). For all other options, where left and right kidney are registered separately, the duration of registration is not linear with the number of pixels present in the image area considered for registration. Registration considering the image cropped to half took the longest (73 ± 1 minutes) and the three other options took about 60 minutes for both kidneys. Based on these results, the non-rigid groupwise registration performs best when considering the entire image and registering both kidneys simultaneously. This option was used for the subsequent measurement comparisons.

The current consensus for renal ASL [Nery et al., 2020] recommends a separate registration of left and right kidney as the kidneys might be subject to different directions of movement during the subject's respiratory cycle. This is especially important when using rigid registration, which would not allow local differences in the transformation field. A non-rigid transformation was considered in this work to better account for the through plane motion of the kidneys during the respiratory cycle. As all images were acquired in a coronal-oblique orientation, motion within and through the imaging plane might be present between the different ASL images. The registration parameters were optimised on the first couple of data sets and the same parameters were used for all data sets. It might be possible to further optimise the registration parameters to obtain good registration even for the more challenging data sets. However, this is a lengthy procedure and it is in no way certain that it will lead to registration parameters that work well for every data set.

5.3.2 Influence of cardiac cycle and respiration strategy

Perfusion values for all kidneys with good registration were below the expected range of 151 ± 37 mL/100g/min for the whole kidney [*Conlin et al.*, 2017], and 278 ± 5 mL/100g/min and 55 ± 25 mL/100g/min for cortex and medulla, respectively [*Roberts et al.*, 1995]. Percentage differences between literature values and mean perfusion values averaged over all kidneys with good registration were equal to or below 32%, 61%, and 53% for whole kidney, cortex, and medulla, respectively. Across all subjects, no statistically significant difference in perfusion and tSNR was found between the four measurements, except for the synchronised breathing measurement when considering the whole left kidney. These results suggest that the choice of respiration strategy and ECG triggering has little impact on renal perfusion quantification using PCASL.

Blood flow in the aorta where labelling occurs for ASL-based renal perfusion quantification is known to be pulsatile and the flow velocity varies with the cardiac cycle [*Kröner*

et al., 2014; *Echeverria-Chasco et al.*, 2021]. The labelling efficiency achieved by adiabatic inversion is dependent on the flow velocity of the spins (equation 2.65) and thus also varies with the cardiac cycle [*Maccotta et al.*, 1997; *Nezamzadeh et al.*, 2010; *Zhao et al.*, 2017; *Schollenberger et al.*, 2020; *Echeverria-Chasco et al.*, 2021]. Therefore, the hypothesis was that because of these physiological attributes, ASL-based renal perfusion quantification depends on the cardiac phase in which the data was acquired. An ECG triggered measurement should ensure a constant labelling efficiency as the labelling always occurs at the same time point of the cardiac cycle. A potential explanation for the absence of difference between triggered and non-triggered acquisition is that multiple control and labelled images are subtracted and averaged to obtain perfusion values. Thus, differences in labelling efficiency between the different images can be averaged out, yielding the same results as in ECG triggered measurements. This work focused on ECG triggering with a trigger delay set to 0 ms to obtain the shortest possible acquisition time. However, the dependence of perfusion quantified with ECG triggered ASL on the chosen trigger delay seems to be subject dependent (Figure 4.45). Choosing a trigger delay of 0 ms instead of a longer delay could also be the reason for the absence of difference between triggered and non-triggered measurements. The ECG triggered measurements lasted up to 150 seconds longer than non-triggered measurements lasting 270 seconds in total. Furthermore, difficulties with low electrode signal were encountered, which lengthened the overall duration of the imaging examination and resulted in an impossibility to perform the measurement in one case. Despite theses challenges, a more detailed analysis would be beneficial for better understanding of the effect of the cardiac cycle on ASL-based renal perfusion quantification.

So far only one published work looked into the difference in renal perfusion quantified by ASL acquisitions with and without ECG triggering [*Takei et al.*, 2018]. They found that only diastolic triggering yielded robust perfusion-weighted images while systolic triggering or no triggering resulted in signal reduction and thus required the acquisition of a larger number of control and labelled images to achieve the same quality of perfusion maps. Most ASL literature focuses on the brain and a few studies have assessed the influence of the cardiac cycle on measured cerebral perfusion. In these studies, triggering was performed either based on a pulse oxymeter or an ECG. The first study found cardiac pulsation to significantly affect the ASL signal [*Wu et al.*, 2006]. *Wu et al.* (2009) compared the effect of pulsatile flow on PASL and CASL and found PASL to be more affected by it, which is to be attributed to the difference in labelling duration between the two labelling schemes. Furthermore, the CASL signal stability was not improved by using triggering. *Fushimi et al.* (2013) looked at the difference in transit delay of the labelled spins to the imaging volume and found it to be longer in diastolic phase than in systolic phase. They found that triggering has a high impact on cerebral perfusion quantification. *Chen et al.* (2017)

investigated the influence of cardiac triggering on the labelling efficiency of PCASL applied to the brain and found an increased stability when using triggering. *Verbree and van Osch* (2018) also focused on PCASL in the brain and evaluated the effect of cardiac triggering applied at the end of the labelling pulses. Their simulations demonstrated that putlsatile flow influences both the generation and the delivery of labelled spins to the imaging volume and that lower heart rates lead to larger signal variations over the cardiac cycle. However, they found no difference in mean ASL signal or temporal evolution of the ASL signal in their in vivo experiments. *Li et al.* (2018b) investigated the effect of pulsatile flow on PCASL acquisitions and showed that non-triggered acquisitions yield unstable signal especially close to large vessels and can even result in ghosting artefacts. They estimated that 44% of the noise in ASL data is to be attributed to pulsatile flow. They found cardiac triggering to increase the SNR and tSNR of PCASL and noticed that both control and labelled images vary with the cardiac phase according to the same pattern. They also observed a higher perfusion signal when triggering occurred in systolic phase instead of diastolic phase. *Franklin et al.* (2020) looked into the dependence of PCASL, VSASL, and AccASL on the cardiac phase. They found signal changes of up to 26%, 36%, 64% for PCASL, VSASL, and AccASL, respectively. They also noticed that the peak of PCASL signal coincides with the flow velocity peak. *Schollenberger et al.* (2020) evaluated the difference between triggered and non-triggered acquisitions in terms of image quality assessed blindly by four observers and by calculating SNR and tSNR for two ROIs as well as contrast-to-noise ratio (CNR). The observers agreed that triggered acquisitions yielded less artefacts from pulsatile flow and thus an improved image quality. While no significant differences in SNR and tSNR were observed, the CNR was significantly better in triggered acquisitions. Overall, the results from these studies in the brain show partly contradictory results and the general use of cardiac triggering is not recommended before further evidence is available [*Hernandez-Garcia et al.*, 2022].

Choosing a synchronised breathing pattern does not make registration redundant as respiratory motion was still visible for all subjects. Furthermore, the registration did not perform better on the measurements in synchronised breathing than on the measurements in free-breathing. It is also difficult to assess whether a subject correctly performs the pattern of synchronised breathing and there is a risk that having to breathe in a specific manner increases a patient's stress level during the imaging examination. Various prospective and retrospective strategies exist to correct for respiratory motion in abdominal imaging when breath-hold is not possible. These include respiratory triggering, synchronised breathing, breathing pattern prediction, image sorting, and image registration [*Martirosian et al.*, 2004; *Robson et al.*, 2009; *Song et al.*, 2017; *Taso et al.*, 2019; *Bones et al.*, 2019]. Each of these approaches either require additional effort for the acquisition and planning (e.g. navigator placement) or for the image post-processing (e.g. lengthy

sorting or registration procedure). In a clinical setting, it is advantageous to minimise the complexity of the imaging examination as a whole and thus free-breathing acquisitions followed by retrospective motion correction are especially well suited. At the same time, however, retrospective motion correction approaches usually make it impossible to visualise a quantified perfusion map directly at the scanner due computational requirements. A different motion mitigation approach can thus be beneficial depending on the context of the imaging.

A compromise between acquisition duration, patient compliance and results always has to be found for applications in the clinical routine. Based on the results presented here, the simplest measurement (free breathing, no ECG triggering) seems to be the best suited option.

Limitations of this study are the low number of subjects as well as their youth and fitness. This does not accurately reflect the patient population who might benefit from completely non-invasive perfusion quantification. These patients might have cardiac or respiratory difficulties and a synchronised breathing pattern or ECG triggering might be even more challenging than in healthy subjects. Future work should look into increasing the number and diversity of subjects considered to increase the relevance of the results.

CHAPTER 6

Conclusion and Outlook

Quantitative assessment of organ perfusion is highly relevant for the evaluation of tissue function, activity, and viability. Arterial spin labelling (ASL) allows completely non-invasive perfusion imaging by magnetic labelling of arterial blood. This technique has tremendous potential for a wide range of medical applications. However, despite recent technical advances, it has not yet been established in the clinical routine due to a lack of standardisation. This work aimed to contribute to the transition of ASL into the clinical routine by investigating sources of variability in ASL-based perfusion quantification in the brain and in the kidneys. To this end, three projects were pursued.

For the first project, a processing pipeline for the analysis of brain ASL data was written. It included multiple options and corrections: four perfusion-weighted image calculation methods, seven outlier removal options, five M0 corrections, four full width at half maximum (FWHM) sizes for the Gaussian smoothing kernel used for the M0 image, and a choice between two images to be used for segmentation. Perfusion and signal-to-noise ratio (SNR) results obtained with different processing options and corrections or with different acquisition parameters were compared using data from the ASL challenge as well as data acquired in healthy volunteers. The pipeline was also used to analyse patient data. For the comparison of processing options and acquisition parameters, no ground truth perfusion data was available and the observed differences were sometimes small despite being statistically significant. This makes proposing recommendations for processing of brain ASL data difficult. The perfusion-weighted image can be calculated by first subtracting control and labelled images and then averaging or by averaging all control and labelled images followed by subtraction of mean control and mean labelled image, as no significant difference in perfusion or SNR was observed between these two approaches. Different options to remove outliers from the ASL time series yielded significantly different perfusion and SNR results. Correcting the M0 image for relaxation effects or for the percentage of blood in different brain compartments also yielded statistically significant

differences in perfusion and SNR. Smoothing the M0 image with Gaussian filters of different kernel sizes yielded significant differences in perfusion and SNR. The segmentation into gray and white matter, necessary to report tissue type specific perfusion, was more accurate when performed on a high resolution T_1-weighted image than on the M0 image. Differences in perfusion were observed with varied number of control and labelled images considered for quantification. However, it was impossible to determine a single number of control and labelled images acquired for ASL-based perfusion quantification, which would have been optimal for all subjects. Perfusion values obtained with 2D or 3D readout were found to be different, with a shift towards higher values for the 3D data. Regional perfusion abnormalities caused by tumours or metastases were observed in patient data, but the analysis of patient data suffered from segmentation inaccuracies.

For the second project, synthetic ASL data sets of the kidneys mimicking in vivo acquisitions were generated using body models from the XCAT phantom, the general kinetic model, and literature values for tissue properties. The data sets included respiratory motion, and both PASL and PCASL labelling schemes were simulated. Healthy perfusion was assumed for ten data sets with two kidneys each. The eleventh data set mimicked a patient with decreased perfusion in the cortex and the medulla of the right kidney and normal perfusion in the left kidney. A processing pipeline for the analysis of renal ASL data was developed and all data sets were used to evaluate it in terms of registration, quantification, and segmentation. The registration performed well for both left and right kidneys, with smoother line profiles after registration and mean structural similarity index measures (MSSIMs) increasing by 25% on average. The quantification yielded cortical and medullary perfusion values which matched the assumed perfusion for healthy kidneys (250 mL/100g/min and 50 mL/100g/min for cortex and medulla, respectively) within 1-52% and for diseased kidney (100 mL/100g/min and 20 mL/100g/min for cortex and medulla, respectively) within 6-17%. Segmentation results from the processing pipeline agreed well with original segmentation masks, with Dice indices ranging 0.80-0.93, 0.78-0.89, and 0.64-0.84 for whole kidney, cortex, and medulla, respectively. The proposed method of generation of synthetic renal ASL data allowed flexible choice of parameters and the generated data sets were well suited for evaluation of the processing pipeline. Efforts should be made to use the generated renal ASL data sets in an international Grand Challenge to achieve the necessary standardisation of ASL-based renal perfusion quantification.

For the third project, ASL data sets of the kidneys were acquired in healthy volunteers and analysed with the pipeline developed in the second project. Four ASL measurements were performed for each subject varying between free breathing or synchronised breathing and with or without cardiac triggering. Groupwise non-rigid registration was performed on different areas of the ASL images and results were compared. Perfusion values obtained for the different measurements were evaluated and tested for statistical difference.

Registration performed best when considering the entire image, with a 87% success rate and a mean duration of 30 minutes. Percentage differences between literature values and mean perfusion values were equal to or below 32%, 61%, and 53% for whole kidney, cortex, and medulla, respectively. Across subjects, perfusion values obtained for the four different measurements were only significantly different between the free breathing and synchronised breathing measurement when considering the whole kidneys. Temporal signal-to-noise ratio (tSNR) was not found to differ significantly between any of the four measurements. Issues with electrode signal and lengthened acquisition duration made cardiac triggered acquisitions more complicated. Renal perfusion was found to differ depending on the chosen trigger delay for the cardiac triggering. The dependence of the assessment of renal perfusion on the cardiac cycle should be investigated further for better understanding of this potential source of variation. The synchronised breathing pattern neither removed the need of a registration nor increased the registration quality compared to free breathing acquisitions, and thus presented no advantage over free breathing acquisitions.

In summary, differences in acquisition parameters and processing options used for analysis of brain ASL data result in significant differences in perfusion quantification. This work demonstrated that it is essential that all studies describe their data acquisition and analysis in full detail to allow meaningful comparisons of results across studies and support the transition of ASL into the clinical routine. Synthetic renal ASL data sets were generated and used to evaluate the developed processing pipeline. This work showed that the developed data sets are well suited for pipeline evaluation and that the pipeline is reliable in terms of registration, quantification, and segmentation. From the results of the study in healthy volunteers, an acquisition in free breathing without cardiac triggering seems to be the best choice for renal perfusion quantification in clinical applications, as these require a compromise between acquisition duration, patient compliance, and result accuracy. Taking all these findings into consideration, the transition of ASL into the clinical routine is within reach and will be an enrichment for clinical perfusion applications, as it provides a good alternative to more invasive perfusion quantification techniques.

APPENDIX A

Brain

A.1 CBF

Mean CBF values for all scenarios averaged over the different subject groups (ASL Challenge data, 2D Cohort 1, 3D Cohort 1, Cohort 2) are listed in Tables A.1, A.2, A.3, A.4, respectively.

Table A.1: Mean and standard deviation of CBF calculated over the whole brain (WB), over gray matter (GM), over white matter (WM), and over GM and WM for all data sets of the ASL Challenge. Statistically significant differences between each scenario and the reference scenario I are indicated with a star ($p<0.05$).

	CBF WB [mL/100g/min]	CBF GM [mL/100g/min]	CBF WM [mL/100g/min]	CBF GM+WM [mL/100g/min]
I	25 ± 5	32 ± 5	18 ± 6	26 ± 5
II	80 ± 80 *	80 ± 70 *	40 ± 30 *	60 ± 50 *
III	25 ± 7	32 ± 7	19 ± 8	27 ± 7
IV	31 ± 9 *	36 ± 6 *	20 ± 6 *	29 ± 6 *
V	25 ± 5	32 ± 5	18 ± 6	26 ± 5
VI	25 ± 5	32 ± 4	18 ± 6	26 ± 5
VII	25 ± 5	32 ± 5	18 ± 6	26 ± 5
VIII	25 ± 5	32 ± 4	18 ± 6	26 ± 5
IX	24 ± 6	31 ± 6	19 ± 6	26 ± 5
X	24 ± 5	31 ± 5	18 ± 6	26 ± 5
XI	25 ± 5	32 ± 4	18 ± 6	26 ± 5
XII	24 ± 5 *	31 ± 5 *	18 ± 6 *	26 ± 5 *
XIII	26 ± 5 *	34 ± 5 *	20 ± 6 *	28 ± 4 *
XIV	26 ± 6 *	34 ± 5 *	18 ± 6 *	27 ± 5 *
XV	28 ± 5 *	36 ± 5 *	20 ± 5 *	29 ± 5 *
XVI	24 ± 5 *	30 ± 5 *	18 ± 6 *	25 ± 5 *
XVII	24 ± 5 *	31 ± 5 *	18 ± 6	26 ± 5 *
XVIII	25 ± 5 *	33 ± 5 *	18 ± 6 *	27 ± 5 *
XIX	26 ± 5 *	34 ± 5 *	19 ± 6 *	27 ± 5 *
XX	25 ± 5	29 ± 5 *	14 ± 6 *	25 ± 5 *

Table A.2: Mean and standard deviation of CBF calculated over the whole brain (WB), over gray matter (GM), over white matter (WM), and over GM and WM for all data sets of Cohort 1 acquired with the 2D EPI readout. Statistically significant differences between each scenario and the reference scenario I are indicated with a star ($p<0.05$).

	CBF WB [mL/100g/min]	CBF GM [mL/100g/min]	CBF WM [mL/100g/min]	CBF GM+WM [mL/100g/min]
I	45 ± 8	60 ± 10	20 ± 4	44 ± 8
V	45 ± 9	60 ± 10	20 ± 4	44 ± 9
VI	48 ± 7	61 ± 9	31 ± 4 *	48 ± 7
VII	45 ± 9	60 ± 10	20 ± 4	44 ± 8
VIII	45 ± 9	60 ± 10	20 ± 3	44 ± 8
IX	40 ± 30	60 ± 30	20 ± 10	40 ± 20
X	45 ± 7 *	60 ± 10 *	20 ± 3	43 ± 7 *
XI	45 ± 8 *	60 ± 10 *	20 ± 3 *	44 ± 8
XII	41 ± 7 *	50 ± 10 *	20 ± 3	41 ± 7 *
XIII	46 ± 8 *	60 ± 10 *	20 ± 3	44 ± 8 *
XIV	48 ± 8 *	60 ± 10 *	20 ± 3	47 ± 8 *
XV	45 ± 8 *	60 ± 10	19 ± 3	44 ± 8

Table A.3: Mean and standard deviation of CBF calculated over the whole brain (WB), over gray matter (GM), over white matter (WM), and over GM and WM for all data sets of Cohort 1 acquired with the 3D EPI readout. Statistically significant differences between each scenario and the reference scenario I are indicated with a star ($p<0.05$).

	CBF WB [mL/100g/min]	CBF GM [mL/100g/min]	CBF WM [mL/100g/min]	CBF GM+WM [mL/100g/min]
I	50 ± 6	63 ± 8	32 ± 4	50 ± 5
V	48 ± 5	61 ± 8	31 ± 4	49 ± 5
VI	48 ± 7 *	61 ± 9 *	31 ± 4 *	48 ± 7 *
VII	49 ± 6	61 ± 9	31 ± 5	50 ± 6
VIII	48 ± 6 *	59 ± 9 *	31 ± 5	48 ± 6 *
IX	30 ± 20 *	40 ± 20 *	20 ± 20	30 ± 20 *
X	48 ± 5	61 ± 7	32 ± 4	49 ± 5
XI	49 ± 6 *	60 ± 9 *	31 ± 4	49 ± 8 *
XII	47 ± 5 *	58 ± 7 *	31 ± 4 *	48 ± 5 *
XIII	50 ± 6	60 ± 10 *	32 ± 4	49 ± 6 *
XIV	53 ± 6 *	66 ± 9 *	31 ± 4 *	53 ± 6 *
XV	50 ± 6	62 ± 9	30 ± 4 *	50 ± 5 *

Table A.4: Mean and standard deviation of CBF calculated over the whole brain (WB), over gray matter (GM), over white matter (WM), and over GM and WM for all data sets of Cohort 2. Statistically significant differences between each scenario and the reference scenario I are indicated with a star ($p<0.05$).

	CBF WB [mL/100g/min]	CBF GM [mL/100g/min]	CBF WM [mL/100g/min]	CBF GM+WM [mL/100g/min]
I	44 ± 5	58 ± 8	22 ± 3	44 ± 5
V	43 ± 3	57 ± 5	22 ± 2	43 ± 3
VI	44 ± 3	57 ± 6	22 ± 3	44 ± 3
VII	46 ± 4	61 ± 5 *	24 ± 2 *	47 ± 3 *
VIII	47 ± 4 *	61 ± 5 *	24 ± 2 *	47 ± 3 *
IX	40 ± 20	50 ± 30	20 ± 20	40 ± 20
X	46 ± 4	60 ± 6	24 ± 3 *	46 ± 4
XI	47 ± 4 *	62 ± 7 *	24 ± 3 *	47 ± 4 *
XII	44 ± 4	58 ± 6	23 ± 3 *	45 ± 4
XIII	48 ± 4 *	61 ± 7 *	24 ± 3 *	47 ± 4 *
XIV	51 ± 5 *	66 ± 7 *	24 ± 3 *	50 ± 4 *
XV	48 ± 4 *	62 ± 7 *	23 ± 3	47 ± 4 *

A.2 SNR

Mean SNR values for all scenarios averaged over the different subject groups (ASL Challenge data, 2D Cohort 1, 3D Cohort 1, Cohort 2) are listed in Table A.5.

Table A.5: Mean and standard deviation of SNR for all brain ASL data. Statistically significant differences between each scenario and the reference scenario I are indicated with a star ($p<0.05$). N/A - *not applicable*

	ASL Challenge	Cohort 1 2D	Cohort 1 3D	Cohort 2
I	0.05 ± 0.02	0.12 ± 0.02	0.12 ± 0.02	0.11 ± 0.01
II	0.1 ± 0.1	N/A	N/A	N/A
III	0.05 ± 0.02	N/A	N/A	N/A
IV	0.10 ± 0.05 *	N/A	N/A	N/A
V	0.05 ± 0.02	0.12 ± 0.02	0.12 ± 0.02 *	0.110 ± 0.009
VI	0.05 ± 0.02	0.12 ± 0.02	0.12 ± 0.02 *	0.109 ± 0.009
VII	0.05 ± 0.02	0.11 ± 0.02 *	0.12 ± 0.02	0.10 ± 0.01
VIII	0.05 ± 0.02	0.06 ± 0.04 *	0.11 ± 0.02 *	0.109 ± 0.009
IX	0.05 ± 0.02 *	0.11 ± 0.02 *	0.04 ± 0.05 *	0.03 ± 0.03 *
X	0.05 ± 0.02 *	0.12 ± 0.02 *	0.11 ± 0.01 *	0.10 ± 0.009 *
XI	0.05 ± 0.02	0.12 ± 0.02	0.12 ± 0.02	0.112 ± 0.009
XII	0.05 ± 0.02 *	0.11 ± 0.02 *	0.11 ± 0.01 *	0.104 ± 0.009 *
XIII	0.05 ± 0.02 *	0.12 ± 0.02 *	0.12 ± 0.02	0.11 ± 0.01 *
XIV	0.04 ± 0.02 *	0.11 ± 0.02 *	0.012 ± 0.02 *	0.108 ± 0.009 *
XV	0.05 ± 0.02 *	0.11 ± 0.02 *	0.11 ± 0.02 *	0.102 ± 0.009 *
XVI	0.02 ± 0.02 *	N/A	N/A	N/A
XVII	0.05 ± 0.02 *	N/A	N/A	N/A
XVIII	0.05 ± 0.02 *	N/A	N/A	N/A
XIX	0.05 ± 0.02 *	N/A	N/A	N/A
XX	0.05 ± 0.02 *	N/A	N/A	N/A

APPENDIX B

Kidney

B.1 Literature values of tissue specific parameters

Table B.1: **Literature values of relative proton density ρ, and T_1 and T_2 relaxation times at a field strength of 3 T.**

organ	T_1 [ms]	T_2 [ms]	ρ
myocardium	1232.9	37.2	80
blood	1984.4	275	95
subcutaneous fat (body)	382	68	70
muscle	1232.9	37.2	80
liver	809	34	90
gall bladder	1142	154	90
lung	1	1	0
esophagus	1718	15.3	70
esophagus content	1142	154	90
stomach wall	1718	15.3	70
stomach content	1142	154	90
pancreas	725	43	90
kidney cortex	1142	154	90
kidney medulla	1545	81	90
adrenal gland	1142	154	90
renal pelvis	382	68	70
spleen	1328	61	90
rib	586	49	25
cortical bone	586	49	25
spine	586	49	25
spinal cord	993	78	70
bone marrow	586	49	25
articulation	1984.4	275	95
vein	1984.4	275	95
ascending colon	1322	65.5	90
transversal colon	1322	65.5	90
descending colon	1322	65.5	90
small intestine	1322	65.5	90
pericardium	382	68	70
cartilage	250	20	25
intestine air	1	1	0
ureter	1718	15.3	70
tracheobronchial tree	1	1	0
skin	382	68	70

B.2 Registration parameter file

B.2.1 Synthetic data

```
// ********************
// * ImageTypes
// ********************
(FixedInternalImagePixelType "float")
(MovingInternalImagePixelType "float")
(FixedImageDimension 3)
(MovingImageDimension 3)
(UseDirectionCosines "true")
// ********************
// * Components
// ********************
(Registration "MultiResolutionRegistration")
(Interpolator "ReducedDimensionBSplineInterpolator")
(ResampleInterpolator "FinalReducedDimensionBSplineInterpolator")
(Resampler "DefaultResampler")
(BSplineInterpolationOrder 1)
(FinalBSplineInterpolationOrder 3)
(FixedImagePyramid "FixedSmoothingImagePyramid")
(MovingImagePyramid "MovingSmoothingImagePyramid")
(Optimizer "AdaptiveStochasticGradientDescent")
(HowToCombineTransforms "Compose")
//Choose on of the following groupwise transforms:
//(Transform "BSplineTransform")
(Transform "BSplineStackTransform")
//(Transform "AffineLogStackTransform")
//Choose one of the following groupwise metrics:
(Metric "PCAMetric2")
//(Metric "PCAMetric")
//Specific for the PCAMetric
(NumEigenValues 3)
// ********************
// * Groupwise Metric settings
// ********************
(SubtractMean "true")
(MovingImageDerivativeScales 1 1 0)
//Choose one of the following settings:
(FinalGridSpacingInPhysicalUnits 8)
//(FinalGridSpacingInPhysicalUnits 16)
//(FinalGridSpacingInPhysicalUnits 32)
// ********************
// * Optimizer settings
// ********************
```

```
(NumberOfResolutions 6)
(AutomaticParameterEs4imation "true")
(ASGDParameterEstimationMethod "Original")
(MaximumNumberOfIterations 500)
// **********************
// * Pyramid settings
// **********************
(ImagePyramidSchedule 10 10 0 8 8 0 2 2 0 4 4 0 2 2 0 1 1 0)
// **********************
// * Sampler parameters
// **********************
(NumberOfSpatialSamples 2048)
(NewSamplesEveryIteration "true")
(ImageSampler "RandomCoordinate")
(CheckNumberOfSamples "true")
// **********************
// * Mask settings
// **********************
(ErodeMask "false")
(ErodeFixedMask "false")
// **********************
// * Output settings
// **********************
(DefaultPixelValue 0)
(WriteResultImage "true")
(ResultImagePixelType "float")
(ResultImageFormat "mhd")
```

B.2.2 In-vivo study

```
// **********************
// * ImageTypes
// **********************
(FixedInternalImagePixelType "float")
(MovingInternalImagePixelType "float")
(FixedImageDimension 3)
(MovingImageDimension 3)
(UseDirectionCosines "true")
// **********************
// * Components
// **********************
(Registration "MultiResolutionRegistration")
(Interpolator "ReducedDimensionBSplineInterpolator")
(ResampleInterpolator "FinalReducedDimensionBSplineInterpolator")
(Resampler "DefaultResampler")
(BSplineInterpolationOrder 1)
(FinalBSplineInterpolationOrder 3)
(FixedImagePyramid "FixedSmoothingImagePyramid")
(MovingImagePyramid "MovingSmoothingImagePyramid")
(Optimizer "AdaptiveStochasticGradientDescent")
(HowToCombineTransforms "Compose")
//Choose on of the following groupwise transforms:
//(Transform "BSplineTransform")
(Transform "BSplineStackTransform")
//(Transform "AffineLogStackTransform")
//Choose one of the following groupwise metrics:
(Metric "PCAMetric2")
//(Metric "PCAMetric")
//Specific for the PCAMetric
(NumEigenValues 3)
// **********************
// * Groupwise Metric settings
// **********************
(SubtractMean "true")
(MovingImageDerivativeScales 1 1 0)
//Choose one of the following settings:
(FinalGridSpacingInPhysicalUnits 8)
//(FinalGridSpacingInPhysicalUnits 16)
//(FinalGridSpacingInPhysicalUnits 32)
// **********************
// * Optimizer settings
// **********************
(NumberOfResolutions 6)
(AutomaticParameterEs4imation "true")
(ASGDParameterEstimationMethod "Original")
(MaximumNumberOfIterations 500)
```

```
// **********************
// * Pyramid settings
// **********************
(ImagePyramidSchedule 2 2 0 2 2 0 1 1 0 1 1 0)
// **********************
// * Sampler parameters
// **********************
(NumberOfSpatialSamples 2048)
(NewSamplesEveryIteration "true")
(ImageSampler "RandomCoordinate")
(CheckNumberOfSamples "true")
// **********************
// * Mask settings
// **********************
(ErodeMask "false")
(ErodeFixedMask "false")
// **********************
// * Output settings
// **********************
(DefaultPixelValue 0)
(WriteResultImage "true")
(ResultImagePixelType "float")
(ResultImageFormat "mhd")
```

APPENDIX C

Publications

C.1 Peer-reviewed Journal Articles

Brumer, I., Bauer, D. F., Schad, L. R., Zöllner, F. G. (2022). Synthetic arterial spin labeling MRI of the kidneys for evaluation of data processing pipeline. *Diagnostics*, 12(8):1854. https://doi.org/10.3390/diagnostics12081854

F. Bauer, D. F., Adlung, A., **Brumer, I.**, Golla, A.-K., Russ, T., Oelschlegel, E., Tollens, F., Clausen, S., Aumüller, P., Schad, L. R., Nörenberg, D., Zöllner, F. G. (2022). An anthropomorphic pelvis phantom for MR-guided prostate interventions. *Magnetic Resonance in Medicine*, 87(3):1605-1612. https://doi.org/10.1002/mrm.29043

Brumer, I., De Vita, E., Ashmore, J., Jarosz, J., Borri, M. (2022). Reproducibility of MRI-based white matter tract estimation using multi-fiber probabilistic tractography: effect of user-defined parameters and regions. *Magn Reson Mater Phys*, 1-9. https://doi.org/10.1007/s10334-021-00965-6

Brumer, I., De Vita, E., Ashmore, J., Jarosz, J., Borri, M. (2020). Implementation of clinically relevant and robust fMRI-based language lateralization: Choosing the laterality index calculation method. *PLoS ONE* 15(3):e0230129. https://doi.org/10.1371/journal.pone.0230129

Hermann, I., Chacon-Caldera, J., **Brumer, I.**, Rieger, B., Schad, L. R., Zöllner, F. G. (2020). Magnetic resonance fingerprinting for simultaneous renal T1 and T2* mapping in a single breath-hold. *Magnetic Resonance in Medicine*, 83 (6), pp.1940-1948. https://doi.org/10.1002/mrm.28160

C.2 Conference Contributions

Brumer, I., Bauer, D. F., Schad, L. R., Zöllner, F. G. (2022) Synthetic arterial spin labelling datasets of the kidneys for pipeline evaluation and comparison. *Proceedings of the International Society for Magnetic Resonance in Medicine*, volume 31, page 3162. London, UK.

Brumer, I., Jonscher, S., Gineitaite, I., Echeverria-Chasco, R., Schad, L. R., Fernandez-Seara, M. A., Zöllner, F. G. (2022) Investigating the influence of ECG-triggering and respiration strategy on renal perfusion quantification using arterial spin labelling. *Proceedings of the International Society for Magnetic Resonance in Medicine*, volume 31, page 5083. London, UK.

Anazodo, U., Pinto, J., McConnell, F. K., Gould van Praag, C., Mutsaerts, H., Oliver-Taylor, A., Petr, J., Pineda-Ordoñez, D., Dounavi, M.-A., **Brumer, I.**, Chan, W. S. M., Toner, J., Hu, J., Zhang, L.X., Bell, L., Woods, J. G., Zhao, M. Y., Croal, P., Paschoal, A. M. (2022). The Open Science Initiative for Perfusion Imaging (OSIPI): Results from the ASL MRI Challenge. *Proceedings of the International Society for Magnetic Resonance in Medicine*, volume 31, page 8046. London, UK.

Franklin, R., De Vita, E., **Brumer, I.**, Jarosz, J., Borri, M. (2022) How does language fMRI activation in tumour patients compare to healthy volunteers? *Proceedings of the International Society for Magnetic Resonance in Medicine*, volume 31, page 2052. London, UK.

Brumer, I., Bauer, D. F., Schad, L. R., Zöllner, F. G. (2022). Synthetic Kidney ASL Data for Evaluation and Comparison of Processing Pipelines. *ISMRM Workshop on Perfusion MRI: From Head to Toe.* Los Angeles, CA, USA - Online.

Brumer, I., Jonscher, S., Gineitaite, I., R. Echeverria-Chasco, Schad, L. R., Fernandez-Seara, M. A., Zöllner, F. G. (2022). Assessing the Influence of ECG-Triggering and Respiration Strategy on ASL-Based Renal Perfusion Quantification: Preliminary Results. *ISMRM Workshop on Perfusion MRI: From Head to Toe.* Los Angeles, CA, USA - Online.

Brumer, I., Bauer, D. F., Schad, L. R., Zöllner, F. G. (2021) Synthetic Arterial Spin Labelling MR Images. *ISMRM Workshop on Kidney MRI Biomarkers: The Route to Clinical Adoption.* Lisbon, Portugal - Online.

Brumer, I.*, Gineitaite, I.*, Schad, L. R., Zöllner, F. G. (2021) Automatic kidney segmentation of ASL-MR images using histogram distribution analysis and thresholding.

ISMRM Workshop on Kidney MRI Biomarkers: The Route to Clinical Adoption. Lisbon, Portugal - Online.

Bauer D. F., **Brumer, I.**, Adlung, A., Golla, A., Russ, T., Oelschlegel, A., Tollens, F., Clausen, S., Aumüller, P., Schad L. R., Nörenberg, D., Zöllner, F.G. (2021) An Anthropomorphic Pelvis Phantom for MR-guided Prostate Biopsy. *Proc. 5th Conference on Image-Guided Interventions*. Virtual.

Ansell, J., **Brumer, I.**, Ashmore, J., De Vita, E., Jarosz, J., Borri, M. (2021). Probabilistic tractography of the arcuate fasciculus: sensitivity and specificity of standardised fMRI and atlas-based approaches. *Proceedings of the International Society for Magnetic Resonance in Medicine*, volume 29, page 4290. Virtual.

Bauer, D. F., Oelschlegel, E., Golla, A.-K., Adlung, A., Russ, T., Hermann, I., **Brumer, I.**, Rosenkranz, J., Tollens, F. Clausen, S., Aumüller, P. Schad, L. R. Nörenberg, D., Zöllner, F. G. (2021). An Anthropomorphic pelvis phantom for prostate brachytherapy and biopsy. *Proceedings of the International Society for Magnetic Resonance in Medicine*, volume 29, page 858. Virtual.

Schuler, F., **Brumer, I.**, Adlung, A., Pusch, T. P., Siegfarth, M., Renaud, P., de Wild, M. (2021). MRI compatibility of additively manufactured auxetic NiTi parts. *Proceedings of [MEET THE EXPERT] Implants*. Virtual.

Borri, M., Lavrador, J. P., **Brumer, I.**, De Vita, E., Ashmore, J., Vergani, F., Bhangoo, R., Ashkan, K., Jarosz, J. (2020). Advanced fMRI and Tractography Preoperative Evaluations Match Intraoperative Findings in a Pilot Cohort of Brain Tumour Patients. *Proceedings of the Annual Meeting of the European Society of Neuroradiology* , volume 43. Virtual.

Brumer, I., De Vita, E., Ashmore, J., Jarosz, J., Borri, M. (2020). What factors influence most the reproducibility of MRI-based white matter tract estimation using probabilistic tractography?. *Proceedings of the International Society for Magnetic Resonance in Medicine*, volume 28, page 4473. Virtual.

Borri, M., Lavrador, J. P., **Brumer, I.**, De Vita, E., Ashmore, J., Vergani, F., Bhangoo, R., Ashkan, K., Jarosz, J. (2020). Do advanced fMRI and tractography preoperative evaluations correspond to intraoperative findings? A pilot evaluation in brain tumour patients. *Proceedings of the International Society for Magnetic Resonance in Medicine*, volume 28, page 1739. Virtual.

Hermann, I., Chacon-Caldera, J., **Brumer, I.**, Weingärtner, S., Schad, L. R., Zöllner, F. G. (2020) Renal magnetic resonance fingerprinting for simultaneous T1 and T2* quantification. *Proceedings of the International Society for Magnetic Resonance in Medicine*,

volume 28, page 3752. Virtual.

Brumer, I., Chacon-Caldera, J., Hubertus, S., Uhrig, T., Dziadosz, M., Barth, M., Schad, L. R., Zöllner, F. G. (2019). Investigating the existence of bias in ASL sequences: evaluation of perfusion measurements in phantom with 2D and 3D EPI pseudo-continuous ASL sequences. *Proceedings the European Society for Magnetic Resonance in Medicine and Biology*, volume 36, page 149. Rotterdam, Netherlands

Brumer, I., Adlung, A., Neumann, W., Uhrig, T., Malzacher, M., Schad, L. R., Zöllner, F. G. (2019). Novel pixel-based approach for artifact evaluation of passive implants in MRI validated on intrauterine devices at 3T. *Proceedings of the European Society for Magnetic Resonance in Medicine and Biology*, volume 36, page 395. Rotterdam, Netherlands

Hermann, I., **Brumer, I.**, Rieger, B., Chacon-Caldera, J., Weingärtner, S., L. Schad, L. R., Zöllner, F. G. (2019). Abdominal magnetic resonance fingerprinting for T1 and T2* quantification of the kidneys. *Proceedings of the Europe an Society for Magnetic Resonance in Medicine and Biology*, volume 36, page 261. Rotterdam, Netherlands

Brumer, I., De Vita, E., Ashmore, J., Jarosz, J., Borri, M. (2019). How reproducible are the results of probabilistic white matter tract estimation?. *Proceedings of the International Society for Magnetic Resonance in Medicine*, volume 27, page 3653. Montréal, Canada

Brumer, I., De Vita, E., Ashmore, J., Jarosz, J., Borri, M. (2019). Relative assessment of language lateralisation with fMRI: evaluation of a novel threshold-independent method. *Proceedings of the International Society for Magnetic Resonance in Medicine*, volume 27, page 3924. Montréal, Canada

Brumer, I., Borri, M., De Vita, E., Ashmore, J., Jarosz, J. (2018). Assessing language lateralisation with fMRI: a simplified approach to robust and threshold-independent laterality index calculation. *Proceedings of Quantitative MRI Institue of Physics and Engineering in Medicine conference.* Belfast, United Kingdom

Brumer, I., Borri, M., De Vita, E., Ashmore, J., Jarosz, J. (2018). Robust fMRI for language lateralisation: How do different threshold-independent methods compare?. *Proceedings of Annual meeting of the British Chapter of International Society for Magnetic Resonance in Medicine.* Oxford, United Kingdom.

Bibliography

Al-Muhanna, A. F. (2022), Gadolinium retention after contrast-enhanced magnetic resonance imaging: A narratative review, *Saudi Journal of Medicine & Medical Sciences*, *10*(1), 12.

Alsop, D. C., and J. Detre (1996), Reduced transit-time sensitivity in noninvasive magnetic resonance imaging of human cerebral blood flow, *Journal of Cerebral Blood Flow & Metabolism*, *16*(6), 1236–1249.

Alsop, D. C., and J. A. Detre (1998), Multisection cerebral blood flow MR imaging with continuous arterial spin labeling., *Radiology*, *208*(2), 410–416.

Alsop, D. C., J. A. Detre, X. Golay, M. Günther, J. Hendrikse, L. Hernandez-Garcia, H. Lu, B. J. MacIntosh, L. M. Parkes, M. Smits, et al. (2015), Recommended implementation of arterial spin-labeled perfusion MRI for clinical applications: A consensus of the ISMRM perfusion study group and the European consortium for ASL in dementia, *Magnetic Resonance in Medicine*, *73*(1), 102–116.

Anazodo, U., and P. Croal (2021), ASL Challenge, OSF, `https://doi.org/10.17605/OSF.IO/6XYU3`.

Anazodo, U., J. Pinto, F. Kennedy McConnell, M.-E. Dounavi, C. Gould van Praag, H. Mutsaerts, A. Oliver-Taylor, A. Paschoal, J. Petr, D. Pineda-Ordóñez, J. Woods, M. Zhao, and P. Croal (2021), The Open Source Initiative for Perfusion Imaging (OSIPI) ASL MRI challenge, in *Proc. ISMRM 29th Annual Meeting (Virtual)*, p. 2714.

Antolak, A. G., and E. F. Jackson (2019), Development and evaluation of an arterial spin-labeling digital reference object for quality control and comparison of data analysis applications, *Physics in Medicine & Biology*, *64*(2), 02NT01.

Aslan, S., F. Xu, P. L. Wang, J. Uh, U. S. Yezhuvath, M. van Osch, and H. Lu (2010), Estimation of labeling efficiency in pseudocontinuous arterial spin labeling, *Magnetic Resonance in Medicine*, *63*(3), 765–771.

Baazaoui, H., S. Hubertus, M. E. Maros, S. A. Mohamed, A. Förster, L. R. Schad, and H. Wenz (2021), Artificial Neural Network-Derived Cerebral Metabolic Rate of Oxygen for Differentiating Glioblastoma and Brain Metastasis in MRI: A Feasibility Study, *Applied Sciences*, *11*(21), 9928.

Bauer, D. F., T. Russ, B. I. Waldkirch, C. Tönnes, W. P. Segars, L. R. Schad, F. G. Zöllner, and A.-K. Golla (2021), Generation of annotated multimodal ground truth datasets for abdominal medical image registration, *International journal of computer assisted radiology and surgery*, *16*(8), 1277–1285.

Bernstein, M. A., K. F. King, and X. J. Zhou (2004), *Handbook of MRI pulse sequences*, Elsevier.

Biagi, L., A. Abbruzzese, M. C. Bianchi, D. C. Alsop, A. Del Guerra, and M. Tosetti (2007), Age dependence of cerebral perfusion assessed by magnetic resonance continuous arterial spin labeling, *Journal of Magnetic Resonance Imaging*, *25*(4), 696–702.

Bloch, F. (1946), Nuclear induction, *Physical review*, *70*(7-8), 460.

Boer, R. (1995), Magnetization transfer contrast part 1: MR physics, *Medicamundi*, *40*(2), 64–73.

Bokkers, R. P., D. A. Hernandez, J. G. Merino, R. V. Mirasol, M. J. Van Osch, J. Hendrikse, S. Warach, and L. L. Latour (2012), Whole-brain arterial spin labeling perfusion MRI in patients with acute stroke, *Stroke*, *43*(5), 1290–1294.

Bones, I. K., A. A. Harteveld, S. L. Franklin, M. J. van Osch, J. Hendrikse, C. T. Moonen, C. Bos, and M. van Stralen (2019), Enabling free-breathing background suppressed renal pCASL using fat imaging and retrospective motion correction, *Magnetic Resonance in Medicine*, *82*(1), 276–288.

Bones, I. K., C. Bos, C. Moonen, J. Hendrikse, and M. van Stralen (2022), Workflow for automatic renal perfusion quantification using ASL-MRI and machine learning, *Magnetic Resonance in Medicine*, *87*(2), 800–809.

Brix, G., F. Kiessling, R. Lucht, S. Darai, K. Wasser, S. Delorme, and J. Griebel (2004), Microcirculation and microvasculature in breast tumors: pharmacokinetic analysis of dynamic MR image series, *Magnetic Resonance in Medicine*, *52*(2), 420–429.

Brown, R. W., Y.-C. N. Cheng, E. M. Haacke, M. R. Thompson, and R. Venkatesan (2014), *Magnetic resonance imaging: physical principles and sequence design*, John Wiley & Sons.

Brumer, I., D. F. Bauer, L. R. Schad, and F. G. Zöllner (2022a), Synthetic arterial spin labeling mri of the kidneys for evaluation of data processing pipeline, *Diagnostics*, *12*(8), 1854.

Brumer, I., S. Jonscher, I. Gineitaite, R. Echeverria-Chasco, L. R. Schad, M. A. Fernandez-Seara, and F. G. Zöllner (2022b), Assessing the influence of ECG-triggering and respiration strategy on ASL-based renal perfuson quantification: preliminary results, in *Proc. ISMRM Workshop - Perfusion MRI: From Head to Toe (Los Angeles, CA, USA - Virtual)*.

Brumer, I., S. Jonscher, I. Gineitaite, R. Echeverria-Chasco, L. R. Schad, M. A. Fernandez-Seara, and F. G. Zöllner (2022c), Investigating the influence of ECG-triggering and respiration strategy on renal perfusion quantified using arterial spin labelling, in *Proc. ISMRM 31st Annual Meeting (London, UK- Virtual)*.

Buxton, R. B., L. R. Frank, E. C. Wong, B. Siewert, S. Warach, and R. R. Edelman (1998), A general kinetic model for quantitative perfusion imaging with arterial spin labeling, *Magnetic Resonance in Medicine*, *40*(3), 383–396.

Cai, Y.-Z., Z.-C. Li, P.-L. Zuo, J. Pfeuffer, Y.-M. Li, F. Liu, and R.-B. Liu (2017), Diagnostic value of renal perfusion in patients with chronic kidney disease using 3d arterial spin labeling, *Journal of Magnetic Resonance Imaging*, *46*(2), 589–594.

Calamante, F., D. L. Thomas, G. S. Pell, J. Wiersma, and R. Turner (1999), Measuring cerebral blood flow using magnetic resonance imaging techniques, *Journal of Cerebral Blood Flow & Metabolism*, *19*(7), 701–735.

Camargo, A., and Z. Wang (2022), Estimating arterial transit time (ATT) from ASL MRI acquired at a single post-labeling-delay time, in *Proc. ISMRM 30th Annual Meeting (London, UK)*, p. 4974.

Çavuşoğlu, M., J. Pfeuffer, K. Uğurbil, and K. Uludağ (2009), Comparison of pulsed arterial spin labeling encoding schemes and absolute perfusion quantification, *Magnetic resonance imaging*, *27*(8), 1039–1045.

Cercignani, M., N. G. Dowell, and P. S. Tofts (2018), *Quantitative MRI of the brain: principles of physical measurement*, CRC Press.

Chandra, A., G. Dervenoulas, and M. Politis (2019), Magnetic resonance imaging in Alzheimer's disease and mild cognitive impairment, *Journal of neurology*, *266*(6), 1293–1302.

Chao, L. L., S. T. Buckley, J. Kornak, N. Schuff, C. Madison, K. Yaffe, B. L. Miller, J. H. Kramer, and M. W. Weiner (2010), ASL perfusion MRI predicts cognitive decline and

conversion from MCI to dementia, *Alzheimer disease and associated disorders*, *24*(1), 19.

Chen, Y., D. J. Wang, and J. A. Detre (2011), Test-retest reliability of arterial spin labeling with common labeling strategies, *Journal of Magnetic Resonance Imaging*, *33*(4), 940–949.

Chen, Z., X. Zhang, C. Yuan, X. Zhao, and M. J. van Osch (2017), Measuring the labeling efficiency of pseudocontinuous arterial spin labeling, *Magnetic resonance in medicine*, *77*(5), 1841–1852.

Cho, S. K., D. G. Na, J. W. Ryoo, H. G. Roh, C. H. Moon, H. S. Byun, and J. H. Kim (2002), Perfusion MR imaging: clinical utility for the differential diagnosis of various brain tumors, *Korean Journal of Radiology*, *3*(3), 171–179.

Conlin, C. C., N. Oesingmann, B. Bolster Jr., Y. Huang, V. S. Lee, and J. L. Zhang (2017), Renal plasma flow (RPF) measured with multiple-inversion-time arterial spin labeling (ASL) and tracer kinetic analysis: Validation against a dynamic contrast-enhancement method, *Magnetic resonance imaging*, *37*, 51–55.

Dai, W., D. Garcia, C. De Bazelaire, and D. C. Alsop (2008), Continuous flow-driven inversion for arterial spin labeling using pulsed radio frequency and gradient fields, *Magnetic Resonance in Medicine*, *60*(6), 1488–1497.

Damadian, R. (1971), Tumor detection by nuclear magnetic resonance, *Science*, *171*(3976), 1151–1153.

Damadian, R., M. Goldsmith, and L. Minkoff (1977), NMR in cancer: XVI. Fonar image of the live human body, *Physiological Chemistry*, *9*, 97–100.

Davies, N. P., and P. Jezzard (2003), Selective arterial spin labeling (SASL): perfusion territory mapping of selected feeding arteries tagged using two-dimensional radiofrequency pulses, *Magnetic Resonance in Medicine: An Official Journal of the International Society for Magnetic Resonance in Medicine*, *49*(6), 1133–1142.

De Bazelaire, C., N. M. Rofsky, G. Duhamel, M. D. Michaelson, D. George, and D. C. Alsop (2005), Arterial spin labeling blood flow magnetic resonance imaging for the characterization of metastatic renal cell carcinoma1, *Academic radiology*, *12*(3), 347–357.

De Bazelaire, C. M., G. D. Duhamel, N. M. Rofsky, and D. C. Alsop (2004), MR imaging relaxation times of abdominal and pelvic tissues measured in vivo at 3.0 T: preliminary results, *Radiology*, *230*(3), 652–659.

Deibler, A. R., J. M. Pollock, R. A. Kraft, H. Tan, J. H. Burdette, and J. A. Maldjian (2008), Arterial spin-labeling in routine clinical practice, part 2: hypoperfusion patterns, *American Journal of Neuroradiology*, *29*(7), 1235–1241.

Detre, J. A., and D. C. Alsop (1999), Perfusion magnetic resonance imaging with continuous arterial spin labeling: methods and clinical applications in the central nervous system, *European Journal of Radiology*, *30*(2), 115–124.

Detre, J. A., J. S. Leigh, D. S. Williams, and A. P. Koretsky (1992), Perfusion imaging, *Magnetic Resonance in Medicine*, *23*(1), 37–45.

Detre, J. A., J. Wang, Z. Wang, and H. Rao (2009), Arterial spin-labeled perfusion MRI in basic and clinical neuroscience, *Current Opinion in Neurology*, *22*(4), 348–355.

Dice, L. R. (1945), Measures of the amount of ecologic association between species, *Ecology*, *26*(3), 297–302.

Dixon, W. T., L. N. Du, D. D. Faul, M. Gado, and S. Rossnick (1986), Projection angiograms of blood labeled by adiabatic fast passage, *Magnetic Resonance in Medicine*, *3*(3), 454–462.

Dolui, S., Z. Wang, R. T. Shinohara, D. A. Wolk, J. A. Detre, and A. D. N. Initiative (2017), Structural Correlation-based Outlier Rejection (SCORE) algorithm for arterial spin labeling time series, *Journal of Magnetic Resonance Imaging*, *45*(6), 1786–1797.

Dong, J., L. Yang, T. Su, X. Yang, B. Chen, J. Zhang, X. Wang, and X. Jiang (2013), Quantitative assessment of acute kidney injury by noninvasive arterial spin labeling perfusion MRI: a pilot study, *Science China Life Sciences*, *56*(8), 745–750.

Dujardin, M., S. Sourbron, R. Luypaert, D. Verbeelen, and T. Stadnik (2005), Quantification of renal perfusion and function on a voxel-by-voxel basis: a feasibility study, *Magnetic Resonance in Medicine*, *54*(4), 841–849.

Ebrahimi, B., S. C. Textor, and L. O. Lerman (2014), Renal relevant radiology: renal functional magnetic resonance imaging, *Clinical Journal of the American Society of Nephrology*, *9*(2), 395–405.

Echeverria-Chasco, R., M. Vidorreta, V. Aramendía-Vidaurreta, D. Cano, J. Escalada, N. Garcia-Fernandez, G. Bastarrika, and M. A. Fernández-Seara (2021), Optimization of pseudo-continuous arterial spin labeling for renal perfusion imaging, *Magnetic Resonance in Medicine*, *85*(3), 1507–1521.

Edelman, R. R., B. Siewert, D. G. Darby, V. Thangaraj, A. C. Nobre, M. M. Mesulam, and S. Warach (1994), Qualitative mapping of cerebral blood flow and functional localization

with echo-planar MR imaging and signal targeting with alternating radio frequency., *Radiology*, *192*(2), 513–520.

Essig, M., M. S. Shiroishi, T. B. Nguyen, M. Saake, J. M. Provenzale, D. Enterline, N. Anzalone, A. Dörfler, À. Rovira, M. Wintermark, et al. (2013a), Perfusion MRI: the five most frequently asked technical questions, *American Journal of Roentgenology*, *200*(1), 24.

Essig, M., T. B. Nguyen, M. S. Shiroishi, M. Saake, J. M. Provenzale, D. S. Enterline, N. Anzalone, A. Dörfler, À. Rovira, M. Wintermark, et al. (2013b), Perfusion MRI: the five most frequently asked clinical questions, *American Journal of Roentgenology*, *201*(3).

Fan, A. P., H. Jahanian, S. J. Holdsworth, and G. Zaharchuk (2016), Comparison of cerebral blood flow measurement with ^{15}O-water positron emission tomography and arterial spin labeling magnetic resonance imaging: a systematic review, *Journal of Cerebral Blood Flow & Metabolism*, *36*(5), 842–861.

Fazlollahi, A., P. Bourgeat, X. Liang, F. Meriaudeau, A. Connelly, O. Salvado, and F. Calamante (2015), Reproducibility of multiphase pseudo-continuous arterial spin labeling and the effect of post-processing analysis methods, *NeuroImage*, *117*, 191–201.

Fick, A. (1870), Über die Messung des Blutquantums in den Herzventrikeln, XVI-XVII, Verhandlungen der Physikalisch-medizinische Gesellschaft zu Würzburg, `https://babel.hathitrust.org/cgi/pt?id=mdp.39015076673493&view=1up&seq=628`, (retrieved 10 February 2021).

Forsén, S., and R. A. Hoffman (1963), Study of moderately rapid chemical exchange reactions by means of nuclear magnetic double resonance, *The Journal of Chemical Physics*, *39*(11), 2892–2901.

Franklin, S. L., S. Schmid, C. Bos, and M. J. P. van Osch (2020), Influence of the cardiac cycle on velocity selective and acceleration selective arterial spin labeling, *Magnetic Resonance in Medicine*, *83*(3), 872–882.

Fushimi, Y., T. Okada, A. Yamamoto, M. Kanagaki, K. Fujimoto, and K. Togashi (2013), Timing dependence of peripheral pulse-wave-triggered pulsed arterial spin labeling, *NMR in Biomedicine*, *26*(11), 1527–1533.

Garcia, D. M., G. Duhamel, and D. C. Alsop (2005), Efficiency of inversion pulses for background suppressed arterial spin labeling, *Magnetic Resonance in Medicine*, *54*(2), 366–372.

Gerlach, W., and O. Stern (1922), Der experimentelle Nachweis der Richtungsquantelung im Magnetfeld, *Zeitschrift für Physik*, *9*(1), 349–352.

Gillis, K. A., C. McComb, J. E. Foster, A. H. Taylor, R. K. Patel, S. T. Morris, A. G. Jardine, M. P. Schneider, G. H. Roditi, C. Delles, et al. (2014), Inter-study reproducibility of arterial spin labelling magnetic resonance imaging for measurement of renal perfusion in healthy volunteers at 3 Tesla, *BMC Nephrology*, *15*(1), 1–10.

Gillis, K. A., C. McComb, R. K. Patel, K. K. Stevens, M. P. Schneider, A. Radjenovic, S. T. Morris, G. H. Roditi, C. Delles, and P. B. Mark (2016), Non-contrast renal magnetic resonance imaging to assess perfusion and corticomedullary differentiation in health and chronic kidney disease, *Nephron*, *133*(3), 183–192.

Grenier, N., F. Cornelis, Y. Le Bras, G. Rigou, J. R. Boutault, and M. Bouzgarrou (2013), Perfusion imaging in renal diseases, *Diagnostic and Interventional Imaging*, *94*(12), 1313–1322.

Griswold, M. A., P. M. Jakob, R. M. Heidemann, M. Nittka, V. Jellus, J. Wang, B. Kiefer, and A. Haase (2002), Generalized autocalibrating partially parallel acquisitions (GRAPPA), *Magnetic Resonance in Medicine*, *47*(6), 1202–1210.

Gudbjartsson, H., and S. Patz (1995), The Rician distribution of noisy MRI data, *Magnetic Resonance in Medicine*, *34*(6), 910–914.

Günther, M., K. Oshio, and D. A. Feinberg (2005), Single-shot 3D imaging techniques improve arterial spin labeling perfusion measurements, *Magnetic Resonance in Medicine*, *54*(2), 491–498.

Guo, J., and E. C. Wong (2015), Increased SNR efficiency in velocity selective arterial spin labeling using multiple velocity selective saturation modules (mm-VSASL), *Magnetic resonance in medicine*, *74*(3), 694–705.

Guo, J., J. A. Meakin, P. Jezzard, and E. C. Wong (2014), Velocity-selective arterial spin labeling using symmetric BIR-8 pulses, *Development and Applications of Velocity Selectivity in MRI*, p. 16.

Hacine-Gharbi, A., P. Ravier, R. Harba, and T. Mohamadi (2012), Low bias histogram-based estimation of mutual information for feature selection, *Pattern Recognition Letters*, *33*(10), 1302–1308.

Hahn, E. L. (1950), Spin echoes, *Physical Review*, *80*(4), 580.

Haller, S., G. Zaharchuk, D. L. Thomas, K.-O. Lovblad, F. Barkhof, and X. Golay (2016), Arterial spin labeling perfusion of the brain: emerging clinical applications, *Radiology*, *281*(2), 337–356.

Heijtel, D. F. R., H. J. M. M. Mutsaerts, E. Bakker, P. Schober, M. F. Stevens, E. T. Petersen, B. N. M. van Berckel, C. B. L. M. Majoie, J. Booij, M. J. P. van Osch, et al. (2014), Accuracy and precision of pseudo-continuous arterial spin labeling perfusion during baseline and hypercapnia: a head-to-head comparison with ^{15}O H_2O positron emission tomography, *Neuroimage*, *92*, 182–192.

Henkelman, R. M., G. J. Stanisz, and S. J. Graham (2001), Magnetization transfer in MRI: a review, *NMR in Biomedicine*, *14*(2), 57–64.

Hernandez-Garcia, L., A. Lahiri, and J. Schollenberger (2019), Recent progress in asl, *Neuroimage*, *187*, 3–16.

Hernandez-Garcia, L., V. Aramendia-Vidaurreta, D. S. Bolar, W. Dai, M. A. Fernández-Seara, J. Guo, A. J. Madhuranthakam, H. Mutsaerts, J. Petr, Q. Qin, et al. (2022), Recent technical developments in ASL: A review of the state of the art, *Magnetic Resonance in Medicine*.

Herscovitch, P., and M. E. Raichle (1985), What is the correct value for the brain-blood partition coefficient for water?, *Journal of Cerebral Blood Flow & Metabolism*, *5*(1), 65–69.

Herscovitch, P., J. Markham, and M. Raichle (1983), Brain blood flow measured with intravenous $H_2{}^{15}O$. I. Theory and error analysis, *Journal of Nuclear Medicine*, *24*(9), 782–789.

Ho, M.-L. (2018), Arterial spin labeling: clinical applications, *Journal of Neuroradiology*, *45*(5), 276–289.

Hueper, K., F. Gueler, J. H. Bräsen, M. Gutberlet, M.-S. Jang, F. Lehner, N. Richter, N. Hanke, M. Peperhove, P. Martirosian, et al. (2015), Functional MRI detects perfusion impairment in renal allografts with delayed graft function, *American Journal of Physiology-Renal Physiology*, *308*(12), F1444–F1451.

Huizinga, W., D. H. Poot, J.-M. Guyader, R. Klaassen, B. F. Coolen, M. van Kranenburg, R. J. M. Van Geuns, A. Uitterdijk, M. Polfliet, J. Vandemeulebroucke, et al. (2016), PCA-based groupwise image registration for quantitative MRI, *Medical Image Analysis*, *29*, 65–78.

Jezzard, P., M. A. Chappell, and T. W. Okell (2018), Arterial spin labeling for the measurement of cerebral perfusion and angiography, *Journal of Cerebral Blood Flow & Metabolism*, *38*(4), 603–626.

Johnson, R. J., J. Feehally, and J. Floege (2014), *Comprehensive clinical nephrology E-Book*, Elsevier Health Sciences.

Kanda, T., T. Fukusato, M. Matsuda, K. Toyoda, H. Oba, J. Kotoku, T. Haruyama, K. Kitajima, and S. Furui (2015), Gadolinium-based contrast agent accumulates in the brain even in subjects without severe renal dysfunction: evaluation of autopsy brain specimens with inductively coupled plasma mass spectroscopy, *Radiology*, *276*(1), 228–232.

Keil, V. C., N. S. Hartkamp, D. J. A. Connolly, G. Morana, M. H. G. Dremmen, H. J. M. M. Mutsaerts, and M. H. Lequin (2019), Added value of arterial spin labeling magnetic resonance imaging in pediatric neuroradiology: pitfalls and applications, *Pediatric Radiology*, *49*(2), 245–253.

Kety, S. S., and C. F. Schmidt (1945), The determination of cerebral blood flow in man by the use of nitrous oxide in low concentrations, *American Journal of Physiology-Legacy Content*, *143*(1), 53–66.

Kim, B. J., H. G. Kang, H.-J. Kim, S.-H. Ahn, N. Y. Kim, S. Warach, and D.-W. Kang (2014), Magnetic resonance imaging in acute ischemic stroke treatment, *Journal of stroke*, *16*(3), 131.

Kim, D. W., W. H. Shim, S. K. Yoon, J. Y. Oh, J. K. Kim, H. Jung, T. Matsuda, and D. Kim (2017), Measurement of arterial transit time and renal blood flow using pseudocontinuous ASL MRI with multiple post-labeling delays: Feasibility, reproducibility, and variation, *Journal of Magnetic Resonance Imaging*, *46*(3), 813–819.

Kim, S.-G. (1995), Quantification of relative cerebral blood flow change by flow-sensitive alternating inversion recovery (FAIR) technique: application to functional mapping, *Magnetic Resonance in Medicine*, *34*(3), 293–301.

Klein, S., M. Staring, K. Murphy, M. A. Viergever, and J. P. Pluim (2009a), Elastix: a toolbox for intensity-based medical image registration, *IEEE transactions on medical imaging*, *29*(1), 196–205.

Klein, S., J. P. W. Pluim, M. Staring, and M. A. Viergever (2009b), Adaptive stochastic gradient descent optimisation for image registration, *International Journal of Computer Vision*, *81*(3), 227.

Kolmogorov, A. (1933), Sulla determinazione empirica di una lgge di distribuzione, *Inst. Ital. Attuari, Giorn.*, *4*, 83–91.

Kröner, E. S. J., H. J. Lamb, H.-M. J. Siebelink, S. C. Cannegieter, P. J. van den Boogaard, E. E. van der Wall, A. de Roos, and J. J. Westenberg (2014), Pulse wave velocity and flow in the carotid artery versus the aortic arch: effects of aging, *Journal of Magnetic Resonance Imaging*, *40*(2), 287–293.

Kwong, K. K., J. W. Belliveau, D. A. Chesler, I. E. Goldberg, R. M. Weisskoff, B. P. Poncelet, D. N. Kennedy, B. E. Hoppel, M. S. Cohen, and R. Turner (1992), Dynamic magnetic resonance imaging of human brain activity during primary sensory stimulation., *Proceedings of the National Academy of Sciences*, *89*(12), 5675–5679.

Kwong, K. K., D. A. Chesler, R. M. Weisskoff, K. M. Donahue, T. L. Davis, L. Ostergaard, T. A. Campbell, and B. R. Rosen (1995), MR perfusion studies with T_1-weighted echo planar imaging, *Magnetic Resonance in Medicine*, *34*(6), 878–887.

Landes, V., A. Javed, T. Jao, Q. Qin, and K. Nayak (2020), Improved velocity-selective labeling pulses for myocardial ASL, *Magnetic Resonance in Medicine*.

Lanzman, R. S., H.-J. Wittsack, P. Martirosian, P. Zgoura, P. Bilk, P. Kröpil, F. Schick, A. Voiculescu, and D. Blondin (2010), Quantification of renal allograft perfusion using arterial spin labeling MRI: initial results, *European radiology*, *20*(6), 1485–1491.

Lanzman, R. S., P. M. Robson, M. R. Sun, A. D. Patel, K. Mentore, A. A. Wagner, E. M. Genega, N. M. Rofsky, D. C. Alsop, and I. Pedrosa (2012), Arterial spin-labeling MR imaging of renal masses: correlation with histopathologic findings, *Radiology*, *265*(3), 799.

Lauterbur, P. C. (1973), Image formation by induced local interactions: examples employing nuclear magnetic resonance, *nature*, *242*(5394), 190–191.

Li, L.-P., H. Tan, J. M. Thacker, W. Li, Y. Zhou, O. Kohn, S. M. Sprague, and P. V. Prasad (2017), Evaluation of renal blood flow in chronic kidney disease using arterial spin labeling perfusion magnetic resonance imaging, *Kidney international reports*, *2*(1), 36–43.

Li, S., F. G. Zöllner, A. D. Merrem, Y. Peng, J. Roervik, A. Lundervold, and L. R. Schad (2012), Wavelet-based segmentation of renal compartments in DCE-MRI of human kidney: initial results in patients and healthy volunteers, *Computerized Medical Imaging and Graphics*, *36*(2), 108–118.

Li, Y., S. Dolui, D.-F. Xie, Z. Wang, A. D. N. Initiative, et al. (2018a), Priors-guided slice-wise adaptive outlier cleaning for arterial spin labeling perfusion MRI, *Journal of Neuroscience Methods*, *307*, 248–253.

Li, Y., D. Mao, Z. Li, M. Schär, J. J. Pillai, J. G. Pipe, and H. Lu (2018b), Cardiac-triggered pseudo-continuous arterial-spin-labeling: A cost-effective scheme to further enhance the reliability of arterial-spin-labeling MRI, *Magnetic Resonance in Medicine*, *80*(3), 969–975.

Lilliefors, H. W. (1967), On the Kolmogorov-Smirnov test for normality with mean and variance unknown, *Journal of the American statistical Association*, *62*(318), 399–402.

Luna, L. P., A. Ahmed, L. Daftaribesheli, F. Deng, J. Intrapiromkul, B. A. Lanzman, and V. Yedavalli (2022), Arterial spin labeling clinical applications for brain tumors and tumor treatment complications: A comprehensive case-based review, *The Neuroradiology Journal*, p. 19714009221114444.

Maccotta, L., J. A. Detre, and D. C. Alsop (1997), The efficiency of adiabatic inversion for perfusion imaging by arterial spin labeling, *NMR in Biomedicine*, *10*(4-5), 216–221.

MacIntosh, B., A. C. Lindsay, I. Kylintireas, W. Kuker, M. Günther, M. Robson, J. Kennedy, R. P. Choudhury, and P. Jezzard (2010), Multiple inflow pulsed arterial spin-labeling reveals delays in the arterial arrival time in minor stroke and transient ischemic attack, *American journal of neuroradiology*, *31*(10), 1892–1894.

Maes, F., A. Collignon, D. Vandermeulen, G. Marchal, and P. Suetens (1997), Multimodality image registration by maximization of mutual information, *IEEE transactions on Medical Imaging*, *16*(2), 187–198.

Mansfield, P. (1977), Multi-planar image formation using NMR spin echoes, *Journal of Physics C: Solid State Physics*, *10*(3), L55.

Mansfield, P., and P. K. Grannell (1973), NMR 'diffraction' in solids?, *Journal of Physics C: solid state physics*, *6*(22), L422.

Mansfield, P., and A. A. Maudsley (1976), Line scan proton spin imaging in biological structures by NMR, *Physics in Medicine & Biology*, *21*(5), 847.

Martirosian, P., U. Klose, I. Mader, and F. Schick (2004), FAIR true-FISP perfusion imaging of the kidneys, *Magnetic Resonance in Medicine*, *51*(2), 353–361.

Maumet, C., P. Maurel, J.-C. Ferré, and C. Barillot (2014), Robust estimation of the cerebral blood flow in arterial spin labelling, *Magnetic Resonance Imaging*, *32*(5), 497–504.

McDonald, R. J., D. Levine, J. Weinreb, E. Kanal, M. S. Davenport, J. H. Ellis, P. M. Jacobs, R. E. Lenkinski, K. R. Maravilla, M. R. Prince, et al. (2018), Gadolinium retention: a research roadmap from the 2018 NIH/ACR/RSNA workshop on gadolinium chelates, *Radiology*, *289*(2), 517.

McRobbie, D. W., E. A. Moore, M. J. Graves, and M. R. Prince (2017), *MRI from Picture to Proton*, Cambridge university press.

Merrem, A. D., F. G. Zöllner, M. Reich, A. Lundervold, J. Rorvik, and L. R. Schad (2013), A variational approach to image registration in dynamic contrast-enhanced MRI of the human kidney, *Magnetic resonance imaging*, *31*(5), 771–777.

Messroghli, D. R., A. Radjenovic, S. Kozerke, D. M. Higgins, M. U. Sivananthan, and J. P. Ridgway (2004), Modified Look-Locker inversion recovery (MOLLI) for high-resolution T_1 mapping of the heart, *Magnetic Resonance in Medicine*, *52*(1), 141–146.

Milani, B., A. Ansaloni, S. Sousa-Guimaraes, N. Vakilzadeh, M. Piskunowicz, B. Vogt, M. Stuber, M. Burnier, and M. Pruijm (2017), Reduction of cortical oxygenation in chronic kidney disease: evidence obtained with a new analysis method of blood oxygenation level-dependent magnetic resonance imaging, *Nephrology Dialysis Transplantation*, *32*(12), 2097–2105.

Mora-Gutiérrez, J. M., N. Garcia-Fernandez, M. F. Slon Roblero, J. A. Páramo, F. J. Escalada, D. J. Wang, A. Benito, and M. A. Fernández-Seara (2017), Arterial spin labeling MRI is able to detect early hemodynamic changes in diabetic nephropathy, *Journal of Magnetic Resonance Imaging*, *46*(6), 1810–1817.

Nery, F., I. Gordon, and D. L. Thomas (2018), Non-invasive renal perfusion imaging using arterial spin labeling MRI: challenges and opportunities, *Diagnostics*, *8*(1), 2.

Nery, F., C. E. Buchanan, A. A. Harteveld, A. Odudu, O. Bane, E. F. Cox, K. Derlin, H. M. Gach, X. Golay, M. Gutberlet, et al. (2020), Consensus-based technical recommendations for clinical translation of renal ASL MRI, *Magnetic Resonance Materials in Physics, Biology and Medicine*, *33*(1), 141–161.

Nezamzadeh, M., G. B. Matson, K. Young, M. W. Weiner, and N. Schuff (2010), Improved pseudo-continuous arterial spin labeling for mapping brain perfusion, *Journal of Magnetic Resonance Imaging*, *31*(6), 1419–1427.

Nishimura, D. G. (1996), *Principles of magnetic resonance imaging*, Stanford University.

Notohamiprodjo, M., M. F. Reiser, and S. P. Sourbron (2010), Diffusion and perfusion of the kidney, *European journal of radiology*, *76*(3), 337–347.

Odudu, A., F. Nery, A. A. Harteveld, R. G. Evans, D. Pendse, C. E. Buchanan, S. T. Francis, and M. A. Fernández-Seara (2018), Arterial spin labelling MRI to measure renal perfusion: a systematic review and statement paper, *Nephrology Dialysis Transplantation*, *33*(suppl_2), ii15–ii21.

Oliver-Taylor, A., T. Hampshire, N. A. S. Smith, M. Stritt, J. Petr, J. Gregori, M. Günther, H. Mutsaerts, and X. Golay (2021a), ASLDRO: Digital reference object software

for arterial spin labelling, in *Proc. ISMRM 29th Annual Meeting (Virtual)*, p. 2731, pypi.org/project/asldro.

Oliver-Taylor, A., K. Sharma, S. P. Sourbron, and X. Golay (2021b), A renal digital reference object for arterial spin labelling, in *Proc. ISMRM Workshop - Kidney MRI Biomarkers: The Route to Clinical Application (Lisbon, Portugal - Virtual)*.

Ordidge, R. J., M. Wylezinska, J. W. Hugg, E. Butterworth, and F. Franconi (1996), Frequency offset corrected inversion (FOCI) pulses for use in localized spectroscopy, *Magnetic Resonance in Medicine*, *36*(4), 562–566.

Oshio, K., and D. A. Feinberg (1991), GRASE (gradient-and spin-echo) imaging: a novel fast MRI technique, *Magnetic Resonance in Medicine*, *20*(2), 344–349.

Pasca, L., F. Sanvito, E. Ballante, M. Totaro, M. Paoletti, A. Bergui, C. Varesio, E. Rognone, V. De Giorgis, and A. Pichiecchio (2021), Arterial spin labelling qualitative assessment in paediatric patients with MRI-negative epilepsy, *Clinical Radiology*, *76*(12), 942–e15.

Pendse, N., M. Wissmeyer, S. Altrichter, M. Vargas, J. Delavelle, M. Viallon, A. Federspiel, M. Seeck, K. Schaller, and K.-O. Lövblad (2010), Interictal arterial spin-labeling MRI perfusion in intractable epilepsy, *Journal of neuroradiology*, *37*(1), 60–63.

Petersen, E., I. Zimine, Y. L. Ho, and X. Golay (2006a), Non-invasive measurement of perfusion: a critical review of arterial spin labelling techniques, *The British Journal of Radiology*, *79*(944), 688–701.

Petersen, E. T., T. Lim, and X. Golay (2006b), Model-free arterial spin labeling quantification approach for perfusion MRI, *Magnetic Resonance in Medicine*, *55*(2), 219–232.

Pettigrew, R. I., L. Avruch, W. Dannels, J. Coumans, and M. E. Bernardino (1986), Fast-field-echo MR imaging with gd-DTPA: physiologic evaluation of the kidney and liver., *Radiology*, *160*(2), 561–563.

Pinto, J., M. A. Chappell, T. W. Okell, M. Mezue, A. R. Segerdahl, I. Tracey, P. Vilela, and P. Figueiredo (2020), Calibration of arterial spin labeling data—potential pitfalls in post-processing, *Magnetic Resonance in Medicine*, *83*(4), 1222–1234.

Pluim, J. P., J. B. A. Maintz, and M. A. Viergever (2003), Mutual-information-based registration of medical images: a survey, *IEEE transactions on medical imaging*, *22*(8), 986–1004.

Poser, B. A., P. J. Koopmans, T. Witzel, L. L. Wald, and M. Barth (2010), Three dimensional echo-planar imaging at 7 Tesla, *Neuroimage*, *51*(1), 261–266.

Provenzale, J. M., S. Mukundan, and D. P. Barboriak (2006), Diffusion-weighted and perfusion MR imaging for brain tumor characterization and assessment of treatment response, *Radiology*, *239*(3), 632–649.

Pruessmann, K. P., M. Weiger, M. B. Scheidegger, and P. Boesiger (1999), SENSE: sensitivity encoding for fast MRI, *Magnetic Resonance in Medicine*, *42*(5), 952–962.

Purcell, E. M., H. C. Torrey, and R. V. Pound (1946), Resonance absorption by nuclear magnetic moments in a solid, *Physical review*, *69*(1-2), 37.

Qin, Q., and P. C. M. van Zijl (2016), Velocity-selective-inversion prepared arterial spin labeling, *Magnetic Resonance in Medicine*, *76*(4), 1136–1148.

Qin, Q., T. Shin, M. Schär, H. Guo, H. Chen, and Y. Qiao (2016), Velocity-selective magnetization-prepared non-contrast-enhanced cerebral MR angiography at 3 Tesla: improved immunity to B0/B1 inhomogeneity, *Magnetic resonance in medicine*, *75*(3), 1232–1241.

Qin, Q., D. C. Alsop, D. S. Bolar, L. Hernandez-Garcia, J. Meakin, D. Liu, K. S. Nayak, S. Schmid, M. J. van Osch, E. C. Wong, et al. (2022), Velocity-selective arterial spin labeling perfusion MRI: A review of the state of the art and recommendations for clinical implementation, *Magnetic Resonance in Medicine*.

Quattrocchi, C. C., and A. J. Van der Molen (2021), Gadolinium retention in brain and body: Clinical and preclinical evidence, in *Imaging in Nephrology*, pp. 67–78, Springer.

Rabi, I. I., J. R. Zacharias, S. Millman, and P. Kusch (1938), A new method of measuring nuclear magnetic moment, *Physical review*, *53*(4), 318.

Radbruch, A., L. D. Weberling, P. J. Kieslich, O. Eidel, S. Burth, P. Kickingereder, S. Heiland, W. Wick, H.-P. Schlemmer, and M. Bendszus (2015), Gadolinium retention in the dentate nucleus and globus pallidus is dependent on the class of contrast agent, *Radiology*, *275*(3), 783–791.

Raichle, M. E., W. R. Martin, P. Herscovitch, M. A. Mintun, and J. Markham (1983), Brain blood flow measured with intravenous $H_2{}^{15}O$.: II. Implementation and validation, *Journal of Nuclear Medicine*, *24*(9), 790–798.

Rayner, H. C., M. E. Thomas, and D. V. Milford (2020), Kidney anatomy and physiology: The basis of clinical nephrology, in *Understanding Kidney Diseases*, pp. 1–9, Springer.

Razek, A. A. K. A., M. Talaat, L. El-Serougy, G. Gaballa, and M. Abdelsalam (2019), Clinical applications of arterial spin labeling in brain tumors, *Journal of computer assisted tomography*, *43*(4), 525–532.

Reeder, S. B. (2007), Measurement of signal-to-noise ratio and parallel imaging, in *Parallel imaging in clinical MR applications*, pp. 49–61, Springer.

Ren, T., C.-L. Wen, L.-H. Chen, S.-S. Xie, Y. Cheng, Y.-X. Fu, N. Oesingmann, A. de Oliveira, P.-L. Zuo, J.-Z. Yin, et al. (2016), Evaluation of renal allografts function early after transplantation using intravoxel incoherent motion and arterial spin labeling MRI, *Magnetic resonance imaging*, *34*(7), 908–914.

Rice, S. O. (1944), Mathematical analysis of random noise, *The Bell System Technical Journal*, *23*(3), 282–332.

Roberts, D. A., J. A. Detre, L. Bolinger, E. K. Insko, R. E. Lenkinski, M. J. Pentecost, and J. S. Leigh Jr (1995), Renal perfusion in humans: MR imaging with spin tagging of arterial water., *Radiology*, *196*(1), 281–286.

Robson, P. M., A. J. Madhuranthakam, W. Dai, I. Pedrosa, N. M. Rofsky, and D. C. Alsop (2009), Strategies for reducing respiratory motion artifacts in renal perfusion imaging with arterial spin labeling, *Magnetic Resonance in Medicine*, *61*(6), 1374–1387.

Rossi, C., F. Artunc, P. Martirosian, H.-P. Schlemmer, F. Schick, and A. Boss (2012), Histogram analysis of renal arterial spin labeling perfusion data reveals differences between volunteers and patients with mild chronic kidney disease, *Investigative radiology*, *47*(8), 490–496.

Runge, V. M., J. A. Clanton, W. A. Herzer, S. J. Gibbs, A. C. Price, C. L. Partain, and A. E. James Jr (1984), Intravascular contrast agents suitable for magnetic resonance imaging., *Radiology*, *153*(1), 171–176.

Schmid, S., E. Ghariq, W. M. Teeuwisse, A. Webb, and M. J. van Osch (2014), Acceleration-selective arterial spin labeling, *Magnetic Resonance in Medicine*, *71*(1), 191–199.

Schnurr, A., C. Drees, L. R. Schad, and F. G. Zöllner (2019), Comparing sample mining schemes for cnn kidney segmentation in t1w mri, in *3rd International Conference on Functional Renal Imaging (Nottingham, UK)*.

Schollenberger, J., C. A. Figueroa, J.-F. Nielsen, and L. Hernandez-Garcia (2020), Practical considerations for territorial perfusion mapping in the cerebral circulation using super-selective pseudo-continuous arterial spin labeling, *Magnetic Resonance in Medicine*, *83*(2), 492–504.

Segars, W. P., G. Sturgeon, S. Mendonca, J. Grimes, and B. M. W. Tsui (2010), 4D XCAT phantom for multimodality imaging research, *Medical Physics*, *37*(9), 4902–4915.

Shamonin, D. P., E. E. Bron, B. P. F. Lelieveldt, M. Smits, S. Klein, and M. Staring (2014), Fast parallel image registration on CPU and GPU for diagnostic classification of Alzheimer's disease, *Frontiers in Neuroinformatics*, *7*, 50.

Shannon, C. E. (1948a), A mathematical theory of communication, *The Bell system technical journal*, *27*(3), 379–423.

Shannon, C. E. (1948b), A mathematical theory of communication, *The Bell System Technical Journal*, *27*(4), 623–656.

Shin, T., B. S. Hu, and D. G. Nishimura (2013), Off-resonance-robust velocity-selective magnetization preparation for non-contrast-enhanced peripheral MR angiography, *Magnetic Resonance in Medicine*, *70*(5), 1229–1240.

Smirnov, N. V. (1939), Estimate of deviation between empirical distribution functions in two independent samples, *Bulletin Moscow University*, *2*(2), 3–16.

Song, H., D. Ruan, W. Liu, V. A. Stenger, R. Pohmann, M. A. Fernández-Seara, T. Nair, S. Jung, J. Luo, Y. Motai, et al. (2017), Respiratory motion prediction and prospective correction for free-breathing arterial spin-labeled perfusion MRI of the kidneys, *Medical physics*, *44*(3), 962–973.

Sourbron, S. P., H. J. Michaely, M. F. Reiser, and S. O. Schoenberg (2008), MRI-measurement of perfusion and glomerular filtration in the human kidney with a separable compartment model, *Investigative Radiology*, *43*(1), 40–48.

Spijkerman, J. M., E. T. Petersen, J. Hendrikse, P. Luijten, and J. J. M. Zwanenburg (2018), T 2 mapping of cerebrospinal fluid: 3 T versus 7 T, *Magnetic Resonance Materials in Physics, Biology and Medicine*, *31*(3), 415–424.

Staffaroni, A. M., Y. Cobigo, F. M. Elahi, K. B. Casaletto, S. M. Walters, A. Wolf, C. A. Lindbergh, H. J. Rosen, and J. H. Kramer (2019), A longitudinal characterization of perfusion in the aging brain and associations with cognition and neural structure, *Human brain mapping*, *40*(12), 3522–3533.

Stanisz, G. J., E. E. Odrobina, J. Pun, M. Escaravage, S. J. Graham, M. J. Bronskill, and R. M. Henkelman (2005), T_1, T_2 relaxation and magnetization transfer in tissue at 3T, *Magnetic Resonance in Medicine*, *54*(3), 507–512.

Student (1908), The probable error of a mean, *Biometrika*, pp. 1–25.

Studholme, C., D. L. Hill, and D. J. Hawkes (1999), An overlap invariant entropy measure of 3D medical image alignment, *Pattern recognition*, *32*(1), 71–86.

Sun, Y., W. Cao, W. Ding, Y. Wang, X. Han, Y. Zhou, Q. Xu, Y. Zhang, and J. Xu (2016), Cerebral blood flow alterations as assessed by 3D ASL in cognitive impairment in patients with subcortical vascular cognitive impairment: a marker for disease severity, *Frontiers in Aging Neuroscience*, *8*, 211.

Takei, N., S. Ishida, N. Kosaka, R. M. Lebel, Y. Matta, H. Kimura, and H. Kabasawa (2018), Free breathing multiple delays renal perfusion MRI using hadamard encoded pCASL, in *Proc. ISMRM 26th Annual Meeting (Paris, France)*.

Tan, H., J. A. Maldjian, J. M. Pollock, J. H. Burdette, L. Y. Yang, A. R. Deibler, and R. A. Kraft (2009), A fast, effective filtering method for improving clinical pulsed arterial spin labeling MRI, *Journal of Magnetic Resonance Imaging*, *29*(5), 1134–1139.

Taso, M., A. Guidon, and D. C. Alsop (2019), Influence of background suppression and retrospective realignment on free-breathing renal perfusion measurement using pseudo-continuous ASL, *Magnetic Resonance in Medicine*, *81*(4), 2439–2449.

Thanvi, B., and T. Robinson (2007), Complete occlusion of extracranial internal carotid artery: clinical features, pathophysiology, diagnosis and management, *Postgraduate medical journal*, *83*(976), 95–99.

Thomas, S., S. Hubertus, A. Lee, S. Vollstädt-Klein, and L. R. Schad (2020), Chronic effects of smoking on the brain oxygenation and perfusion using ASL and quantitative BOLD MRI, in *Proc. ISMRM 28th Annual Meeting (Virtual)*.

Thomsen, H. S., P. Marckmann, and V. B. Logager (2007), Nephrogenic systemic fibrosis (NSF): a late adverse reaction to some of the gadolinium based contrast agents, *Cancer Imaging*, *7*(1), 130.

van Gelderen, P., J. A. De Zwart, and J. Duyn (2008), Pittfalls of MRI measurement of white matter perfusion based on arterial spin labeling, *Magnetic Resonance in Medicine*, *59*(4), 788–795.

van Laar, P. J., J. van der Grond, and J. Hendrikse (2008), Brain perfusion territory imaging: methods and clinical applications of selective arterial spin-labeling MR imaging, *Radiology*, *246*(2), 354–364.

Verbree, J., and M. J. P. van Osch (2018), Influence of the cardiac cycle on pCASL: cardiac triggering of the end-of-labeling, *Magnetic Resonance Materials in Physics, Biology and Medicine*, *31*(1), 223–233.

Vidaurreta, V. A. (2020), Non-invasive evaluation of myocardial perfusion in humans using arterial spin labeling magnetic resonance imaging, Ph.D. thesis, Universidad de Navarra.

Wang, J., D. C. Alsop, H. K. Song, J. A. Maldjian, K. Tang, A. E. Salvucci, and J. A. Detre (2003), Arterial transit time imaging with flow encoding arterial spin tagging (FEAST), *Magnetic Resonance in Medicine*, *50*(3), 599–607.

Wang, Z. (2012), Improving cerebral blood flow quantification for arterial spin labeled perfusion MRI by removing residual motion artifacts and global signal fluctuations, *Magnetic resonance imaging*, *30*(10), 1409–1415.

Wang, Z., A. C. Bovik, H. R. Sheikh, and E. P. Simoncelli (2004), Image quality assessment: from error visibility to structural similarity, *IEEE transactions on image processing*, *13*(4), 600–612.

Wang, Z., S. R. Das, S. X. Xie, S. E. Arnold, J. A. Detre, D. A. Wolk, A. D. N. Initiative, et al. (2013), Arterial spin labeled MRI in prodromal Alzheimer's disease: a multi-site study, *NeuroImage: Clinical*, *2*, 630–636.

Wen, Q., and D. B. Chklovskii (2005), Segregation of the brain into gray and white matter: a design minimizing conduction delays, *PLoS Computational Biology*, *1*(7), e78.

Wilcoxon, F. (1992), Individual comparisons by ranking methods, in *Breakthroughs in statistics*, pp. 196–202, Springer.

Williams, D. S., J. A. Detre, J. S. Leigh, and A. P. Koretsky (1992), Magnetic resonance imaging of perfusion using spin inversion of arterial water, *Proceedings of the National Academy of Sciences*, *89*(1), 212–216.

Wintermark, M., D. Lepori, J. Cotting, E. Roulet, G. van Melle, R. Meuli, P. Maeder, L. Regli, F. R. Verdun, T. Deonna, et al. (2004), Brain perfusion in children: evolution with age assessed by quantitative perfusion computed tomography, *Pediatrics*, *113*(6), 1642–1652.

Wintermark, P., and S. K. Warfield (2012), New insights in perinatal arterial ischemic stroke by assessing brain perfusion, *Translational stroke research*, *3*(2), 255–262.

Wissmann, L., C. Santelli, W. P. Segars, and S. Kozerke (2014), MRXCAT: Realistic numerical phantoms for cardiovascular magnetic resonance, *Journal of Cardiovascular Magnetic Resonance*, *16*(1), 1–11.

Wolff, S. D., and R. S. Balaban (1989), Magnetization transfer contrast (MTC) and tissue water proton relaxation in vivo, *Magnetic Resonance in Medicine*, *10*(1), 135–144.

Wong, E. C., R. B. Buxton, and L. R. Frank (1996), Quantitative imaging of perfusion using a single subtraction (QUIPSS), *NeuroImage*, *3*(3), S5.

Wong, E. C., R. B. Buxton, and L. R. Frank (1997), Implementation of quantitative perfusion imaging techniques for functional brain mapping using pulsed arterial spin labeling, *NMR in Biomedicine*, *10*(4-5), 237–249.

Wong, E. C., R. B. Buxton, and L. R. Frank (1998a), A theoretical and experimental comparison of continuous and pulsed arterial spin labeling techniques for quantitative perfusion imaging, *Magnetic Resonance in Medicine*, *40*(3), 348–355.

Wong, E. C., R. B. Buxton, and L. R. Frank (1998b), Quantitative imaging of perfusion using a single subtraction (QUIPSS and QUIPSS II), *Magnetic Resonance in Medicine*, *39*(5), 702–708.

Wong, E. C., M. Cronin, W.-C. Wu, B. Inglis, L. R. Frank, and T. T. Liu (2006), Velocity-selective arterial spin labeling, *Magnetic Resonance in Medicine*, *55*(6), 1334–1341.

Wu, W.-C., Y. Mazaheri, and E. C. Wong (2006), The effects of flow dispersion and cardiac pulsation in arterial spin labeling, *IEEE transactions on medical imaging*, *26*(1), 84–92.

Wu, W.-C., M. Fernández-Seara, J. A. Detre, F. W. Wehrli, and J. Wang (2007), A theoretical and experimental investigation of the tagging efficiency of pseudocontinuous arterial spin labeling, *Magnetic Resonance in Medicine*, *58*(5), 1020–1027.

Wu, W.-C., B. L. Edlow, M. A. Elliot, J. Wang, and J. A. Detre (2009), Physiological modulations in arterial spin labeling perfusion magnetic resonance imaging, *IEEE transactions on medical imaging*, *28*(5), 703–709.

Xu, G., H. A. Rowley, G. Wu, D. C. Alsop, A. Shankaranarayanan, M. Dowling, B. T. Christian, T. R. Oakes, and S. C. Johnson (2010), Reliability and precision of pseudo-continuous arterial spin labeling perfusion MRI on 3.0 T and comparison with ^{15}O-water PET in elderly subjects at risk for Alzheimer's disease, *NMR in Biomedicine*, *23*(3), 286–293.

Zaharchuk, G. (2007), Theoretical basis of hemodynamic MR imaging techniques to measure cerebral blood volume, cerebral blood flow, and permeability, *American Journal of Neuroradiology*, *28*(10), 1850–1858.

Zhang, J. L., and V. S. Lee (2020), Renal perfusion imaging by MRI, *Journal of Magnetic Resonance Imaging*, *52*(2), 369–379.

Zhang, K., H. Herzog, J. Mauler, C. Filss, T. W. Okell, E. R. Kops, L. Tellmann, T. Fischer, B. Brocke, W. Sturm, et al. (2014), Comparison of cerebral blood flow acquired by simultaneous [^{15}O] water positron emission tomography and arterial spin labeling magnetic resonance imaging, *Journal of Cerebral Blood Flow & Metabolism*, *34*(8), 1373–1380.

Zhang, N., M. L. Gordon, and T. E. Goldberg (2017), Cerebral blood flow measured by arterial spin labeling MRI at resting state in normal aging and Alzheimer's disease, *Neuroscience & Biobehavioral Reviews*, *72*, 168–175.

Zhang, X., E. T. Petersen, E. Ghariq, J. B. De Vis, A. G. Webb, W. M. Teeuwisse, J. Hendrikse, and M. J. P. Van Osch (2013), In vivo blood T_1 measurements at 1.5 T, 3 T, and 7 T, *Magnetic Resonance in Medicine*, *70*(4), 1082–1086.

Zhao, L., M. Vidorreta, S. Soman, J. A. Detre, and D. C. Alsop (2017), Improving the robustness of pseudo-continuous arterial spin labeling to off-resonance and pulsatile flow velocity, *Magnetic Resonance in Medicine*, *78*(4), 1342–1351.

Zöllner, F. G., R. Sance, P. Rogelj, M. J. Ledesma-Carbayo, J. Rørvik, A. Santos, and A. Lundervold (2009), Assessment of 3D DCE-MRI of the kidneys using non-rigid image registration and segmentation of voxel time courses, *Computerized Medical Imaging and Graphics*, *33*(3), 171–181.

Zöllner, F. G., E. Svarstad, A. Z. Munthe-Kaas, L. R. Schad, A. Lundervold, and J. Rørvik (2012), Assessment of kidney volumes from MRI: acquisition and segmentation techniques, *American Journal of Roentgenology*, *199*(5), 1060–1069.

Zöllner, F. G., A. Šerifović-Trbalić, G. Kabelitz, M. Kociński, A. Materka, and P. Rogelj (2020), Image registration in dynamic renal MRI—current status and prospects, *Magnetic Resonance Materials in Physics, Biology and Medicine*, *33*(1), 33–48.

Zöllner, F. G., M. Kociński, L. Hansen, A.-K. Golla, A. Šerifović-Trbalić, A. Lundervold, A. Materka, and P. Rogelj (2021), Kidney segmentation in renal magnetic resonance imaging-current status and prospects, *IEEE access*, *9*, 71,577–71,605.

Declaration

I hereby certify that I have only used the sources or materials indicated and have not made unauthorised use of services of a third party. Where the work of others has been quoted or reproduced, the source is always given.

I hereby affirm that I have not yet presented this thesis or parts thereof to a university as part of an examination or degree.

I hereby agree that the thesis may be checked under use of electronic data processing programmes on compliance with generally applicable scientific standards.

I hereby certify that the information provided in this declaration is true and correct. I am aware of the importance of a sworn affidavit and the criminal prosecution in case of a false or incomplete affidavit.

I hereby affirm that the above is the absolute truth to the best of my knowledge and that I have not concealed anything.

Mannheim, September 9^{th} 2022

Irène Elisabeth Brumer